Faculty of Science and Engineering

Western Australia School of Mines: Minerals, Energy and Chemical Engineering

Rock Physics Properties of Artificial Shales: Effect of Organic Matter Characteristics

Matthieu Cauchefert

This thesis is presented for the Degree of

Doctor of Philosophy

of

Curtin University

March 2019

Declaration

To the best of my knowledge and belief this thesis contains no material previously published by any other person except where due acknowledgment has been made.

This thesis contains no material which has been accepted for the award of any other degree or diploma in any university.

Signature: _____

Date: 12/03/2019 _____

Acknowledgements

The thesis project presented in this document is experimental at its core. Having a project centred on shale rock physics was exciting to me because there is a lot of possibilities yet unexplored in this field. The engineering of the two scientific apparatuses I developed specially for the purpose of this project was the most challenging yet the most rewarding aspect of my project. However its success relied on all the persons who helped me throughout the years.

Hence I wish to warmly thank my supervisors for their continued support and guidance throughout my thesis project. I thank Maxim Lebedev for his scientific expertise and practical skills that greatly helped me both in the laboratory and in my thought process. I thank Stephanie Vialle for her sound scientific contribution as well as pushing me to communicate and not to keep the struggle to myself. I thank Lionel Esteban without whom the development of the compaction cell would not have been possible and also for putting up with me on a daily basis.

I am truly grateful to all the persons who dedicated some of their time to help with the design and implementation of the scientific apparatuses created for the purpose of this project: Joel Sarout and Jeremie Dautriat, researchers at CSIRO. Bruce Maney, special projects manager at CSIRO, Sam Battah, Nareng engineering. Ian Penny, mechanical machine specialist at CSIRO. Neil Sturrock, instrumentation and electrical specialist at CSIRO. And Shane Kager, Rock Mechanics laboratory manager at CSIRO.

I also want to thank the CSIRO staff who shared their skills and scientific expertise on a wide array of disciplines that were crucial to the success of the project: Matthew Josh, Joel Sarout, Jeremie Dautriat, Belinda Godel and Claudio Delle Piane.

Additionally I want to thank Ausama Giwelli for introducing me to the subject area of artificial samples and Marina Pervukhina, the project leader of the SHARPP project who played a decisive role in the award of my scholarship.

Last but not least I thank my family and friends who were always behind me in the good times as much as in the hard times with their encouragements and moral support.

I am forever grateful that I was given the opportunity to work for more than three years at Curtin University and CSIRO. On this journey I was constantly surrounded with great minds that challenged my way of thinking, in an environment with equipment and resources truly out of the ordinary.

The research presented in this thesis was funded through the Curtin International Postgraduate Research Scholarship (CIPRS) in association with the CSIRO Shale Rock Physics and Petrophysics (SHARPP) project sponsored by Total.

Abstract

With the recent worldwide blooming of gas- and oil-shales exploration in unconventional petroleum systems, organic matter (OM) became of critical importance to understand the gas storage capacity and economic production to name a few. However the relationship between OM and its physical response remains poorly understood. The thesis proposes to evaluate the influence of organic matter (OM) on the physical response of 11 artificially designed shale samples, using a range of different variables including (i) OM thermal maturity, (ii) kerogen type, (iii) organic particles texture and (iv), their mode of deposition. To infer OM characteristics influence on physical properties, two sets of properties were investigated. They are of particular interest because of their classical use in laboratory testing and in well logging and geophysics measurements in petroleum systems: these are elastic and dielectric properties.

To this end, an advanced compaction cell was developed to artificially produce analogue shales under full control of all their physical parameters including OM components. The compaction cell reproduces the primary and secondary mechanical consolidation of a synthetic fresh sediment while continuously measuring elastic properties under controlled compaction. In particular, an innovative way to compute off-axis group and phase velocities was developed. The compaction cell apparatus is also able to discriminate between the loss of pore fluid and the elastic compression of solid particles in the volume decrease of the samples during compaction. Moreover the ultrasonic measurements were shown to be sensitive to the effect of pore pressure dissipation during compaction.

The 11 artificial shale samples presented here were then further characterized with dielectric tests, Rock-Eval pyrolysis and imaging techniques.

The results indicate that porosity reduction in early consolidation is related to the OM stiffness and in turn samples containing OM with a marine origin (kerogen type II) displayed a greater porosity decrease compared to land OM (kerogen type III) because marine OM is more compliant. At higher uniaxial compaction stresses when the solid particles are tightly packed the porosity decrease was correlated with the thermal maturity. The more mature samples contain kerogen with a higher internal porosity and lose more pore space via pore collapse mechanisms. The higher consolidation

state of mature samples induced an increase in P-wave anisotropy and a decrease in Vp/Vs ratio. The maximum anisotropy of the real part of the dielectric permittivity was positively correlated to the OM dry density which is an indicator of the kerogen to bitumen volume ratio.

Besides, The OM particle texture influences the elastic anisotropy parameters ε, δ, and the anisotropies of the imaginary dielectric permittivity and of the conductivity, with bigger OM particles increasing these parameters. The samples with marine OM, with a higher degree of consolidation, have higher dielectric anisotropies for all three parameters and are much more conductive than the land and inorganic samples.

Furthermore, the deposition method also affects the properties anisotropy. When the initial mixture has a high water content and the solid particles are allowed to settle by gravity (sedimentation method), the samples show a better initial distribution of grain contacts that subsequently increases the mechanical compression and grain creeping, in the vertical direction, during compaction. This induces an increase, in the vertical direction, of the samples ability to carry electrical charges and in compressional stiffness. Consequently the P-wave anisotropy ε and dielectric properties anisotropy were decreased compared to the samples prepared with the mixing method.

Finally linear relationships between P-wave vertical velocities and vertical conductivity were defined, as they both evolve linearly with porosity and were compared with data from the literature. Cross-property relationships depend on many unrelated parameters. Hence further work is necessary to define models with a physical basis that can take into account all the different variables of the sample set.

The outcomes of this project are two-fold. Firstly, the design and implementation of the new compaction cell is invaluable as it provides a robust way to simulate shale sediment in the laboratory with well controlled parameters and no preservation issues with elastic testing throughout compaction. Secondly, these findings can be used for the interpretation of sonic and dielectric logs, to account for anisotropy in the inversion of seismic imaging data and to customize theoretical property models. Notably, the relationships between physical properties and maturity brings a new outlook to the interpretations of logging data for the identification of HC rich shale reservoirs and the OM type and texture relationship with elastic anisotropy adds to the understanding of the elastic behaviour of organic-rich shales.

Table of contents

Chapter 1: Introduction

1-1- Context

For most of the history of oil and gas exploration and production, shale formation studies were limited to their role as cap rocks. The main objective of such studies was essentially to evaluate their sealing capacity and how to drill safely a well to access a conventional sandstone reservoir. Before the oil crisis of 1973 the oil and gas prices were low and the hydrocarbons (HC) present in source rocks such as shales were considered economically unviable, not to mention the lack of technological advancement to exploit them at the time. Moreover shales are notoriously difficult to study. Their very low hydraulic conductivity makes laboratory rock mechanics experiments very long and resource consuming due to the lack of control over their internal pore pressure gradient. Also the high clay content and its physical and chemical interactions with water such as swelling and the ion exchange reactions makes the preservation of natural shale samples a challenge. Small changes in water content can drastically alter the physical properties of shales. As a result this rock type remained understudied for a long time. However several factors gradually changed the industry. The two first oil crisis of 1973 and 1979 increased the crude oil price from just 20USD/barrel in early 1973 to 120USD/barrel in 1980. However the causes were mainly political. The lowering of the oil and gas prices in the late 80's and throughout the 90's prevented the development of interest for unconventional resources.

But from 2000 onward the steady increase in oil and gas demand, along with the increasing global awareness of the finiteness of oil and gas resources, especially conventional resources in the medium term resulted in a rising climate of uncertainty for the future of the industry and the prices started to rise again. Consequently the interest for unconventional oil and gas increased and the advances in directional well drilling and hydraulic fracturing allowed the first economic production of unconventional shale gas in 2009 in the United States. In the meantime the need for a better understanding of the physical properties of shales for exploration and petroleum engineering led to a growth of academic and industry shale studies.

1-2- Motivations

Nevertheless there still are many gaps in our understanding of shales from a rock physics point of view. Organic rich shales (gas- and oil-shales) act both as source rock and HC reservoirs. Thanks to their OM content they generate gas and/or oil with an economic value but remain hard to exploit. Indeed they have a very low hydraulic conductivity because of their clay-rich tight mineral matrix, along with amounts of HC trapped in nano-pores and a generally low TOC. The physics of OM are poorly understood because it is hard to characterize and separate from the mineral matrix. For instance, isolation of OM by chemical methods is problematic as some of its compounds are insoluble in organic solvents but some other are. Hence for any extraction method the resulting product will only partly represent the total organic content of a rock. However the OM of shales is of prime importance in many branches of the unconventional oil and gas industry (logging while drilling; laboratory testing; storage vs. sealing capacity; friability) because the properties of OM contrast from the mineral properties and therefore influences greatly the physical properties and their anisotropy in shale formations.

The two main caveats that were identified during the literature review (cf. chapter 2) are (i) Poor evaluation of anisotropy in shales. It was found that the lack of characterization of the full vertical transverse isotropic (VTI) stiffness tensor in shales leads to significant errors in sonic log and density log data when using empirical relationships to extrapolate missing information (Vernik & Milovac, 2011). A poorly defined stiffness tensor was also found to induce "incorrect estimates of rock and fluid properties" from seismic data (Sayers, et al., 2015). (ii) Under-estimation of the complexity of organic matter (OM) and its effect on the physical properties. A lot of studies use a single parameter to represent OM, mostly the Total Organic Carbon (TOC) but otherwise consider OM as a material of constant properties, which is an oversimplification to say the least. For instance different OM characteristics are linked to elastic properties in organic-rich shales such as their compliance (Sayers, et al., 2015), their thermal maturity (Allan, et al., 2015); (Curtis, et al., 2012) and indirectly their texture through the impact it has on maturity (Rahman, et al., 2018).

Besides, a few studies have linked elastic properties with electrical properties through cross-property relationships (Josh, 2014); (Carcione, et al., 2007). This shows that OM

characteristics that have an influence on elastic properties can potentially affect the electrical and dielectric properties as well and the combination of the two sets of measurements could therefore help to characterize the OM content of shale samples. Moreover the contrasting resistivity and polarizability of OM compared to inorganic minerals such as clays are a further indication that the dielectric method has the potential to become a strong tool for OM identification.

Due to the complexity of shales with many different factors contributing to the variability of their physical properties and the difficulty to obtain quality data on natural samples, it is arduous to identify the impact of a single parameter on a physical response. That is why it was decided to use an artificial sample approach to the problem. That way, we can produce samples with a simple, homogeneous structure, well-controlled characteristics and avoid preservation issues by testing samples during their consolidation and also right after production before degradation occurs. The sample set we present here is designed so that samples are mostly identical, with only a few characteristics being changed from sample to sample to assess their impact on physical properties. Among all the samples characteristics, hereafter the ones that remain unchanged across the sample sets will be referred to as "constant parameters" while the characteristics that differs between samples will be referred to as "target variables". The four target variables this project focuses on are: (1) the OM maturity, (2) its origin (land vs. marine), (3) its texture and (4) the deposition method before compaction.

1-3- Objectives

For the purpose of this project, two apparatuses were designed from scratch: the artificial maturation system by hydrous pyrolysis to obtain different levels of thermal maturity. And a compaction cell to produce artificial samples by applying a vertical uniaxial stress on a mix of initial components such as minerals, OM and pore fluid. This cell is equipped with sensors measuring the porosity, the bulk density, the mass of expelled pore fluid and the full transversely isotropic (TI) elastic tensor during compaction. To perfect the sample preparation process as well as to improve the design of the two apparatuses and increase the quality of the data acquired during compaction, tests were performed and a process of trial and error was carried out with the production of 15 samples in two initial sample sets. However these tests and early

experiments are not central to answering the thesis objectives (see appendices). Therefore, in the body of the thesis, the equipment and the workflow in its final most advanced state will be presented, along with the last sample set only, which is the largest and was designed as an improvement of the previous sample sets. This sample set is composed of 11 artificial shale samples with OM of two different origins analogous to kerogen type II and type III, three different levels of maturity, two different texture types and two deposition methods.

After compaction the samples went through a series of experiments to further characterize them: CT-scan, dielectric tests, optical microscopy images and Rock-Eval pyrolysis.

With that information in mind, the main objectives of the thesis are to:

- Demonstrate that the artificial samples are a suitable approach to the problem by verifying the stability of the constant parameters across the sample set and showing that measurement errors are low.

- Show that the OM characteristics have a strong impact on the elastic and dielectric properties by confirming already existing theories and finding new trends.

- Explain the variations seen between samples with the help of characterization tests such as porosity and bulk density measurements, Rock-Eval pyrolysis, CT-scan and optical microscopy images.

- Show the potential of elastic and dielectric data to be used in conjunction to characterize OM properties.

- Explore the possibilities of dielectric/elastic cross-property relationships which can be useful when one of the property is unavailable or more expensive to obtain.

1-4- Outline

To answer these objectives we first start by presenting, in Chapter 2, a review of published works with the aim to (i) understand the basic physics and geochemistry of organic shales relevant to the project, (ii) present the important aspects of unconventional reservoir exploration to identify how this work could contribute to the industry, (iii) introduce basic theoretical concepts for the properties of interests (iii)

evaluate the relevance of artificial samples with all the advantages and disadvantages, (iv) assess what characteristics are reproducible and what it means when comparing our results to natural samples dataset and.

Afterwards each tool used to produce and analyse the samples will be presented in two chapters. They provided different types of data that will be presented separately, in the chronological order of testing. The sections dedicated to each tool are mostly structured the same way: the principles and methodology, followed by the data processing and finally the results.

In Chapter 3 is describe everything that leads to the production of the artificial samples. First, by describing the sample preparation along with the complete workflow carried out on each sample and the list of the samples in the set that highlight the essential differences between them. Then the design of the two apparatuses created for the purpose of this project is detailed: the compaction cell and the hydrous pyrolysis apparatus. The processing of the data acquired during compaction will be presented and finally the results obtained from such data. The compaction data includes porosity and bulk density, mass of expelled pore fluid and ultrasonic response. In terms of results Chapter 3 has a focus on the data acquired continuously during the consolidation of the artificial samples.

Chapter 4 is dedicated to the tests carried out after compaction. A set of physical, geochemical and structural characterization of the final samples was carried out that represents the state of the samples at a single point in time. Hence further down the line most of the continuous data recorded during compaction with the compaction cell sensors can only be compared to the Chapter 4 results for the final values at the very end of the consolidation process. The post-compaction analysis includes: CT-scan imaging, used to assess the homogeneity of the samples and the structure of OM macro-particles; the dielectric tests measuring the dielectric permittivity and equivalent conductivity of slices of the samples under an alternative electric field over a wide range of frequencies and in two different directions; the optical microscopy images for the purpose of characterizing the texture of OM and inorganic particles at the microscopic scale and Rock-Eval pyrolysis that helps us quantify the maturity of the OM and the differences between the different OM origins employed (land and marine).

All the results will be combined in the interpretation Chapter 5. Observations of the variations in the physical properties and in the different characterization techniques will be employed to attempt explaining their physical cause. The significant cross-property relationships among the sample set between porosity, densities, elastic response, dielectric measurements and geochemical parameters will also be shown. The first three sections are intended to highlight the influence on physical properties of the intrinsic properties of OM such as maturity, texture and OM origin. Then the impact of the deposition method on the final properties of the samples is assessed and finally the effect of distribution of pore pressure on the elastic properties throughout the compaction experiments will be investigated.

In the conclusion, presented in Chapter 6, the findings are summarized and the answers the project brought to the initial objectives shown. We also demonstrate the applicability of our findings for unconventional exploration and laboratory testing on natural organic shales. We then detail the limitations of the project and the possibilities for improvement of the methods employed, as well as potential further work on the current dataset. Finally we explain the potential outcome in the field of shale rock physics in terms of modelling.

Chapter 2: Literature review of shales – formation and rock properties

Despite recent advances in petroleum technologies for exploration, prospection and enhanced oil/gas recovery in unconventional shale reservoirs, this sedimentary rock type -the most abundant on Earth- still remains under-studied and poorly understood.

The geological definition of shales differs somewhat from the industry definition. For the latter the definition arises mainly from their economic prospect. For example any ultra-tight and organic-rich sedimentary rock can be classified as "black shale". However to remain consistent from an academic point of view we will stick to the classical definition of shale: a clastic sedimentary rock with clay to silt-sized particles, presenting laminations and containing OM or not. This structure implies a low permeability. In terms of mineralogy, shale rocks present an important clay fraction (mainly illite, smectite and kaolinite), detrital silts (frequently quartz, feldspar) along with minerals with a diagenetic origin such as pyrite and cement (quartz and calcite). The OM content measured with the TOC varies between formations and can exceed 10%. However most shale formations have a much lower TOC with an average of 0.8% for all shales and 2.2% for shale source rocks (Law, 1999).

In this review we will present in the first two sections the extent of the knowledge about organic rich shales. I will show how they form and evolve through diagenetic processes and then we will explain how the industry treats such formations as unconventional reservoirs and the methods that are used to estimate how much HC can be produced from this rocks. Thereafter I will review in more details the literature for the two techniques of central interest in this project: Elastic testing and dielectric testing. These two sections will display the challenges and shortcomings the current literature has and how this project can bring new information to the fill gaps in knowledge, and how this is relevant to the industry. Then I will explain why we choose to carry out our project with artificial samples over natural ones. Finally I will summarize the key points of this review that form the premises of this project.

2-1- Natural formation of organic rich shale formations

2-1-1- Consolidation process of natural shale sediments

The process that leads to the formation of shale rocks involves a variety of physical and chemical mechanisms that occur at different times after the initial deposition. The whole process of formation of organic rich shales is summarized in the scheme presented in

Deposition

The untransformed original minerals of shales are very fine grained and thus typically deposit in bodies of water with a calm environment where the vertical distance between the surface waves and the floor is important, also named *fondo* depositional environment (Rich, 1951). Such an environment will generate sediments that alternate between thin silt and clay layers. The initial sediment presents the aspect of a mud and has a very high water content. Over time, as more material accumulates on the sea- or lake-bed the sediment undergoes burial and the vertical consolidation stress and temperature increase, leading to the slow consolidation of the sediment.

Mechanical consolidation

The first mechanism to occur after deposition is the primary mechanical consolidation. With the increase of the vertical load the water is expelled from the elastic porous medium during the primary consolidation (Biot, 1941) which leads to a decrease in porosity and an increase of the number of grain contacts. If OM is present it will deform to fill the pore space as it is more compliant than the mineral grains. When the matrix becomes tighter and most of the load has been transferred from the pore fluid to the mineral matrix, the consolidation continues during the secondary consolidation. It occurs at a slower rate than the primary consolidation. The mineral matrix deforms by creeping and compression. This mechanism is aided by the rise in temperature during burial. At high pressure, the individual grains will fuse together at the points of grain contacts. All these mechanisms increase the cohesion, compressive and shear strength of the sediment.

Chemical consolidation

In addition to the mechanical compaction, various chemical processes also increase the strength and cohesion of shale sediments. The main source of chemical consolidation is the replacement of porous space by cement that occurs when ions in the pore water precipitate to form minerals. The cementation process can occur very early in the burial of a sediment, before mechanical consolidation when highly saline pore brine precipitates mineral crystals of anhydrites or dolomite (Delle Piane, et al., 2015). More frequently the cementation occurs later on at temperature higher than 50^0C when the degradation of other minerals such as K-Feldspar and smectite clays release the necessary elements to re-precipitate as quartz and calcite (Boles & Franks, 1979). The different types of cement have the same effect on the overall sediment. They reduce porosity and increase the cohesion by bonding with the detrital grains. Cement can fill up the primary porosity as well as seal secondary porosity such as cracks generated post-deposition.

2-1-2- The evolution of OM in shale source rocks

This summary of OM evolution in shale sediments was made using the information from the work of Orem & Finkleman (2003), Pepper & Dodd (1995), and Alpern (1980). Before entering in more details on the subject, it is worth clarifying some definitions of OM to avoid confusion between different terms:

• Total organic carbon: Measure of the weight percentage (wt. %) of organic carbon. Not to be confused with total carbon which also gathers the inorganic carbon such as carbonate minerals. Also it does not correspond to the total amount of OM in a rock as OM also presents non-negligible amounts of hydrogen and oxygen, even at high maturities.

• Organic matter (OM): All compounds in a rock with a biological origin. Namely hydrocarbon, kerogen and bitumen for lithified sediments.

• Kerogen: chemical compounds non-soluble in organic solvents found in OM that yields to hydrocarbon generation during diagenesis.

• Bitumen: Soluble chemical compounds found in OM that has a lower molecular weight than kerogen. It can result directly from degradation of fresh OM via low-

temperature degradation processes but is mainly produced along with HC during the thermal cracking of kerogen.

The vast majority of OM that deposits on the surface of fresh sediments will be degraded through microbial degradation. In the best case scenario in terms of OM preservation, 90% of the OM deposited will still re-enter the biological cycle. Very particular conditions must be achieved to preserve OM in sediments and the stored chemical energy within it in order to later produce HC.

First of all the conditions at the site of deposition must be anoxic to prevent degradation by aerobic microorganisms. This happens when the water column is stratified and few exchanges between the oxygen-rich surface water and the water at the base of the water column happen. Also the accumulation rate of sediments is important for the preservation of OM. Areas where the sedimentation rate is the fastest such as near a river estuary or delta typically contain less degraded OM, as microorganisms have less time to metabolize it. In these conditions the OM is going to undergo little aerobic degradation until the trapped oxygen in the sediment is depleted. Anaerobic bacteria will then further biologically degrade the OM but at a much slower rate compared to aerobic organisms. This degradation will produce some amount of biogenic methane, water and CO2.

At some point the OM will reach a depth greater than any living organism can survive. The preserved OM then is still very functionalized, i.e. they contain highly reactive functional groups bound to large organic macro-molecules such as proteins, lipids, alcohols, etc. As the temperature slowly starts to increase the OM will be further transformed into smaller molecules by low temperature (<50°C) hydrolysis reactions with water that breaks carbon-carbon bonds to form smaller molecules. That is when the organisms composing the initial OM become difficult to recognize and the OM turns into kerogen and to a lesser extent, bitumen. The biological and inorganic reactions of OM in the early diagenesis will greatly decrease the OM oxygen content.

At higher temperature, starting at around 60° the catagenesis phase starts when the kerogen starts to crack into HC and bitumen. As burial and temperature increases, the cracking reactions will form lighter HC molecules. The kerogen becomes stiffer and more porous as the process continues. The amount of kerogen decreases in favor of

HC and bitumen. The type and amounts of HC produced per unit of kerogen depends on two factors.

(i) The temperature: Higher temperatures will provide more energy to break the carbon-carbon bonds of kerogen and of larger trapped HC molecules to form ever smaller HC molecules. The transition between the generations of different types of HC occurs progressively. The peak generation of each HC type in chronological order is: oil, wet gas and dry gas (methane).

(ii) The organofacies, or type of kerogen and source rock also has a great influence on the HC generation. We will focus here on the two organofacies used in this project: marine algal (kerogen type II) and terrestrial waxy (kerogen type III) in sediments of the siliciclastic type such as shales. An oil or gas window describes the temperature range over which the ratio of produced HC to generative kerogen potential goes from 10% to 90%. The classification for a reference temperature increase in-situ of 2°C per million years, positions the oil window between 105 and 145°C for type II and between 120 and 160°C for type III whereas the gas window is between 140 and 210°C for type II and 175 and 220°C for type III. The OM type affects the temperature at which HC generation occurs but also affects the relative amounts of different HC. Type II kerogen will produce more oil whereas type III kerogen will produce more gas. These differences between OM types are linked to the initial O/C and H/C ratios. Typically type II kerogen is more hydrogen rich whereas type III is more oxygen rich.

2-1-3- The role of clay in the diagenetic process

Clays are one of the main components of shales and are chemically more reactive than other minerals. They interact with water and OM and undergo changes with temperature and pressure.

Clays are the most important components driving the degree of mechanical compaction. The final porosity of a shale sediments for a given compaction stress depends on the type of clay. Smectite clay is the least compressible and will have the highest final porosity, followed by illite and kaolinite (Mondol, et al., 2007). The water saturation is important too as wet clay will be lubricated and more compressible.

Moreover the clay composition of sediments evolves during burial through illitization of smectite. With increasing temperature and the availability of potassium ions (K^+)

the smectite will transform to illite (Pytte & Reynolds, 1989). As illite is more compressible than smectite, this diagenetic transformation will therefore increase the consolidation of the sediment. Also, as mentioned before, the by-products of this reaction will promote quartz cementation, further reducing porosity and increasing stiffness.

Finally the clay-OM interactions play an important role in the thermal maturation and in the HC mobility. Firstly clays act as catalysts for kerogen cracking reactions. Even though clays are known to be negatively charged, they possess acid sites at the edges of their crystallites as well as cations in their interlayer spaces to neutralize their charges that promote cracking reactions (Johns, 1979) and effectively reduces the HC generation temperature. This effect is more prominent for the more reactive swelling clays such as smectite. Besides clays possess adsorptive properties. Solid OM as well as hydrocarbons tend to get adsorbed on the clay surfaces. The polar and high molecular weight compounds such as heavy oils are more prone to the adsorption effect (Tannenbaum, et al., 1986) so that light HC will be more mobile in shale source rocks. The catalytic and adsorptive effects are directly dependent on the surface area of contact between clay and OM. Therefore the texture of OM will be a determinant factor in the HC generation and in the retention capacity of shales. OM with a nano-composite texture whereby very small OM particles are embedded in the clay matrix and have a very high surface of contact will produce HC more easily and have less mobility after generation (Rahman, et al., 2017) than OM occurring in particulate texture that have a smaller surface contact with clay minerals.

The following diagram in *Figure 2-1* summarizes the different consolidation mechanisms occurring in natural shale samples presented in this section.

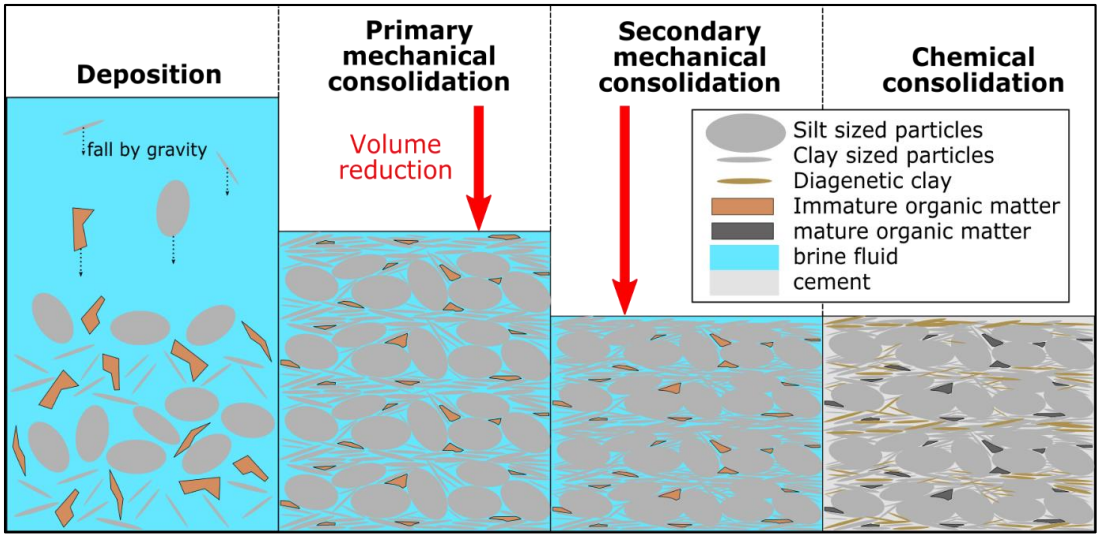

Figure 2-1: Visual summary of the formation of natural organic-rich shales from deposition to diagenetic lithification. Deposition: alternate deposition of silt-sized and clay-sized particles along with OM. Very high initial water volume content in the mud (>80%). Primary mechanical consolidation: rearrangement of particles along the bedding plane. Loss of water. Increase of the number of grain contacts. Ductile and compressible OM loses volume and deforms to fit pore space in between stiffer mineral particles and starts to acquire a lenticular texture. Secondary mechanical consolidation: Further loss of water. Creeping and compression of mineral particles. Fusion of mineral grain at the grain contact interface. Porosity falls below 20%. Shale acquires its laminated structure. Chemical consolidation: With heat and pressure, diagenetic processes result in the filling of the pore space by cement (mainly calcite and quartz), Smectite-to-Illite clay transformation. Maturation of OM to form bitumen, kerogen and HC. Porosity decreases further (often <10%).

This characterization of shale consolidation and diagenetic processes allowed the determination of the design parameters of the artificial samples as detailed in section 2-5-. The next section will present the tools the oil and gas industry employs to investigate shale source rocks during the exploration phase.

2-2- Exploration of unconventional shale reservoirs: an overview

Some background concepts are important to understand the relevance of this subject to the geophysical exploration of tight reservoirs.

2-2-1- Primary objectives of the exploration for the industry

The ultimate goal of the exploration and reservoir evaluation phase, whether we are talking about conventional or unconventional resources, is summed up in a simple question: How much HC can we produce from this formation, and at what cost? However answering this question involves a complex process. In essence, it consists in confirming the presence or absence of HC in a formation and thereafter locate them precisely, evaluate their type (oil or gas), their quantity, and finally how much of this total amount is recoverable.

Modern exploration primarily comprises three phases that are the choice of the zone to explore, the choice of the location of the wells and the wider monitoring of the researched area. In addition to that, in the case of tight shale reservoirs, the exploration must provide information to evaluate if the production can be enhanced with hydraulic stimulation and design the stimulation requirements (composition of the drilling mud, horizontal well location and spacing, fracture design). There are a host of different methods used to assess the potential of a shale formation for economic hydrocarbon production. Depending on the company, the formation location (onshore vs. offshore) and the financial resources allocated to the exploration campaign, a different set of these methods are employed concurrently to achieve this goal. The different methods are divided in two groups: the techniques carried on from the surface and the methods requiring the drilling of a well. Later on I will explain how the gathered data from all methods are combined to answer the primary objectives.

2-2-2- Surface methods

2-2-2-1- Seismic imaging

Seismic tomography is a method for estimating the parameters of a formation from seismic data on a large scale. The measured parameters can be represented by the spatial distribution of P-wave velocity, S-wave velocity and with further modelling, of porosity, density, saturation and anisotropic parameters. In seismic prospecting a low-frequency acoustic source is used at the surface to generate pulses of energy propagating downward, using either explosives or a mechanical vibrator. When the acoustic waves encounter an interface between two layers of different acoustic impedance, they are partially reflected back to the surface. An array of detectors

(geophones) at the surface, typically close to the source, detects the reflected waves that generate a detectable signal. By studying these signals, we can calculate the depth and structures of buried geologic formations.

The result of inversion is graphically presented as a 2-D image or a 3-D render consisting of several individual slices, with each pixel containing the value of the parameter of interest. The final data is used to estimate the geometry and lithology of geologic layers, and can help exploration geophysicists assess the properties of the studied formation.

One of the key element to interpret seismic data in terms of rock properties is to link the different imaged structures (seismic lobes) to borehole measurements. Successful inversion of seismic data requires calibration to well-log measurements so that inverted results translates directly to rock properties.

The frequencies used to obtain seismic data are much lower than the frequencies employed in downhole acoustic logging or laboratory acoustic testing. The higher frequencies are sensitive to fine layering and very small variations in acoustic impedance and their energy is scattered quickly. Therefore they have a low penetration depth. On the contrary, low frequencies used in seismic prospecting detect only major interfaces and can travel several hundreds to several thousand meters and still generate a measurable signal. It is essential to link acoustic and seismic data for borehole to formation calibration. The acoustic properties obtained by the ultrasonic measurements are usually applied to seismic data interpretation directly, without taking into account their frequency dependency (Zhao, et al., 2013). Theoretical models have been developed to calibrate acoustic moduli to low frequency seismic data [Biot (1956), Dvorkin & Nur (1993), King & Marsden (2002)].

2-2-2-2- Controlled source electromagnetic (CSEM)

This technique is employed mainly offshore, especially in deep water, where the cost of drilling wells is high and the risk to drill a dry well must be minimised. It is used in conjunction with seismic imaging as it has a lower spatial resolution and cannot detect structural and stratigraphic information as well as the latter. However it can identify more accurately areas rich in hydrocarbons and is an efficient tool to distinguish horizontal variations such as changes of facies.

In this type of surveying, an electromagnetic source is towed near the seabed, along an array of receivers positioned on the seabed. The electromagnetic field will propagate from the source into the subsurface and back to the receivers. Zones of high resistivity in the formation will induce less attenuation of the electromagnetic field and the receivers will detect a response with a higher amplitude. After an inversion process, 2D resistivity profiles can be created. In some cases the receivers are positioned in a grid pattern and further processing allows to create 3D profiles. Formations bearing important amounts of hydrocarbon will display an anomalously high resistivity. The use of this technique can be motivated by different reasons such as analysing mature fields to make sure no economically viable areas were missed before getting rid of an offshore asset. In a context of exploration it is mainly employed to provide the necessary information to confidently place a well on the most promising spots for further investigations as well as to complement seismic imaging in the identification of HC sweet spots.

Most unconventional reservoirs exploited today are located onshore, where CSEM is seldom employed. Therefore CSEM surveys were applied to conventional resources so far. But offshore unconventional reservoirs are currently under consideration, such as the Kimmeridge clay in the North Sea (Raji, 2018).

2-2-3- Borehole methods

2-2-3-1- Logging

The information presented in this section comes from the book: *Well logging for earth scientists* (Ellis & Singer, 2007). Logging is essentially the measurement of rock characteristics by passing a measuring device in a wellbore. Traditionally the logging devices are located on a probe that is attached to a cable and is lowered into the borehole after drilling. The measurements are then performed continuously as the probe is slowly raised to the surface. This type of logging is called wireline logging. A more recent method has the logging tools directly integrated into the drill collar close to the drill bits to form a single unit. The tools carry out continuous measurements at different angles as the drill collar rotates. This type of logging is known as logging while drilling (LWD). Modern LWD units are equipped with tools performing measurements very similar to traditional wireline logging tools. Furthermore logging methods are complemented by the analysis of cuttings retrieved

from the drilling mud. The most common instruments in well logging are presented below, with a focus on the properties measured rather than on the design and technical implementation of the tools:

Electrical tools

Resistivity tools: The resistivity can be measured using electrode devices or induction devices. In simple terms, electrode devices uses metallic electrodes to transmit alternative current at low frequency (<1000 Hz) directly into the formation and record the attenuation of the current after going through the formation with different electrodes. The induction devices use a transmitter coil that generates a magnetic field at medium frequencies (10 to 100 kHz) that will induce electric eddy currents in the formation. This electric currents will in turn induce an attenuated magnetic field that is measured by a receiver coil. The choice of either method depends on the conductivity near the borehole and the conductivity of the formation. Electrode devices are preferred when the near borehole conductivity is high (e.g. water based drilling mud) and the formation conductivity is comparatively low. The induction devices are preferred in the opposite conditions (e.g. oil based drilling mud and high formation conductivity). Arrays of electrical sensors, coupled with inversion processes allow to compute resistivity at different depth from the borehole, giving information on the resistivity in the mud invaded zone and the intact deep formation as well as computation of resistivity in different orientations, in the case of anisotropic formations. The resistivity of the formation is probably the most important property to evaluate since it behaves vastly differently in brine bearing rocks compared to HC bearing rocks. The conductivity of sedimentary rock is mainly due to the electrolytes contained in the pore fluids whereas the solid phase is essentially an insulant. Namely oil is insulating and brine is conductive. But its behaviour is also driven by other parameters. Its value is determined by the salinity of the brine, the ratio of water/HC mixture, the amount of pore space and the temperature. The presence of clays also affects it.

Spontaneous potential (SP): The difference in salinity between formation water and drilling mud generates a small electric field due to diffusion processes in the pore fluid. It can be detected with a simple electrode. This measurement can help determine the formation brine resistivity and make rough permeability estimations. Clays display

negatively charged surfaces that decrease the mobility of ions. Therefore the SP is weakened by shaly layers and can be used to quantify the amount of clay in the formation.

Dielectric tool: Tools that only measure resistivity operate at rather low frequencies (<100 kHz). Therefore their measurements are not affected by dielectric processes. Attenuation and phase shift at induction frequencies are small and corrected as 'skin effect'. However at higher frequencies (MHz to GHz) the dielectric processes become dominant and dielectric tools operating at these frequencies do not measure the actual resistivity but rather record the phase shift and attenuation. The dielectric properties and conductivity are then deduced from them. The dielectric behaviour of rock formations is very rich in information as it is influenced by salinity, clay content, water and HC content, porosity, and mineral texture. Relative dielectric permittivity can be used to differentiate HC from water of any salinity.

Besides the dielectric response is affected by mineralogy such as clay content and clay type and different geological settings may significantly affect the microstructure of sediment and consequently its properties (Beloborodov et al., 2016b). The anisotropy of dielectric properties of shales is crucial for the interpretation of dielectric well-logs, especially in deviated wells, and may affect the efficiency of production via the dielectric heating in unconventional shale reservoirs (Donadille, 2016, Josh et al., 2016). Improving the understanding of the dielectric response in shales with varying organic matter characteristics is thus important for log-interpretation purposes.

Nuclear tools

Gamma-ray devices: Minerals in rocks contain various amounts of decaying radioactive elements. When they decay this elements emit various energetic radiations. Gamma radiations are electromagnetic waves with very short wavelength and thus a very high photon energy. Gamma ray devices measure passively this natural radioactivity. There are three radioactive elements that emit the majority of the gamma radioactivity in rocks: Potassium (K), Thorium (Th) and Uranium (U) isotopes. Potassium is a fairly common element in Earth's crust as it constitutes more than 1% of its mass (Mackenzie & Garrels, 1971), though only a fraction of it is radioactive. Potassium rich minerals include evaporites, some feldspars, some micas and clay minerals of the illite group. On the contrary thorium and uranium are much rarer.

Because of a high cation exchange capacity, clays are able to retain significant trace amounts of thorium, when other minerals are not. Uranium compounds are soluble and end up absorbed into living organisms that later composes the OM of shale source rocks. The presence of potassium in clays and silts (feldspars), retained thorium in clays, and uranium in OM (if present) makes shales particularly radioactive. Therefore, similarly to the spontaneous potential, the gamma ray reading has a higher value in shale formations, and one application of gamma ray logs is to identify shale layers. Another application is to correlate the logged depth with the recovery depth of cores by running gamma ray measurement on the cores and comparing the core measurements with the gamma ray log. These applications can be carried out with a gamma ray tool, which measures the total flux of gamma radiation expressed in American Petroleum Institute (API) units. It is simply a count of gamma rays hitting a detector calibrated against a standard sample with known concentrations of radioactive elements. However the application of such a detector are limited because the relative concentrations of potassium, thorium and uranium are variable in different formations. Spectral gamma ray devices, on the other hand, can sort the radiation counts by their energy level. In turn spectral gamma ray devices can quantify the concentration of each radioactive element. Spectral gamma ray thus allow the determination of the formation lithology to a certain extent, with assumptions on the radio-signature of different types of minerals. The chart in *Figure 2-2* is an example of interpretation of the information provided by the spectral gamma ray tool for lithology determination. The typical depth of investigation of gamma ray devices is 30cm.

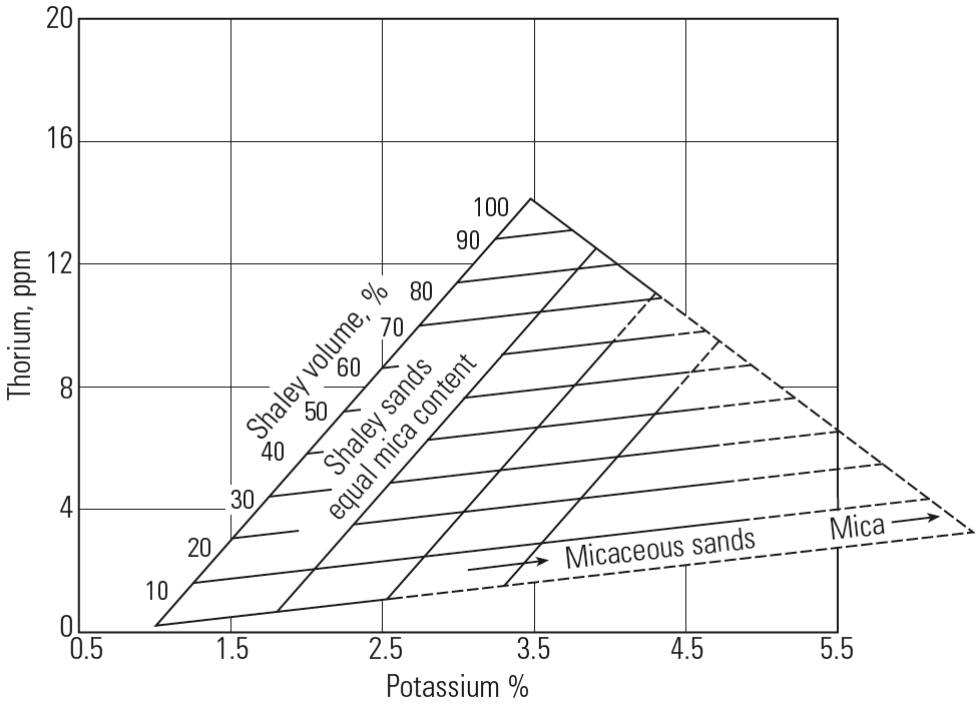

Figure 2-2: A cross plot of thorium (ppm) and potassium (wt. %) for determining shale and mica content. Shale here means clay and silt-rich fine grained rock. From Hodson et. al. (1975)

Density logging: The density tool uses an active source of gamma rays and uses usually two detectors to count the gamma rays that are scattered back. At the energy levels used for this tool the dominant effect is the Compton's scattering, where the gamma ray energy is transmitted to electrons. The scattering effect is mainly correlated to the bulk density of the traversed material. The gamma ray count at the detector decreases exponentially with increasing formation bulk density. The formation density can be computed using only one detector but several detectors are used to apply corrections for the presence of mudcake in between the density tool and the formation. Some density tools also have a detector sensitive to gamma rays at lower energy levels, whose energy was attenuated by the photoelectric effect. The attenuation due to the photoelectric effect is non-linearly proportional to the atomic mass of the scattering atoms. The lower energy detector can be used to compute the photoelectric factor that in turn will indicate the average atomic number of the formation, which is related to the elemental composition of the formation. This can be used to determine the lithology. The attenuation of gamma rays occurs quickly and therefore the density tool has a shallow depth of investigation (<150mm) and usually measures the invaded zone.

Neutron devices: Neutrons with a high energy (several MeV to 14.1 MeV) are generated by a source located against the borehole wall. The energy level of a neutron corresponds simply to its velocity. These neutrons penetrate the formation and interact with matter through different mechanisms which will scatter the incident neutrons and bring them to lower energy levels. Neutrons with high energy (high velocity) are slowed down more efficiently when colliding with particles of similar mass via elastic scattering. Therefore, Hydrogen nuclei are more effective at reducing the neutrons energy than higher mass elements. In formations containing enough low mass elements, the high energy neutrons will be brought very quickly (in the order of a millisecond) to thermal energy levels. A cloud of neutrons of low energy surrounds the source. This low energy neutrons end their journey by being absorbed into atoms nuclei. The only two elements present in rock formations that absorb thermal neutrons efficiently are hydrogen and chlorine. Since hydrogen is mostly present in the form of water or HC in the pore space, neutron tools measurements are well correlated to the porosity. The presence of chlorine ions, and thus the salinity, also effect strongly the neutron cloud. In neutron devices, one or two receptors are located at an offset distance from the source. These detectors are either sensitive to epithermal energy (0.4 to 10 eV) thermal energy (<0.4 eV) or to gamma rays that are generated when neutrons are absorbed. Neutrons or gamma rays that interact with the detectors are counted. The relative concentration of hydrogen per unit of volume compared to that of pure water is called the hydrogen index (HI). Formations with a high HI will absorb more neutrons and have lower counts, and when properly calibrated the count can be converted to HI. In an ideal case of a formation whose minerals do not contain hydrogen or chlorine, saturated with fresh water, the HI will equal the porosity (e.g. clean limestone). Therefore, neutron logs are expressed in limestone porosity units, even though a variety of factors other than porosity affect its value. Oil has a similar HI to water so the equality still stands for oil bearing formations. Light hydrocarbon such as natural gas lower HI as they have a lower density, inducing an underestimation of the porosity. High chloride contents, such as in formation brine or in drilling muds, will induce an overestimation of HI. Clay minerals contain bound water that do not participate to the porosity. Therefore even though HI may be read accurately, the presence of clay will induce an overestimation of the formation porosity.

Nuclear magnetic logging: Single protons in hydrogen nuclei normally spin around a random axis, and form a magnetic dipole oriented along the axis of rotation. When submitted to a static magnetic field, these protons act as microscopic gyroscopes and their spin axis precesses around the magnetic field direction. To induce nuclear magnetic resonance (NMR), a pulse of oscillating magnetic field with carefully chosen parameters of magnetic intensity, direction, frequency, and application time can induce the protons to precess in phase, generating a net magnetization perpendicular to the static magnetic field that can be measured. When the pulse ends, the protons precession de-phase and the net magnetization is no longer detectable. The rate of de-phasing, and thus the rate of decay of the measurable signal depend on the characteristics of the material containing the protons just as much as it does on the properties and parameters of the magnetic fields. However, by applying an oscillating magnetic field according to the CPMG sequence, the effects of the decay due to the magnetic field properties can be cancelled out by a re-phasing of the protons at regular intervals, forming echoes of the initial magnetization. After each re-phasing the maximum net magnetization will be lower than at the previous peak which denotes an irreversible de-phasing due to processes occurring within the material. The envelope of such peaks forms an exponential decay related to a time constant called T_2. The total initial magnetization corresponds to the total number of protons being magnetized and thus is directly proportional to the porosity. The T_2 decay is primarily driven by the pore shape, as protons in smaller pores interact with the grain surfaces and thus de-phase faster than protons in large pores. Therefore the T_2 decay is a sum of exponential decays weighed by the relative volume ratios of different pore size populations. The decay can thus be inversed into a pore size distributions. In turn, this pore size distribution can be used to estimate permeability with the assumption that pore size is correlated to pore throat size, and attributing a particular size to each value of the T_2 constant. Finally, by altering the CPMG sequence, diffusion phenomena can be enhanced so that they have significant impact on the T_2 decay. The rate of decay due to diffusion is related to the molecular composition and viscosity of the fluids the protons are a part of. Therefore, two measurement of the same zone with different settings allow for the distinction between different fluid types: water, oil or gas.

Acoustic tools

Acoustic logging: In transmission mode, the most recent acoustic logging tools are equipped with several sources that generate acoustic energy at around 20 kHz and arrays of receivers, both monopole and dipoles with varying spacing that allow the recording of compressional waves (P-wave) and shear waves (S-waves) in the formation. The anisotropy of the P- and S-waves can also be measured. The velocity of acoustic waves in rocks depends on 6 factors: porosity, mineral composition, effective pressure, temperature, pore fluid composition, and the rock texture. The most common application of sonic logs is to determine porosity and lithology. It is also used to estimate excess pore pressure and the mechanical properties of the formation. Besides, the signal attenuation can be used to detect fractures as well as the quality of the borehole cement casing. In reflection mode, a source with a higher frequency (500 kHz) is used to image the borehole wall.

One very important feature of P-wave velocity is its relationship with porosity. For a given lithology, the P-wave velocity evolves linearly with porosity according to the Willie time-average equation.

2-2-3-2- Core analysis

Core analysis, if available, is employed to define the sedimentary structures, essential for the understanding of depositional environments and facies within a reservoir, as well as depth matching to integrate seismic, logging and laboratory data in a coherent set of information.

In conventional reservoirs the geomechanical properties of extracted cores or plugs are often measured in the laboratory with acoustic sensors under a confining pressure and pore pressure similar to the in-situ conditions. However the recovery of such intact samples is costly and time-consuming and is usually only carried out in separate discrete locations of the well. In unconventional reservoirs, an added difficulty is that such samples can be clay-rich and thus be more friable, easily fractured and typically difficult to preserve after retrieval. Therefore specific sonic logging tools must be used instead, to determine shear and compressional acoustic velocities directly in the well.

2-2-4- Integration of obtained information to answer the primary objectives

The different techniques presented above are complementary. Discrete but accurate and information rich data acquired from core analysis can be integrated with continuous logging data to determine rock properties along vast vertical sections of an exploration well. In turn the information obtained in the vicinity of the well from core analysis and logging can be extrapolated to a much larger area of the sedimentary basin by combination with seismic imaging and CSEM, thanks to the principle of lateral continuity. Each tool only provides a limited amount of information and the interpretation of the data must use a coherent combination of them to estimate the reservoir characteristics. I will present here a non-exhaustive list of the measured properties relevant to the field of unconventional reservoir exploration and then will explain how they can be used for the purpose of designing hydraulic stimulation operations and assessment of the production potential.

2-2-4-1- Determination and Computation of important reservoir parameters

Geological parameters

Lithology and structural features: The analysis of layering and fractures from the formation scale down to the centimetric resolution of logging tools is one of the earliest task done in exploration. Interlayers of sand-sized particles in shale formation or existing fractures will greatly enhance the prospect of HC recovery for instance.

Mineralogy: The most basic and most important mineralogical information is the clay content as it has a significant impact on well-bore stability, formation mechanical properties and permeability. The identification of shale layers (read: clay-rich) is the first step in identifying source rocks that are potentially HC rich. The clay content and clay type is the prime parameter to model permeability, elastic stiffness and brittleness. Diagenetic clays such as illite will be more stiff and brittle than smectite for example and therefore will be more prone to maintain open fractures after hydraulic stimulation. More advanced mineralogical information obtained with spectral gamma ray tools or X-ray fluorescence testing on recovered core samples can be used in conjunction with bulk density to estimate porosity or to run advanced fluid flow modelling.

Petrophysical parameters

Bulk density can be most easily determined from density logging. It is used to compute the acoustic impedances of adjacent layers for seismic interpretation and for estimating overburden pressure. It can also be used to compute the porosity if the mineralogy is known.

Porosity: The ratio of volume filled by fluids to the total volume of a rock. The value of the porosity is essential to compute the amount of HC in place in the formation if the fluid content is also known. Porosity also affects the resistivity reading because the fluids, especially brine, have a higher conductivity than the solid matrix. It can be reasonably well defined from the combination of density logs and neutron logs, as well as determining the lithology by analysing the divergence between the two curves. Pyrite, which is common in organic shales, tends to skew the density measurement with its high density (5g/cm3).

Permeability is hard to obtain even with core samples that are representative of the formation. It is one of the main focus of the exploration phase and a lot of time and resources are invested in its estimation. Many different models are using an array of different parameters intend to estimate it depending on the type of data available. Estimating permeability with several methods also allows to verify the results validity as the error margins in permeability can be quite high. NMR techniques, carried out in the borehole or in the laboratory can give reasonable estimation. Other methods model permeability based on pore-throat size with Mercury Injection capillary pressure (MICP), porosity or mineralogy.

Oil/gas saturation: The ratio of water to HC in the formation pore space is another crucial information to compute the amount of HC in place. When the porosity and brine salinity is known, it can be estimated from the resistivity reading. NMR also provide an alternative method to determine the HC saturation.

OM characteristics

Total Organic Carbon (TOC) is calculated with the Passey method or the Schmoker correlations. The Passey method uses the separation of resistivity and porosity curves to highlight presence of organic-rich intervals whereas in lean intervals the curves overlay (Passey, et al., 1990) whereas the Schmoker method uses the density log,

assuming the densities of the OM and the surrounding rock matrix and fluids are known (Schmoker, 1979). With a lower density and higher ductility compared to the mineral matrix, OM influences many formation properties. For instance it decreases P- and S-wave velocities, especially in the vertical direction, and thus affects the elastic anisotropy of the formation. In most cases, TOC is the sole parameter used to quantify the OM impact on the overall rock properties.

Kerogen type and maturity are difficult to determine from logs alone. The Z method using calculated water saturation and the neutron log has produced useful results, but it is rarely the focus during reservoir exploration. However it is an important parameter for unconventional reservoirs as different kerogens have different physical attributes and the maturity indicates the presence or absence of HC as well as their location in the pore space (adsorbed onto OM where they were generated or displaced to the mineral pore-space).

Geomechanical characteristics

The Young's modulus represents the longitudinal stiffness of a solid along a particular direction, and is equal to the ratio of an applied uniaxial stress to the induced uniaxial elastic strain.

The Poisson's ratio represents the ratio of transversal strain to axial strain when a uniaxial stress is applied along a given direction.

Brittleness relates to the ability of a material to undergo plastic deformation. A brittle material will have a shorter plastic deformation under load, and will mostly react elastically before failure (Bai, 2016). It can be computed with an array of methods involving different parameters such as mineralogy or elastic moduli. A common empirical method developed by (Rickman, et al., 2008) uses the Young's modulus and Poisson's ratio according to the following formula:

$$Brittleness\ Coefficient = \left(\frac{E-1}{14} + \frac{0.4-\nu}{0.5}\right) \quad (1)$$

Some argue that elastic properties and brittleness are poorly correlated because rock's elasticity has little to do with rock failure (Hall, 2013) and therefore such empirical relationships may have limited applications.

Fracability is not equivalent to brittleness. It relates to the rock failure under the ultimate rock strength. A brittle formation may not be easily frackable. Shale formations can have varying **degree of consolidation** that will affect their elastic and mechanical response. Quantifying this properties allow to assess the prospect for the borehole wall stability as well as the ability of the formation to allow fluid flow and to maintain open fractures.

Fracture pressure closure is the pressure required to maintain and extend a fracture in a given formation. It can be computed from the Poisson's ratio and the bulk compressibility. This provides the information of horizontal stress needed to produce a vertical fracture at different depths.

Overburden stress can be computed at any given depth by integration of the bulk density over the depth of the well.

The most important tools to determine the elastic properties of a formation are the density, sonic and borehole imaging devices. Sonic logs also help estimate the porosity and TOC. Sonic tools can be single source/receivers or arrays of multiple source/receivers. In certain cases the transducers can record both P- and S-wave signals. Without vertical acoustic measurement the anisotropy of the formation can be inferred from the difference in arrival time between S-waves and Stoneley waves.

Image logs will allow to evaluate the shape of the well and determine the **stress field orientation**. Typically, in the plane orthogonal to the well direction, the borehole will deform so that in direction with the minimum stress will feature a breakout, whereas the direction with the maximum stress will present a fracture.

2-2-4-2- Fracture design

Mechanical parameters of ultra-tight shale formations are a crucial information for fracture design. For instance the rock brittleness will be a key information to determine if a formation can readily form fractures upon hydraulic stimulation and whether the fractures can be maintained open or will heal rapidly by ductile deformation. The more brittle sections will form fractures whereas the more ductile ones will act as a barrier preventing the connection of fracture networks between brittle sections (Perez & Marfurt, 2013). Besides, permeability and adsorption dictate the productivity of hydraulically stimulated formations and helps the choice of fractures location and spacing. Ultimately, the choice of the location for hydraulic stimulation and the

estimates for fracture propagation, fracture connectivity and fracture closure parameters will influence the estimation of producible HC, as explained in the following section.

2-2-4-3- Production potential

Indeed, the final goal of estimating the volume of recoverable HC involves a combination of different parameters: porosity and fluid saturation for the total volume of HC and fluid transport properties after hydraulic stimulation. In the context of this project, the focus is set on the presence of OM as it impacts every parameter necessary for production potential evaluation: its structure, its maturity, its internal porosity, the type of HC it contains, whether it is hydrocarbon or water wet, whether the HC are adsorbed onto the OM surface or exist in macro-porosity and the connectivity of the OM. These organic characteristics will affect the estimate of HC in place and the movement of fluids, including oil and gas, and in turn how much of the HC is recoverable. However the industry often limits itself when modelling, interpreting logs or lab measurements on recovered sample by underestimating the complexity of OM. The influence of OM on the output of a model or in the interpretation of logs or laboratory results is often too simplistic. In some cases OM is considered as a phase with constant properties and the only consideration it is given is by the value of TOC. Less frequently the maturity and the type of the OM will be taken into account but the complexity of OM remains widey overlooked. However we want to show with this work that varying OM characteristics in shales, at constant TOC, can influence significantly parameters relevant to the exploration industry as well as the academic field of rock physics.

The following *Figure 2-3* summarizes the process of exploration of an unconventional reservoir explained in this section. The image on the lower left was acquired during a survey of the Spekk formation in the Norwegian Sea (Løseth, et al., 2011). The authors of the study identified an organic-rich shale source rock that presented a high contrast of acoustic impedance compared with the surrounding areas. This was confirmed by gamma ray logs that showed a positive anomaly in the identified source rock section.

In the next two sections, the physical response of organic-rich shales will be presented in more details, for the two main set of properties of interest to this project: Rock mechanics and dielectric testing.

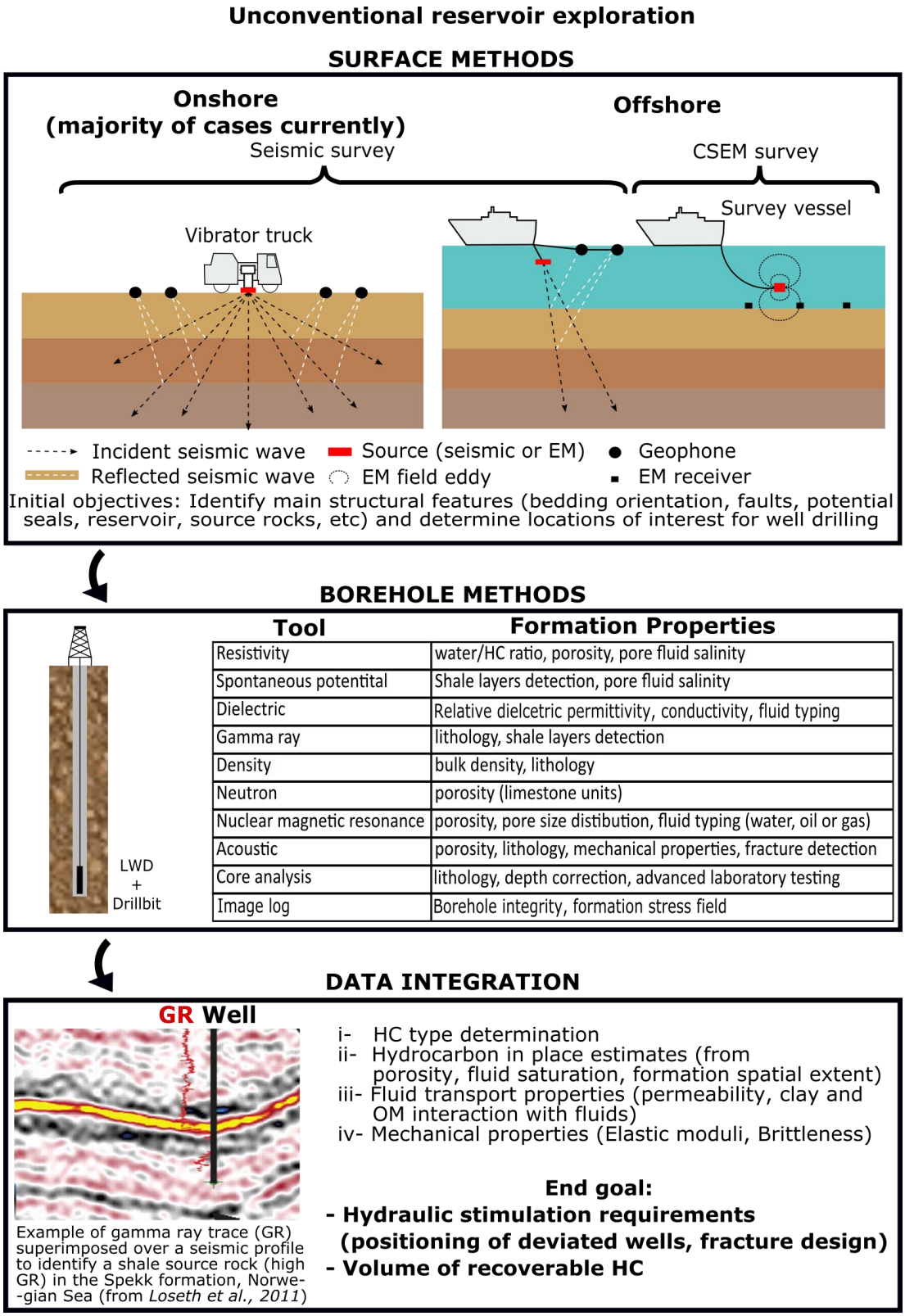

Figure 2-3: Summary of the process of data acquisition and interpretation in the context of unconventional reservoir exploration.

2-3- Rock mechanics of organic rich shales

Highly lithified and diagenetically mature shales have P-wave velocities up to 5km/s and S-wave velocities up to 2.5-3km/s and they display a strong elastic anisotropy. The elastic response of shales is governed by multiple parameters: stress rate, stress history, clay type and content, organic matter, microstructure, pore-fluid interactions, existing fractures and cementation to site the main ones (Edwards et al. 2015; Holt et al. 2003; Vernik and Liu 1997, Dewhurst and Siggins 2006). Consequently although our main objective is to assess the organic matter influence on the elastic response, a full understanding of all the other factors affecting it is still required. The two following sections will first present the theoretical aspects of elastic testing of anisotropic shale sediments and then summarize how the impact of OM on the elastic properties of organic shales was evaluated in previous studies.

2-3-1- Theory of elasticity in transversely isotropic materials

2-3-1-1- Stiffness tensor

According to Hooke's law the elastic tensor of a vertically transverse isotropic (VTI) medium can be fully described with 5 independent stiffness coefficients (C_{ij}) relating stress (σ_{ij}) to elastic strain (ε_{ij}). In an orthonormal Cartesian reference frame aligned with the symmetry axes of the VTI medium, and using Voigt's convention for tensorial notation, the elastic tensor reads

$$\begin{bmatrix}\sigma_{xx}\\ \sigma_{yy}\\ \sigma_{zz}\\ \sigma_{yz}\\ \sigma_{xz}\\ \sigma_{xy}\end{bmatrix} = \begin{bmatrix} c_{11} & c_{11}-2c_{66} & c_{13} & 0 & 0 & 0\\ c_{11}-2c_{66} & c_{11} & c_{13} & 0 & 0 & 0\\ c_{13} & c_{13} & c_{33} & 0 & 0 & 0\\ 0 & 0 & 0 & c_{44} & 0 & 0\\ 0 & 0 & 0 & 0 & c_{44} & 0\\ 0 & 0 & 0 & 0 & 0 & c_{66}\end{bmatrix}\begin{bmatrix}\varepsilon_{xx}\\ \varepsilon_{yy}\\ \varepsilon_{zz}\\ \varepsilon_{yz}\\ \varepsilon_{xz}\\ \varepsilon_{xy}\end{bmatrix} \quad (2)$$

The determination of four of the stiffness coefficients is straightforward as each of them is directly proportional to the square of a P- or S-wave velocity along the symmetry axes (which coincide with the Cartesian reference frame), i.e.,

$$c_{11} = V_{ph}^2\rho \quad (3)$$

$$c_{33} = V_{pv}^2 \rho \quad (4)$$

$$c_{44} = V_{s1}^2 \rho \quad (5)$$

$$c_{66} = V_{sh}^2 \rho \quad (6)$$

Where V_{ph} and V_{pv} are the horizontal and vertical P-wave velocity, respectively, V_{s1} is the S-wave velocity propagating vertically and polarised horizontally, V_{sh} is the horizontally polarised S-wave velocity propagating horizontally, and ρ is the bulk density of the sample.

The coefficient c_{13} on the other hand requires the measurement of an off-axes quasi P-wave phase velocity, the phase angle (measured with respect to the symmetry axis of the VTI medium) of the given phase velocity and a combination of the stiffness coefficients above. From here on we will refer to off-axis quasi P-waves as off-axes P-waves for sake of simplicity. From the Eigensolutions to the Christoffel equation in VTI media given for instance in Dewhurst and Siggins (2006) we can express c_{13} for any phase angle θ with phase velocity V_{phase} as

$$c_{13} = \frac{\sqrt{(c_{11}sin^2\theta + c_{44}cos^2\theta - \rho V_{phase}^2)(c_{44}sin^2\theta + c_{33}cos^2\theta - \rho V_{phase}^2)}}{cos\theta\ sin\theta} - c_{44} \quad (7)$$

From the elastic stiffness coefficient determined above we can now compute more intuitive elastic parameters describing transversely isotropic (TI) media such as Thomsen's anisotropy parameters, Young's modulus or Poisson's ratio.

2-3-1-2- Thomsen's anisotropy parameters

A common way to describe the elastic properties of a TI elastic medium are Thomsen's weak anisotropy parameters α, β, ε, γ, and δ (Thomsen, 1986), which are a combination of the 5 independent stiffness coefficients c_{ij}, i.e.

- α and β represent the "isotropic" parameters since an isotropic elastic material can be fully described with only two independent parameters. α is the vertical P-wave velocity and β is the vertical S-wave velocity

$$\alpha = \sqrt{\frac{c_{33}}{\rho}} \quad (8)$$

$$\beta = \sqrt{\frac{c_{44}}{\rho}} \tag{9}$$

- ε, γ, and δ characterize the deviation from isotropy (anisotropy) of the TI medium. ε is the P-wave anisotropy, γ is the S-wave anisotropy, while δ relates to the anellipticity of the P wavefront. They are defined as follows

$$\varepsilon = \frac{c_{11} - c_{33}}{2c_{33}} \tag{10}$$

$$\gamma = \frac{c_{66} - c_{44}}{2c_{44}} \tag{11}$$

$$\delta = \frac{(c_{13} + c_{44})^2 - (c_{33} - c_{44})^2}{2c_{33}(c_{33} - c_{44})} \tag{12}$$

Comparing equations (3) to equation (7) and (10) to (12), we observe that ε and γ only require measurement of either P-wave or S-wave velocities along the symmetry axes of the TI medium, whereas δ involves both vertical velocities (P and S) along the symmetry axis, and one off-axes P-wave velocity (in parameter c_{13}).

2-3-1-3- Young's modulus

The Young's modulus E (Pa), is a widely used elastic parameter in rock mechanics and other engineering disciplines because of its intuitive physical meaning. It represents the longitudinal stiffness of a solid along a particular direction, and is equal to the ratio of an applied uniaxial stress to the induced uniaxial elastic strain. For isotropic material, Young's modulus is unique and independent of the direction of application of the stress. For TI materials however, Young's modulus admits two independent values necessary to describe the longitudinal stiffness of the material in any direction: one along the axis of symmetry of the material, which corresponds to the vertical direction in normally compacted shales, and one in the plane of isotropy perpendicular to the symmetry axis. They are called E_3 and E_1, respectively. They can be expressed as a function of the stiffness coefficients c_{ij} as

$$E_3 = c_{33} - \frac{c_{13}^2}{c_{11} - c_{66}} \tag{13}$$

$$E_1 = 4c_{66}\left(1 - \frac{c_{33}c_{66}}{c_{11}c_{33} - c_{13}^2}\right) \quad (14)$$

Those quantities help us evaluate the quality of the ultrasonic data acquired during a compaction experiment. Indeed the Young's moduli E_1 and E_3 should be equal at the start of a compaction experiment as the mixture is a liquid at this stage. They should then increase throughout the experiment as the stiffness of a compacting sample increases with consolidation.

2-3-1-4- Poisson's ratio

Another important parameter is Poisson's ratio. In the elastic regime, Poisson's ratio represents the ratio of transversal strain to axial strain when a uniaxial stress is applied along a given direction. This ratio is conventionally defined with a minus sign so that Poisson's ratio is a positive number in general because if the axial strain is positive (taken as compression here) for instance, then the transverse strain is generally negative (dilation).

In a VTI material, Poisson's ratio takes three independent values. One corresponds to the strain in the isotropy plane in reaction to a strain along the symmetry axis (ν_{31}), and the two other correspond to the strains in the isotropy plane and in the symmetry axis direction in response to a strain applied within the plane of isotropy, i.e., ν_{12} and ν_{13}, respectively (see Figure 2-4 for a schematic representation). Poisson's ratio can be expressed as a function of the c_{ij} coefficients as follows

$$\nu_{31} = \frac{c_{13}}{2(c_{11} - c_{66})} \quad (15)$$

$$\nu_{13} = \frac{2c_{13}c_{66}}{c_{11}c_{33} - c_{13}^2} \quad (16)$$

$$\nu_{12} = 1 - \frac{2c_{33}c_{66}}{c_{11}c_{33} - c_{13}^2} \quad (17)$$

The value of the Poisson's ratio for isotropic elastic materials cannot be higher than 0.5 because of the requirement for other moduli to be positive: Young's modulus, the shear modulus and bulk modulus (Gercek, 2007). For instance this can be easily seen in the relation between young's modulus E, bulk modulus K, and Poisson's ratio: E/K=3(1-2v). This limit extends to materials that are weakly transversely isotropic. In

the context of rock physics, only highly anisotropic materials such as heavily thermally micro-cracked granite can have experimental Poisson's ratios higher than 0.5. In the scope of this project, the artificial shale samples are expected to be weakly transversely isotropic and thus to have Poisson's ratio values below 0.5. This allows to check the quality of ultrasonic data. Also, when comparing ν_{13} to ν_{12} we infer that:

$$if\ c_{13} = c_{33}\ \ then\ \ \nu_{12} = 1 - \nu_{13} \tag{18}$$

If we look at the stiffness tensor of an isotropic material and compare it to the stiffness tensor of a TI material we find that the condition $c_{13} = c_{33}$ is only fulfilled if the material is isotropic and with no shear stiffness (because $c_{44} = 0$), which corresponds to a liquid state. Hence, the equality in equation (18) should hold at the start of a compaction experiment when the mineral-water mixture is a fluid slurry. Then gradually ν_{12} and ν_{13} should evolve independently with compaction when the sample progressively transits from a liquid state to a transversely isotropic solid state.

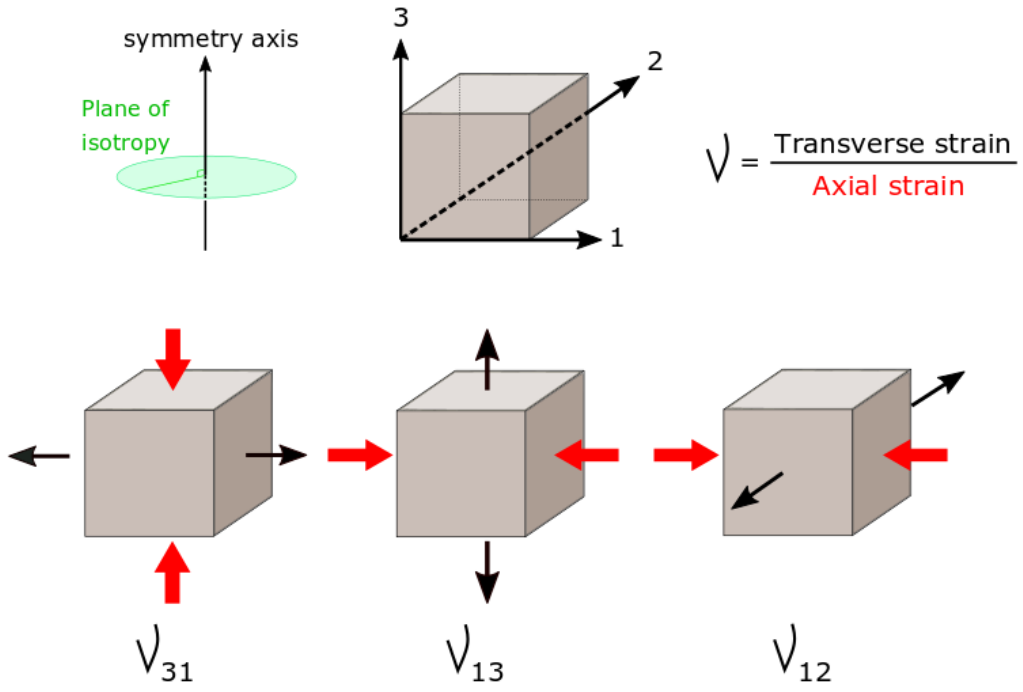

Figure 2-4: Visual explanation of the Poisson's ratios (ν) in a VTI material. The axial strains are in red and the transverse strains in black. There are two values of the Poisson's ratio for an axial strain in the plane of isotropy and one value for an axial strain along the symmetry axis.

2-3-2- Assessment of the impact of OM in previous studies

It was found that for shales with low amount of organic matter, the rock composition had a more important effect on elastic properties than the organic matter itself (Labani & Rezaee, 2015). But we can note that the only parameter used to characterise the organic phase in this paper is the total organic carbon (TOC in wt.%).

Different studies characterised directly the elastic properties of kerogen as an isolated material (Yan & Han, 2013) or within an inorganic mudrock matrix with a nano-indentation technique (Ahmadov, et al., 2009); (Emmanuel, et al., 2016) quantified the stiffening of kerogen with increasing maturation with the same technique. This is valuable information but it remains unclear how this influences the macroscopic behaviour of the host shale. To do so the parameters of the organic matter itself (type, maturity) must be combined with spatial information such as the distribution, the shape and orientation of the organic particles.

OM is more ductile, friable and has a lower density than the rock matrix. A study of the Vaca Muerte shale formation (Dietrich, 2015) and a study of synthetic shale samples (Altowairqi, et al., 2015) recorded a strong correlation between the TOC content and Young's modulus showing a decrease of both P- and S-wave velocities with an increase of TOC content. But results for other elastic properties against TOC are not that straightforward. In the Vaca Muerte shale the Poisson's ratio and Thomsen anisotropy parameters were weakly correlated to TOC content. In the synthetic samples study, despite a wide range of TOC content, the correlations with the Vp/Vs ratio and Poisson's ratio exist but are weak as the values are almost steady. A study of samples from several different organic shale formations (Vernik & Milovac, 2011) suggests that the clay content has a lesser influence than the kerogen content on the bedding-normal compressional stiffness

Other OM characteristics were linked to elastic properties in organic-rich shales. The compliance of OM particles will lead them to deform during compaction and fill the adjacent porous space in a preferential horizontal direction and thus increase the elastic anisotropy (Sayers, et al., 2015). Thus OM from different origins with different compliances will affect the anisotropy differently.

Allan et al. (2015) mentions that velocity anisotropy changes due to OM maturity variations are not well documented in the literature. However they showed for their natural organic shale samples that the intrinsic anisotropy (alignment of mineral matrix, distribution of organic matter) was more important than extrinsic anisotropy (preferred orientation of cracks) under any confining pressures. Increasing thermal maturity induces an increase in kerogen internal porosity (Curtis, et al., 2012). This will impact the OM structure during compaction as porous kerogen will be more prone to pore-collapse.

Furthermore the distribution of organic matter in shales was shown to be laminations parallel to the bedding planes (Vernik & Nur, 1992). Such distribution of organic matter plays a significant role in the geomechanical responses as demonstrated by the good fit between elastic laboratory data of Bakken shale samples and a model taking into account the kerogen distribution (based on the anisotropic effective field theory, (Sayers, 2013). The texture of OM also has an indirect effect on the elastic properties as small particles with more surface contact with clay catalysts will show an increased maturity (Rahman, et al., 2018).

This shows that all aspects in the characteristics of OM in shales play a role of prime importance in the elastic behaviour and its anisotropy. Therefore neglecting one or the other of these characteristics can easily weaken the validity of experimental results and mislead models developments. The effect of shale's OM on the elastic properties is obviously an ambitious challenge to investigate as shales combine already complex properties with great variety of possible OM content, type, distribution and maturity.

Elastic Anisotropy

There are some well identified sources of elastic anisotropy in shales: Clay platelets preferred orientation, OM lenses with a sub-horizontal axis, Microcracks forming along weak sub-horizontal matrix planes and their fluid saturation. The *Figure 2-5* illustrates these anisotropic features with microscopy images of natural shales. But the overall anisotropy remains poorly evaluated. Identifying when the anisotropy develops in the evolution of a sediment and evaluating the impact of each source would help improve the accuracy of predictive models. Does the anisotropy develop during deposition, mechanical consolidation or chemical diagenesis?

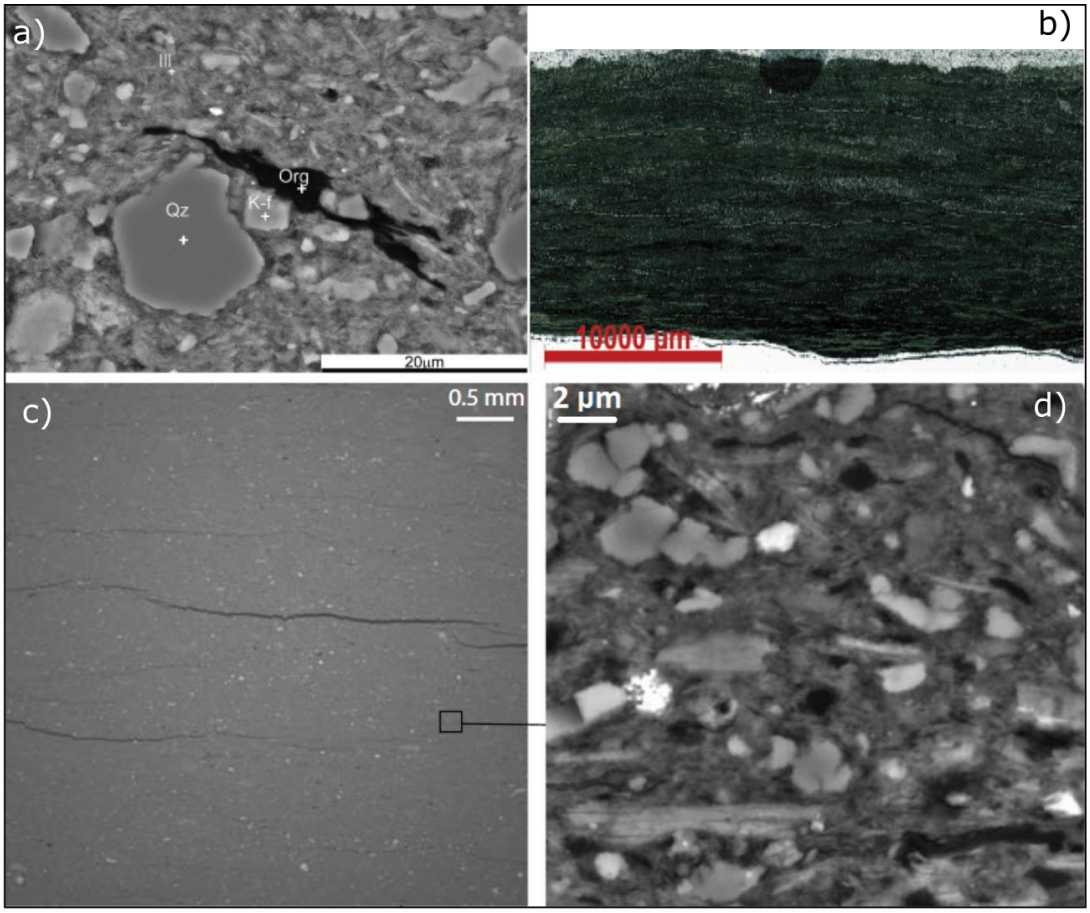

Figure 2-5: microscopy images of natural shales showing their anisotropic features. a) Goldwyer formation, scanning electron microscope (SEM) image centred on a lenticular particle of OM aligned with the bedding plane. Org: OM, K-f: K-feldspar, Qz: Quartz. Ill: illite. b) Goldwyer formation, optical microphotograph of a thin section showing the laminated texture of this organic-rich shale. c) Muderong shale, optical microscopy image showing bedding-parallel microcracks. d) Muderong shale, SEM image showing the bedding-parallel alignment of silt-sized particles within the clay matrix. Sources: a) and b) Goldwyer formation, Canning basin, Australia, from (Delle Piane, et al., 2015). c) and d) Muderong shale, Canning basin, Australia, from (Dewhurst & Siggins, 2006).

The re-orientation of clay platelets by porosity reduction occurs during mechanical compaction (Kaarsberg, 1959) and the texture strength of clay crystallites increases with compression pressure. (Voltolini, et al., 2008). However this effect is only partially responsible for the overall anisotropy as clay mixtures show only a small increase of P-wave anisotropy compared to S-wave anisotropy during compaction (Mondol, 2012). It was shown that the porosity reduction and smectite-to-illite

transformation are responsible for anisotropy increase with compaction (Vernik & Liu, 1997). Another study claims that compaction/burial has no first order influence on elastic anisotropy and deposition is suggested as a more prominent source (Pervukhina & Rasolofosaon, 2015).

Besides anisotropy is strongly positively correlated with organic richness (Vernik & Nur, 1992) because kerogen forms an anisotropic network (Vernik & Landis, 1996). The elastic anisotropy at high confining pressure increases strongly with maturity (Allan, et al., 2014) and crack-induced anisotropy is of second order compared to intrinsic anisotropy (Allan, et al., 2015).

To sum up anisotropy is mainly driven by the intrinsic distribution and orientation of clay and OM particles. This anisotropy can be enhanced by extrinsic sources such as micro-cracks but their orientation depends on the intrinsic microstructure in which they develop. However it remains unclear whether the anisotropic structure of clay and OM is entirely developed through processes occurring during consolidation or if the structure at the time of deposition plays a role. For instance can initial parameters such as the presence of OM or the particle size distribution play a role in the final observed anisotropy? The two different deposition methods implemented during this project (cf. sample preparation Section 3-1-) aim at answering this question.

2-4- Dielectric testing of organic rich shales

2-4-1- Theoretical principles

The dielectric response of a material under an alternating electrical field is influenced both by its electrical polarizability and its electrical conductivity. The dielectric tool used in this project measures both of these properties.

The dielectric constant ε_r, which is also called relative permittivity, is a measure of the electrical polarizability of a material (Von Hippel, 1954) while the electrical conductivity σ is the inverse of electrical resistivity that measures the ability of the electrical current to travel through a material. When a sample is placed in an alternating electric field, the charge carriers within the sample may undergo a translational path through the sample (electrical conduction, in S/m) and a temporary

displacement and/or a reorientation that result in an induced field within the sample (electrical polarization, dimensionless).

The dielectric response is governed by multiple processes that occur within the rock and is heavily frequency-dependent with larger scale processes dominating the dielectric response at low frequency and small scale processes detectable at high frequency, from the electron scale to the pore scale (Figure 2-6) and each process (absorption and/or dissipation of energy) is characterized by the speed at which it occurs (Guéguen & Palciauskas, 1994). Resolving these multi first-order responses over certain frequency ranges is based on the most commonly used model in dielectric spectroscopy, the Cole-Cole model (1941):

$$\varepsilon_r^r(\omega) = \frac{\varepsilon_S - \varepsilon_\infty}{1 + (i\omega\tau)^{1-\alpha}} + \varepsilon_\infty \qquad (19)$$

Where ε_∞ is the relative permittivity at "infinite" frequency, ε_S is the static (S) relative permittivity, ω is the angular frequency, τ is the electrical relaxation time and α is a smoothing parameter in the interval [0-1]. In the Fourier domain, ε becomes a mathematical complex number ($j\omega$) that split the function into two members. The real ($\varepsilon'_r(\omega)$ also described as the dispersion) and imaginary ($\varepsilon''_r(\omega)$ also described as the absorption) parts that can be written in the form of:

$$\varepsilon_r(\omega) = \varepsilon'_r(\omega) - j\varepsilon''_r(\omega) \qquad (20)$$

The real permittivity ε'_r can be regarded as a measure of the intensity of the polarization and the imaginary permittivity ε''_r is related to the work exerted by the different mechanisms. The dielectric properties of rocks are important petrophysical parameters because they are linked to many different characteristics of the rock material at different frequencies.

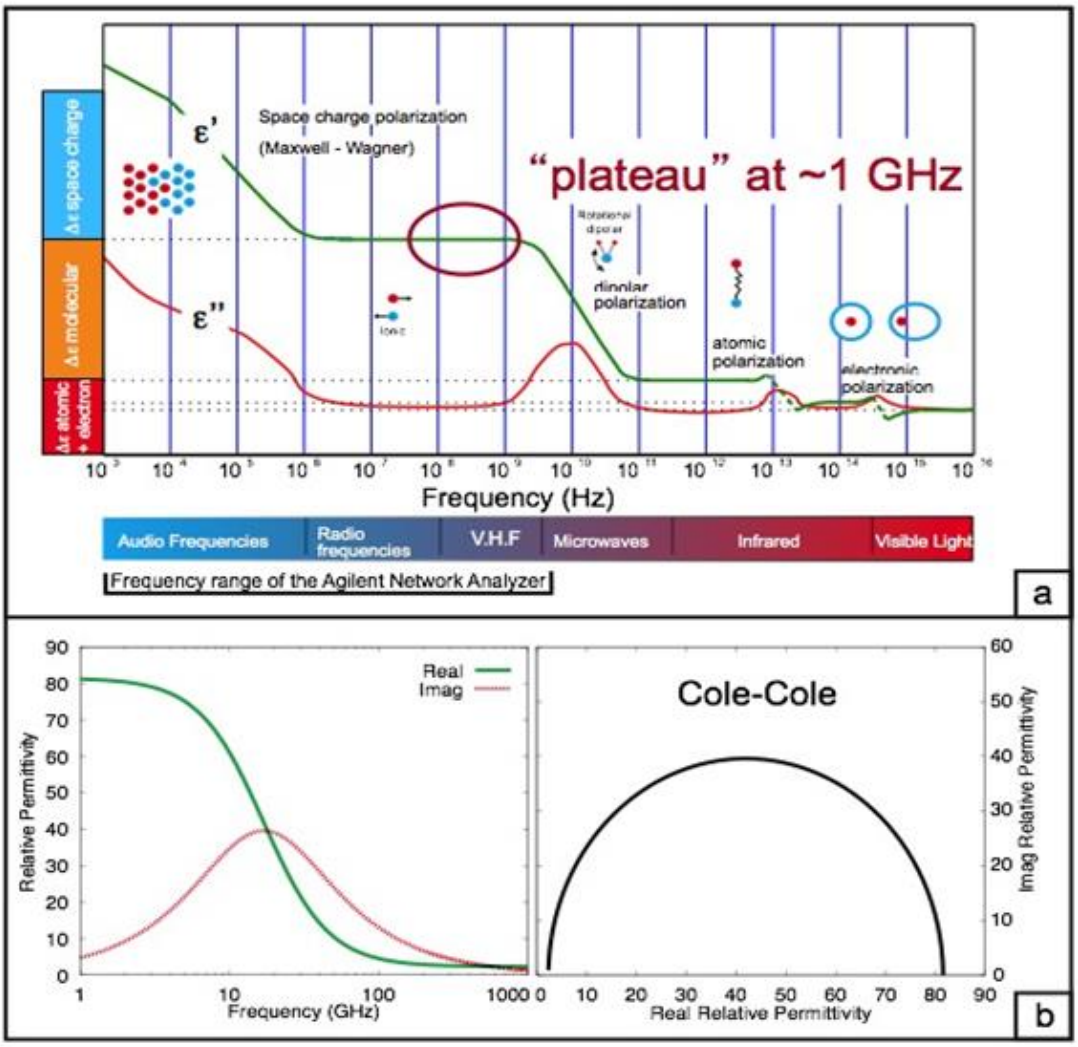

Figure 2-6: Dielectric principles. (a) From Guéguen and Palciauskas (1994). *Variation of the real part and the imaginary part of the relative permittivity with frequency due to different polarisation processes. (b) Example of real and imaginary dielectric response of water with frequency on the left and direct relation between real and imaginary part of water in the Cole-Cole model.*

2-4-2- Laboratory dielectric testing

3 main types of electrical polarization occur in a rock at the microscopic scale: electronic, molecular dipole, interfacial (Maxwell-Wagner, electrical double layer polarization in clays). These three polarization types occur at three different scales. The larger the scale, the more time is needed under a constant electric field to achieve full polarization. Therefore, under an alternating electric field of increasing frequency, the larger scale mechanisms have only time to achieve a partial polarization and if the

frequency is raised high enough, they no longer occur at all. When the frequency is low enough, the polarization types occurring at the larger scales will dominate the dielectric response compare to the lower scale polarization types.

Electronic polarization happens at the atomic level when the electron density around the nucleus increases preferentially in the direction of the electric field. This polarization can happen up to very high frequencies (> 10^{12} Hz).

Molecular polarization happens when a dipolar molecule (i.e. water molecule) is oriented along the direction of the electric field. It occurs at frequencies up to 10^{10} Hz.

Interfacial polarization occurs at the grain scale. Maxwell-Wagner polarization occurs when there are interfaces between materials with vastly different conductivities, i.e. interface between water and mineral grain or oil. In these cases the ions in the water are prevented to travel along the electric field by the insulant materials and will accumulate on their surfaces. Other examples of interfacial polarization exist when minerals happen to have electrically charged surfaces. Clay particles for instance have negatively charged surfaces that bound cations from the pore fluid to the grain's surface while repulsing anions. It is logical that such polarization is increased when the pore shapes are more tortuous and the insulant grains have a platy shape as this will impede electrical conduction of the ions and favour polarization. Higher brine salinities increases the magnitude of interfacial polarization. This larger scale polarization occurs only up to 10^{8} Hz.

The mineral matrix, if clay-free, is only submitted to electronic polarization. The pore water is sensitive to electronic and molecular polarization of the dipolar water molecules. The rock as a whole displays all three mechanisms.

To interpret dielectric measurement there is a need for inversing the permittivity values to extract petrophysical information such as the rock texture. One popular model to do so is a mixing law called complex refractive index method (CRIM) model that is a simple volumetric interpretation of the dielectric response with a power law such as:

$$\sqrt{\varepsilon_{eff}} = \Phi S_w \sqrt{\varepsilon_w} + \Phi(1 - S_w)\sqrt{\varepsilon_h} + (1 - \Phi)\sqrt{\varepsilon_{ma}} \qquad (21)$$

Where φ is the porosity, S_w the water saturation, ε the relative permittivity, and eff, w, h and ma refer to the whole rock, water, hydrocarbon and the solid matrix, respectively. This method works well when the dielectric response is caused exclusively by electronic and dipolar polarization as these are independent from the rock structure. Hence CRIM model works well at high frequencies (10^9 Hz). However at lower frequencies the interfacial polarization processes are dominant and the dielectric response is thus only loosely related to the relative volumes of the different phases and depends more on the pore and grain structures. Therefore effective medium theories are better at modelling lower frequency dielectric responses. Different methods exist where spherical or elliptical particles of water/oil/minerals are added to a background matrix computed with the CRIM model.

By measuring the permittivity independently at different frequencies in the range 10^6 Hz to 10^9 Hz, the CRIM model and some variations of the effective medium model can potentially be solved for the texture of the different components, the salinity of the brine and the water saturation.

Dielectric logging is useful and preferable to resistivity in cases where water salinity is low, unknown or very variable. Indeed water saturation can be deducted from dielectric measurements in these conditions whereas resistivity measurements can have a hard time differentiating hydrocarbon from fresh water, or correcting for changes in salinity when formations have been invaded by drilling mud or have been hydraulically stimulated. In other instances dielectric measurements can be combined with resistivity to compute the cementation exponent. Besides, dielectric measurement is sensitive to all the water in the rock whereas electrode resistivity measurements only respond to connected pore water.

The depth of investigation of dielectric logging tools depends on the frequency, with higher frequencies giving smaller penetration depth and also on the formation resistivity where high resistivity zones have very low attenuation of the signal through conduction processes, and therefore a deeper penetration of the signal.

There are two types of dielectric tools used in logging. The electromagnetic propagation tool operates at high frequency tools (10^7 to 10^9 Hz). Its penetration depth vary between 5 and 30cm. It computes the permittivity and the conductivity as described above. The other tool operates at a lower constant frequency (usually $2x10^6$)

to obtain a deeper penetration depth. At this low frequency the signal is dominated by the imaginary part of the permittivity (energy loss) and the polarization amplitude is minimal. Hence the phase shit and attenuation are converted in two conductivity values.

Beyond classical petrophysical investigations, dielectric testing was recently developed and applied in shales and revealed to be sensitive to several useful characteristics of shales. Dielectric is the study of a material's response to an alternating electric field where conduction and electrical polarisation processes occur related to different transport mechanisms at different scales. The measured dielectric properties help to discriminate the influence of each process as they occur at different frequency range: As the frequency of the alternating field increases the large scale processes have no longer the time to happen and the remaining dielectric response is the result of smaller scale processes. A rock's dielectric response depends on several factors such as the matrix composition and structure, the pore fluid composition and saturation and the solid/liquid interface mechanisms. The complexity and the variety of possibilities make the dielectric response over a broad frequency range very rich in physical information about a rock.

For most of rock types the rock matrix itself acts as an electrical insulant. Thus the dielectric response is usually dominated by mechanisms occurring in the pore fluid and at the fluid/solid interface. In the case of shales, the porosity is usually low and the clay content gives a high specific surface area and negatively charged grain surfaces. Therefore a consequent portion of pore fluids is strongly bound to the mineral grains' surface as an "electrical double layer" (Stern, 1924) so that clays play an important role in the dielectric response. A thorough electrical study of compacted clays (Comparon, 2005), performed both on synthetic and natural clays, showed a strong influence of the water content as well as an important impact of pore-fluid interface mechanisms at low frequencies on both the electrical conductivity and the dielectric permittivity.

(Delle Piane, et al., 2018) demonstrated that the presence of highly mature OM leads to unusually high conduction and dielectric permittivity within a shale, and Josh et.al. (2016) substantiate this finding with compacted synthetic shales and numerical simulation showing that both non-conductive and conductive OM can play a role.

A strong anisotropy of dielectric properties caused by the clay microstructure exists in shales. We can see the analogy to the shale elastic anisotropy. Beyond the structural relationships with dielectric properties, other works demonstrated dependency of the dielectric response with other properties including: porosity, pore network geometry (Seleznev, 2005), mineralogy with clay minerals in particular, CEC, SSA and even elastic properties of shales (Patchett, 1975; Josh et al., 2012; Josh, 2014) which are meaningful information for shale characterisation. The later relationship with dielectrics arises from a correlation found between CEC and geomechanical properties (Dewhurst, et al., 2008). Also by expressing electrical conductivity and P-wave velocities as a function of porosity in constitutive equations, Carcione et al. (2007) modelled velocity/conductivity relationships for shaly and sandy materials with good agreement with well log data.

This shows that OM characteristics that have an influence on elastic properties can potentially affect the electrical and dielectric properties as well and the combination of the two sets of measurements could therefore help to characterize the OM content of shale samples. Moreover the contrasting resistivity and polarizability of OM compared to inorganic minerals such as clays are a further indication that dielectric method has the potential to become a strong tool for OM identification.

2-5- Artificial sample approach

Natural shale samples present many disadvantages for rigorous laboratory testing. They often have heterogeneous structures and compositions with a high vertical variability, a complex mineralogy and a complex compaction-diagenesis history. They are hard to preserve after coring as the clay they contain is highly chemically reactive and highly sensitive to desiccation (Ewy, 2015). In turn a decrease in saturation of just a few percent or a pore brine that doesn't match the in-situ salinity will modify greatly the properties of the sample. To reproduce in-situ conditions in a laboratory a sample often has to be re-saturated but this process can take months because of the very low permeability of consolidated shales (Mesri & Rokhsar, 1974). Finally a natural sample has to be subjected to an extensive characterization workflow to link its characteristics with its physical response.

On the other hand the advantage of testing artificial samples over natural ones is threefold (i) Obtain a material with a lessened complexity compared to natural ones

by creating samples with no cracks, a homogenous mineral matrix with a simple structure and a constant bulk density to have identical properties in any region of the final sample. (ii) Produce samples with a great repeatability and well characterized by having a strict control of the characteristics such as compaction parameters, pore fluid and mineral compositions. (iii) Avoid the preservation issues encountered with natural samples by creating saturated samples in the laboratory and test the physical properties during and immediately after compaction.

However artificial samples present the obvious drawback of in-situ representativeness. We must determine with certainty what characteristic of natural samples are wanted and can realistically be reproduced in the laboratory if we want to be able to compare the results we obtain with artificial samples to the physical behaviour of natural shales.

The literature of artificial shales is plentiful. However the methods employed vary greatly across the board and each method corresponds to precise initial objectives. The common starting point that all studies share is the mineralogical composition that must match the minerals and grain size of natural samples. The methods of deposition and compaction are where the differences arise.

Some examples involve the mixing of the dry minerals with liquid adhesive and the successive compaction of thin layers to form laminations typical of natural samples (Luan, et al., 2016), (Gong, et al., 2018). This method presents the advantage of increasing the consolidation obtained with mechanical compaction with the simulation of cement in the form of liquid adhesive. Moreover the compaction of successive layers avoid inhomogeneous compaction due to pressure differences between the top and bottom of the sample. This method may be a good way of reproducing the elastic properties of natural shales but the replacement of water by adhesive results in highly unnatural electrical properties by changing the chemistry of clay minerals.

A more commonly employed method consists of preparing a homogeneous mixture of water, clay and silts and apply pressure with a high-stress oedometer to consolidate the artificial sample in a single compaction as described notably by Mondol, et al., (2007), Voltolini, et al., (2008) and Beloborodov, et al., (2016). This method is primarily employed for the analysis of mechanical compaction trends as it doesn't offer any opportunity to simulate chemical compaction. The addition of adhesive and water is possible but as the sample mechanically consolidates, the permeability

decreases and the dissipation of excess pore pressure becomes very slow. The addition of adhesive would mean a chemical stiffening after several hours at best. The presence of early cement was shown to hinder the mechanical consolidation and associated particle re-orientation (Delle Piane, et al., 2015). Hence a complete mechanical consolidation with extensive dissipation of pore fluid pressure is not compatible with the addition of adhesive. Besides the initial mixing of the minerals doesn't reflect the initial particle texture in a natural setting at the time of deposition and its potential influence on the physical properties after consolidation.

Another method allows for a natural-like deposition via a settlement experiment (Guo, et al., 2015). It consists in letting mineral particles settle by gravity in a column of water with a low initial mineral concentration. This method was designed to study the initial deposition and pore pressure dissipation in fresh sediments. To produce a consolidated sample with a natural-like initial settlement would require to combine the settlement column with a compaction rig apparatus (with all the associated sensors for physical measurements) to compact the sample at higher stress after the initial settlement by gravity. However this method presents the drawback of separating materials of different density by buoyancy which makes the sample inhomogeneous. Repeatedly alternating settlement of small amounts of minerals of different density would be a solution but would make the experiment unpractically long.

The analysis of different methods of producing artificial shales gave us insights for the design of our samples. The time limitations of laboratory experiments do not allow to reproduce all the characteristics of a natural sample that consolidated over millions of years.

It was decided to produce samples from an initial mineral-water mixture to preserve the electrical properties of the OM-clay-water structures and to not add adhesives to ensure a better mechanical compaction and dissipation of pore pressure without the time limiting factor of the stiffening of the adhesive. To analyse the influence of the initial deposition we will perform two types of sample preparation: one that consists in mixing homogeneously the initial constituents and one that is aimed at reproducing the settlement by gravity. I chose to perform compaction on a single layer of mixture. In turn this doesn't allow us to observe the impact of laminations on the physical properties but rather observe the intrinsic properties for a given layer. The use OM at

different maturity levels introduced in the artificial sample before compaction was decided. Therefore the results will reflect the impact of the intrinsic properties of OM rather than the consequences that thermal maturation has on the surrounding matrix such as over-pressure and micro-cracks formed after HC generation. The absence of simulated cement means the samples will have a higher porosity than natural samples with the same stress history. To obtain the lowest porosity possible through mechanical compaction the main mineral ingredient was set as the clay type for which the clay-water mixture is the most compressible: Kaolinite. However due to the importance of swelling clays in the maturation of OM, the addition of smectite to the OM for the maturation process (that occurs separately before compaction) was preferred.

To summarize the artificial samples will allow to study the changes in physical properties due to the intrinsic characteristics of shales during their mechanical consolidation. The final samples will be equivalent to young (cement-free) normally consolidated organic shales.

2-6- Project premises

As a conclusion to this review of the literature, this section is a rundown of the information presented above that justifies the significance of this project to the industry for the exploration of unconventional shale reservoirs but also to the broader field of shale rock physics.

- The maturity of OM is regularly overlooked during exploration in favour of direct estimates of HC in place. However in unconventional source rock reservoirs, the volume and type of HC is directly linked to the kerogen maturity. Therefore I want to establish links between organic maturity and commonly measured physical properties such as elastic and dielectric properties, which could help in the detection of HC sweet-spots early on in the interpretation of logging data.
- The transverse anisotropy of shales elastic properties must be measured downhole or in the laboratory to correct seismic data inversion and obtain the true 3-dimensional structure of a formation. OM is a strong source of anisotropy in shales, but its impact on anisotropy is generally applied too

simplistically to only one parameter (TOC). For that reason I want to measure the impact of OM type (terrestrial vs. marine) as well as its texture on the elastic properties and their anisotropy to provide a better appreciation of the effect these parameters have on the overall anisotropy.

- Most of the OM characteristics studied in this project refer to the intrinsic features of the organic material (maturity, type and aspect ratio). However the variations in measured properties between different organic shale formations may also be caused by external factors such as the deposition environment. Hence in addition to the main objectives, I want to explore the impact of two different methods of deposition for organic rich samples and inorganic control samples on the measured properties of interest (dielectric and elastic).

In the next chapter all the information related to the production of the artificial sample set will be presented, from the sample preparation and the design of the apparatuses to the results obtained with the compaction cell sensors.

Chapter 3: Fabrication of the artificial shales

3-1- Sample preparation

The final set of compaction experiments presented in this document is both the largest and the most advanced in terms of design of the samples as well as the span of the investigated variables. The issues encountered in the previous sample sets were solved and the full elastic tensor was recorded during each experiment, followed by a series of tests after compaction to characterize and image the samples. A total of 11 synthetic samples were produced for this set. In this section we describe the target variables of the sample set, then we explain how we set all the constant parameters across the sample set. Thereafter, the experimental workflow carried out on each sample will be presented and a list summarizing the purpose of each sample will be laid out.

3-1-1- Target variables

The objective is to highlight the influence of a few variables on the measured properties. That is why the samples were designed so that most of their characteristics remain identical within the intrinsic experimental errors of the apparatus and methodology. Namely the inorganic mineral composition, the brine composition, the inorganic mineral volume, the uniaxial stress magnitude and the loading times were the same for all samples. The variables investigated include:

3-1-1-1- OM type

Fresh OM with two different origins was used (i) continental origin type III Kerogen and (ii) marine origin type II Kerogen:

(i) Continental OM type: Peat coming from peatlands (as pictured in Figure 3-1– top) from the manufacturer *Annapolis valley peat moss Co*. in Nova Scotia, Canada). This material is composed mainly of *Sphagnum peat moss*. This type of moss develops in wetlands and under the right conditions can accumulate over several metres. There are also remains of higher fibrous plants present in the peat. The decomposition of Sphagnum and the other plant debris embedded in it is very slow. This is due to the presence of chemicals present in the moss cells (phenol groups) that impedes the activity of micro-organisms and the low oxygen level encountered inside any wetland soils that slows down aerobic decay by the micro-organisms. Therefore, after burial in a column of sediment, the preserved peat will undergo diagenetic transformations that will lead to the production of hydrocarbons. In turn, peat is believed to be the primary

source of type III kerogen. This kerogen type is gas prone and is found in many source rocks and unconventional shale gas reservoirs.

(ii) Marine OM type: dry microalgae material coming from an algae farm in Queensland, on the North-eastern coast of Australia from the manufacturer *Plankton Australia Pty. Limited*. The exact species of algae is *Dunaliella Salina*. It is recognisable for its reddish-orange colour caused by carotenoids (coastal pond saturated with this algae is visible in Figure 3-1 – bottom). Despite its appearance, it is classified as a photosynthetic green micro-algae and is a type of marine phytoplankton. After its death, phytoplankton deposits on the ocean floor and start being degraded by micro-organisms under anaerobic conditions within the sediments. Under certain circumstances, it is accumulated in an anoxic environment. If the conditions after the time of deposition remain anoxic, the marine OM will be preserved after burial in sediments. With heat and pressure, it will produce type II kerogen. This kerogen type is both gas and oil prone and can be found in unconventional shale reservoirs.

In this sample set, part of the sample collection was mixed with both OM types, continental and marine, always with no more than one OM type per sample. Some artificial shale samples were produced without OM for the sake of comparison with the organic-rich samples. The water content of the peat and of the microalgae were 40% and 10% in weight as received, respectively. The particle size indicated by the manufacturer ranged between 100µm and several millimetres (higher plant debris) for the peat whereas it comprised between 150µm and 425µm for the microalgae. To eliminate these initial disparities in water content and particle size, both OM types were oven-dried at 90^0C for 48h to eliminate most of the water and ground into a fine powder (<10 to 100µm).

The choice of these materials was justified by the relevance of the organisms they are composed of. Indeed peat and phytoplankton are important biomasses cited as some of the main sources of kerogen (Jianzhong, et al., 2014), (Petersen, et al., 2009). Also their availability in large quantities was a determining factor. Other possible OM sources were considered such as directly extracted kerogen from source rocks by chemical processes. However this method requires the dissolution of the surrounding inorganic matrix and non-kerogen OM in organic solvents or acids. Hence the

extracted OM represents only a portion of the original OM embedded in the source rock and it typically produces only small quantities of kerogen. It was therefore not suitable for the requirements of our experiments. Despite numerous advantages, the use of fresh OM has one main drawback: a higher oxygen content than in-situ OM. The OM we are using did not undergo an anoxic degradation and will thus have a higher Oxygen-to-Carbon ratio than young source rocks containing buried land or marine OM. This will in turn lead to a difference in the chemical compounds produced by the maturation processes undergone during the in-situ diagenesis compared to the artificial maturation of fresh organic matter (cf. hydrous pyrolysis section 3-2).

Figure 3-1: Top - picture of a Peatland in front of a boreal pine tree forest, in Algonquin Park, Ontario, Canada. From Nina Stavlund. Bottom – Aerial Picture of a salt water pond spanning several hundred metres containing high concentrations of Dunaliella Salina micro-algae on the shore of the San Francisco bay, California, USA. From David Searls.

3-1-1-2- Maturity

The fresh OM mentioned above was incorporated into the synthetic samples at three different maturity levels:

- Fresh: the oven-dried and powdered organic materials were used without undergoing any thermal maturation in a series of samples.
- Maturity level 1: this maturity level was reached by submitting the fresh OM to three weeks of hydrous pyrolysis at 200^0C.
- Maturity level 2: the OM was matured in the same conditions as level 1, but for a duration of six weeks.

The OM was matured in a hydrous pyrolysis vessel on its own and was then mixed in a high-power blender to homogenise it and break down any agglomerated particles. The resulting mixture (Figure 3-2) was then added to the synthetic samples during the liquid mix phase. For more information on the hydrous pyrolysis and the sample preparation procedures, please refer to the hydrous pyrolysis experimental principles (Section 3-2-) and the compaction cell experimental protocol (Section 3-3-2-2-).

For each maturity level, one sample of each OM type was produced, resulting in four final samples containing artificially matured organic matter.

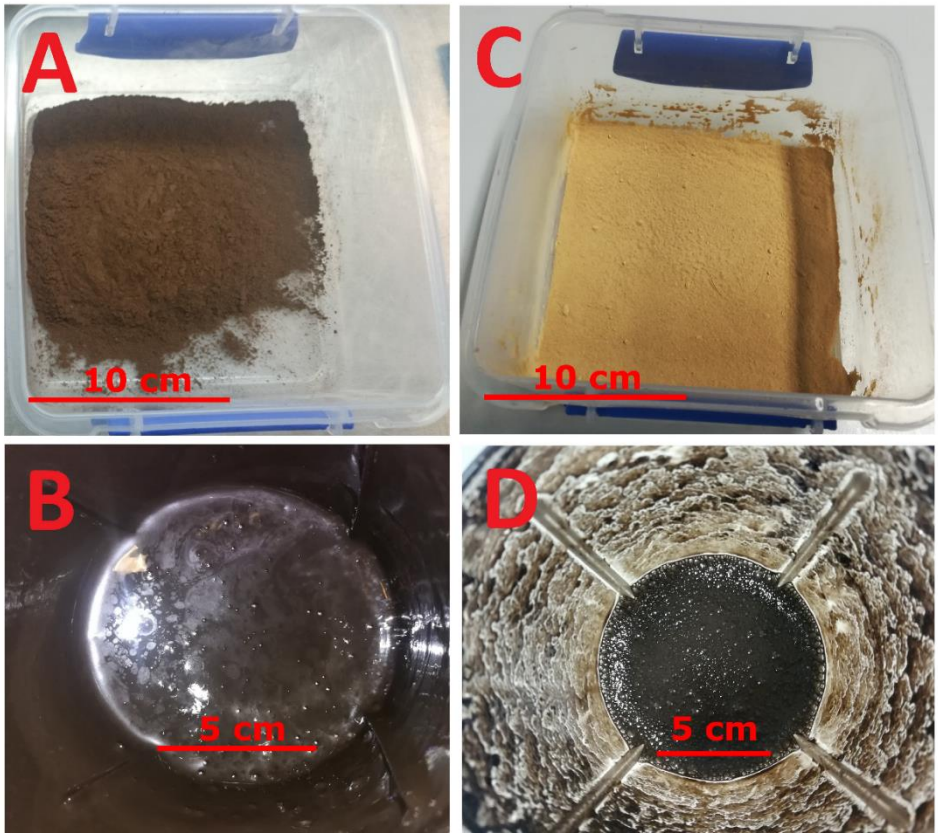

Figure 3-2: Picture of the prepared OM. A) Dried and ground fresh land OM; B) Matured and blended land OM (level 1); C) Dried and ground fresh marine OM; D) Matured and blended marine OM (level 1). A) & C) photographed in storage plastic container. B) and D) photographed in blender plastic container. The visual aspect of maturity level 1 and 2 were very similar for both OM types. Please refer to the text for more details on the maturity levels.

3-1-1-3- Organic particles texture

To investigate the effect of particle size, shape and orientation, two types of OM particles were designed. The first one, that we described earlier in section 3-1-1-1-, is the dry thin powder composed of particles smaller than 100µm with a mean value of 20µm in size and with a high shape aspect ratio (i.e. ~1, close to a circular shape). To contrast that particle type we created another OM particle type with a much bigger particle size at a mean value of 50µm and up to 2300µm and with a lower shape aspect ratio.

The desired OM particle shape ratio was achieved by compacting the initial powdered OM of each type (land and marine) in a cylindrical cell in a mix of 50% brine at 15g/L NaCl and 50% OM at a uniaxial stress of 20MPa for 48h in drained conditions. We

obtained a solid cylinder for each OM type. A small offcut of each cylinder was weighed wet and dry to determine the proportion of brine remaining in each sample. The cylinders were then reduced to flakes using a stainless steel shredder before to pass them through a sieve with a mesh size of 2.3mm to get rid of the coarse flake sizes. The resulting particles shown in Figure 3-3 ranged from 200µm to 2.3mm with an aspect ratio lower on average than the powder particles.

The flake particles were all made of non-matured OM. They were then integrated into the synthetic shale samples following the same procedures than the powder particles. It is noteworthy to mention that during the liquid mixing phase with the inorganic minerals, some of the flakes particles broke down into smaller pieces, especially for the marine OM that wasn't as cohesively compacted compared to the land OM. Hence some particles smaller than the previously mentioned 200µm lower limit are present in the artificial samples containing flakes.

Figure 3-3: Flake particles produced with fresh land OM. The bigger particles (left) were sieved out. The final flake particles (right) range in size between 200µm and 2.3mm, with a low aspect ratio (<0.25).

3-1-1-4- Deposition method

The basic constituents of each synthetic sample are a mixture of a solid phase (powdered minerals and OM) and pore fluid (water and salts). Depending on the purpose of the experiment the user must choose the components and set the right amounts of constituting materials to be poured in the cell. Ideally the initial mixture must have a high water content so that the mix is in a liquid state. To keep track of the density and porosity from the measured volume change during compaction, the exact amount and density of each initial constituent must be known. Hence the density of

each constituent was measured using a helium pycnometer (Micromeritics AccuPyc II 1340) with a precision of ±0.01 g/cm^3. Their weight was measured with a conventional mass balance with a precision ±0.05 g.

The dry powdered minerals (with or without OM) are first mixed manually and thoroughly in a bowl to achieve a visually homogeneous colour/texture. If chunks remain after manual mixing, they are ground and possibly oven-dried at 60°C beforehand to get rid of any significant amount of moisture that could not be quantified. According to the amount of final (post-compaction) material needed, the required initial volumes of each constituent are computed and weighed with an accuracy of ±0.01 g.

The pore fluid is prepared separately with deionized water and controlled amounts of salts. The amount of water is determined by the required initial sample volume. Namely the sum of the volume of the solid phase and the brine must equal the volume of the chamber of the compaction cell when the piston is at its highest position. Salts are then added to the deionized water to match the target brine composition. The brine is then degassed for 24h under vacuum.

Once the brine and the dry mix are ready, the next step of the preparation can be done in two different ways. Most samples were prepared following a mixing method. A few samples were prepared following a sedimentation method to explore the influence of the deposition method on the ultrasonic and dielectric properties. The two deposition methods are visually explained in the diagram in Figure 3-4.

- Mixing method

This method involves a liquid mixing phase after the dry mixing phase that prohibits specific spatial organisation of the particles (i.e. isotropic distribution and orientation of the particles) with a final mixture viscosity high enough to stop decantation/redistribution of the particles by gravity within the experimental period of time. Any anisotropy in the particle distribution and/or orientation is hence developed during the compaction process.

The degassed brine and the minerals are then combined and mixed manually for several minutes until the wet mixture presents a homogeneous appearance

(colour/texture). The amount of brine added to the mixture is key at this stage as a high water content will form a mixture much easier to homogenize and handle.

Finally, the mixture is poured into the compaction cell using a funnel. All the tools used for the liquid mixing and the pouring are weighed right after use and after cleaning and drying. The difference between the two weights corresponds to the material lost during preparation and can represent up to 2% in volume of the initial brine-mineral mixture. This quantity is used to correct the amount of brine and minerals initially present in the cell at the initiation of the compaction experiment.

- Sedimentation method

The deposition of shale sediments occurring naturally differs drastically from the mixing method described above. We wanted to investigate to what extent the anisotropy of elastic and dielectric properties is linked to mechanical compaction processes and if the initial deposition had any influence. To study this we developed a deposition method that resembles more the natural process of clay sediment accumulation at the bottom of a water column (i.e. low energy deposition environment/deep marine environment). The idea behind this is that non-spherical particles in calm depositional environments - typical of shales - would settle on the floor along their long axis rather than randomly.

Two samples were created with a natural sedimentation-like deposition method: (i) artificial shales containing land OM flake particles and (ii) artificial shales without OM (inorganic shales). Each of them was matched with a twin sample whose only difference was that it was prepared using the mixing method (i.e. isotropic initial particles distribution and orientation). The sedimentation method involves mixing 5% in volume of solid constituents (minerals and OM if applicable) with 95% in volume of brine (Figure 3-5). When homogeneously mixed, this concentration of minerals is low enough to have very few interactions between solid particles but high enough so that the less dense particles cannot readily rise above the denser particles. This mixture is then placed in the compaction cell equipped with an acrylic extension in order to form a high column of water. It is then allowed to settle for 72h. While the solid phase settles, a back-pressure is applied to the water column with a vacuum pump to remove any air inclusions. After that period the free water above the deposited solid phase and

the acrylic extension are removed and the sample undergoes a compaction according to the standard procedure (see section 3-3-2-).

The issue of whether this deposition method is a true analogue to a natural deposition is discussed in the interpretation section (section 5-4-).

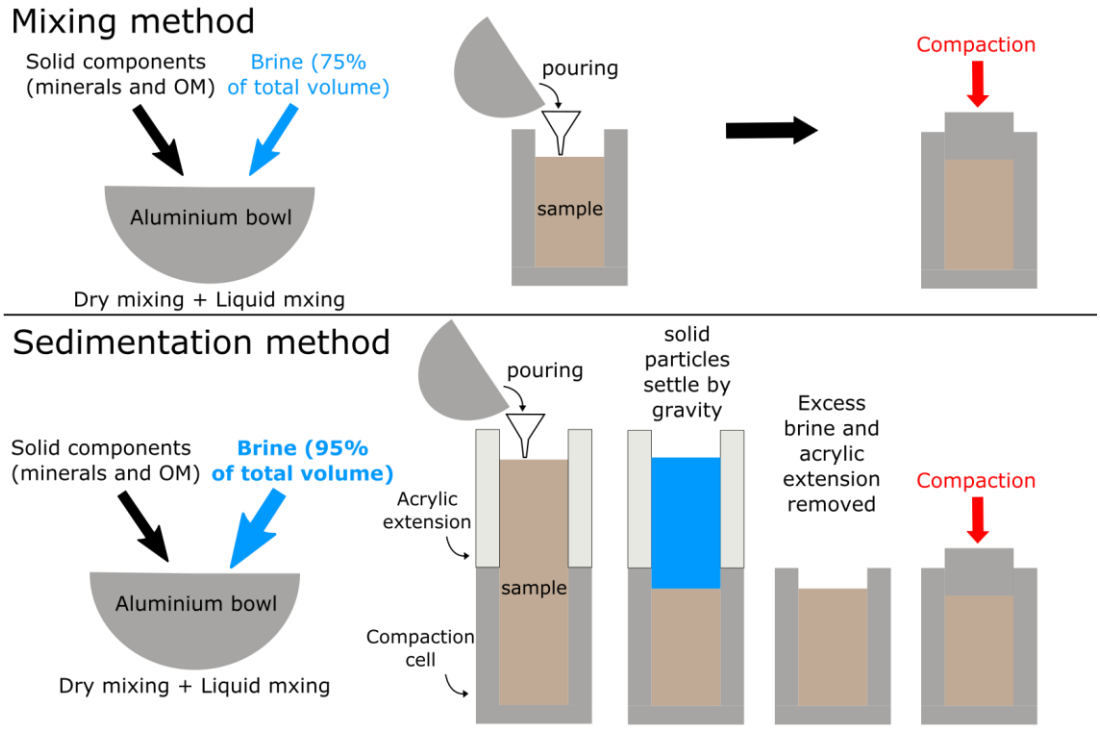

Figure 3-4: Diagram summarizing the two deposition methods. In the sedimentation method the initial sample has the same solid volume as in the mixing method but a much greater brine volume. The mixing method involves pouring the initial mixture into the compaction cell and starting the compaction experiment right away. The deposition method requires a settlement period of 72h during which the solid particles will settle by gravity at the bottom of the cell while most of the brine will separate to the top of the apparatus.

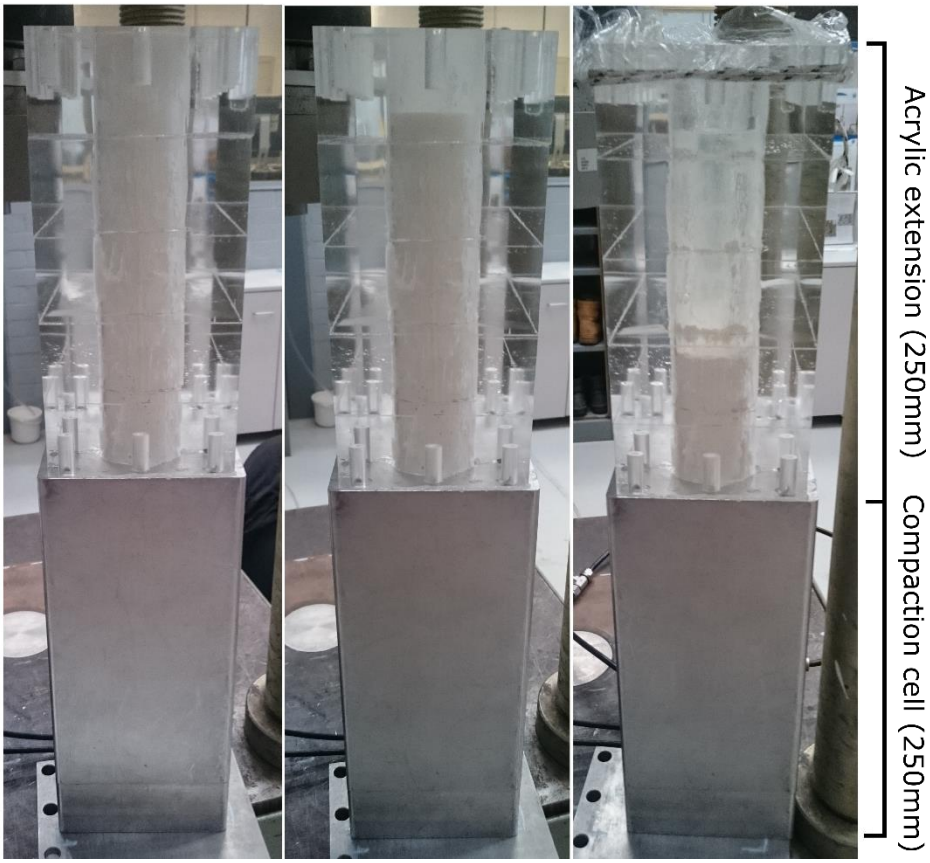

Figure 3-5: Picture of the compaction cell equipped with the acrylic extension on top of it for a total height of 500mm. A mixture of brine and inorganic minerals (95% water in volume) was placed inside and allowed to settle 72h. Left: t = 1min after the mixture was placed in the cell. Middle: t = 1 hour. Right: t = 22 hours. After 72 hours, the mineral to free water interface was below the acrylic extension level.

3-1-2- Constant parameters

To ensure that comparison between samples evaluates the effect of OM only on the physical properties of the synthetic shales, the samples were compacted with the same consolidation behaviour and made with the same inorganic matrix.

3-1-2-1- Mineral composition

The mineral composition developed for the previous sample sets was re-used for this sample set. It represents an average composition of the main minerals found in a database of European natural shale formations (Hillier, 2006). It comprises 4 different mineral components: clay, quartz, feldspar and carbonates – with relative volume ratios of 6:2:1:1, respectively. For each mineral group the most abundant mineral of the group was chosen for our samples. Namely, the carbonate group is represented by

calcite, the feldspar group by K-feldspar (Orthoclase). Kaolinite was used to represent clays. It is only the third most abundant clay in shales after smectite and illite but its mechanical properties were more suitable for the experiments and it is also easier to find in its pure component than other clay types. Indeed kaolinite has a better hydraulic conductivity (little swelling effect with water interaction) and its booklet micro-structure allows to trap less water than illite and the swelling clay smectite. The chemical and structure properties of kaolinite-based samples lead to an easier water drainage and an experimentally time efficient consolidation.

Nevertheless this composition had to be slightly modified in order to be able to relate the results obtained on organic rich samples and inorganic comparison samples. To get a similar inorganic composition between an organic-rich sample and an inorganic sample, the initial approach used in the previous sample sets was to maintain the mineral composition of an "average" shale and replacing the OM volume content by clays and the other minerals in order to maintain the inorganic ratio mentioned above (situation 1 on the diagram of Figure 3-6). However this results in a higher clay volume ratio in the inorganic samples. Clays are one of the most important if not the most important factor governing the physical behaviour of shales. Hence the influence of OM on the elastic and dielectric responses may be confused with the one of clays in the situation 1. For that reason, we chose to maintain a constant clay volume ratio in the new approach (number 2 in Figure 3-6). The OM is replaced solely by the non-clay minerals in the inorganic samples.

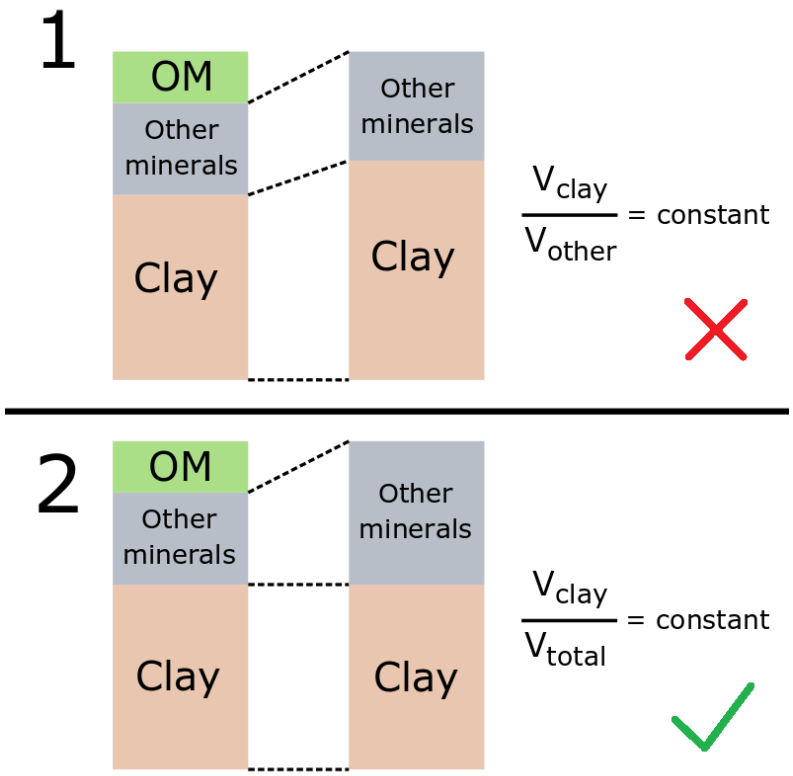

Figure 3-6: Diagram showing the relative solid composition of organic rich (left) and inorganic samples (right). The old approach (number 1) maintains the ratio of the inorganic constituents. However this leads to an important difference in clay content between inorganic and organic samples. The new approach (number 2) used for this sample set used a constant clay content and the OM is replaced by non-clay inorganic minerals in the inorganic samples.

3-1-2-2- Pore fluid

The pore fluid we used for all samples had to fulfil two functions: representativeness of natural samples and preservation of the cell's parts. The majority of in-situ shale pore fluids are brine with salinities ranging from moderate to very high. Using fresh water or deionised water would affect the mineral matrix in ways not seen in natural shales, especially the chemical water-clay mineral equilibrium. For instance a water with a very low salinity would interact with clays interlayer ions and thus modify their physical properties. However, a too high brine salinity (> 30000 ppm) in the synthetic samples is not recommended, as it would lead to corrosion of the cell's metal parts. This would increase the wear on the compaction cell and render it inoperable after few experiments. For these reasons it was decided to set the salinity value to a moderate

value of 15g/L (i.e. 15,000 ppm). Deionised water and sodium chloride (NaCl) were mixed to produce this brine.

3-1-2-3- Uniaxial stress path and loading times

In natural fresh sediments and under calm geological conditions (i.e. no tectonic stresses or upwelling), the uniaxial vertical stress continuously increases as a column of sediments accumulates by decantation in the water column. Considering the geological time scale of this natural deposition, the lithological stress naturally increases inside the sediment column, the resulting excess pore pressure has a very long time to dissipate and the natural shale formation can be considered at the pressure equilibrium at all time during the gradual increase of the vertical load by sediment accumulation. However this type of stress increase is hard to reproduce at a laboratory scale due to the experimental time it involves. Because of the very long consolidation times and pore pressure equilibration times clay-rich samples require, the approach that we used in previous sample sets where the stress was gradually increased over several hours was not ideal. Indeed if we want to have a pore pressure that equilibrates in drained conditions along a very gradual stress increase from room conditions to several MPa, the production of each synthetic sample would require months.

For this reason we chose to apply stress in three steps. When the stress is increased to a target stress much higher than the previous equilibrated state, the pore pressure reaches its maximum immediately and fluid circulation and drainage occur at the fastest rate at this stage before slowing down as pore pressure dissipates. This method drastically diminishes experiment times over the gradual increase method. Each step was designed to last until 90% of the pore pressure has dissipated. The pore pressure state was monitored using the consolidation curve as explained in section 3-4-2-.

- Step 1: Pressure of 1 MPa maintained for 18 hours. This stage serves as an initialization of the experiment. When the sample is first placed into the compaction cell its water content is very high and it is in a liquid state. As our objective is to observe the behaviour of consolidated shale and not fresh deposits, we maintain an initial pressure as low as 1MPa to drain most of the brine out of the sample until the sample is consolidated enough to act as a solid. Notably, by the end of step 1 the S-wave ultrasonic sensors start to detect a

clear S-wave signal, indicative of the transmission of shear waves through the sample.

- Step 2: Pressure of 7 MPa maintained for 7 hours. This is an intermediate stress between the initial 1 MPa and the final stress. This allows us to have 3 data points (one at the end of each step) for density and elastic responses when the sample's pore pressure is dissipated at 90%.

- Step 3: Pressure of 14 MPa for 7 hours. This is the final stage of the experiment. By the end of step 3 the sample conducts shear waves very efficiently and the volume reduction by mechanical compaction is minimal due to the mineral particles being tightly packed together. The final sample is equivalent to a young and normally consolidated cement-free natural shale to a maximum burial depth of ~ 1400 m for a typical lithostatic gradient of 22.6 MPa/km (Lyons and Plisga, 1984) and a hydrostatic gradient of 12.5 MPa/km.

The stress increase rate between the different steps is 0.6MPa/min. This fast pace makes the stress increase almost instantaneous at the scale of the experiment time (≈ 32 hours). At the end of step 3 the sample is unloaded and left under the residual pressure from the position of the piston that stops the mineral matrix from expanding after the stress release. This time varies between a few hours and a day. The sample is then unmoulded from the cell according to the experimental protocol (cf. section 3-3-2-).

3-1-2-4- OM content by volume

To highlight the influence on physical properties of OM characteristics unrelated to TOC or any other measure of the organic content of the samples, a constant volume proportion of OM across the sample set was maintained. As the two types of OM have different density values, this gives a range of TOC across the sample set. The amount of OM that can be put in an artificial sample was limited by the volume of the hydrous pyrolysis vessel (200mL) and the minimum solid volume required to produce a final synthetic sample with a sufficient thickness to record the horizontal ultrasonic response of the sample until the end of the experiment. These technical constraints gave us an upper limit of 8% of OM in volume.

3-1-3- Experimental workflow

First, the volume content of each individual constituent (inorganic mineral, fresh and mature OM) of the samples was measured by weighing a small quantity after drying at 105^0C for 24 hours. Then their dry density was measured using a helium-pycnometer AccuPyc 1340 II from Micromeritics Ltd., with a precision of ± 0.01 g/cm^3. This allowed accurate quantification of solid volumes placed in the compaction cell.

Then the samples were prepared and placed into the compaction cell according to the standard experimental protocol (cf. section 3-3-2-2-), using either the mixing or the sedimentation method. During the compaction, stress, density, porosity, expelled pore fluid mass and ultrasonic response in different directions were monitored.

After each experiment, the weight and volume of the unmoulded sample were measured manually, using a mass balance with a precision of ± 0.01 g and an electronic Vernier caliper with a precision of ±0.05 mm. This is to double-check the density reading of the compaction rig and to measure the volume expansion of the sample after stress release.

Immediately after unmoulding, each sample was CT-scanned with a medical CT-scanner (Definition AS 64 slices from Siemens) before evaporation of the sample pore water could occur at a voxel resolution of ~ 200 µm and a CT attenuation accuracy of ± 15 Hounsfield unit [HU]. The CT images were used to check the homogeneity of the sample (CT attenuation distribution), the presence of air inclusions (> 200 µm) and the orientation of the bigger particles that are larger than the CT image resolution limit (> 200 µm).

After XCT imaging, two 10mm thick slices were taken from each sample for dielectric measurements in two orthogonal directions to evaluate the dielectric anisotropy: (i) horizontal direction (orthogonal to the compaction axis) and (ii) vertical direction (along the compaction direction axis). One thin section was also produced from each sample to analyse the particles texture at a better resolution (2.6 µm) than the CT-scan. Finally, a small amount of each organic sample was sent to be analysed by Rock-Eval pyrolysis to ISTeP (Institut des Sciences de la Terre de Paris, France) to measure the hydrocarbon content and maturity of the samples.

After unmoulding and between each sample handling, the samples were kept in an air-tight container, cling-filmed and refrigerated to avoid desiccation and microbial degradation of the organic samples. Figure 3-7 summarizes the main aspects of this workflow, and the data that is obtained. Moreover the schemes in Figure 3-8 gives a visual representation of the whole process of fabrication of a sample and Figure 3-9 shows how each compacted sample was processed to perform further testing.

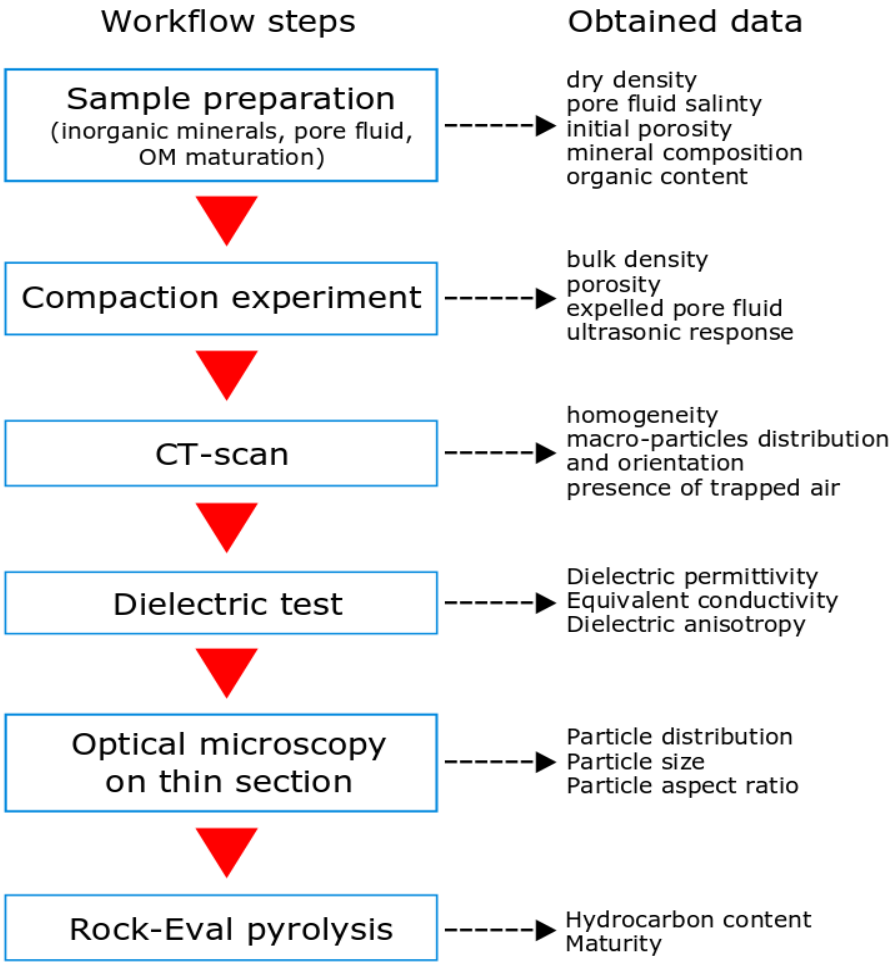

Figure 3-7: Simplified workflow performed on each synthetic sample in a chronological order.

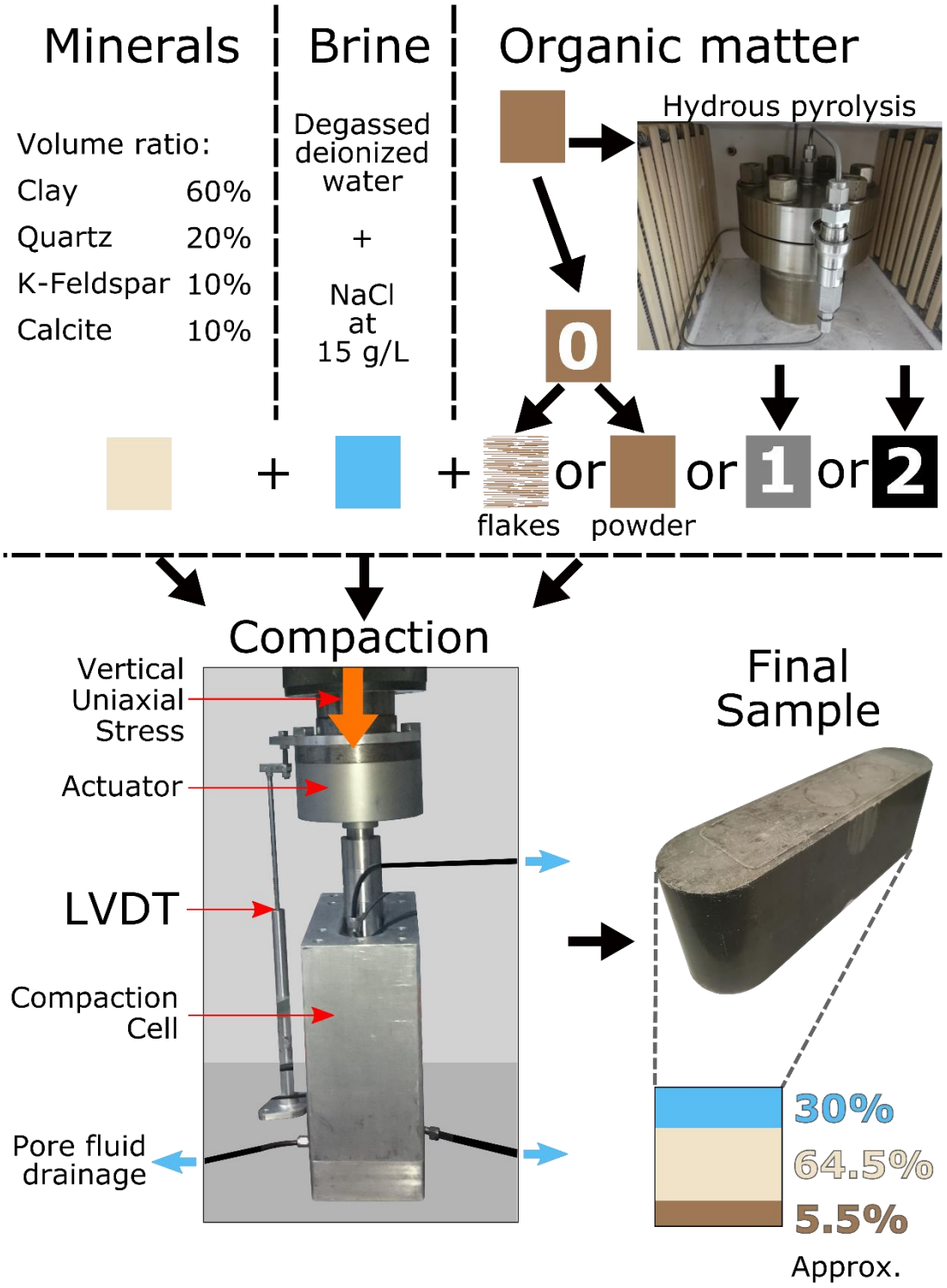

Figure 3-8: Summary of the sample fabrication. Upper left: mixing of the different inorganic components. Upper right: Addition of fresh or matured OM, in flake or powder form. Lower left: Compaction of the samples in the in-house designed compaction cell. Lower right: Final samples, with approximate volume composition of the different phases

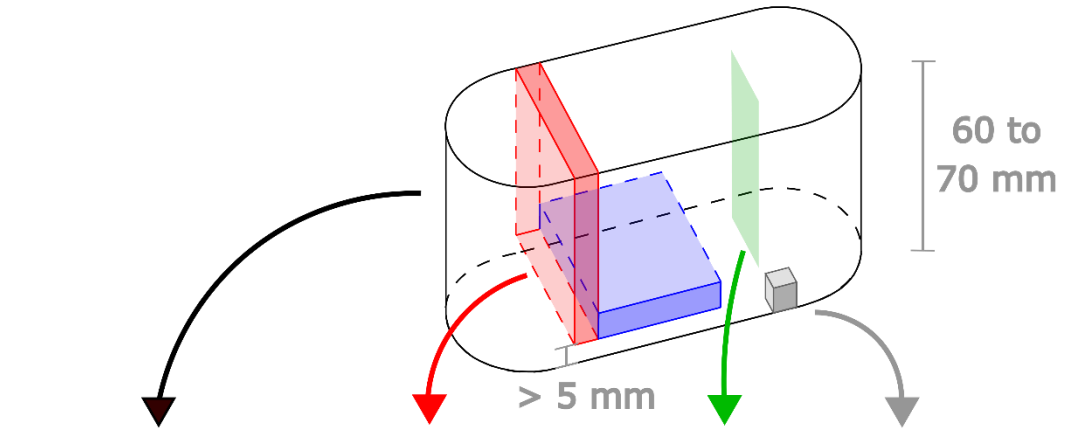

Sub-sample			
Whole sample	10mm thick slices (x2)	Thin section	100mg dried and powdered
Test			
CT-scan	Dielectric	Optical microscopy	Rock-Eval Pyrolysis
Relevant information acquired			
- Bulk density - Homogeneity - Macro-particles analysis (size, orientation and aspect ratio)	- Real and imaginary parts of the relative dielectric permittivity - Equivalent conductivity	- Micro-particles analysis (size, orientation and aspect ratio)	Maturity indicators - Tmax - Oxygen index - Hydrogen index

Figure 3-9: Location of sub-samples for testing after compaction.

3-1-4- Sample list

The sample set was optimized to test all the target variables with a reasonable number of artificial samples. The set was then subdivided in different subgroups of samples that would be used later on to present the results.

In Table 3-1 is a presentation of the name given to each sample and its objective regarding the target variables investigated in the sample set. The flakes and sedimentation experiments were carried out with the readily available fresh OM.

Because of the limited amounts of mature OM we can obtain with the hydrous pyrolysis cell, the mature samples are only made with the mixing method and with initially powdered OM.

Sample name	OM type	OM Particle type	Maturity	Deposition method
Inorganic mixing	Inorganic	N/A	N/A	Mixing
Inorganic sedim	Inorganic	N/A	N/A	Sedimentation
Land 0 powder	Land	Powder	Fresh	Mixing
Land 0 flakes	Land	Flakes	Fresh	Mixing
Land 0 flakes sedim	Land	Flakes	Fresh	Sedimentation
Land 1	Land	Powder	Level 1	Mixing
Land 2	Land	Powder	Level 2	Mixing
Marine 0 powder	Marine	Powder	Fresh	Mixing
Marine 0 flakes	Marine	Flakes	Fresh	Mixing
Marine 1	Marine	Powder	Level 1	Mixing
Marine 2	Marine	Powder	Level 2	Mixing

Table 3-1: Summary of each synthetic shale sample with its role in the investigation of the different targeted variables.

3-2- OM maturation by hydrous pyrolysis

One of the objectives of this thesis is to assess the influence of OM thermal maturity on the physical properties of shales. When assessing the different possibilities to do so, two main constraints were identified. Firstly the quantities of OM needed to be large enough to have a significant impact on the overall physical behaviour of the artificial shale samples. Secondly that OM from different maturities had to come from the same source. Indeed the properties of OM being driven by many different factors, different levels of maturity of an organic material with the same biological origin, chemical precursors and microstructure were needed. For that reason it was decided to design a hydrous pyrolysis apparatus to artificially mature fresh OM.

3-2-1- Objective

To reproduce as closely as possible the processes occurring during the diagenesis of OM of in-situ source rocks, important factors were identified, that influence the structure and the chemical composition of increasingly mature OM and the generated hydrocarbons (HC).

Naturally the most important factor is heat. The kinetics of diagenetic reactions transforming buried OM into kerogen and bitumen and the cracking of kerogen into HC are dependent on temperature. Though temperature influences the speed at which OM is transformed, it doesn't impact the products of the reactions until high temperatures (>374^{0}C). HC can start forming in situ at temperatures as low as 60^{0}C but for practical laboratory application the temperature should be as high as the equipment allows it to shorten the maturation time.

The second most important element is the absence of oxygen. Heating OM in an oxygen rich environment leads to oxidation processes that produce only CO_2 and mineralize the OM. The maturing OM should thus be in an enclosed chamber.

Another ingredient of hydrous pyrolysis, as its name indicates, is water. It was found that maturation of OM in the presence of water gives HC products that are a better match to natural petroleum products. For a given type of OM, the availability of hydrogen from water makes the cracking of kerogen produce more oil and bitumen whereas dry pyrolysis produces light gas and pyrobitumen (Lewan, 1992).

Finally to reproduce the maturation process occurring in shales in particular, the presence of clay minerals is decisive. Clay have a catalytic effect on the cracking of kerogen as the acid sites present in the clay structure promote the thermal cracking of kerogen (Johns, 1979). The catalytic effect of clays is directly related to the amount of surface contact between OM and clay. Small OM particles in contact with clays with a high specific surface area, such as swelling clays, will give the best results (Rahman, et al., 2017). Finally the adsorption of high molecular weight HC and bitumen by clays change the composition of expulsed HC and the composition of residual OM after cracking (Tannenbaum, et al., 1986). To reproduce the maturation processes occurring in shale source rocks it is thus necessary to include swelling clay with a great surface interface with OM.

The impact of pressure on the thermal maturation of OM is minimal and high pressures were found to inhibit kerogen cracking reactions (McTavish, 1978). Therefore the only source of pressure used is the pressure generated from water vapour and gaseous cracking products.

In conclusion the objective of our maturation apparatus is to reproduce a standard confined hydrous pyrolysis vessel with the addition of swelling clays to reproduce the effects of OM maturation in a shale source rock.

3-2-2- Design and operation

A sealing pressure vessel CF-0.2 from Keda Machinery and Instrument Equipment Co., Ltd. was acquired for the main component of the apparatus. The sample chamber has a capacity of 200mL. It is composed of a stainless steel cell body lined with a ceramic container and a lid secured to the body with six concentric bolts (picture in *Figure 3-10*). The sealing between the lid and the body is realised with a static seal. It works by applying pressure between two perfectly fitting steel surfaces. The pressure is applied by tightening the bolts two by two, by pairs of opposite position, to apply a torque symmetrically and ensure a uniform pressure is applied on the static seal.

Initially the fresh organic matter is dried and powdered to obtain small sized particles (<0.1mm) and thoroughly mixed with smectite clay powder to maximize the clay/OM contact surface. Water is then added to the mix. The following volume ratio of the three different constituents were used: 50% water, 45% OM and 5% smectite. There

was no possibility to incorporate more smectite to the mix because of the requirement on the quantity of mature OM that has to be incorporated in artificial samples.

The mix was then placed into the ceramic container and enclosed into the sample chamber. During a maturation operation the vessel is placed into an oven to apply the required heat. The oven is placed under a ventilation hood to evacuate emitted gas. A hydraulic tubing system links the sample chamber to a pressure gauge, a pressure relief valve and a ball valve located outside the oven (cf. schematic representation in Figure 3-11). The pressure gauge is used to record the generated gas pressure and ensure that it remains below the maximum operating pressure. The pressure relief valve is a safety feature that is set to release excess gas if the pressure in the sample chamber exceeded the maximum pressure. After the sample was matured for a pre-set amount of time, the oven was turned off and the pyrolysis vessel was left to cool down to room temperature for 24h. The water vapour pressure dropped as the water vapour went back to a liquid state; the residual pressure was present, due to the gas generated during maturation. The ball valve was then opened to release this residual pressure and the matured OM was then taken out of the cell.

The maximum operating pressure and temperature are 10MPa and 300^0C, respectively. However, after early trials of the pyrolysis vessel, it was understood that because of the pressure generated by the combination of water vapour and HC gas, the temperature limit had to be set to 200^0C to remain under the pressure limit so that HC gas doesn't leak out continuously through the pressure relief valve. This is especially true for gas prone OM such as type III kerogen. Most confined hydrous pyrolysis equipment uses a temperature of at least 300^0C for a typical period of 72h. To compensate for the lower temperature of our apparatus, we chose to mature our fresh OM for 3 weeks and then 6 weeks, to create two levels of maturity (level 1 and 2). The fresh OM is referred to as maturity level 0.

Two different types of fresh OM were used in the course of this project: Land OM, precursor of kerogen type III and marine OM, precursor of type II kerogen (cf. sample preparation section 3-1 for more details). A total of 4 maturation cycles were carried out to obtain two maturity levels per OM type. During a maturation operation the pressure increases in the first 24h and then reaches a plateau until the end of the maturation period. The pressure plateau for the land OM was around 9.5MPa and the

pressure relief valve released gas at more or less regular intervals (every few days). The pressure plateau for the marine OM was around 3.5MPa and stayed below the pressure limit for the whole duration of the maturation period.

Figure 3-10: Picture of the hydrous pyrolysis cell positioned in the oven.

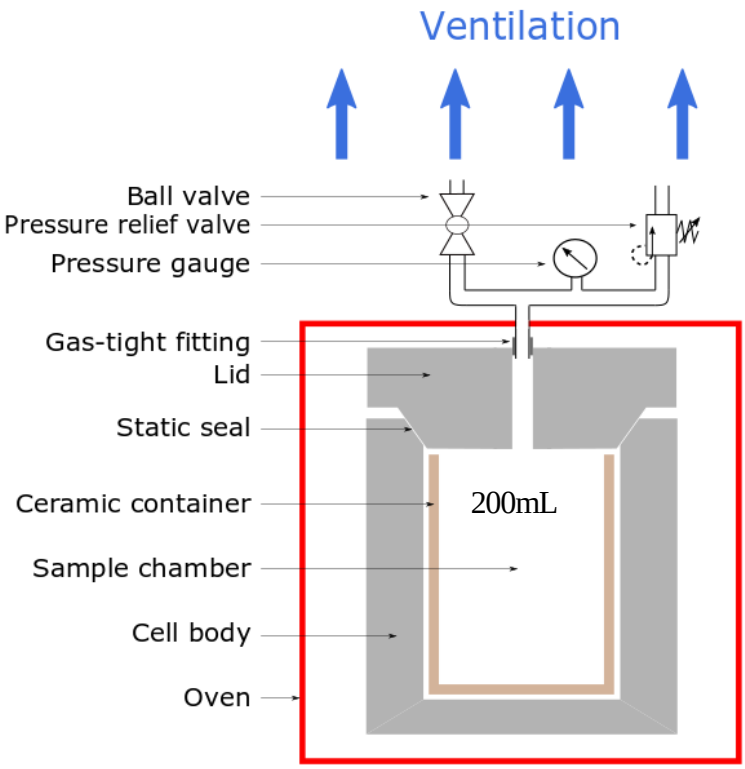

Figure 3-11: Schematic representation of the hydrous pyrolysis apparatus.

3-3- Compaction of the samples

3-3-1- Design

The new compaction cell presented here was designed and manufactured during this PhD project. This equipment was subsequently used to manufacture artificial shale samples with various organic matter characteristics. During compaction the evolution of the elastic properties and anisotropy of the compacting artificial material can be monitored, and the full elastic stiffness tensor evaluated. In this section the design criteria used to develop this compaction cell are described.

3-3-1-1- Previous cell

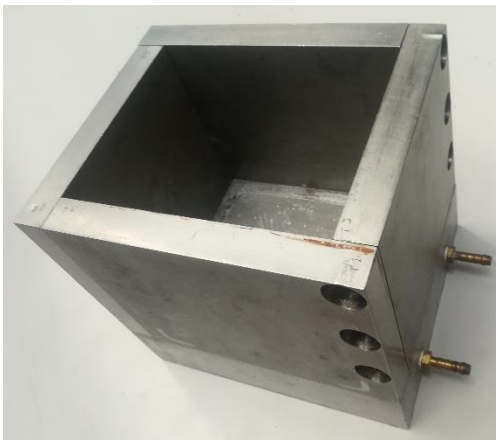

Figure 3-12: Picture of the previous rectangular cell used to determine the requirements for the design of the new cell (the dimensions of the sample chamber are 120mm x 150mm x 120mm). The pore fluid outlets are visible on the bottom right.

A compaction cell designed at CSIRO was initially used to create the early samples of this project. For several reasons explained here this cell was inadequate for the requirements of the project. However its different shortcomings were used as a basis to define the key criteria for designing the new cell. The old cell is pictured in Figure 3-12. Its rectangular design produced cuboid-shaped samples and is good to obtain a uniform compaction. A corresponding rectangular piston was inserted at the top of the cell to apply the vertical uniaxial stress. However this shape did not make a good seal for the fluids expelled during compaction. If the initial water content of the mixture placed in the chamber was too high, water would leak out of the sample into the atmosphere through the wall-piston interface. The initial samples manufactured were limited to an initial water content lower than 55 wt %, which gives the mineral mixture

the consistency of a thick paste. The issue with a low water content is the trapping of air bubbles during the mixing process. Attempts to remove the air bubbles with back pressure were unsuccessful as the paste was too viscous to let the air out and would instead clog the vacuum lines. Another challenge was the design of a drainage system to allow the water expelled by the compacting sample to flow out in a controlled manner, without loss toward the atmosphere. To this end, the bottom of the cell was equipped with a steel plate perforated with 0.1mm holes linked to water outlets on the side of the cell. This plate would be covered with filter paper during a compaction, in principle to prevent the finest minerals (e.g., clays) from clogging the drainage lines. Unfortunately, this simple technique was not effective and the drainage lines were often clogged with fine clays, greatly impeding the rate of compaction.

Furthermore the relatively large dimensions of the sample chamber (length 150mm; width 120mm; height 120mm) required substantial amounts of initial mineral mixtures that result in relatively thin final samples at the bottom of the cell. Indeed, the sample's volume reduces considerably by water expulsion and porosity reduction during compaction, leading to a significant reduction in the original height of the sample. This constitutes a serious limitation if sample plugs or slices of sufficient dimensions are to be cored for subsequent characterisation and testing. Also, because this project involves measuring the elastic properties of the compacting samples, we tested the idea of attaching ultrasonic transducers to the outside of the cell walls to measure a horizontal ultrasonic velocity. Unfortunately, the final height of the sample limits our ability to measure the ultrasonic response until the end of the compaction without experiencing shortcuts of the propagation path through the steel components of the cell (ultrasonic waves travel significantly faster in steel than in the compacting material). As a result, any elastic wave propagating in the vertical direction late in the compaction experiment, i.e. when the sample is the thinnest, travels through the compaction cell walls instead of traversing the sample.

All the above points allowed me to define a list of design criteria for the new cell:

- Water tightness, especially between the moving parts (e.g. piston and walls).
- Possibility to apply back pressure for air removal.

- Fluid drainage system that efficiently drains the water out of the sample, while preventing the fine minerals from migrating with the water out of the sample chamber.
- Ability to record ultrasonic measurements in several directions without shortcuts through the cell body.
- Greater cell height to be able to start compaction experiments with a high water content, while ensuring a sufficient final height of the compacted sample for subsequent plugging and sub-sampling.
- Reduce the cross-sectional area of the cell to minimize the initial amounts of minerals to be mixed, while still ensuring the above criterion is met (sufficient final height of the compacted sample).

3-3-1-2- Dimensions of the new cell: Ultrasonic wave propagation

To minimise the risks of ultrasonic shortcuts within the cell, we used a simple model of propagation paths to compute the P-wave travel times for a cell of varying dimensions (see Figure 3-13). We carried out calibration measurements on the old cell already available to check the validity of the travel path model. We placed a couple of transducers at three different positions on the external walls of the cell (P1, P2 and P3 in Figure 3-13) and recorded the transmitted ultrasonic waveform through the empty cell and through the cell filled with water. We also measured the ultrasonic velocities in the cell's steel walls and in water. Knowing the P-wave velocity in each material (steel and water), we computed the theoretical travel times for the various possible travel paths described in Figure 3-13. The experimental waveforms and the corresponding travel times are compiled in Figure 3-14.

Dimensioning the cell for shortcuts using water to simulate the compacting mixture is a conservative approach because the P-wave velocity in water is low compared to consolidated sediments. A mixture of minerals and water can have a compressional velocity lower than the compressional velocity in water when the porosity is higher than approximately 60% (Gwang, 1996). For the purpose of this project, the objective is to measure the elastic properties when the sample is consolidated and most of the pore pressure resulting from the uniaxial compaction stress has dissipated. Even at the lowest level of compaction, the samples are expected to have a porosity below 50%. At the start of a compaction experiment the mineral-water mixture will exhibit a P-wave velocity similar to that in water, and this velocity may decrease before increasing again as the sample stiffens.

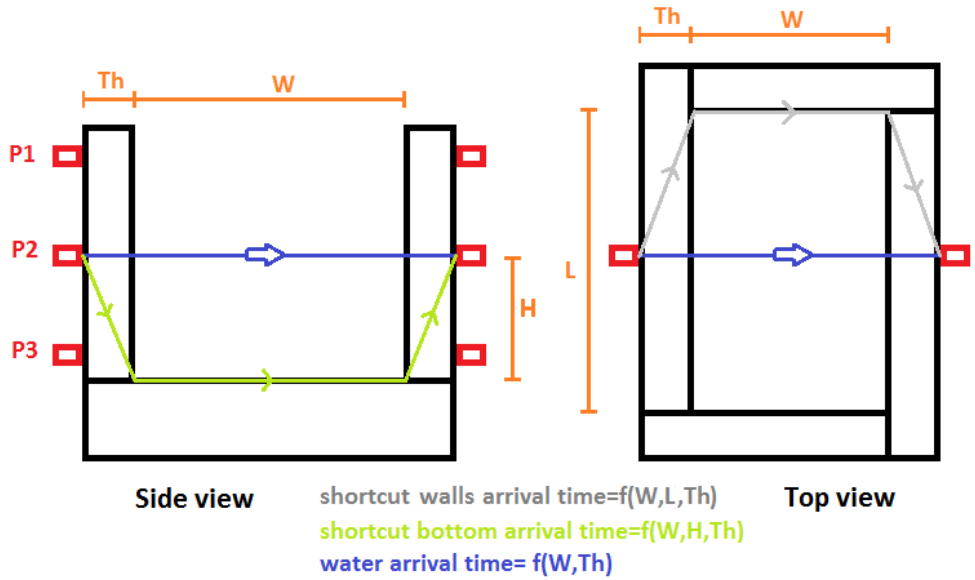

Figure 3-13: Simple model for the P-wave paths used to compute P-wave travel-times in the rectangular cell.

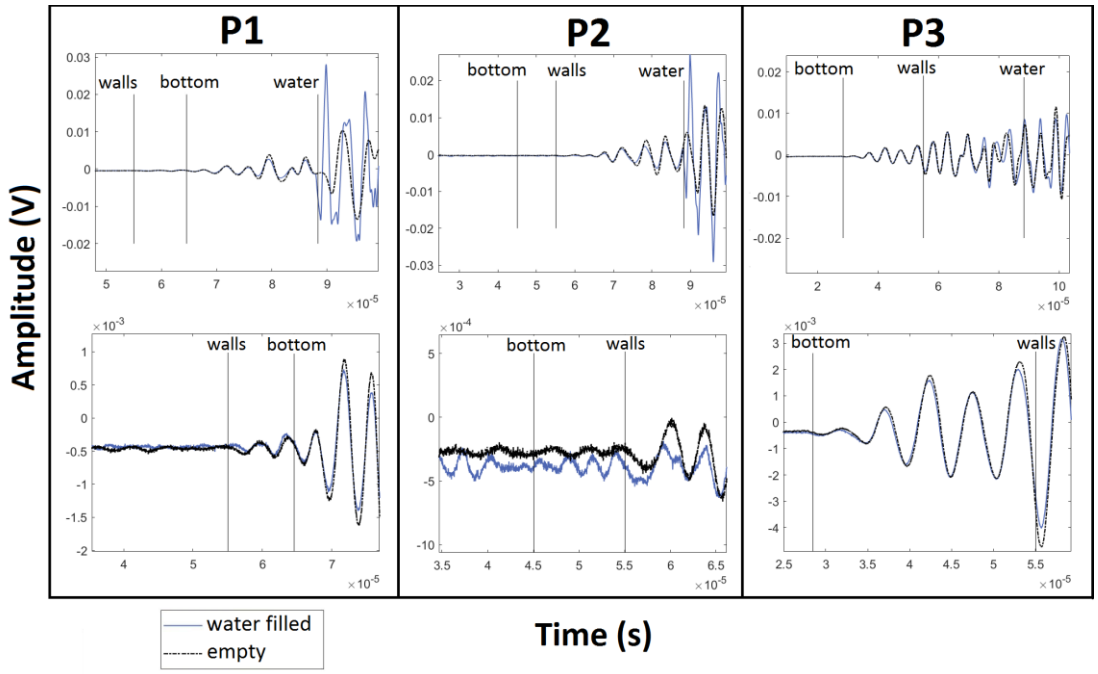

Figure 3-14: Results of the ultrasonic measurements on the empty and water filled rectangular cell with a couple of P-wave transducers positioned at three different heights along the cell's vertical walls. The theoretical travel times are indicated by the vertical lines. The three lower graphs are zoomed-in views of the upper graphs on the shortcut arrivals.

For all three positions we can see in the three top graphs of Figure 3-14 the two shortcut arrival times (named "walls" and "bottom") are smaller than the arrival time of the wave propagating through the water. As expected the signal amplitude obtained in the empty cell and in the water filled cell diverge at the theoretical arrival time of water for positions P1 and P2. However this is not the case for P3 where the signal seems to be dominated by the shortcut components. When looking at the zoomed-in portions of the graphs (three bottom graphs of Figure 3-14) we see that the first break of signal P1 corresponds to the shortcut travel through the steel walls, whereas that of signal P3 corresponds to the shortcut travel through the steel bottom plate of the cell. An intermediate situation is observed for signal P2 for which the propagation through the bottom steel plate is the fastest, yet the first break seems to correspond to the propagation through the walls. In other words, the shortcut propagation through the bottom plate is largely attenuated so as to not interfere in practice with the travel time picking. This higher attenuation through the bottom plate is attributed to the additional interfaces and drainage components imbedded therein (porous plate, bolts etc.).

This analysis of the wave propagation paths within the cell suggest the following conclusions:

- The simple model of ultrasonic wave propagation within the cell is realistic in view of the experimental data recorded;

- The transducers should be attached to the vertical walls of the cell at locations away from the cell's edges (e.g., position P3) to avoid propagation shortcuts in the cell body;

- At a sufficient distance from the bottom plate the shortcuts, only the vertical walls of the cell can induce propagation shortcuts.

Based on the above analysis, the expected travel times for shortcuts through the vertical walls and for propagation through water were computed for a series of distinct combinations of cell dimensions, i.e., length, width and wall thickness. The results are shown in Figure 3-15. In this parametric space, we aim for the region where the arrival time of the wave propagating through the water (blue surface in Figure 3-15) is shorter, and therefore do not interfere with that of the shortcut wave (red surface in Figure 3-15). This criterion leads to the determination of the optimal shape of the cell: an elongated cell with a length significantly larger than the width.

The cell length is practically limited by the maximum size that the workshop could machine (12 inch). On the other hand, a lower bound for the sample width was fixed at 1.5in so as to allow the subsequent coring of standard cylindrical plugs 1.5 inch in diameter. These design criteria are compiled graphically in Figure 3-16, i.e., the region in the space of widths and lengths in which all the above criteria are met is shown in green. It can be seen that the dimensions of the old cell lies outside the optimal green area. Looking at the lines of constant area we see that the cells with the smallest area lie towards the left corner of the green triangle. The decision was made to make a cell of 200mm by 50mm because this elongated shape ensures travel times in the sample are much shorter than the potential shortcuts and it allows the extraction of several standard cylindrical plugs from a single compacted block. Finally, this area is in the low range within the green area requiring less mineral mixture to start with.

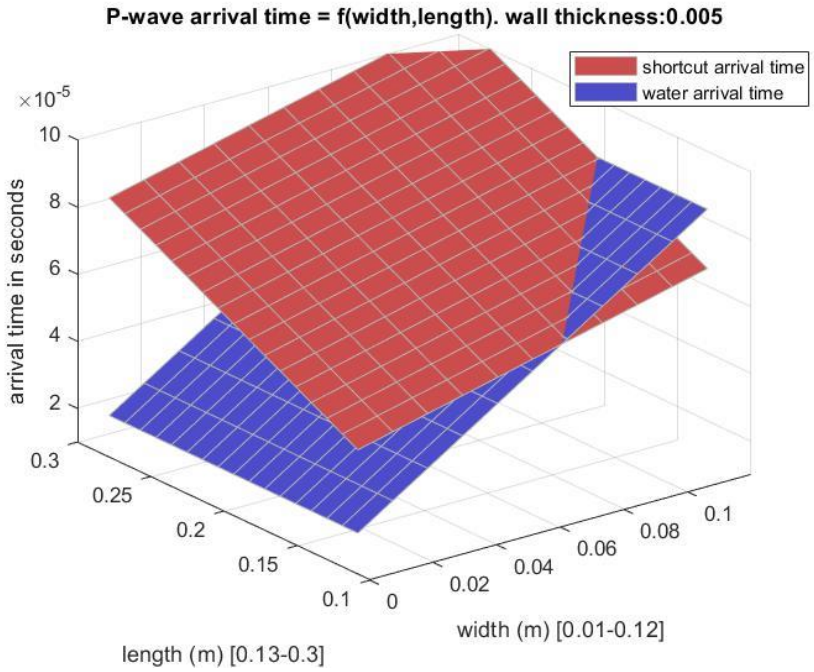

Figure 3-15: Result of shortcut and water arrival time computation for an array of lengths and widths and a wall thickness of 5mm.

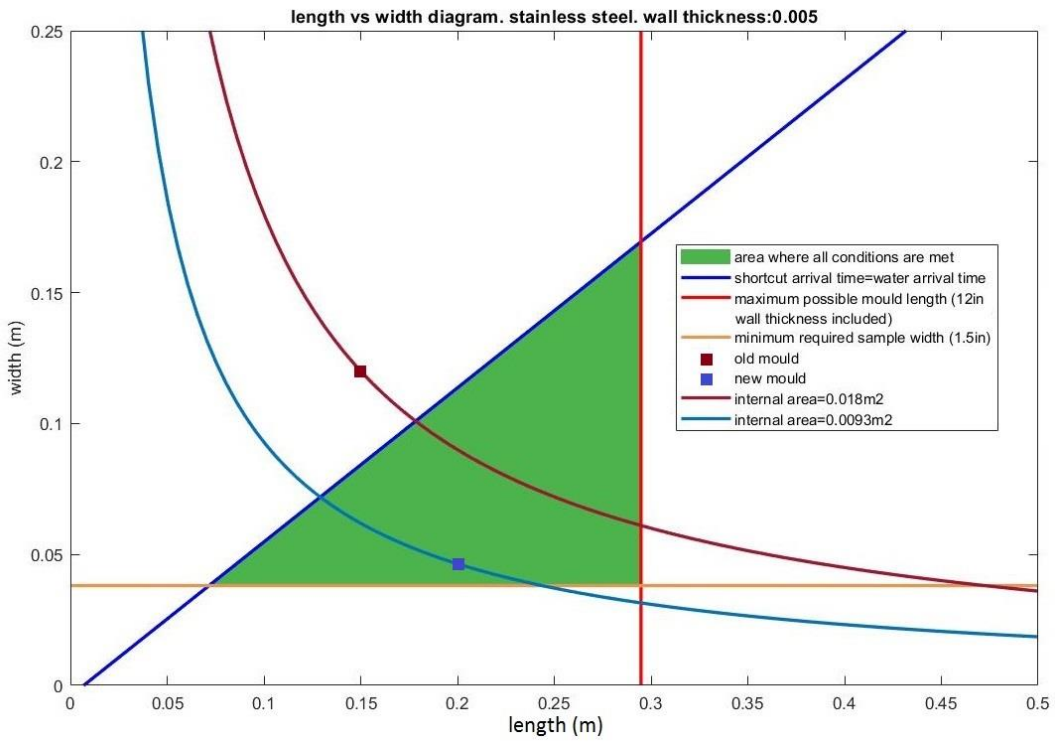

Figure 3-16: Summary plot of the requirement for the new cell's dimensions. The sweet spot where all the conditions are met is coloured in green. Two lines of constant cell area are plotted. One corresponds to the old cell area and one corresponds to the chosen dimension for the new cell.

3-3-1-3- Fluid sealing and drainage capacity of the new cell

The behaviours of the fluids during a compaction experiment have to reproduce the mechanical processes occurring during natural compaction. This involves parameters such as the shape of the sample chamber and classical sealing design at the interface of both static and moving parts.

First the fluids must be collected through the pore lines. No leak must occur between fixed or moving parts. The static interfaces are the easiest to deal with. A simple O-ring with sufficient pressure against the interface makes it watertight. For the bottom plate to walls interface, the pressure is applied by bolts fastened into the walls. For the transducer casings, the pressure generated by the stress inside the sample chamber is used with a step-like shape to secure the transducer casing in place as shown on the zoom view on the left of *Figure 3-17*. For the moving parts i.e. the piston/walls interface the sealing is a bit more complex. To place O-rings on the piston's surface the rectangular shape was changed to an oval, with two half circles at each end of the

elongated shape, as seen in Figure 3-18. A scraper seal was also paced before the O-ring. Its function is to prevent mineral particles from passing through the O-ring and damaging the walls surface where the pressure between the O-ring and the walls is the highest. Finally two Teflon strips are located at the top and bottom of the piston to maintain the piston in an optimal position while it slides in the sample chamber (cf. section 3-3-1-4-).

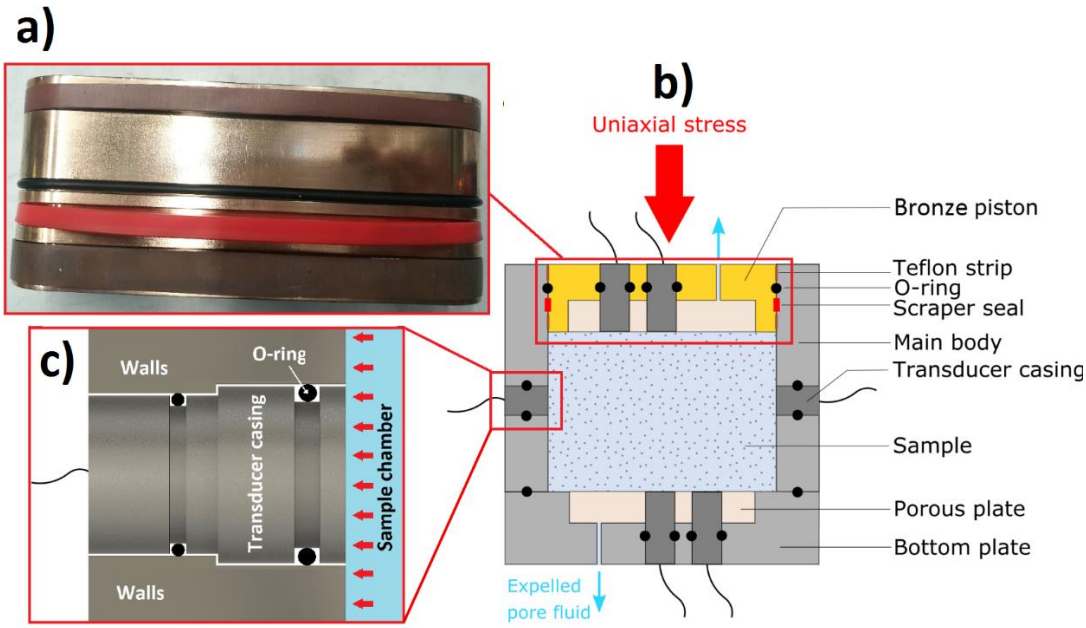

Figure 3-17: a) A picture of the actual piston with its seals. Piston length = 200 mm b) Schematic representation of a vertical cross-section of the cell with the fluid management features: O-rings, scraper seals, Teflon strips, porous plates, pore lines. c) Accurate scheme of the transducer casings placed in the various parts of the cell.

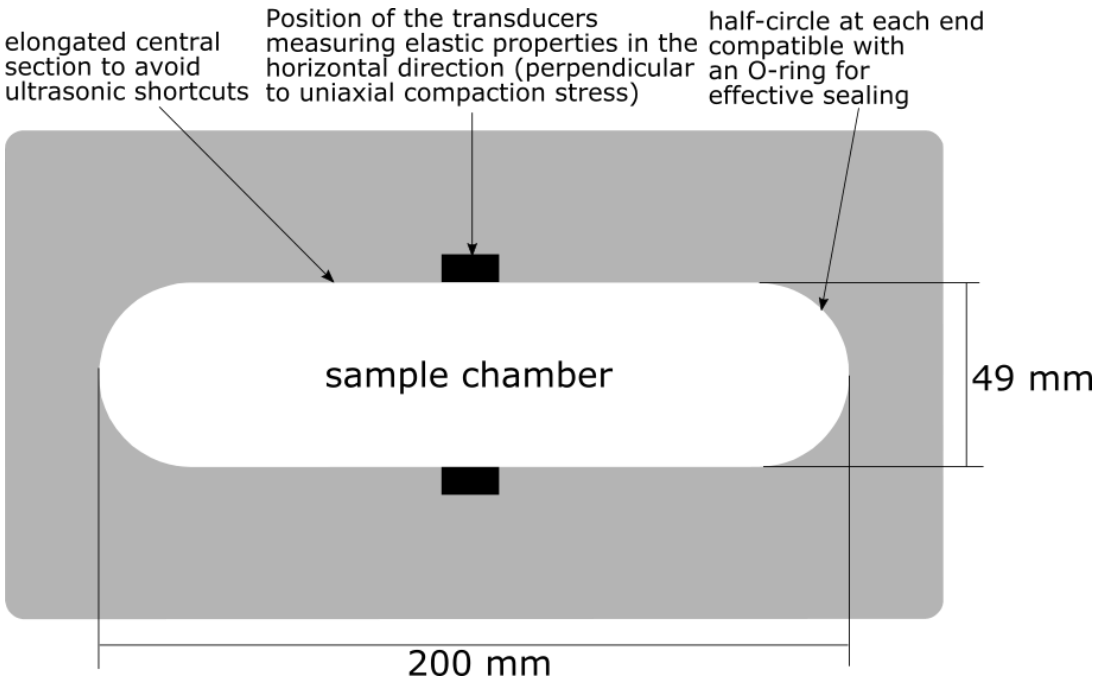

Figure 3-18: Drawing to scale of a top-view cross-section of the new cell showing the chosen oval shape, which avoids ultrasonic shortcuts but is compatible with an O-ring.

Besides the cell must retain the solid phase throughout the experiment. The minerals remain in the sample chamber and the fluids are drained out thanks to the combination of porous plates in the piston and the bottom plate and ultra-tight filter paper (<0.1µm) affixed on the surface of the porous plates. The porous plates are made of alumina with a grade of high compressive strength. This material is both extremely porous (φ=0.2) and very permeable (>1D).

Also to obtain a homogeneous final sample the pore pressure must dissipate as much as possible by the end of the experiment. The presence of porous plates at both ends of the sample covering most of the sample area allow a faster dissipation of the pore pressure. After an increase of the compaction stress the pore pressure immediately rises in the whole sample and then starts to decrease close to the porous plates before the decrease propagates to the centre of the sample. The tighter the mineral matrix gets the longer the dissipation process will take. The loading times should be designed to reach at least 90% of pore pressure dissipation according to the Taylor method (cf. section 3-4-2-).

Finally the initial water content must be high to prevent too many air inclusions from occurring and the final sample height has to be sufficient to obtain a good quality of the recording of ultrasonic signals up until the end of the compaction. To do so the sample chamber was designed to be as high as the machining limitations allowed it to be at 250mm. Hence we can make initial mineral mixtures containing a lot of water (about 80% of the initial volume) filing most of the chamber's volume. This type of mixture has a low viscosity and with the help of a back pressure applied on the pore lines before the start of the compaction we can easily get rid of any trapped air. On the contrary a sample with an initial water content lower than about 55 to 60% will form a thick paste that is very efficient at trapping air in small pockets. The sample then greatly reduces in height during the compaction, losing most of its pore water and with careful selection of the compaction parameters (stress magnitude, loading time and mineral composition) the sample will reach a final height meeting the aforementioned requirements.

3-3-1-4- Stress loading capacity of the new cell

The unusual elongated shape of the cell and associated piston make them more prone to damage, uneven loading stress, and fluid sealing issues than conventional cylindrical pistons. In addition, the presence of brine and hard, sharp mineral particles at the interface enhances the wear due to corrosion.

Upon application of the vertical compaction load, the piston with its elongated shape tends to misalign with the cell walls and can induce undesired additional friction, uneven stress on the compacting fluid/mineral mixture, and possibly mechanical galling of the metal parts in contact, and failure of the seals. In the worst-case scenario, a tilted piston can be locked in place irreversibly within the cell. To overcome these issues several design features were implemented in the new cell.

First, the cell walls are made of materials with contrasting surface hardness to avoid mechanical galling. Two surfaces undergo galling when they slide against each other with a too large normal force and the metal on one surface deforms plastically and adheres locally to the opposite surface. Further motion of the piston within the cell will damage irreversibly the contacting metal surfaces. In the new cell, the piston is made of bronze and the cell walls are made of an aluminium and steel alloy. The

greater hardness of the piston over the cell walls preserves its integrity during compaction.

Furthermore, in order to distribute the vertical stress uniformly on the compacting water/mineral mixture, a specific vertical loading assembly was implemented between the piston and the vertical hydraulic actuator. This assembly comprises a spherical seat and a three-point loading beam (see Figure 3-19). As the two lower contact points are at equal distance from the centre of the spherical seat, the load is distributed evenly between the two ends of the elongated piston.

In addition to the above, and for monitoring possible tilting of the piston during compaction, we installed a pair of inclinometers on the surface of the steel beam (seen in Figure 3-19). One inclinometer measures the longitudinal tilt of the beam-piston assembly, while the other one measures the orthogonal (transverse) tilt. At the start of a compaction experiment the upper surface of the piston and the cell body are carefully aligned before a reference reading of the output of each inclinometer is recorded. As the piston moves downward within the cell, the inclinometers reading is monitored, and if the difference between the current and reference readings exceeds a predefined threshold tilt angle the loading is halted, the experiment is interrupted, and the issue addressed before damage occurs. By design the piston has slightly smaller dimensions than the cell body, a functional gap allowing the piston to slip within the cell without excessive friction. Knowing the exact longitudinal and transverse dimensions of the piston and cell walls, the threshold tilt angle for each inclinometer was calculated as the maximum tilt of the piston when it is in contact with the cell body at two points. Note that a different threshold tilt angle is necessary for each inclinometer.

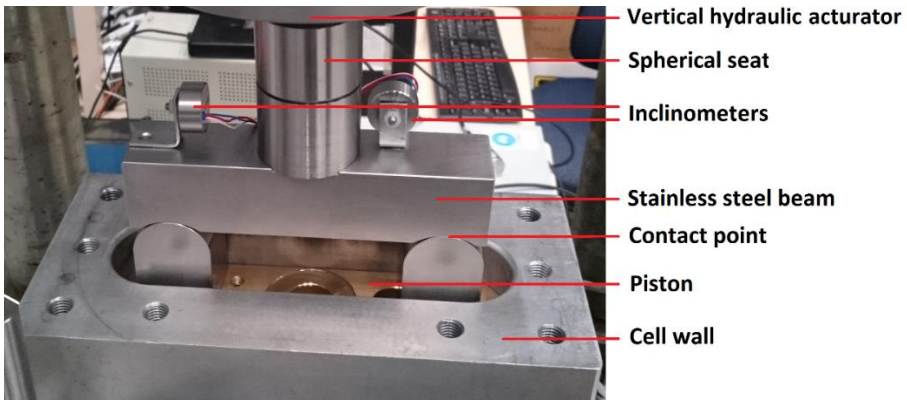

Figure 3-19: Picture of the piston sliding into the body of the cell with the different safety features: inclinometers, beam with two contact points, spherical seat.

Prior to each experiment the piston is lubricated with Teflon based spray (PTFE lubricant) and between every experiment the cell walls and the piston are thoroughly cleaned and polished to prevent any irregularities on the surfaces that would increase the risk of jamming the piston.

Finally, several calibration tests were conducted to assess the amount of friction exerted by the mineral particles at the wall/piston interface. To do so the cell walls were coated with a mix of water and different types of minerals, while the cell remained empty (as per picture in Figure 3-20). The piston was then lubricated as described above and inserted in the coated cell. A constant stress of 0.05 MPa was then applied to the piston to allow it to travel down at a very slow pace. The vertical position of the piston was recorded with an LVDT (Linear Variable Differential Transformer). The results are presented in Figure 3-21. We can see that different displacement rates are achieved for the same applied stress of 0.05 MPa for different mineral mixtures. The mixture containing only kaolinite has the fastest piston displacement as clays effectively act as a lubricant. Other mixtures make the travel of the piston slightly slower but overall follow the same trend. However this is not the case for one of the two quartz powders used during the tests where the travel of the piston was greatly impeded by friction and the displacement eventually stopped after 140 mm of vertical displacement, i.e., 0.05 MPa was no longer sufficient to move the piston downward. This phenomenon is attributed to the nature of the mineral powder used, i.e., bigger sharp grains causing excessive friction. Note that for this specific sand mixture the displacement started at the same rate as for the other mixtures, but as the larger and sharp quartz particles progressively accumulated in the piston/wall interface, they progressively jammed the piston. This shows that minerals with a great hardness such as quartz should be used with caution for compaction experiments and that each mineral should be tested for friction to ensure that it is safe to use during an actual compaction experiment.

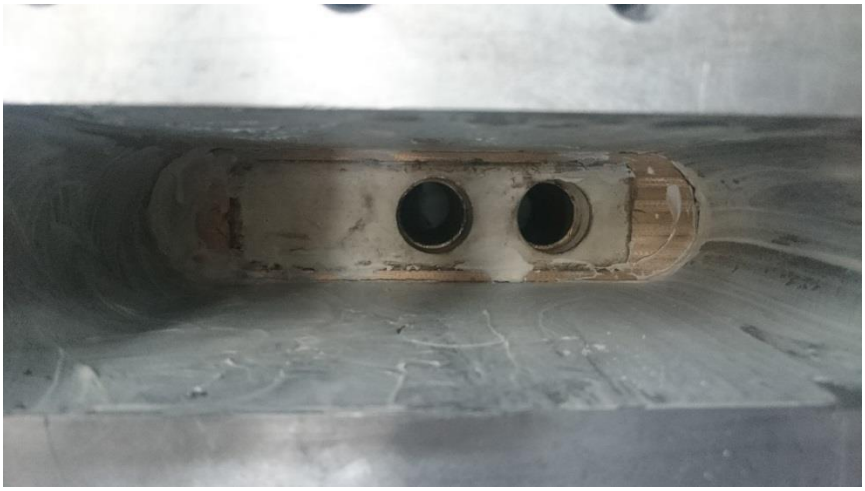

Figure 3-20: Friction tests. The cell chamber (49mm x 200mm) is empty and the walls are coated with a mixture of water and mineral particles.

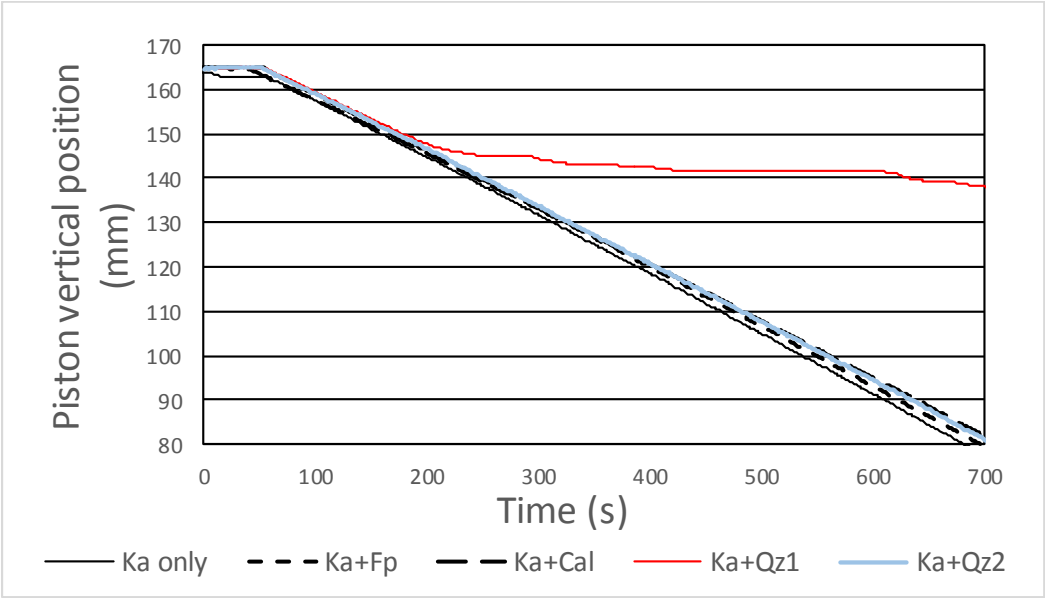

Figure 3-21: Results of the friction tests. With a constant stress, the vertical position of the piston doesn't vary at the same pace for different mineral mixtures because of the friction at the piston/wall interface. Ka: Kaolinite; Fp: K-feldspar; Cal: Calcite; Qz1: Quartz sharp; Qz2: Quartz smooth.

3-3-1-5- Transducer design

After stirring and mixing, it is assumed the mineral mixture is initially homogeneous when poured into the compaction cell. In view of the symmetry of the compaction experiment (geometry and boundary conditions), we postulate that the elastic symmetry of the compacting material within the cell will transit from isotropy to transverse isotropy because the mineral grains will transition from a random

orientation distribution to a horizontally aligned arrangement, with a vertical symmetry axis when the vertical stress is applied during compaction.

Therefore the ultrasonic monitoring system in the cell was designed to allow the estimation of at least five independent ultrasonic wave velocities, which can be used to compute the five independent elastic constants Cij of the stiffness tensor, as well as Thomsen's anisotropy parameters α, β, ε, γ, and δ (Thomsen, 1986).

To measure the horizontal and vertical velocities (V_{pv} P-wave with vertical propagation; V_{ph} P-wave with horizontal propagation; V_{s1} S-wave with vertical propagation and horizontal polarisation; V_{sh} S-wave with horizontal propagation and horizontal polarisation) the transducer holes were simply plugged in the cell body with acrylic plugs and placed commercial S-wave transducers Panametrics V153 at the surface of the acrylic on the outer side of the cell. The travel time in the acrylic plugs was measured before the experiments for both P- and S-waves. The P-wave first breaks were measured from the S-wave signals.

But the acrylic plug method wasn't suitable to measure the off-axis P-wave velocity. Contrary to the vertical and horizontal transducers, the two off-axis transducers do not face each other. The P-waves travel path in the different cell parts and the sample depend on the geometrical configuration that changes continuously during a compaction experiment (reduction of the sample height). In this case, according to Snell's law the ultrasonic P-waves will preferentially travel in the fastest materials (bronze piston and aluminium bottom plate) and limit the travel distance in the slower materials (sample). As a result, in the case of commercial transducers affixed onto acrylic plugs, the fastest travel path will involve a group angle in the sample close to the vertical as can be seen in Figure 3-22. For that reason hollow transducer casings were designed, in which we place a circular P-wave piezoelectric crystal excited by an electric current via a metal part and coaxial cables linked to a pulser-amplifier (Figure 3-23). The metal part is fastened to the transducer casing with a thread and ensures a good coupling between the crystal and the aluminium. With this design we reduce the distance between the P-wave crystal and the surface of the sample to the minimum (Aluminium alloy with a 5mm thickness). Therefore the distance travelled in metal is greatly reduced and the group angle in the sample is much higher.

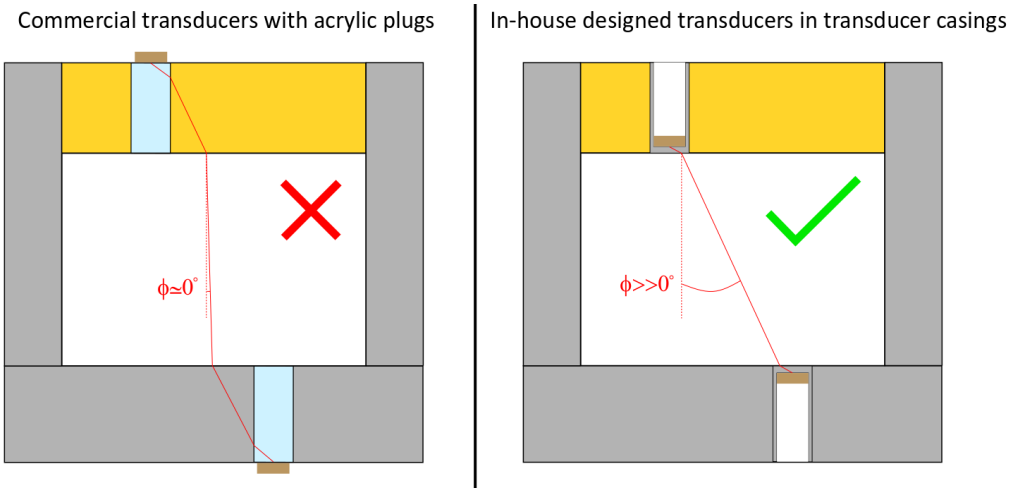

Figure 3-22: Travel path of P-waves in the off-axis direction. In the case of the acrylic plugs, the group angle Φ is almost vertical, in the in-house transducer case, the group angle is much higher because the travel distance in materials with a fast P-wave velocity is reduced.

Figure 3-23: Picture of the transducer casing and the steel part that transmits electrical current from a pulser to the piezoelectric crystal (10mm in diameter).

3-3-2- Experimental setup

3-3-2-1- Compaction rig presentation

The compaction cell described in the previous section was manufactured and integrated into a larger apparatus consisting of a stiff reaction frame, a hydraulic actuator and a pump, and a number of pressure and displacement sensors, ultrasonic transducers, and the two inclinometers. A computer is used to control the application of the load and monitor the output of all transducers. A picture of the whole

experimental setup is shown in Figure 3-24, and a schematic representation of the apparatus is presented in Figure 3-25, where all the components and their functional links are shown. In this section the key features of this equipment are described, which allowed the production of artificial blocks of shale with various mineral compositions and organic matter content, but also to measure the evolution of their elastic properties and anisotropy during the compaction process.

A Linear Variable Differential Transformer (LVDT) is attached to the hydraulic actuator to record its position, and thus to compute the change in volume of the sample during compaction. The cell is then set on the reaction frame table, directly under the actuator, and the actuator is moved down into contact with the cell's piston via the vertical assembly described in the previous section, i.e., a spherical seat and a three-point beam aimed at minimizing the risk of tilt of the piston during compaction. The pore lines are connected to the bottom plate, which hosts the porous plates, and to the piston. They allow the expelled fluid to flow towards the mass balance, which records its mass. Six ultrasonic transducers record quasi-continuously the ultrasonic travel times within the compacting sample. Three of them act as receivers whereas the other three act as sources. The pulser-amplifier provides the voltage pulse signal, and an electronic switch box redirects this signal in turn to the three sources within a 60 second cycle.

The apparatus is controlled and operated with a computer running a dedicated software implemented in a LabVIEW™ environment. The computer also logs the data emanating from the various sensors (LVDT, mass balance, transducers and load cell), computes in real time the parameters of interest from the sensors data (porosity, current volume, uniaxial stress), controls the imposed stress rate, constantly monitors the inclinometers' output to check whether any detrimental tilt of the piston occurs. During a normal compaction experiment the user sets the target (uniaxial) stress value and the rate in terms of stress increase per unit time. Via a feedback loop, the computer then regulates the actuator displacement to achieve the requested rate of increase of the applied axial stress.

The stress can be applied in an uninterrupted way with a small increase rate over the course of several hours or several days to reproduce the natural increase of overburden stress (mechanical compaction only) undergone by natural sediments but in a shorter

time frame. The operator can also set a target porosity value, calculated from the expelled mass of fluid and amount of compaction undergone by the sample. The hydraulic actuator halts once the target value is reached. The stress can also be applied discontinuously (stepwise) allowing the stabilisation of the sample deformation between steps.

Figure 3-24: The compaction apparatus. The cell is located on the reaction frame. The instruments measure different variables continuously throughout the experiment: The stress (load cell), the expelled fluid (scale), Ultrasonic recording (transducers), and sample height (LVDT), piston inclination (inclinometers). All the instruments are connected to the computer where the experiment is operated via a LabVIEW software.

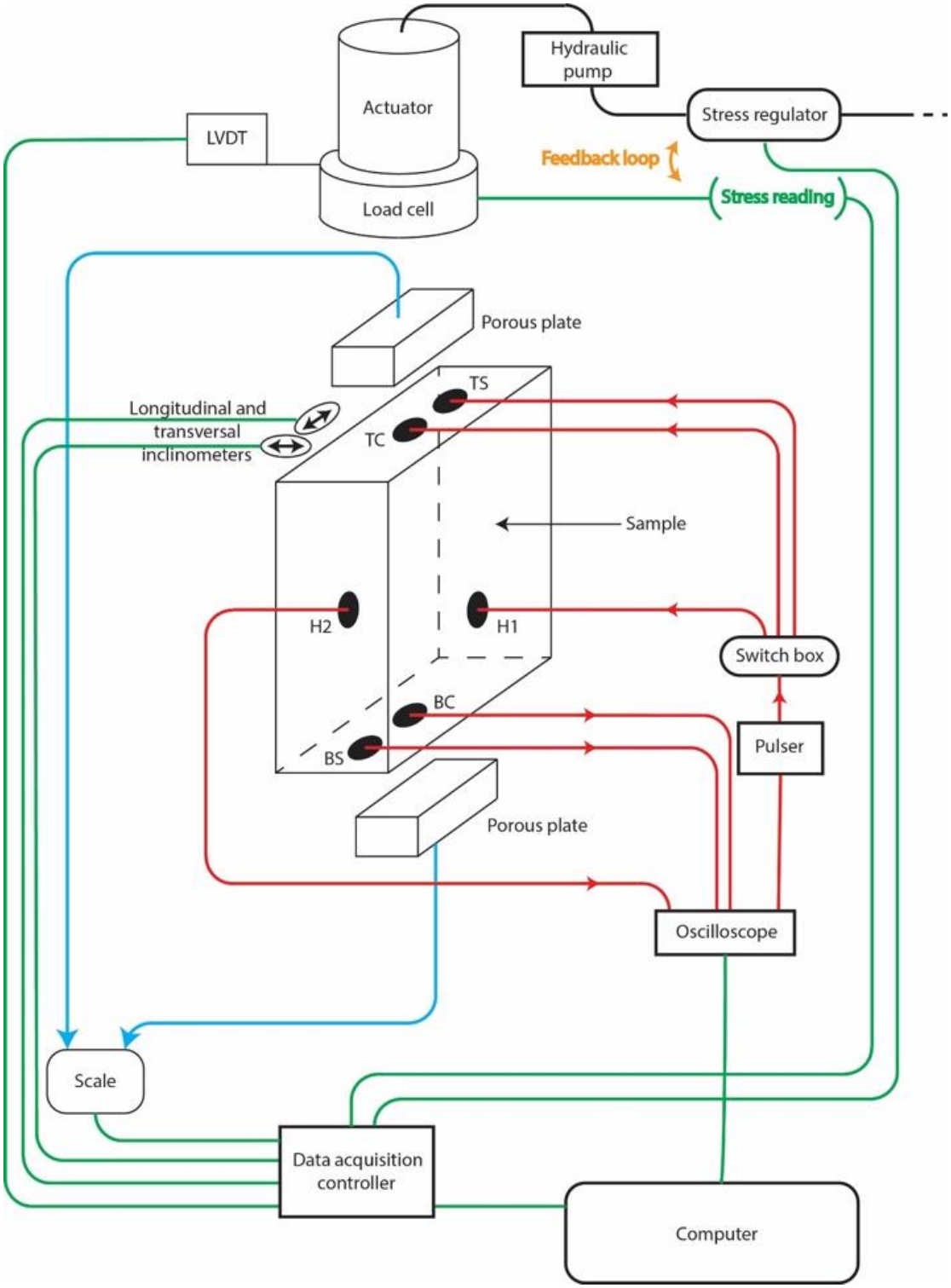

Figure 3-25: Schematic representation of the compaction apparatus. The data links are shown in green, the transducer cables in red and the pore lines in blue. Six transducers are present: TC – top centre, TS – top side, BC – bottom centre, BS – bottom side, H1 and H2 – horizontal transducers. Distances between transducers: H1-H2 49mm; centre-side transducer offset 45mm; top-bottom 160mm to 50mm (decreases during compaction).

3-3-2-2- Experimental protocol

The samples are prepared and deposited into the compaction cell following a mixing method or a sedimentation method that are detailed in section 3-1-1-4-. This section describes the key stages of the testing protocol, with specific emphasis on: (i) compaction initialisation; and (ii) end of the experiment.

- Compaction initialization

Once the initial amount of mixture is set into the cell, the oval piston is installed on top to close the compaction chamber. In its initial position the top surface of the piston is aligned with the upper surface of the main body of the cell, which corresponds to an initial sample height of 165mm. Ideally the initial sample should be a few millimetres higher than 165mm so that when the piston is installed the pore lines get filled with brine and the sample chamber is devoid of free air. The pore lines are then connected to a vacuum pump for at least 2 hours to extract air inclusions that may have been trapped in the sample during the mixing.

While the sample is under vacuum the operator connects all the transducers to the cell, the oscilloscope/switchbox/pulser-amplifier, attaches the LVDT to the actuator, installs the container for the expelled pore fluid on the scale and tares it, connects the inclinometers, turns on the LabVIEW software and feeds it the initial compaction parameters: initial sample height, grain volume, stress increase rate, etc. The operator then turns on the oscilloscope, the switchbox, the pulser-amplifier and records the exact start time of the switchbox cycles to help the automatic processing of the ultrasonic data recorded during the experiment.

The actuator is then put into contact with the piston via the axial load assembly, i.e., spherical seat and three-point beam. The hydraulic pump is then connected to the stress regulator and the operator can start the compaction experiment through the LabVIEW software to control the application of the uniaxial compaction stress.

Unless a multi-step experiment is planned, the rest of the experiment is fully automated requiring no additional input form the operator.

- End of the experiment

When the compaction experiment is finished (target stress or deformation reached), the data recording is halted and the uniaxial load is released by moving the hydraulic

actuator up, freeing the axial load assembly (spherical seat and three-point beam) and the compaction cell. The bottom plate of the cell is then separated from the main body by unscrewing the tightening bolts. The cell is then placed back in the reaction frame and the actuator is brought back into contact with the piston. A very low pressure is then applied so that the compacted sample is pushed out of the cell body through the bottom opening. Once the sample is unmoulded, the pressure is maintained to remove the piston from the chamber through the same opening.

The sample is immediately weighed and its height is measured with a Vernier calliper. It is then wrapped in cling film and stored before subsequent testing. The grooves that are occupied by O-rings in the piston, bottom plate and transducer holders are generally filled with minerals and brine that escaped the sample chamber. This material is collected and weighed. It is then dried and weighed again to determine its water content. This additional information is used to correct the final composition of the compacted sample. Overall, the amount of material lost during sample preparation and after compaction can reach up to 3% of the initial volume and significantly affects the porosity and bulk density calculations.

3-3-2-3- Calibration and error analysis

For an accurate measurement of the physical properties of the samples and to estimate the uncertainty on the measurements, the compaction rig sensors were calibrated against highly accurate standard calibration instruments.

3-3-2-3-1- Load cell calibration

The load cell of the compaction rig was put into contact with a calibration load cell and both load cells were loaded with the actuator across a range of loads from 0 to 370kN. The voltage of the compaction rig load cell was measured and a linear relationship was computed between the voltage and the calibration loading values as illustrated in Figure 3-26. The coefficient of determination is higher than 99.999% and shows the high accuracy of the load cell used in the compaction rig.

The load values were then recalculated from the load cell voltage readings with this linear relationship. The error of these calculated values against the calibration loading values was computed and is shown in Figure 3-27. To understand the meaning of this error in the compaction experiments, it is plotted against the equivalent uniaxial pressure that these loads would generate on the piston of the compaction cell. The

error at low pressures is higher because the reading of the load cell is close to the load cell's sensitivity in this range. Above 1.5MPa, the error remains systematically under 1%. For this reason we chose to define the uncertainty on the load measurement at ±4% under 1.5MPa and at ±1% above 1.5MPa. On the error graph, these error margins are represented by an orange and green line, respectively.

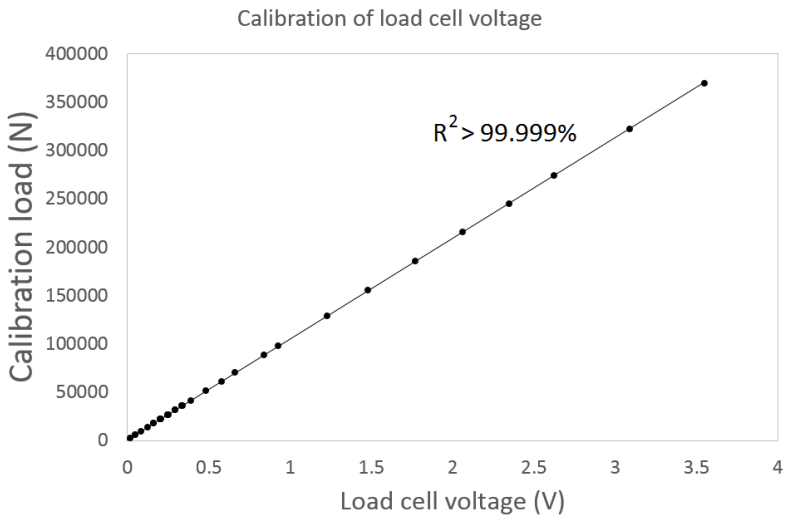

Figure 3-26: Calibration of the voltage of the load cell of the compaction rig against the loads value given by the calibration load cell. The linear relationship has a very high coefficient of determination.

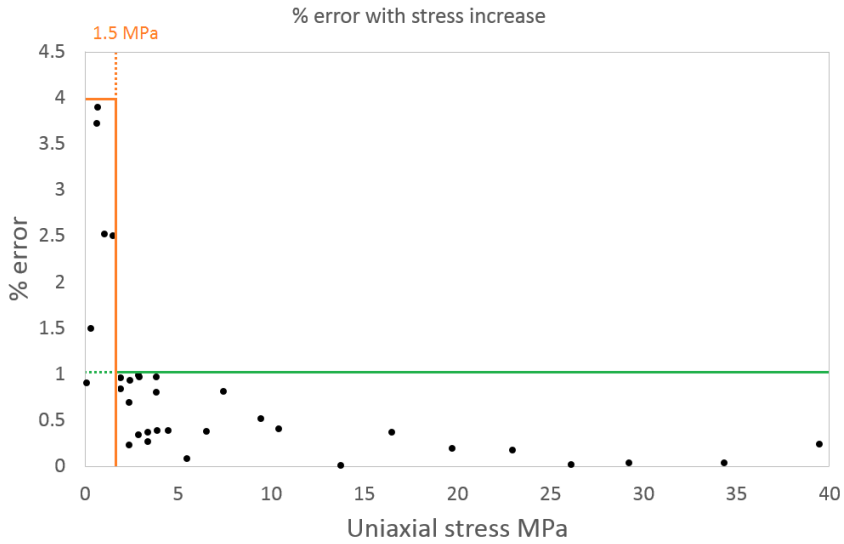

Figure 3-27: % error on the compaction cell loading values plotted against the equivalent uniaxial stress the loads would generate on the piston of the compaction cell. The error is higher at low pressure (<1.5MPa).

The load and uniaxial stress are linked by the relationship $\sigma_u = L/A$ where σ_u is the uniaxial stress in N/m², L is the load in N and A is the piston area in m² which is accurately defined with a negligible uncertainty. The uncertainty on the uniaxial stress $u(\sigma_u)$ is then expressed as:

$$u(\sigma_u) = \sigma_u \sqrt{\left(\frac{u(A)}{A}\right)^2 + \left(\frac{u(L)}{L}\right)^2} \approx \frac{\sigma_u}{L} u(L) \qquad (22)$$

An example of the uncertainty on the uniaxial stress for different stress values used during the compaction experiments is given in Table 3-2. We see that the uncertainty on the stress is similar to the uncertainty on the load (1.5% and 1%).

Uniaxial Stress σ_u	Standard Combined uncertainty
1 MPa	0.04 MPa (4%)
7 MPa	0.07 Mpa (1%)
10 MPa	0.1 MPa (1%)
14 Mpa	0.14 MPa (1%)

Table 3-2: Standard combined uncertainties for different values of uniaxial stress on the compaction cell.

3-3-2-3-2- LVDT calibration

The LVDT used during the compaction experiments was attached to a reference height gauge with a much higher accuracy and a resolution of 0.01mm, when the LVDT has a resolution of only 0.1mm. With a common origin, the two distance measuring devices travelled the whole range of the LVDT (160mm). The values acquired with the LVDT were plotted against the values of the height gauge in Figure 3-28. We can see that the extreme positions around 0 and 160mm don't display a linear behaviour.

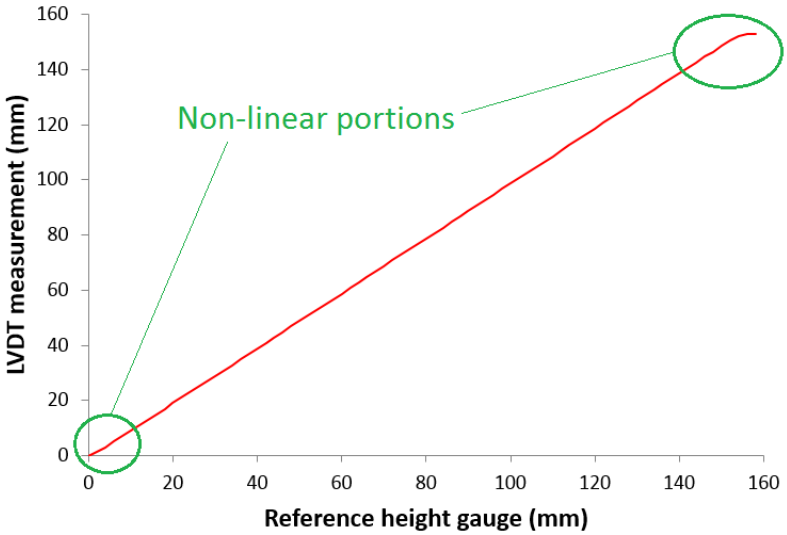

Figure 3-28: Values taken by the LVDT against the ones of the reference gauge on the whole 160mm range of the LVDT.

To better characterize the linear range of the LVDT where its accuracy is maximum we plotted the difference between the displacement measurement from the height gauge and the LVDT (Figure 3-29). This difference increases the most outside the linear range of the LVDT. On the zoomed in portion of the graph we can note that the cumulated difference is almost constant between the positions 30 and 130mm at approximately 1.3mm. The maximum change in sample height during a compaction experiment is about 110mm. Hence the most linear portion of the LVDT range for this application is 25 to 135mm.

If the origin of the displacement measurements is set at the LVDT position 25mm, the error on the measured displacement remains below 0.4% within the range 25 to 135mm for the LVDT. As can be seen in Figure 3-30, the error is even near zero when the difference between the LVDT and height gauge displacement is below the sensitivity of the LVDT. As the maximum measured error is 0.36%, the uncertainty on the displacement measured by the LVDT was set at that value.

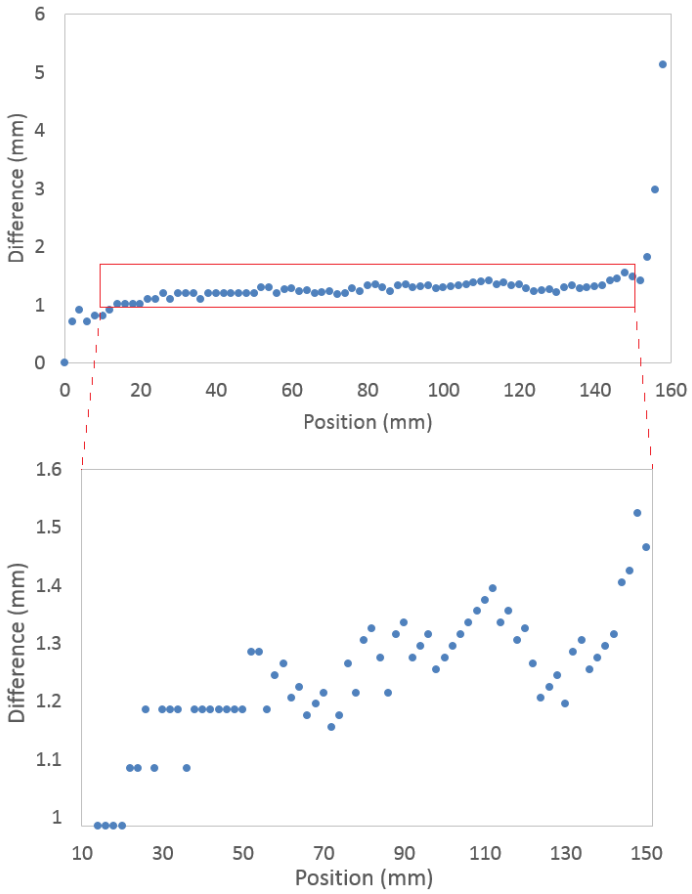

Figure 3-29: Cumulated difference in measured distance from origin between LVDT and reference height gauge.

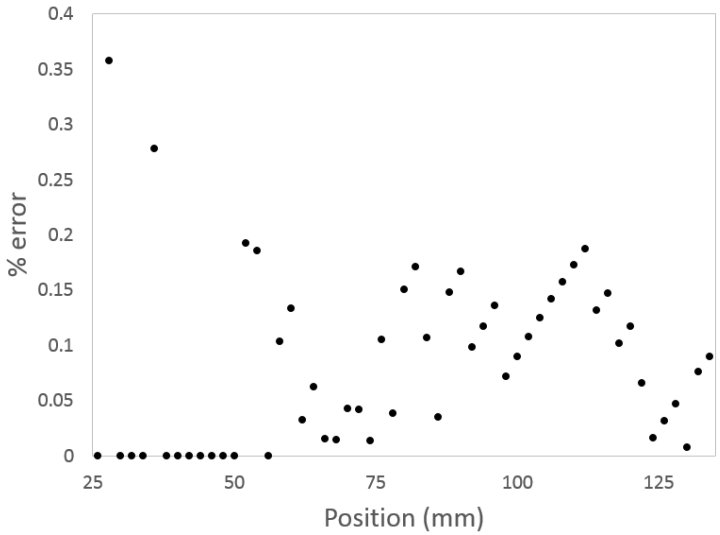

Figure 3-30: Percentage of error of the displacement measurement of the LVDT on the linear range between the positions 25mm and 135mm.

The combined standard uncertainties on the properties computed from the LVDT displacement measurements are estimated using the method reported by Taylor (1982). The sample properties of interest here and their relationship with the LVDT displacement measurement are detailed below:

- The total volume of the sample V_{tot} (cm^3):

$$V_{tot} = AH = A(H_i - \Delta H) \tag{23}$$

where A (cm^2) is the horizontal cross sectional area of the sample, H (cm) is the sample height, H_i (cm) is the initial sample height at t=0 and ΔH is the displacement measured by the LVDT.

- The volume of brine saturating the pore space (left within the sample at any given time during the compaction (variable)

$$V_w = V_{tot} - V_s \tag{24}$$

Where V_s (cm^3) is the volume of solid or grain volume. This expression arises from the assumptions that the loss of volume in the sample is only due to drainage of brine because the mineral grains are negligibly compressible, hence keep a constant volume during compaction. In other words, this assumption means that only structural changes (porosity reduction), and the associated fluid expulsion accommodate the applied compaction stress, not the deformation of each individual grain. Based on the experimental protocol described earlier, we also assume that the amount of air trapped in the sample is negligible, i.e., the pore space is fully saturated with the brine used to manufacture the initial mixture.

- Porosity (at any given time during compaction (variable)

$$\Phi = \frac{V_w}{V_{tot}} \tag{25}$$

- The bulk density ρ_b (g/cm^3)

$$\rho_b = \frac{M_s + M_w}{V_{tot}} \tag{26}$$

where M_s (g) is the mass of solid and M_w (g) is the mass of the brine left in the sample and is equal to:

$$M_w = V_w \rho_w \tag{27}$$

Where ρ_w is the brine density (at room temperature, ~20°C). The combined uncertainties (u) of these parameters were then computed from the individual uncertainties of the different instruments. The uncertainty of the LVDT u(ΔH), defined earlier, was set at 0.36% of the measured distance. The uncertainty of the scale u(M) used to weigh the different components and the pycnometer u(ρ) used to measure the solid densities are 0.05g and 0.01g/cm^3, respectively. These two instruments are accurate (well calibrated) and precise (repeatable measurements). Their uncertainty was thus defined as half their resolution. The uncertainty of the sample's initial height u(H_i) is 5e^{-3} cm and the uncertainty on the sample horizontal area u(A) is linked to the compaction cell machining process and is negligible compared to the other experimental uncertainties.

The standard combined uncertainty on the total volume of the sample u(V_{tot}) at any one time of the experiment is given by

$$u(V_{tot}) = \frac{V_{tot}}{(H_i - \Delta H)^2} \sqrt{u^2(H_i) + u^2(\Delta H)} \tag{28}$$

The standard combined uncertainty on the volume of water in the sample chamber u(V_w) at any one time reads

$$u(V_w) = \sqrt{u^2(V_{tot}) + u^2(V_s)} \tag{29}$$

The solid volume V_s is defined as

$$V_s = \sum_{i=1}^{n} \frac{M_i}{\rho_i} \tag{30}$$

Where n stands for the number of different components of the mixture with a mass M_i and a density ρ_i. Hence the uncertainty u(V_s) is

$$u(V_s) = \sqrt{\sum_{i=1}^{n} \left(\frac{M_i}{\rho_i}\right)^2 \left(\left(\frac{u(M_i)}{M_i}\right)^2 + \left(\frac{u(\rho_i)}{\rho_i}\right)^2\right)} \tag{31}$$

The standard combined uncertainty on the porosity u(φ) is

$$u(\Phi) = \Phi \sqrt{\left(\frac{u(V_w)}{V_w}\right)^2 + \left(\frac{u(V_{tot})}{V_{tot}}\right)^2} \quad (32)$$

The standard combined uncertainty on the bulk density $u(\rho_b)$ is

$$u(\rho_b) = \rho_b \sqrt{\left(\frac{u(V_{tot})}{V_{tot}}\right)^2 + \left(\frac{\sqrt{u^2(M_s) + u^2(M_w)}}{M_s + M_w}\right)^2} \quad (33)$$

The uncertainty on the solid volume $u(M_s)$ is

$$u(M_s) = \sqrt{n} \times u(M) \quad (34)$$

Because u(M) is identical for all n components. The uncertainty on the brine volume $u(V_w)$ is

$$u(M_w) = V_w \rho_w \sqrt{\left(\frac{u(V_w)}{V_w}\right)^2 + \left(\frac{u(\rho_w)}{\rho_w}\right)^2} \quad (35)$$

Table 3-3 shows an example of the values of these uncertainties at the end of a typical compaction experiment, at a maximum uniaxial stress of 14MPa, for an inorganic synthetic sample made with four initial minerals.

Computed parameter	Value at the end of the experiment	Standard combined Uncertainty	Relative uncertainty
Total volume V_{tot}	617 cm^3	0.51 cm^3	0.08 %
Brine volume V_w	181 cm^3	1.17 cm^3	0.64 %
Solid volume V_s	436 cm^3	1.05 cm^3	0.24 %
Porosity φ	29.3 %	0.19 %	0.65 %
Bulk density ρ_b	2.15 g/cm^3	0.004 g/cm^3	0.18 %

Table 3-3: Properties of an inorganic synthetic shales computed with the LVDT reading and other instruments during the sample preparation, along with their standard combined uncertainties and relative uncertainties.

3-3-3- Raw data processing and velocity measurements

3-3-3-1- Data sorting and visual processing

A software programmed in Matlab environment was developed to process the ultrasonic data acquired during the compaction experiments. Ultrasonic waveforms are recorded approximately every 3 seconds on the three receiver transducers. The three source transducers fire in turn for 20 seconds completing a cycle every 60 seconds. As of today the recording oscilloscope and the source firing system aren't synchronized or controlled collectively. Therefore a pre-processing step is necessary to synchronize all data recordings with the appropriate source and select the correct waveform for a given time and source/receiver pair.

Three recordings are selected every firing cycle (one per source). Hence for a given source/receiver pair the maximum time resolution is 1 waveform per minute. For an average experiment (35h) this corresponds to more than 2000 waveforms. To visualize this data we stack the waveforms vertically with the waveforms amplitude visible as a grayscale. The user of the data processing software can choose to limit the number of waveforms to plot with the "skim factor" on the Graphical User Interface (*Figure 3-31*) that will reduce the number of waveforms to display if performance of the computer is limited. An example is given in *Figure 3-32Figure 3-32* where a skim factor of 5 was used which gives an image made of approximately 400 waveforms.

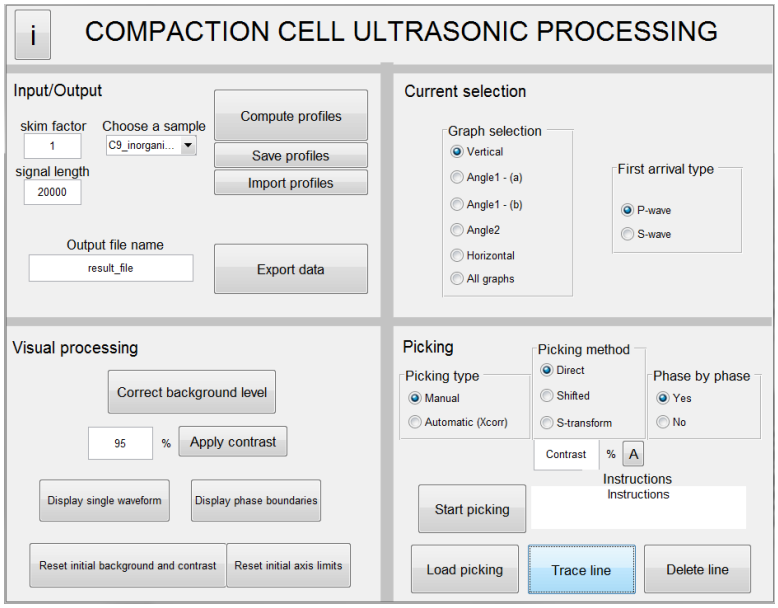

Figure 3-31: User interface menu for the processing of ultrasonic data obtained with the compaction cell.

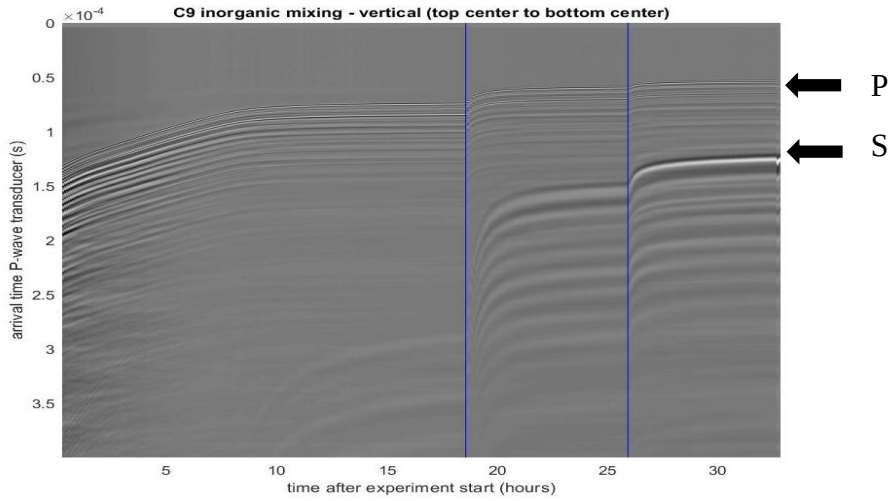

Figure 3-32: Raw ultrasonic profile in the vertical direction of an inorganic sample. Time origin is located on the upper left corner. The arrival of both P and S waves are clearly visible. The phase boundaries (step increase of uniaxial stress) are displayed in blue.

After the data is uploaded and plotted the user can modify the appearance of the images to ease the picking process in the "Visual processing" section. An example of this process is presented in Figure 3-33. Between the top left and top right image the contrast has been enhanced. At high contrast the minimum and maximum of the grayscale (black and white) are reduced to smaller values so the low amplitude variations are more visible while the detail of high amplitude variations is lost. Oftentimes the zero level of the amplitude of ultrasonic waveforms isn't centred exactly on 0V, i.e., DC offset. This results in either a very light or very dark appearance at high contrast and it varies from waveform to waveform. From the top right image to the bottom left image this DC offset is corrected by subtracting from the recorded waveform the average level of the background noise (before the first P-wave arrival) for each waveform. The bottom right image in Figure 3-33 shows a picked first arrival.

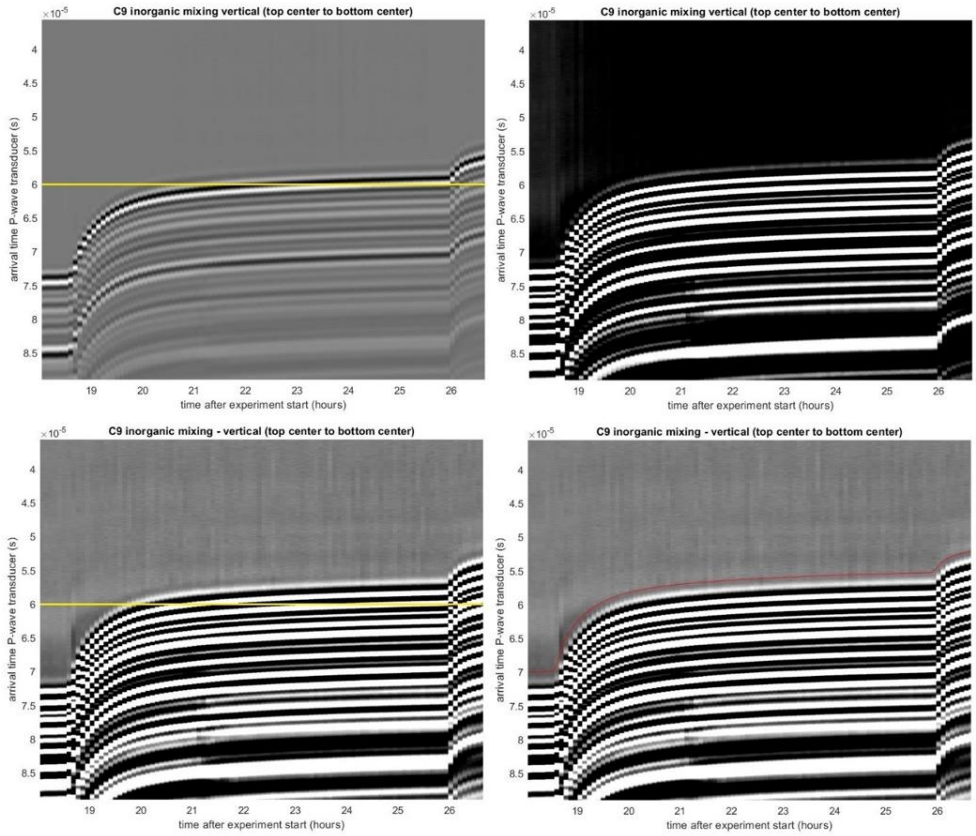

Figure 3-33: Example of visual processing on a zoom of the image in Figure 3-32 onto the P-wave arrival of the second phase section of the image. Upper left: raw image. Upper right: contrast enhanced. Lower left: zero level corrected. Lower right: First arrival picked with a cross-correlation algorithm (red line). The yellow line on the left images indicates 60 µs. We can note, on the unprocessed image, the low amplitude first arrival part of the signal is not visible.

3-3-3-2- First break picking

As can be seen on the menu in *Figure 3-31* the user of the processing software can choose from a number of different picking methods. Most of the time this requires the user to visually identify specific features on the images. The different methods and the procedure for the picking of P- and S-wave first arrivals are presented below.

3-3-3-2-1- Picking type: Automatic or manual

The choice between the two types depends on the data quality and quantity. If the waveforms are too noisy the automatic picking algorithm is less likely to successfully pick the true arrival time. In that case the user can pick manually the arrival times on each waveform and form a line on the waveform stack in Figure 3-32 or Figure 3-33. For waveforms with sufficient signal-to-noise ratio (SNR), an automatic picking

algorithm can be used. This algorithm uses cross-correlation to pick an arrival time on every displayed waveform relative to a reference arrival time determined from a reference waveform with a good SNR. This reference arrival time is determined by a different picking algorithm (see next section), which requires the user to choose a time window where the algorithm is to be applied. The cross-correlation algorithm then takes a small section of the signal around the reference arrival time and finds for the most similar section in the other waveforms within the selected time window. The automatic picking is favoured every time the data allows it because it provides numerous equally spaced data points picked in a systematic and repeatable fashion.

3-3-3-2-2- Picking methods: Direct, Shifting or the S-transform spectrogram

Using either of the aforementioned picking type the user can then choose between:

- Direct method: The manually picked line or the reference point of the cross-correlation algorithm will correspond to the first arrival time.
- Shifting method: The user will have to select another point where the first break is the most visible and the picked line will be shifted to pass through this point. This is typically used where the first break is too faint and mingled into background noise to be picked directly and it is better to pick a later, higher amplitude, more visible peak. For best results the later peak should be as close to the first arrival as is practically possible to minimize the impact of wave dispersion and associated distortion of the waveform coda during the course of the compaction experiment.
- The S-transform spectrogram method: This method is the same as the shifting method above, except that the picking of the reference arrival time in the reference waveform is carried out by analysing the S-transform spectrogram of that waveform. The S-transform is a time-frequency distribution, similar to the Fourier transform, well suited for geophysical data. The S-transform of a given waveform results in a spectrogram (2-D contour plot) displaying the waveform amplitude as a function of time and frequency (see Figure 3-34). At any given time along the x-axis of this graph the spectrogram represents the local frequency spectrum of the waveform at that particular time. At any given frequency along the y-axis of this graph the spectrogram represents the waveform amplitude in the time domain for that particular frequency. For a

waveform with good SNR obtained with a pair of S-transducers (source and receiver) the S-transform spectrogram typically feature two regions of high amplitude, corresponding to the precursory P-phase (left), and to the subsequent S-phase arrival (see Figure 3-34). Later regions of high amplitude are disregarded if present as they are likely related to high energy reflections reaching the receiver transducer. With our typical S-transducers we observe on this figure that the first P-arrival has a higher frequency content that the subsequent S-arrival. This feature is also used by the analyst to discriminate between the P and S phases. Indeed, these two wave modes are not affected the same way by the dispersive/attenuative nature of the sample being compacted, which acts as a high-pass filter for the P-phase, whereas it acts as a low-pass filter for the S-phase. Depending on whether P- or S-wave arrivals are sought, the user has to manually select the earliest time (first break) at which the phase of interest is located in the spectrogram. This time is used as a reference for the shifting method described above.

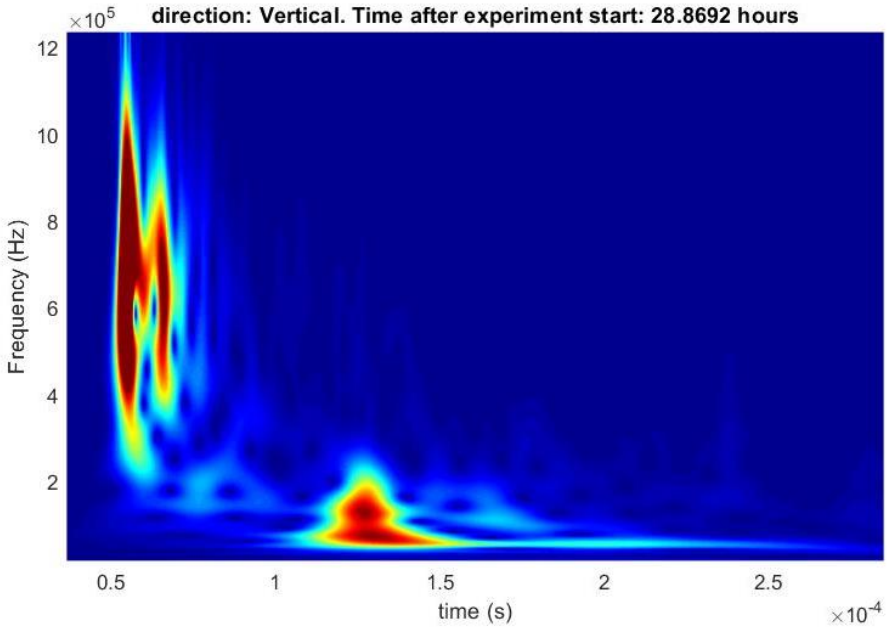

Figure 3-34: S-transform of a waveform taken from the stacked image in Figure 3-32 at t ≈ 29 hours after the start of the compaction experiment.

3-3-3-2-3- P-wave picking

The first break of P-wave signals is typically weak with low first amplitudes on the data obtained with the compaction cell. For the horizontal and vertical directions this

is due to the nature of the transducers, i.e., S-transducers are used not only to determine the travel time of S-waves, but also the travel time of the precursory P-wave. The first P-wave break is therefore not as sharp as it would be with a dedicated P-wave transducer. For the off-axes direction, P-wave transducers are used and their first break amplitude is also weak due to the fact that the source and receiver transducers do not face each other and the ultrasonic wave front thus reaches the receiver "sideways". This results in a P-waveform of increasing amplitude as the first wave front progressively hits the receiver. But the signal becomes strong after a few oscillations. Therefore, for the vast majority of samples tested the off-axes P-wave first arrival was picked using the semi-automatic shifting method for arrival time picking. The faint first arrival (reference arrival time) in the reference waveform was manually picked, then the cross-correlation algorithm was routinely used on the part of the signal with higher amplitudes.

3-3-3-2-4- S-wave picking

Several approaches were tested before a systematic and reliable procedure was devised. The S-wave signal quality is very unequal throughout a compaction experiment, with a signal-to-noise ratio changing from below 1 early in the compaction to over 10 once the sample behaves like a solid. The sample starts off as a liquid that transmits virtually no shear waves and the S-wave signals go from non-existent to very faint over the first 20 hours of compaction. Eventually their amplitude drastically improves when the compaction stress increases.

For that reason it is not possible to pick the S-wave first arrival for a single experiment over the entire pressure range due to the faint amplitude of the S-phase at low pressure. In that case, different methods and points of reference are used. Automatic picking was used when possible but manual picking had to be used on a regular basis, especially for the early stage of each experiment when the S-wave signal is hazy and indistinct (Figure 3-35).

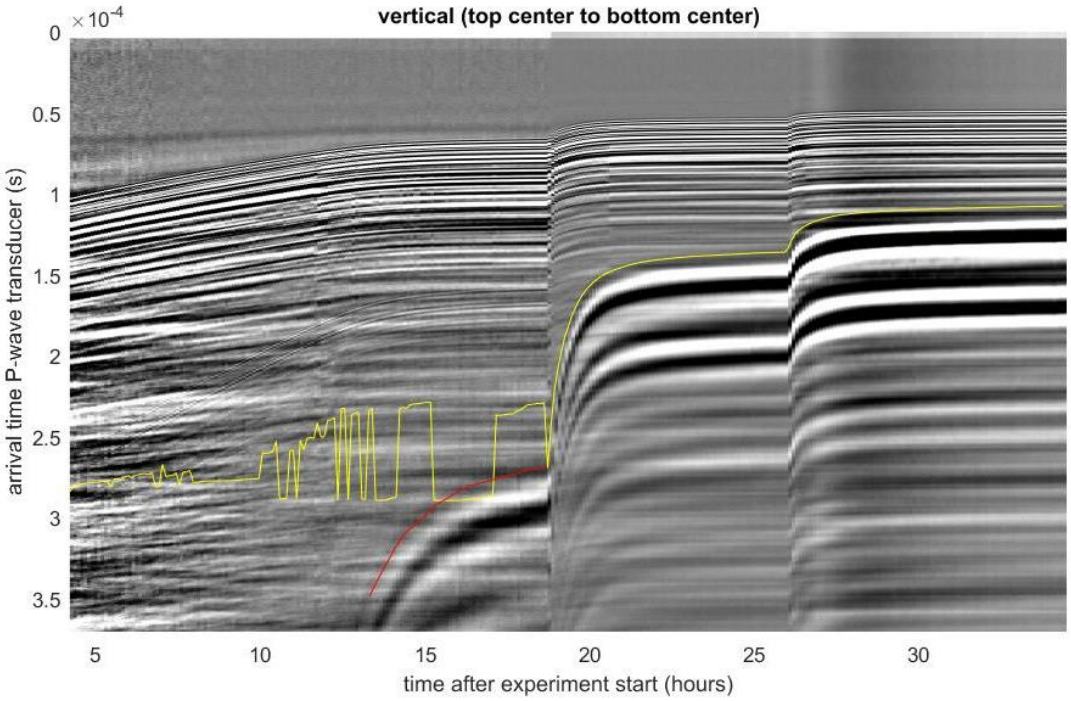

Figure 3-35: S-wave picking. Automatic picking with cross-correlation algorithm (yellow line) where the data is of better quality and manual picking (Red line).

The shifting method turned out to be the most efficient method to pick S-waves because of the behaviour of the Vp/Vs ratio in compacting sediments and its consequences on the visual identification of the S-wave velocity with respect to the P-wave velocity in each waveform.

When sediments undergo compaction, the Vp/Vs ratio decreases (Lee, 2003). This decrease is particularly pronounced in the early stages of compaction. Conversely this effect can be viewed as the S-wave velocity increasing faster than the P-wave velocity throughout the compaction. Graphically we can observe this effect on the stacked image where the S-wave lines don't run parallel to the P-wave lines but with a steeper slope. The more pronounced this effect is, the easier it is to spot the S-wave first arrival. To illustrate this we generated "ideal" P and S signals (Figure 3-36-A). The S signal has a maximum amplitude four times smaller than the P signal to demonstrate the detection works even when the S-wave first break is low. As experimentally observed the S signal also has a lower frequency and starts at a later time than the P signal. We then created stacked images with P and S signals running parallel (Figure 3-36E) and P and S signals plotted at an angle (*Figure 3-36*-F). We can see the first S-wave arrival is much more easily identified on the latter.

On that account the reference points for the picking of S-waves were taken where the S-wave lines are the most inclined in relation to the P-wave lines: Just after the phase boundaries where velocities increase the most. A real example is presented in Figure 3-37.

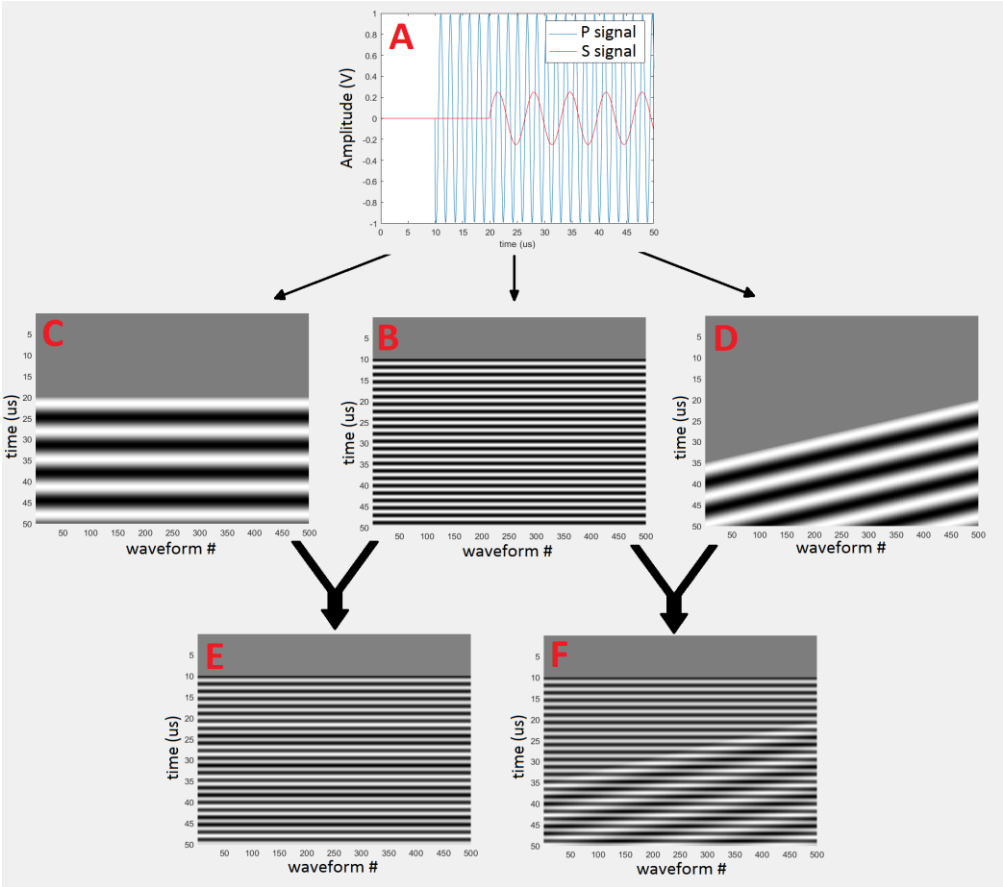

Figure 3-36: How the reduction of the Vp/Vs ratio facilitates S-wave first arrival detection. A) Ideal P and S signals. B) Stacked image of the P signal with 500 waveforms. C) Stacked image of the S signal on 500 waveforms. D) Stacked image of the S signal on 500 waveforms with increasing velocity. E) Sum of B and C. F) Sum of B and D. When P and S lines don't run parallel, the S-wave first arrival is more visible.

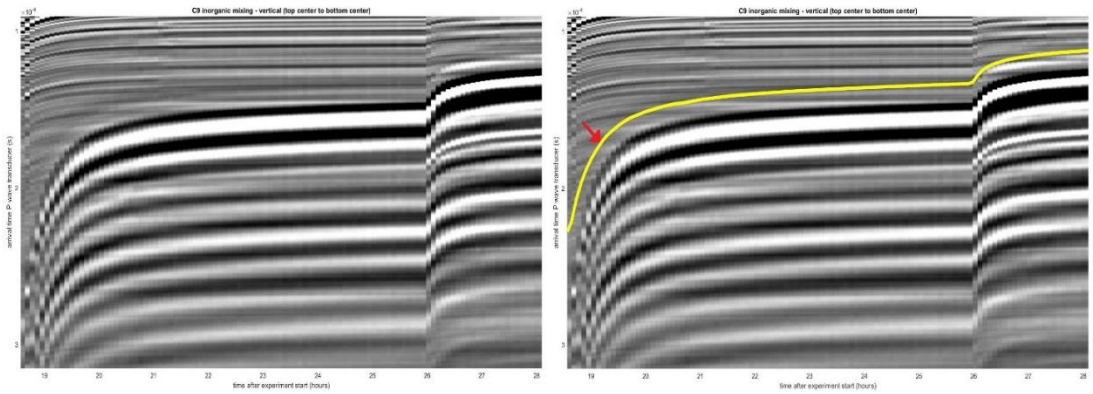

Figure 3-37: Example of S-wave picking with cross-correlation algorithm. The reference point used for the shifting method is indicated by the red arrow. On the left the faint S-wave first arrival is more clearly visible where the S-wave lines have a steeper slope.

3-3-4- Processing of the off-axis measurements

The off-axes velocities measured with the compaction cell are group velocities. The process of computing the off-axis group velocity, group angle, phase velocity, phase angle and ultimately c_{13} is detailed in the next two sections.

3-3-4-1- Off-axis longitudinal group velocity and group angle

The computation of the off-axes P-wave group velocity and group angle is challenging due to the particular design of the new compaction cell. Indeed, the source and receiving P-transducers do not face each other, and their respective position is variable throughout the compaction experiment (reduction in the sample's height). Moreover the dimensions of the transducer casing (27.9mm in diameter) and the embedded piezo-ceramic crystal (10mm in diameter) do not allow us to consider the source and receiver as being punctual because they represent more than 10% of the distance between transducers in most geometrical configurations.

Consequently, the dead-time (time the ultrasonic wave travels through the transducer casing) is variable and the angle to the vertical direction of the incident rays in the sample depends on several parameters such as the velocities and thicknesses of the materials the waves propagates through and the relative position of the source and receiver. Therefore to compute a velocity from the picked travel time data we must choose a model to determine the travel distances in the transducer casings and the sample as well as the angle of the incident rays from source to receiver.

To this end, we carry out a preliminary calibration experiment by simulating a pseudo-compaction with the most obvious isotropic material with a known P-wave velocity: water. We equipped the cell with 6 identical in-house designed P-wave transducers and recorded vertical, horizontal and off-axes ultrasonic P-wave velocities at various sample heights within the cell and tested different wave propagation models until we found one that satisfactorily fits the water calibration data. The different source-receiver configurations tested in that regard are illustrated schematically in Figure 3-38. The paths "Angle 1a" and "Angle 1b" were only used for calibration purposes. In the actual experiments only the path "Angle 2" was used for the determination of the off-axes P-wave velocity. The transducers located at the centres of the piston and bottom plate (vertical ray path) were S-wave transducers used to determine both the S-wave travel time and the travel time of the precursory P-wave.

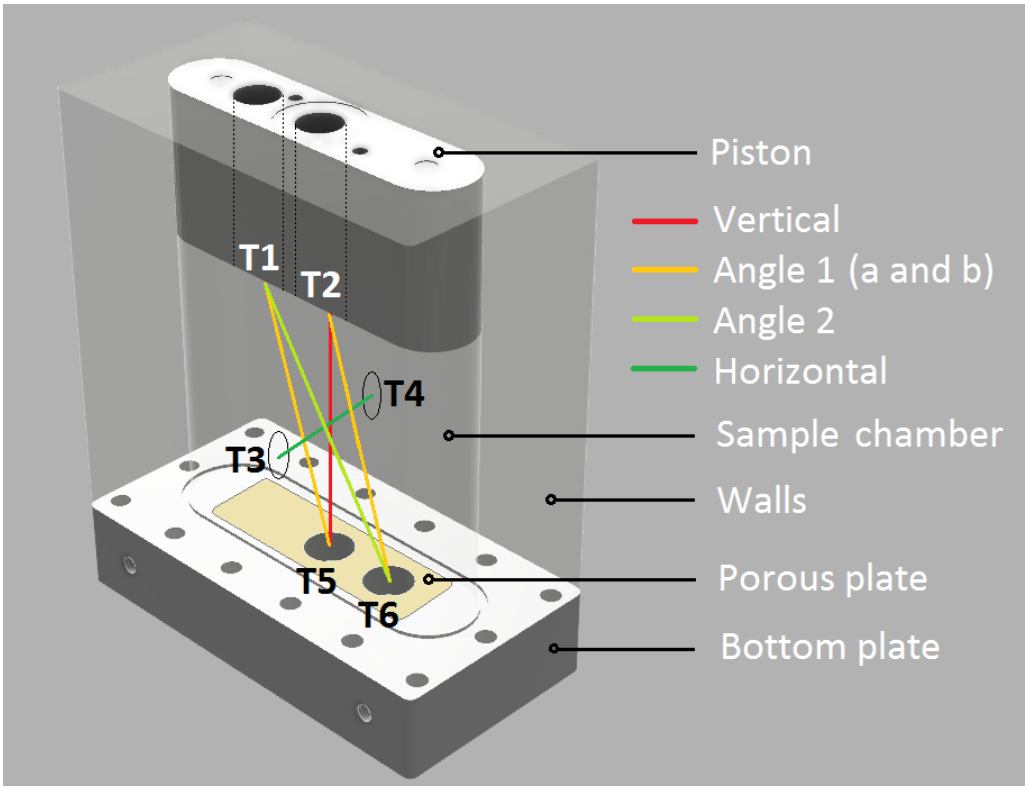

Figure 3-38: Representation of the different parts of the compaction cell along with the different source-receiver paths. The horizontal distance remains constant whereas all other travel paths change during a compaction experiment. The transducers location are numerated from T1 to T6. The bottom porous plate is the only one visible here but the piston is also equipped with a porous plate.

Prior to the calibration experiment the P-wave velocity in the transducer casing, in the porous plate and in the water were independently measured on the bench. The travel paths were computed using Snell's law, i.e.

$$\frac{sin\Phi_1}{sin\Phi_2} = \frac{V_1}{V_2} \tag{36}$$

Where a P-wave ray passes through the interface from a medium of velocity V_1 to another medium of velocity V_2 with an incident angle φ_1 and a refraction angle φ_2.

3-3-4-1-1- Simple three-layer model

For sake of simplicity we modelled the propagation of ultrasonic waves within the compaction cell as a stack of three layers: aluminium – sample – aluminium (see Figure 3-39). I computed the theoretical arrival time from the source's centre to the receiver's centre with an iterative algorithm and the known parameters: P-wave velocity in water and in aluminium, thickness of the aluminium and water layers, and the horizontal offset between the transducers. The algorithm uses Snell's law and computes multiple ray paths at different emission angles from the source to find the angle of the ray that will reach the receiver centre with a precision much greater than the experimental measurement error. The results are presented in Figure 3-40.

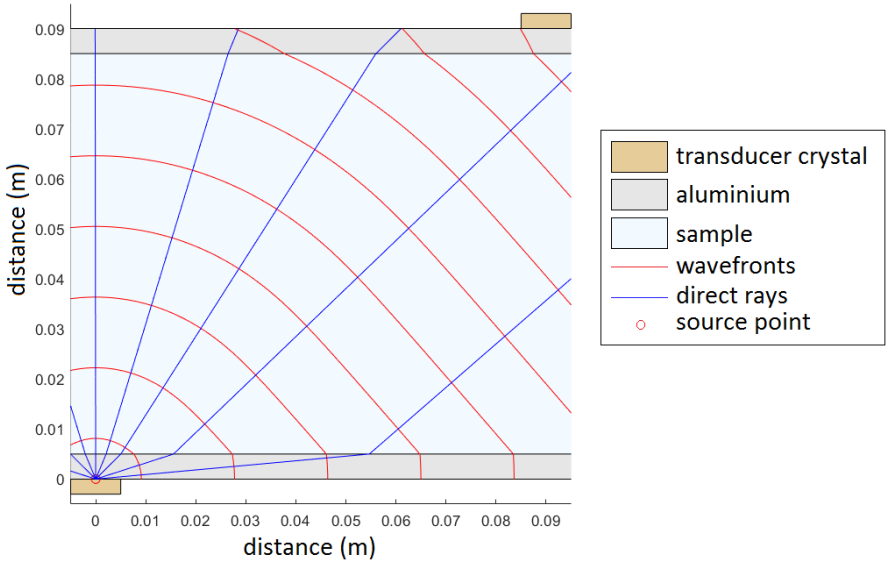

Figure 3-39: Scheme of the three layer model. The height of the sample (in blue) is variable throughout the experiment.

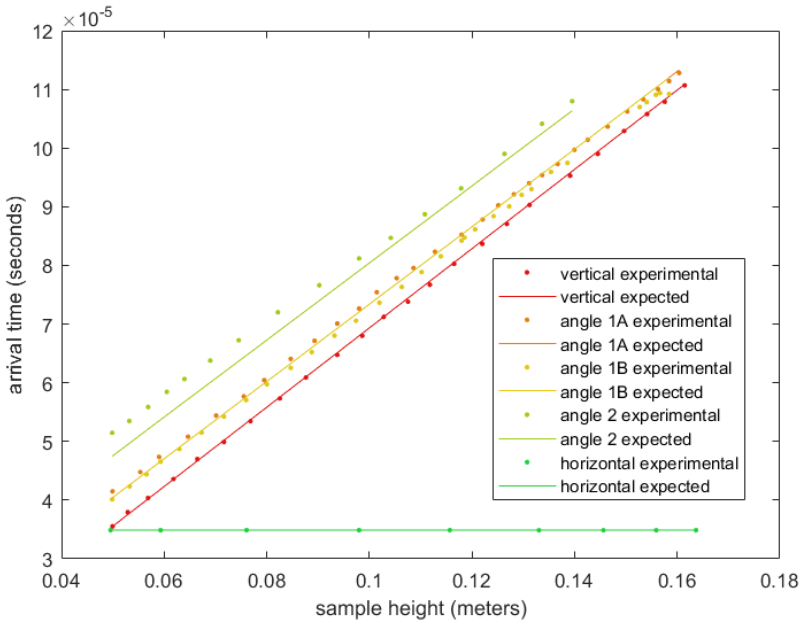

Figure 3-40: Arrival times computed with the three layer model (lines) and experimental calibration data obtained with water (dots) for each source-receiver configuration plotted against the sample height.

The horizontal travel time is constant since the horizontal propagation distance remains constant during compaction, and the P-wave velocity in water is also constant. The error between experimental data and theoretical predictions is reported in Figure 3-41. Naturally the model fits well the vertical and horizontal data for which there is no horizontal offset between the transducers. The horizontal data is of best quality with quasi-zero error, whereas the vertical data show that we can expect an experimental error lower than 1%. The experimental error for the propagation angles 1a and 1b is slightly higher than the vertical error but remains reasonably lower than 3%. However, for angle 2 the experimental error can reach 9% when the thickness of the water sample is the smallest. This suggest that the simple propagation model used is particularly inaccurate when the travel distance in the aluminium layer increases. This observation guided the design of an improved propagation model to better correct the experimental error.

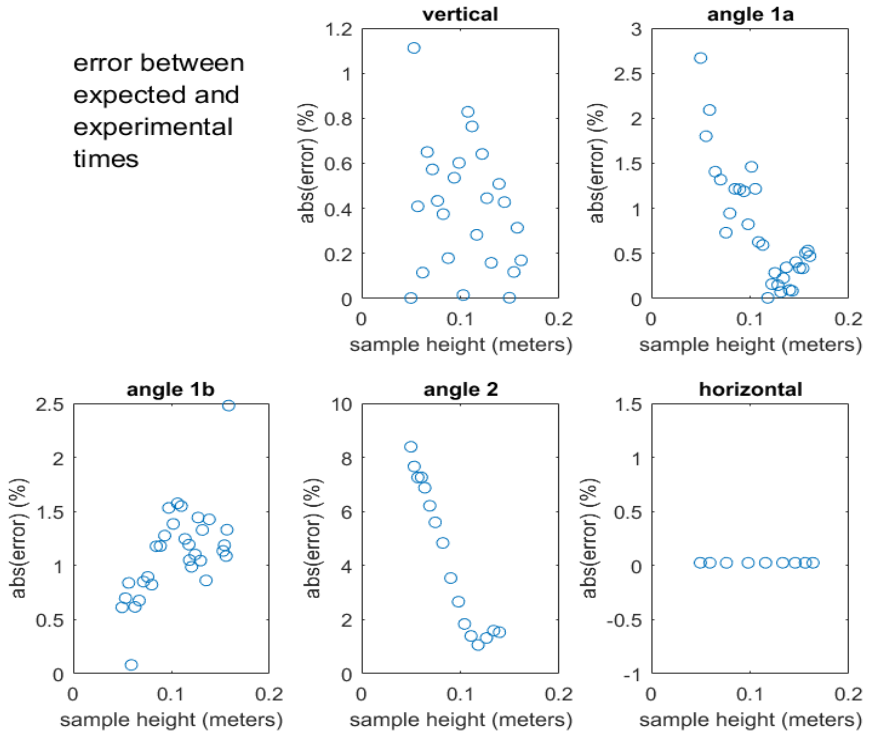

Figure 3-41: Absolute value of the error between theoretical and experimental travel times for the three layers model. The sample height corresponds to the water thickness for this calibration data.

3-3-4-1-2- Advanced segmented dead-time layer model

We divided the bottom and top layers in two different segments made of aluminium for the transducer casing and of alumina to represent the porous plates. This model is more complex and features two material interfaces where diffraction and reflection occur (see Figure 3-42). We divided the source and receiver crystals in 100 points each and computed the travel time for each point source/point receiver couples for all thicknesses of the water sample. Depending on the source and receiver locations (stage of the compaction) as well as the horizontal offset and the thickness of the water sample, the fastest path can take a variety of forms. By determining the location of key ray paths (diffraction ray paths and ray path at critical angles – illustrated in Figure 3-43) we can deduce the subset of paths common to the source and the receiver, and narrow down the problem. Finding the optimal (fastest) ray path in this subset is solved iteratively to yield the propagation angle in the water layer and the distances travelled in the different layers.

The solution is a ray that passes through the bottom and top plates as well as in the water. The source/receiver ray path in the top and bottom plates depends on the

geometrical configuration (sample height) and can involve two to four different components of the propagation model (bottom aluminium casing, bottom porous plate, top aluminium casing and top porous plate). The travel time in the materials other than water is called dead time and is equal to:

$$t_{dead\,time} = \sum_{i=1}^{n} \frac{H_i}{V_i cos\Phi_i} \tag{37}$$

where n is the number of material layers, H_i the height travelled in the i^{th} material, V_i the P-wave velocity in the material and φ_i the ray angle in the material. The overall arrival time is then computed as follow:

$$t = \frac{H_i - \Delta H}{V_{group} cos\Phi} - t_{dead\,time} \tag{38}$$

where H_i is the sample's initial height, ΔH is the displacement measured by the LVDT during compaction, V_g is the group velocity and φ is the ray angle within the sample. This theoretical arrival time t is computed by an iterative ray path finding algorithm that I developed from scratch for the purpose of this project, based on Snell's law.

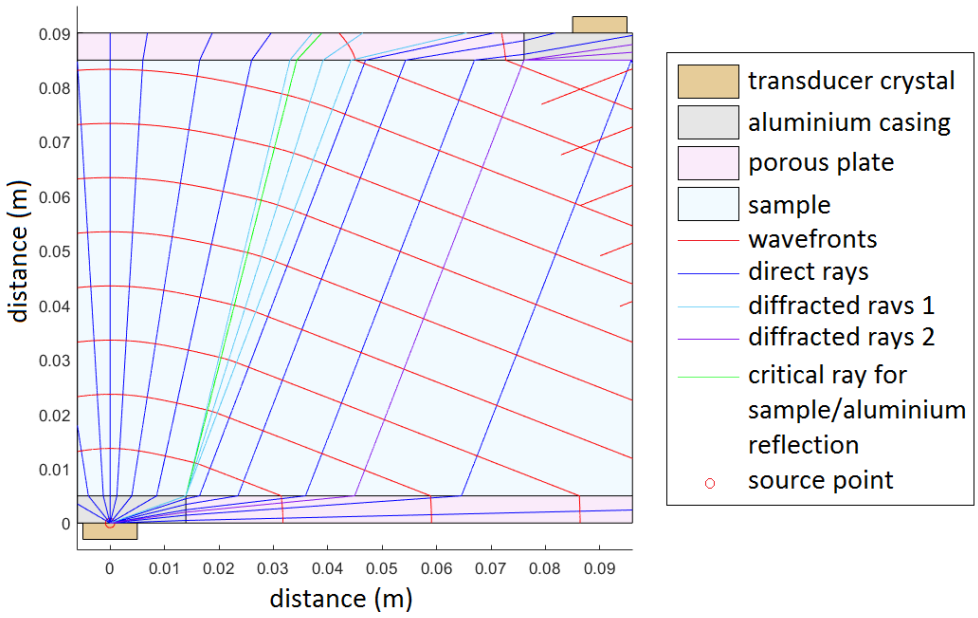

Figure 3-42: Scheme of the segmented dead-time layer model. The two triple points aluminium/porous plate/sample at the top and bottom generate diffraction points. The diffracted rays are marked in blue (bottom) and purple (top). In this configuration the

rays incoming from the sample onto the top aluminium surface arrive at an angle greater than the water/aluminium critical angle and are thus reflected.

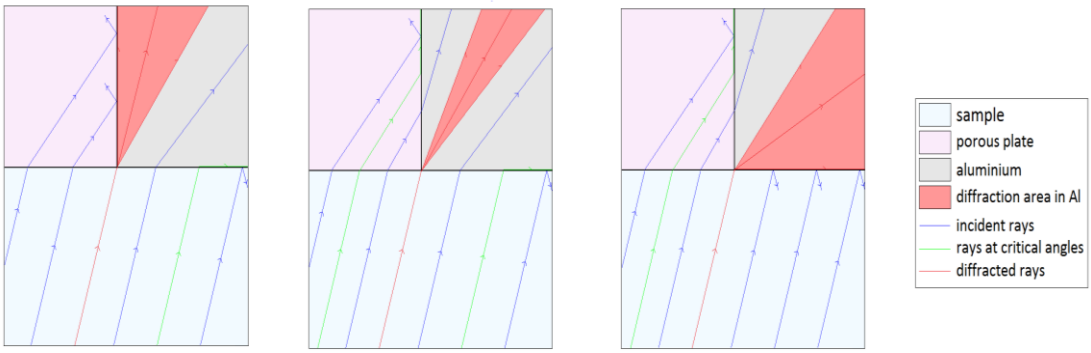

Figure 3-43: Schematic of the diffraction point at the top layer interface. Depending on the geometrical configuration the second diffraction point can produce different arrays of ray paths. This is due to the relative position of the ray paths with critical angles (in green) and the ray path of the diffraction point (in red) in the sample. The receiver is located somewhere on the right side of the porous plate/aluminium interface.

The results of the theoretical arrival times and the experimental arrival times for the propagation along angle 2 are presented in Figure 3-44 along with the absolute value of the error between the two. For each pair of finite-size source and receiver the minimum and maximum values of the model travel times were assumed to occur for the inner and outer edges of the transducer's piezo-ceramic crystals, respectively. The experimental data fall well within the limits of the model and the error never exceeds 1.2% which is within the expected error range of the travel time data.

This model was thus selected to compute the off-axis group velocities and group angles in the actual compaction experiments with a point source and a point receiver at the centre of the transducer’s crystals as this generates satisfactory error values.

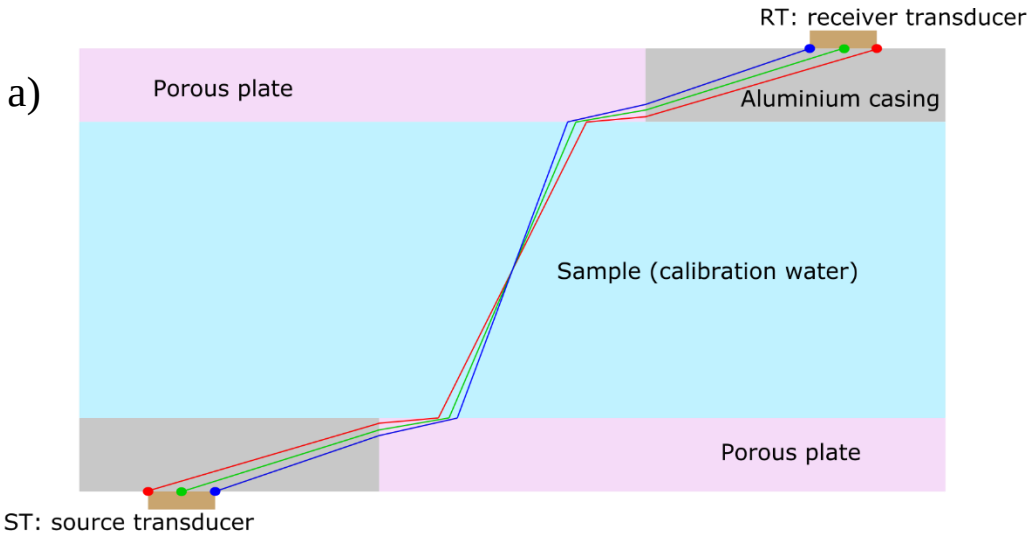

Three-layer segmented model with point source to point receiver ray path finding algorithm performed several times to account for the finite width of the transducers:

Configuration	point source	point receiver	computed travel time	colour
outer edge to outer edge	left corner of ST	right corner of RT	max model	
inner edge to inner edge	right corner of ST	left corner of RT	min model	
centre to centre	centre of ST	centre of RT	average model	

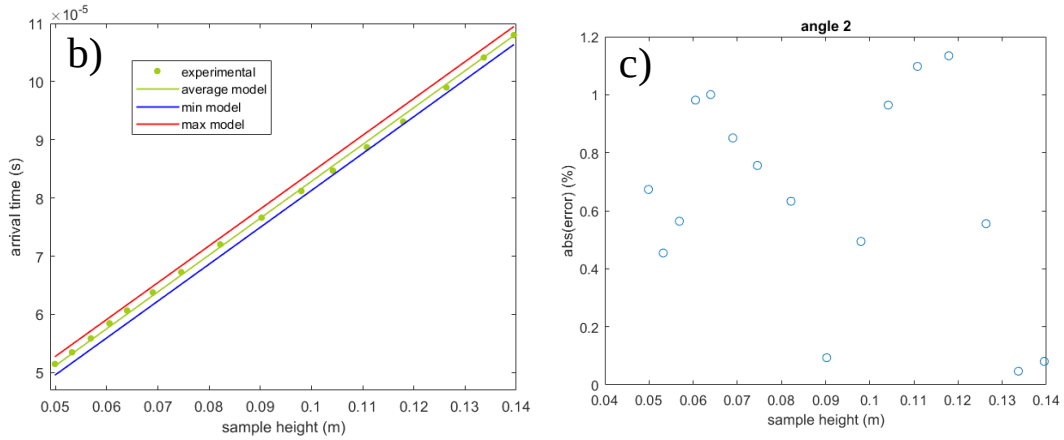

Figure 3-44: a) Segmented dead time layers model with point source and point receiver used in different configurations to account for the finite width of the transducers. In this particular configuration (not to scale), the ray paths are refracted at four different interfaces. This occurs when the sample height is low and the horizontal offset between transducers is similar or larger than the sample height. b) Results of the segmented dead-time layers for the "angle 2" path with the arrival times plotted against water thickness. c) The absolute value of the error between theoretical and experimental values. The error was computed with the average model values (green line in b). The average travel time is not a true average of the extreme values. It is only equal to the average of the equal values if the configurations of the three ray paths (number of refraction interfaces) are the same.

3-3-4-2- Off-axis phase velocity and phase angle

In order to compute the elastic stiffness coefficient c_{13} we need to determine the phase angle and the phase velocity. The method described by Dewhurst and Siggins (2006) was employed. This method consists in solving simultaneously two non-linear equations (42) and (43) with two unknowns: the phase angle θ (measured with respect to the vertical symmetry axis of the VTI medium), and the stiffness coefficient c_{13}. The derivation of these equations is briefly recalled in the following.

By definition, the ratio of the projection of the group velocity on the x-axis to its projection on the z-axis is the group angle, i.e.

$$\frac{V_{gx}}{V_{gz}} = tan\phi \tag{39}$$

The relationship between group and phase velocity can be written as (Tsvankin (2001)

$$V_{gx} = V_{phase}\, sin\theta + \frac{\partial V_{phase}}{\partial \theta}\, cos\theta \tag{40}$$

$$V_{gz} = V_{phase}\, cos\theta + \frac{\partial V_{phase}}{\partial \theta}\, sin\theta \tag{41}$$

Combining equations (39), (40) and (41) yields the first equation to be solved, i.e.

$$V_{phase}(sin\theta - cos\theta\, tan\phi) + \frac{\partial V_{phase}}{\partial \theta}(cos\theta + sin\theta\, tan\phi) = 0 \tag{42}$$

On the other hand, Berryman (1979) showed that the group and phase velocity are related through

$$V_{group}^2 - V_{phase}^2 - \left(\frac{\partial V_{phase}}{\partial \theta}\right)^2 = 0 \tag{43}$$

Where V_{gx} and V_{gz} are the horizontal and vertical components of the group velocity V_{group}, respectively, V_{phase} is the phase velocity, φ is the group angle and θ the phase angle. In addition, according to Thomsen (1986), V_{phase} is related to the stiffness coefficients c_{ij} through

$$V_{phase}(\theta) = \sqrt{\frac{1}{2\rho}\left[c_{33} + c_{44} + (c_{11} - c_{33})sin^2\theta + D(\theta)\right]} \tag{44}$$

With $$D(\theta) = \sqrt{[(c_{44} - c_{33})cos^2\theta + (c_{11} - c_{44})sin^2\theta]^2 + (c_{13} + c_{44})^2 sin^2(2\theta} \quad (45)$$

Where c_{11}, c_{33}, c_{44} and c_{13} are stiffness coefficients and ρ is the bulk density. The two equations (42) and (43) are solved simultaneously for c_{13} and θ using a Levenberg-Marquardt iterative minimization algorithm implemented in Matlab. The Levenberg-Marquardt algorithm minimizes the distance (in the least square sense) between the model and the measurements. The method solves the non-linear system of equations without imposing bounds on the sought parameters (global minimization) bounds by minimizing the sum of squares of the equations (least-square problem).

3-3-5- Error analysis of the ultrasonic measurements

The experimental error on the ultrasonic measurements was determined accounting for the uncertainty on the picking of the wave travel times, and for the uncertainty on the sample dimension measurements. The expression of the different velocities along the symmetry axes of the compacting mixture read

$$V_{11} = V_{ph} = \frac{d_h}{t - t_p} \quad (46)$$

$$V_{33} = V_{pv} = \frac{H_i - \Delta H}{t - t_p} \quad (47)$$

$$V_{12} = V_{sh} = \frac{d_h}{t - t_s} \quad (48)$$

$$V_{31} = V_{s1} = \frac{H_i - \Delta H}{t - t_s} \quad (49)$$

where V_{ph} and V_{pv} are the horizontal and vertical P-wave velocity, respectively; V_{s1} is the velocity of the S-wave propagating in the vertical direction (along the symmetry axis) and polarised in the horizontal direction, also known as the slow S-wave in sedimentary rocks, or as Thomsen's shear wave anisotropy parameter γ; V_{sh} is the velocity of the S-wave propagating in the horizontal direction (within the symmetry plane or plane of isotropy) and also polarised in the horizontal direction, also known as the fast shear wave); d_h is the propagation distance between the horizontal pair of transducers (constant during compaction); H_i is the initial height of the sample, ΔH is the displacement measured by the LVDT from the start of the compaction experiment;

t is the travel time for the given signal, and t_p and t_s are the dead-times of P-wave and S-wave transducers, respectively.

The dead time is the sum of the instruments lag time (time for the electric pulse signal to be converted to an ultrasonic wave) and the time for the ultrasonic wave to propagate from the surface of the piezo-ceramic crystal to the sample's surface, through the transducers' housing and cell body. Because S-waves propagate more slowly than P-waves this dead time is different for the two wave types. It was determined experimentally by measuring the arrival times of P- and S-waves of the transducer pairs directly coupled to each other with the same equipment (transducers, pulser-amplifier, switchbox and oscilloscope) used during the actual compaction experiments.

The picking of ultrasonic wave arrival times, whether it is a dead time or during an experiment, comes with an inherent uncertainty due to the noise level around the first break, the amplitude of the first break (signal-to-noise ratio SNR), as well as the resolution of the digitized ultrasonic signal. The uncertainty on the dead time is typically lower than during an actual experiment because the signal recorded from two transducers put in direct contact has a higher amplitude so that the first arrival is easily identified. For each wave type, the uncertainty on the picking value was repeatedly determined graphically on multiple signals. Figure 3-45 shows a typical ultrasonic waveform on which the arrival time was picked and represented by a red disk on the graph. The shown red interval indicates the bounds outside of which we are absolutely confident the first break doesn't occur. A summary of the uncertainties calculated for the different types of ultrasonic signal measurements is shown in *Table 3-4*.

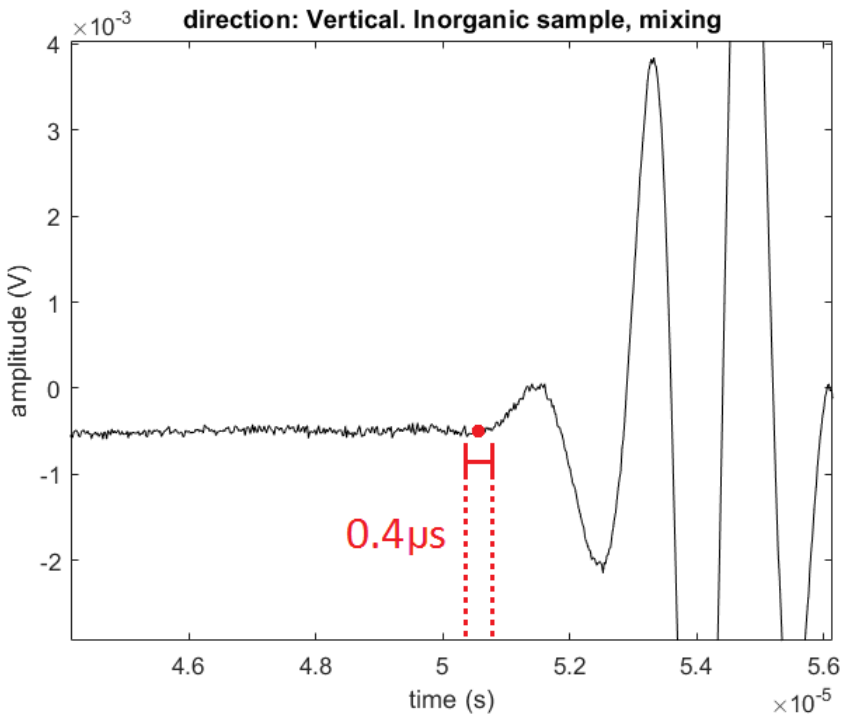

Figure 3-45: P-wave signal first break during the compaction of an inorganic synthetic shale sample. The uncertainty was graphically determined at 0.4µs.

U(Measurement)	Uncertainty Value
P-wave arrival time u(t)	0.4 µs
S-wave arrival time u(t)	2 µs
P-wave dead time $u(t_p)$	0.06 µs
S-wave dead time $u(t_s)$	0.3 µs

Table 3-4: Presentation of the standard combined uncertainties and relative uncertainties of a synthetic shale sample at two times after the start of the compaction experiment: 10h - sample poorly consolidated; 32h - sample well consolidated.

It is important to note that these uncertainty values are valid for most but not all measurements made with the compaction cell. In particular the S-wave first arrival can have a higher uncertainty. At the start of a compaction experiment the sample is essentially in a liquid state, which does not allow the propagation of shear waves. When the mineral matrix compacts, it consolidates, the medium starts progressively to transmit S-waves, although weakly initially. At this stage the S-wave signal has a very low amplitude and the uncertainty was determined to be as high as 10µs.

However, at this stage the S-wave velocity is also small, hence the travel time is long (usually around 300µs) which yields a relative uncertainty of approximately 3%.

The uncertainty on the horizontal distance d_h is linked to the machining of compaction cell and is negligible compared to the other experimental uncertainties. The uncertainty on the initial height H_i and the LVDT displacement ΔH were defined in Section 3-3-2-3-2- as $5x10^{-5}$m and 0.36% of the measured displacement, respectively.

Based on the above estimates, the combined standard uncertainties u(x) of the different velocities read (Taylor, 1982)

$$u(V_{ph}) = \frac{V_{ph}}{t - t_p}\sqrt{u^2(t) + u^2(t_p)} \tag{50}$$

$$u(V_{pv}) = V_{pv}\sqrt{\frac{u^2(H_i) + u^2(\Delta H)}{(H_i - \Delta H)^2} + \frac{u^2(t) + u^2(t_p)}{(t - t_p)^2}} \tag{51}$$

$$u(V_{sh}) = \frac{V_{sh}}{t - t_s}\sqrt{u^2(t) + u^2(t_s)} \tag{52}$$

$$u(V_{s1}) = V_{s1}\sqrt{\frac{u^2(H_i) + u^2(\Delta H)}{(H_i - \Delta H)^2} + \frac{u^2(t) + u^2(t_s)}{(t - t_s)^2}} \tag{53}$$

The uncertainty of the off-axis group velocity V_{group} cannot be computed directly from the uncertainties of the instruments because this velocity is computed with an iterative minimization algorithm as described in the previous sections (optimization of the wave propagation model of the compaction cell). This uncertainty is therefore governed by the uncertainty of the instruments, the precision of the numerical solution of the iterative algorithm, and the validity of the model. To define the uncertainty of the off-axis group velocity we use the experimental error computed with the calibration experiment with water presented in Section 3-3-4-1-. The maximum error we obtained is just below 1.2% of the arrival time. We multiplied that error with the maximum arrival time obtained during the calibration. This gives us an uncertainty on the computation of the off-axis travel time $u(t_{group}) = 1.3x10^{-6}$ seconds. The expression of the group velocity V_{goup} from the ray propagation model presented in Section 3-3-4-1-2- is:

$$V_{group} = \frac{H_i - \Delta H}{\cos \Phi \, (t_{group} - t_{dead\,time})} \tag{54}$$

Where φ is the group angle and $t_{dead\ time}$ is the travel time in the top and bottom plates. As φ and $t_{dead\ time}$ are computed precisely with the model, we set their uncertainty at $u(\varphi) = 0$ and $u(t_{dead\ time}) = 0$. The uncertainty on the group velocity $u(V_{group})$ is then:

$$u(V_{group}) = V_{group} \sqrt{\frac{u^2(H_i) + u^2(\Delta H)}{(H_i - \Delta H)^2} + \left(\frac{u(t_g)}{t_g}\right)^2} \tag{55}$$

To give an example of the range of values of uncertainty obtained during a typical compaction experiment, we computed the error on the velocities at two different times during the compaction of an inorganic artificial sample (*Table 3-5*): Early in the experiment, when the sample is poorly consolidated and the quality of the ultrasonic signal is relatively low (low signal to noise ratio), and at the end of the experiment when the sample is well consolidated with a strong ultrasonic signal.

The uncertainty on S-wave velocities is higher than the uncertainty on P-waves. Note the uncertainty actually increases between t=10h and t=32h for P-waves because the error on the LVDT measurement increases with the measured displacement.

Velocity	Value 10h (m/s)	Standard combined uncertainty 10h (m/s)	Relative uncertainty 10h (%)	Value 32h (m/s)	Standard combined uncertainty 32h (m/s)	Relative uncertainty 32h (%)
V_{ph}	1755	26	1.5	2604	56	2.1
V_{pv}	1679	14	0.8	2179	32.7	1.5
V_{sh}	407	34	8.3	1312	71.1	5.4
V_{sv}	376	16	4.2	996	31	3.1
V_{group}	1685	32	1.9	2300	69	3

Table 3-5: Presentation of the standard combined uncertainties and relative uncertainties of a synthetic shale sample at two times after the start of the compaction experiment: 10h - sample poorly consolidated; 32h - sample well consolidated.

3-4- Results: data obtained during compaction

3-4-1- Sample set overview: composition and petrophysical characterizations

The following Table 3-6 summarises the grain densities of the different pure minerals and OM at different maturity levels used to prepare the artificial shales. It was measured by helium pycnometry (cf. sample preparation section 3-1-1-4-), on dry powders immediately after cooling down under vacuum when drying at 90ºC (i.e. no residual moisture from atmosphere). As expected OM records a lower density (< 1.9 g/cm^3) than the inorganic phase at around 2.6 g/cm^3 (for the "average" synthetic shale composition made of Clay, Quartz, Calcite and Feldspar with the ratios 6:2:1:1, respectively). A difference can be observed between land and marine OM densities. The land OM has a lower density (≤ 1.6 g/cm^3) than marine OM (~ 1.8 g/cm^3), which will result in a lower TOC for the land samples compared to the marine samples at equal volume content of OM. A correlation with maturity level can also be noted: for both OM types, the density increases between its fresh state and the maturity level 1 and goes back down at maturity level 2. This effect is more pronounced for land OM.

component	Dry density (g/cm^3)
Kaolinite	2.55
Quartz	2.7
K-Feldspar	2.62
Calcite	2.76
Fresh land OM	1.45
Mature land OM 1	1.61
Mature land OM 2	1.43
Fresh marine OM	1.84
Mature marine OM 1	1.88
Mature marine OM 2	1.82

Table 3-6: Summary of the grain densities of the different mineral and OM components used to prepare the synthetic shale samples set.

Table 3-7 shows the initial and post-compaction experiment petrophysical parameters of each sample presented in Table 3-1. The initial porosities for sedimentation deposition methods record much higher values (94.8%) than the mixing method at around 76%, regardless of the particle type and mineralogy/OM type. The final porosities (unconfined, i.e. after unmoulding, when the sample was in atmospheric conditions, free from any stress of the compaction cell) of inorganic and land samples are very similar, around 33%. On the other hand the marine samples display a much lower final unconfined porosity than other samples at around 28%. This results in a higher final wet bulk density for marine samples than for land samples. Note that final unconfined porosities (i.e. after unmoulding from the compaction cell) exceed the porosities under stress by 3 to 5% due to the elastic unloading of the mineral matrix. The volumetric organic content is fairly constant across all organic samples (≈8%) though marine samples display a higher TOC than land samples. This is explained by the higher grain density of marine OM (Table 3-6) and by the lower porosity of marine samples, which means that less brine is left in the sample by the end of the compaction. Despite different initial parameters, the samples produced with the sedimentation method display similar final porosities and densities to their corresponding samples made with the mixing method.

Sample name	Total porosity (%)			Wet bulk density (g/cm^3)		Final OM content	
	Initial	Final (under stress)	Final (Unconfined)	Initial	Final (Unconfined)	% Wt. solid phase	% Vol. solid phase
Inorganic mixing	76.2	29.8	33.2	1.39	2,09	0	0
Inorganic sedim	94.8	29.3	32	1.09	2.09	0	0
Land 0 powder	76	29.2	34.1	1.37	2	4.87	8.05
Land 0 flakes	76.7	30	33.4	1.36	2.01	4.72	7.83
Land 0 flakes sedim	94.8	30.5	33.5	1.09	1.98	4.85	8.02
Land 1	77.7	31.2	34.4	1.34	1.99	5.35	7.98
Land 2	77.4	29.7	33.3	1.35	1.99	5.41	8.35
Marine 0 powder	76.3	24.4	27.9	1.37	2.08	6.14	8.01
Marine 0 flakes	76.4	23.8	27.6	1.37	2.07	6.26	8.16
Marine 1	76.2	25.3	28.4	1.37	2.08	6.33	8.07
Marine 2	76.5	24.5	28.6	1.37	2.07	6.06	8

Table 3-7: Petrophysical parameters computed before and after the compaction experiments for each sample. All the synthetic sample were mixed with 15 g/L (± 0.1 g/L) of NaCl brine.

3-4-2- Compaction monitoring

The compaction data includes the information logged during the compaction experiments by three different instruments: (i) the load cell that records the applied stress on the sample, (ii) the mass balance that records the expelled pore fluid and (iii) the LVDT that records the sample height. Because the transverse section area of the sample in the cell remains constant during experiments, the sample volume evolution with time is computed from the LVDT reading during compaction.

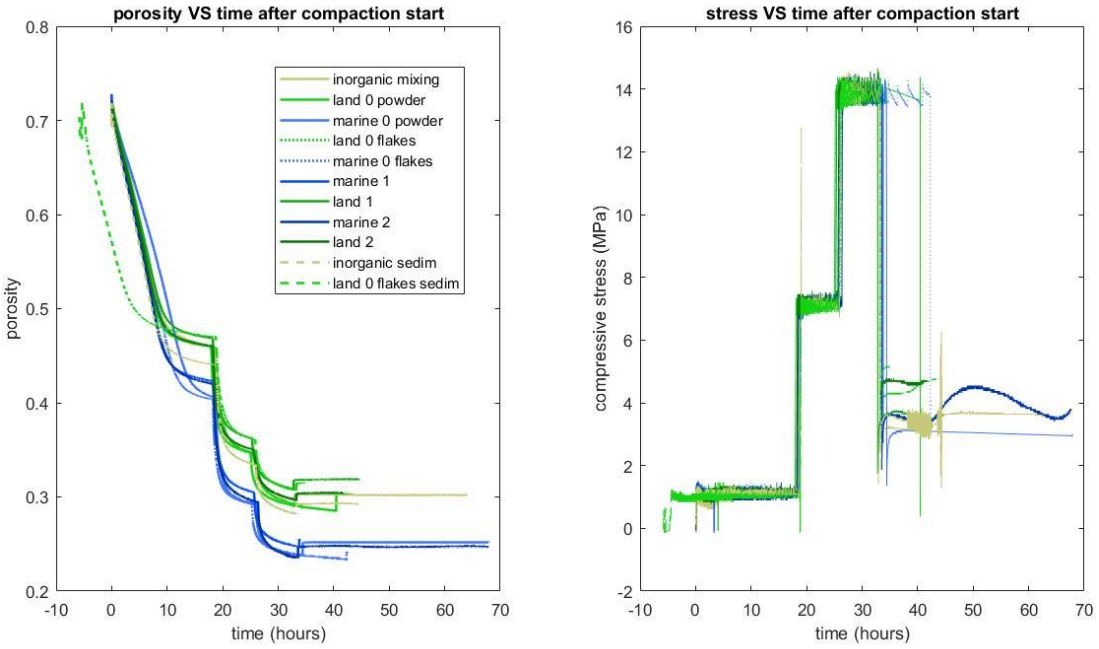

Figure 3-46: Porosity curves over the time of the experiment (left) and uniaxial stress over time (right) for the whole sample set.

The Figure 3-46 shows a summary of the porosity as computed from LVDT monitoring and uniaxial stress curves recorded by the load cell as a function of time for the whole sample set (right graph). On the stress curves, the three distinct loading steps applied on the samples at 1, 7 and 14 MPa are visible, along with the residual stress after the actuator load is released (after 32 hours experiment) at the end of the experiments (elastic unloading effect from the sample). The variability of the residual stress is mainly due to the temperature conditions in the laboratory at the time of the stress unloading that can slightly change (17 to 21°C). The applied loading steps and unloading stage are also visible in the porosity curves, with the faster decrease rate happening at the very beginning of each step. The unloading stage generates a porosity

increase of about 3 to 5% on all the samples. As the mineral matrix relaxes (elastic rebound), the piston is pushed up and the sample volume increases. This volume change raises a question about the accuracy of the porosity values under stress. The porosity is actually computed from the LVDT reading with the assumption that the mineral phase is quasi-incompressible and thus, the mineral volume is constant. This curves show that this is not the case: there is a difference in the computed porosity of about 3% between a uniaxial stress of 14MPa and the residual stress between 3 and 5 MPa.

The difference in porosity between marine samples and the rest of the sample set is quite remarkable. The porosity decrease rate is initially similar for all samples, but at around 8 hours into the compaction this rate greatly slows down for land and inorganic samples whereas the marine samples porosity continues to decrease at the same initial rate for another two hours approximately. The difference in porosity between marine and other samples is thus acquired during the first step of compaction and then remains similar until the end of the compaction.

Additionally it is necessary to define a reference point to compare the samples porosities during and after compaction. Because the porosity decrease rates vary across the sample set, choosing an arbitrary point in time or a specific porosity would not have any physical basis. To properly compare the porosity monitoring between samples, the point at which 90% of the pore pressure has dissipated was determined, after a step increase of the compaction stress, from the height reading of the LVDT.

There are several different methods available for this task. They were originally designed to determine the coefficient of consolidation from consolidation curves. Two of these methods were chosen for our sample set: (i) the Taylor method and (ii) the inflection point method. These are suitable for our sample set, as they do not require full dissipation of the pore pressure. The quality of the compaction data can be checked by comparing how the results of each method match the other. To present them, the compaction data obtained on the sample Land 1 will be used.

- Taylor method (Taylor, 1942)

This method was developed by Taylor (1942) and uses the shape of a consolidation curve (or height of a consolidating sediment) as a function of square root of time to compute the time when 90% of the pore pressure has dissipated (t_{90}). It postulates that

the initial portion of the curve, before 60% consolidation, should be a straight line. The compaction curve in Figure 3-47 shows such a curve. The asymptote to the linear portion of the curve will cross the y-axis at a value H_0 equivalent to 0% consolidation. We determine the asymptote of the curve by selecting the constant section of the derivative of the settlement curve with respect to the square root of time. A line passing by (t=0, H=H_0) with a slope 15% higher than the asymptote slope will cross the consolidation curve at t_{90}. The 15% value was determined experimentally in the original study.

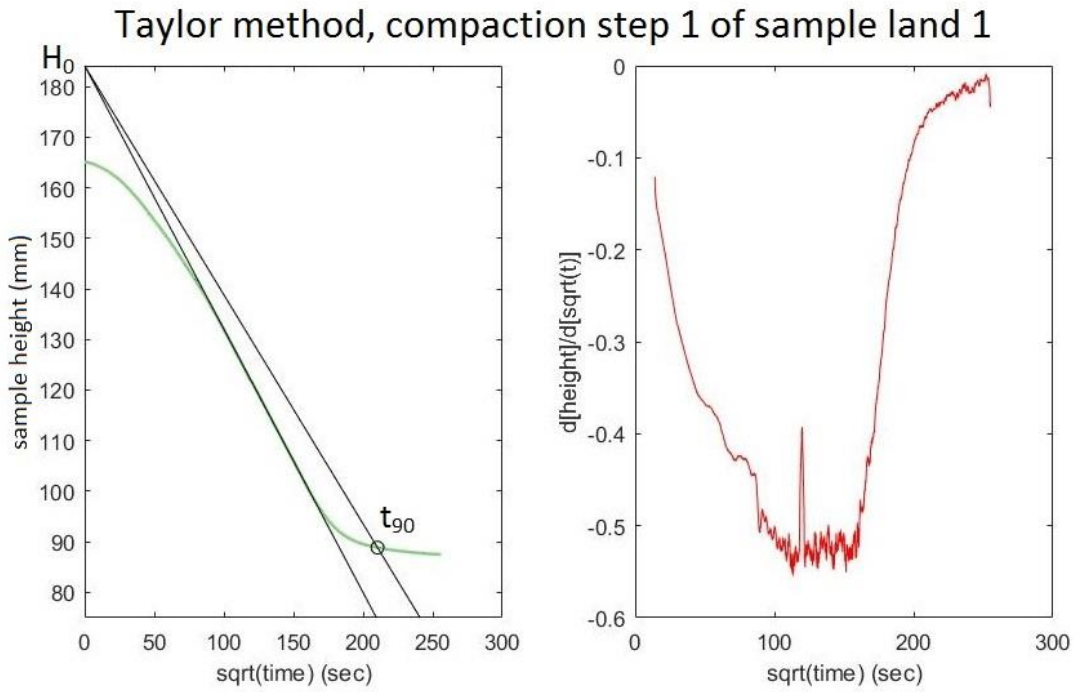

Figure 3-47: Consolidation curve of the step 1 of the compaction of sample land 1 (1 MPa during 18 hours). The derivative of the height with respect to the square root of time (right) is used to determine the asymptote to the linear part of the settlement curve (left). A line passing by the zero consolidation point and with a slope 15% higher than the asymptote slope will pass through the settlement curve at t_{90} indicated here with a black circle.

- Inflexion point method

This method is also a graphical determination of t_{90} but it uses the consolidation curve plotted against the $\log_{10}$ of time. It uses the fact that the inflexion point of the consolidation curve corresponds to a time factor T with a value T_i = 0.405. The time

factor is an empirical value related to the coefficient of consolidation of the sample, the time of consolidation t and the sample height H as follow:

$$T = \frac{c_v t}{H} \tag{56}$$

The value taken by the time factor at t_{90} was determined experimentally as $T_{90} = 0.636$. We can thus write that

$$t_{90} = \frac{t_i T_{90}}{T_i} = \frac{t_i 0.636}{0.405}. \tag{57}$$

To determine the inflexion point, we selected the lowest point of the derivative of the consolidation with respect to $\log_{10}$ of time. Then we computed t_{90} using equation (57). The graph in Figure 3-48 illustrates this method.

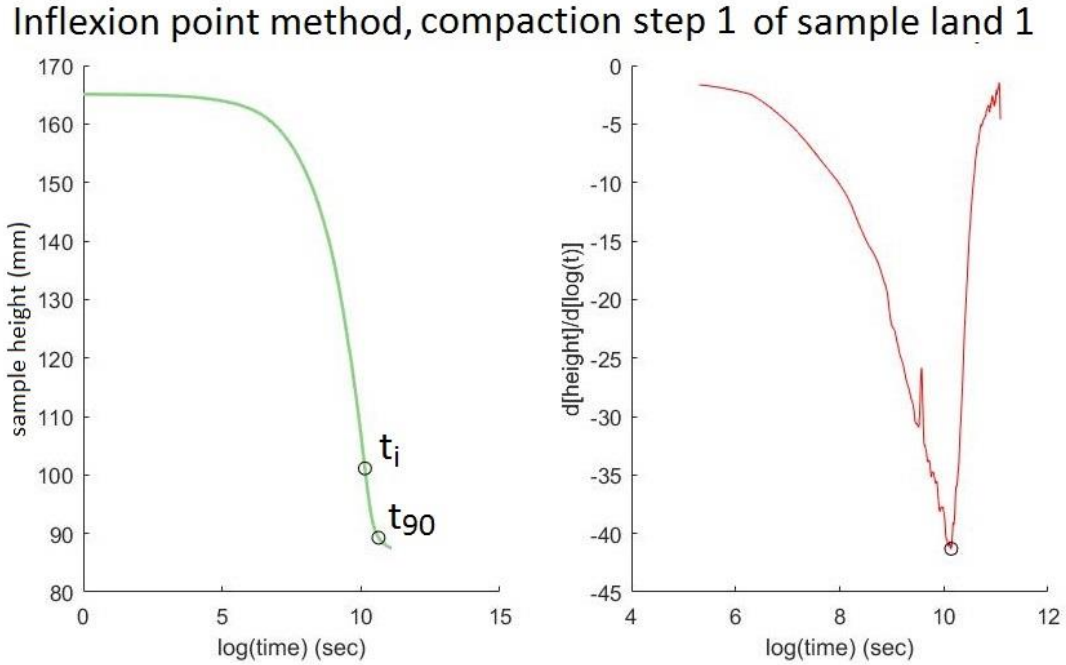

Figure 3-48: Consolidation curve of the step 1 of the compaction of sample land 1 (1 MPa during 18 hours). The derivative of the height with respect to the log $_{10}$ of time (right) is used to determine the inflexion point on the consolidation curve (left). The time t_i of the inflexion point was then used to compute t_{90}.

t_{90} was computed for every compaction step of each sample with the two methods and compared the times obtained with each method. An example of a consolidation curve as a function of time with the two t_{90} is presented in Figure 3-49. Most consolidation curves in the sample set have very similar t_{90} values with less than 15% of difference.

The average of the two methods was taken as a reference point to compare the porosity values with each other. In the third step of compaction (14 MPa) the consolidation curves turned out to be too short to determine t_{90}. The hydraulic conductivity of the samples at this final stage of compaction was lower than expected and the pore pressure dissipation did not reach 90%. Consequently the porosity 7 hours after the beginning of the third compaction step was employed as a reference point. In hindsight the compaction stress should have been maintained for longer as the pore pressure dissipated slower than anticipated.

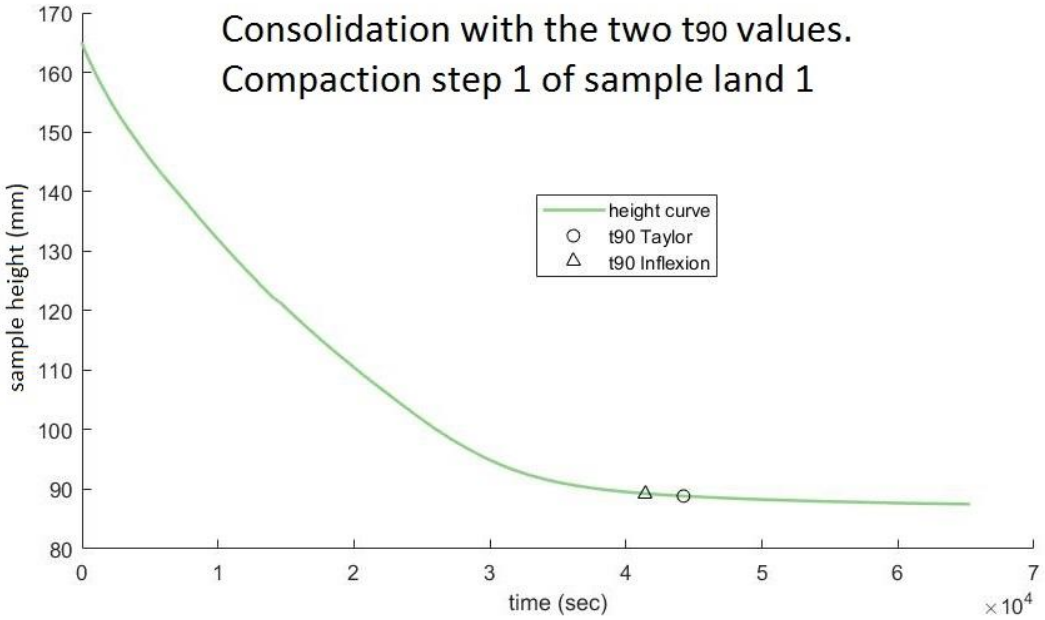

Figure 3-49: Consolidation of the first step of the compaction of the synthetic organic sample "land 1" (1 MPa during 18 hours). The values of t_{90} obtained with the Taylor method and the inflexion point method are marked.

- Permeability estimation

An indirect estimation of the coefficient of permeability can be made using the compaction curves using Terzaghi's theory of consolidation for 1-dimensional consolidation (constant cross-sectional area, vertical water drainage path) as described by Terzaghi and Peck (1967). The compaction curves allow us to determine the coefficient of compressibility of the samples after a change in effective stress. In turn this is related to the coefficient of permeability k for the same stress increment as follow:

$$k = c_v m_v \gamma_w \tag{58}$$

c_v is the consolidation coefficient:

$$c_v = \frac{0.848 d^2}{t_{90}} \tag{59}$$

m_v is the volume compressibility coefficient:

$$m_v = \frac{1}{H_0}\left(\frac{H_0 - H_1}{\sigma_1' - \sigma_0'}\right) \tag{60}$$

And γ_w is the unit weight of water:

$$\gamma_w = \rho_w g \tag{61}$$

where d is the distance to drainage boundary (half the sample height here), H_0 is the sample height at the start of the step increase in effective stress, H_1 is the sample height after displacement due to primary consolidation, σ_1'- σ_0' is the increase in effective stress, ρ_w is the brine density and g is the acceleration of gravity (9.81 m/s^2).

In the compaction experiments, the effective stress is equal to the uniaxial stress increase because the samples are in drained conditions, i.e. pore pressure is considered equal to 0 before the stress increase. The permeability was computed for the steps 1 and 2 of the experiments where a t_{90} value is available. The effective stress increase is taken as 1 MPa for step 1 and 6 MPa for step 2. The results are presented in Table 3-8.

Sample name	k step 1 (Darcy)	k step 2 (Darcy)
Inorganic mixing	20.79	0.07
Inorganic sedim	21.36	0.04
Land 0 powder	11.68	0.04
Land 0 flakes	23.70	0.05
Land 0 flakes sedim	15.53	0.04
Land 1	18.70	0.05
Land 2	18.93	0.06
Marine 0 powder	17.48	0.05
Marine 0 flakes	22.44	0.05
Marine 1	19.22	0.05
Marine 2	22.93	0.05

Table 3-8: Permeability coefficient determined for compaction steps 1 and 2 from the consolidation curves (height as a function of time) obtained during the compaction experiments.

The permeability coefficient for step 1 is very high for all samples (>10 D), that is typical of unconsolidated clays and is thus expected as the sample go from a liquid

state to a poorly consolidated state at this stage. The value then decreases drastically to below 100mD for the compaction step 2. This corresponds to permeabilities exhibited by some permeable limestones. We can surmise the final samples have a coefficient of permeability (after stress increase of step 3) significantly lower than step 2. Besides, no significant differences can be observed between the different samples. This shows the permeability depends mainly on the constant inorganic matrix (clay in particular) and that the OM variables have little influence on it.

- Compaction effect on porosity

The results of porosity decrease are presented in bar charts (Figure 3-50 to *Figure 3-52*) as the porosity drops between the beginnings of each step (at the moment of the step stress increase) and the time when 90% of the pore pressure has dissipated (t_{90}) for steps 1 and 2 and after 7 hours of consolidation for step 3. We made groups of samples according to the target variables. Figure 3-50 focuses on the sample's OM maturity level. The land and marine samples are separated to also evaluate the influence of the OM type. The same inorganic shale is added within the land and marine group of samples for a visual comparison.

Compaction step 1 reflects what was seen previously: the marine samples lose much more porosity than the land samples in this step (0.3 against 0.25).

While the compaction step 1 observation is continued in the compaction steps 2 and 3 for mature marine samples, it is reversed for the fresh marine sample that has a lower porosity drop than the fresh land sample and the inorganic sample.

- OM maturity effect on compaction trend and porosity

The maturity of the different samples in each OM type does not have an effect on the porosity drop during the compaction step 1. This contrast with the compaction steps 2 and 3 where the mature land samples have a smaller porosity drop than the fresh land sample whereas the mature marine samples display a higher porosity drop than the fresh marine sample.

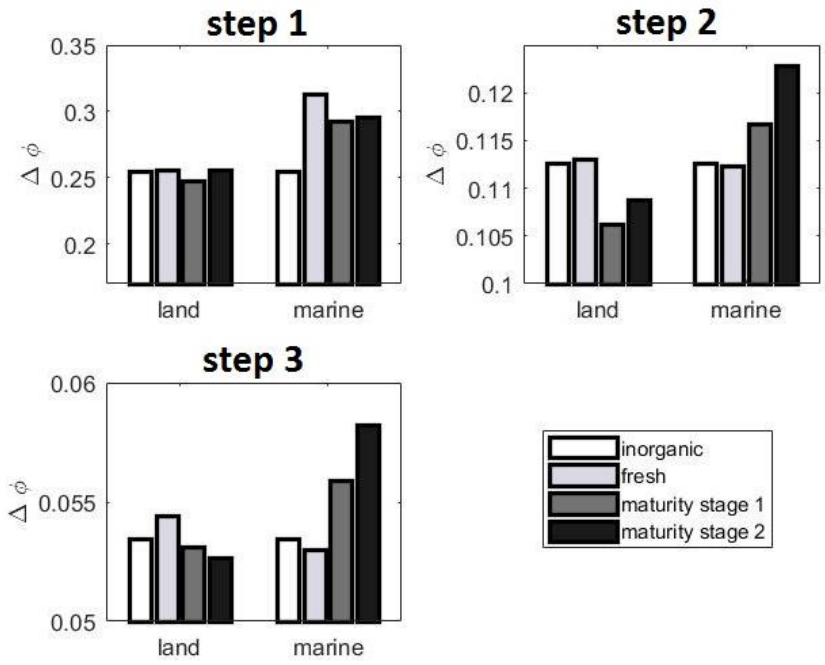

Figure 3-50: Porosity drop at each compaction step for samples of different OM maturities and for inorganic shale sample. These organic shale samples were produced using the mixing method with OM particles of the powder type.

- Effect of deposition on compaction trend and porosity

The depositional type effect, mixing versus decantation sedimentation, on the compaction monitoring is presented in Figure 3-51 and summarised using the same presentation as for the previous Figure 3-50. Each deposition method features an inorganic sample and a sample containing land flake particles. The two samples made with the mixing method show very little differences in all the three compaction steps. On the other hand, the difference between the inorganic and the land sample is more pronounced for the sedimentation method. The inorganic sample decreases in porosity substantially more than the land sample in the compaction step 1 before it decreases slightly less in the compaction steps 2 and 3. Overall results show a subtle difference in amplitude among the samples set with respect to the OM type effect (Figure 3-50) that were especially strong during the compaction steps 2 and 3 (≥ 7 MPa).

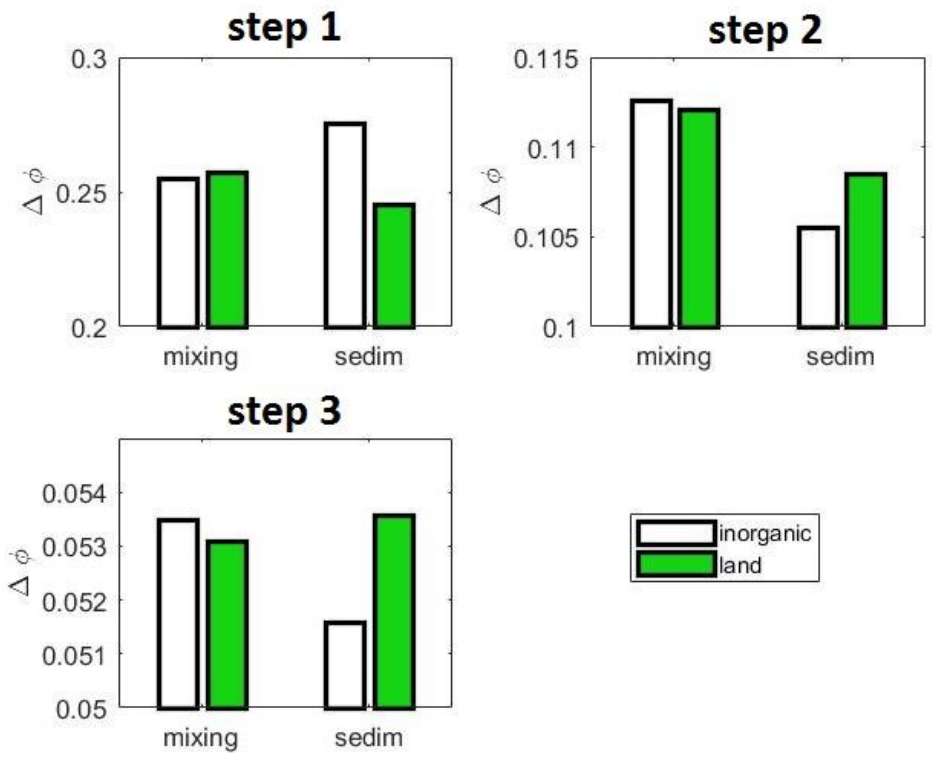

Figure 3-51: Porosity drop at each compaction step for samples placed in the compaction cell with two different depositional methods: the standard mixing method and the sedimentation method. The organic rich samples were made using OM particles of the flake type only. The amplitude of the differences between samples is quite small, particularly in step 3.

• Effect of the particle type on compaction trend and porosity

The results obtained on different particle types are shown in Figure 3-52 for both land and marine organic samples. In the compaction step 1, the marine samples lose once again more porosity than land samples but the particle type has no visible influence. In the compaction steps 2 and 3, the marine samples have slightly lower porosity drops than land OM rich samples. The flake samples have smaller porosity drops in the two last compaction steps. The amplitude of the differences in those compaction steps 2 and 3 are small, though the observations are consistent nonetheless.

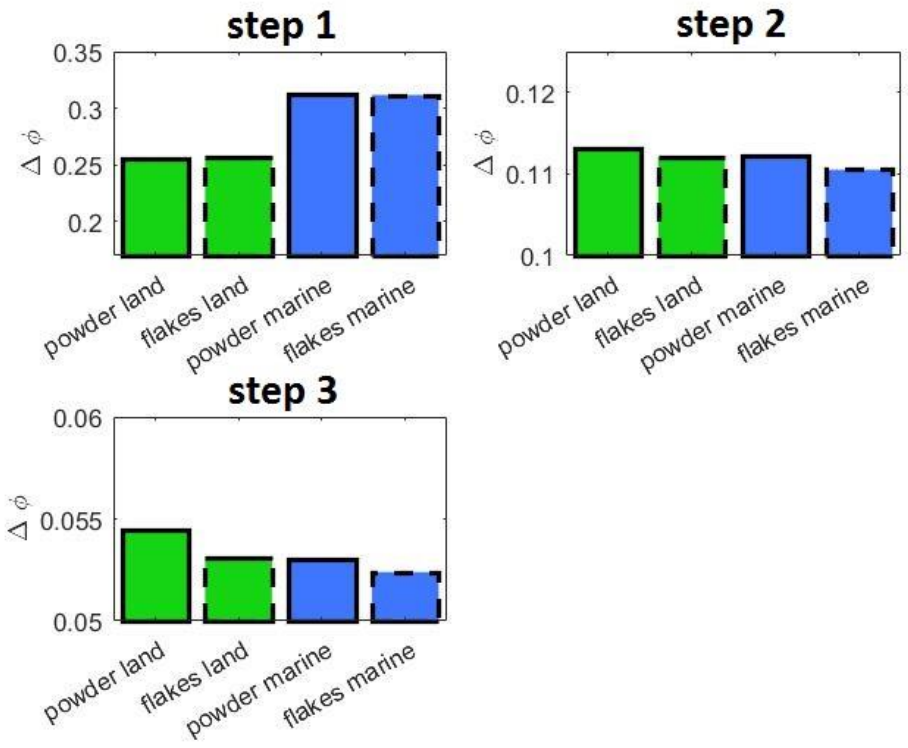

Figure 3-52: Porosity drop at each compaction step for samples made using different OM particle types: powder and flakes. The samples were deposited in the compaction cell using the mixing method and the OM was fresh.

All the porosities presented above are computed from the LVDT (cf. Section 3-3) reading and are based on the assumption that the volume loss during compaction is only due to the drainage of brine expelled in the pore lines and that the compressibility of the solid phase is negligible. To verify this assumption we used the measured mass of expelled fluid and compared the expelled pore fluid volume to the sample's volume decrease measured with the LVDT. As an example a graph of volume loss at each compaction step for the sample containing fresh land flake organic particles deposited with the mixing method is presented in Figure 3-53.

At the start of each experiment the pore lines were already flooded with pore fluids so that the drainage at the beginning of the compaction would generate an immediate reading on the mass balance. During the experiments, the container on the mass balance collecting the expelled fluid was not sealed and evaporation occurred to some degree. Unfortunately, attempting sealing such container to avoid evaporation led to an imprecise mass reading (strong variability in mass). The volume of expelled fluid was computed taking into account the density of the brine as the salinity increases its

density. We also took into account the evaporation rate thanks to a probe that measured the temperature and the relative humidity independently during the experiment.

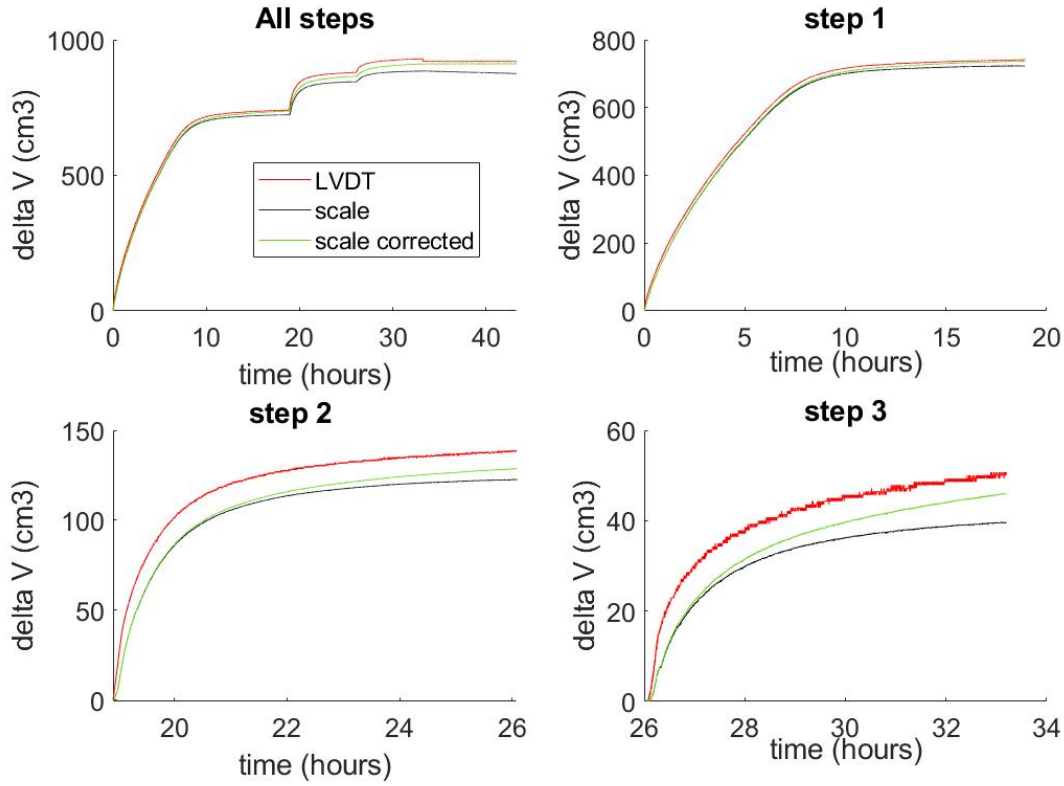

Figure 3-53: Volume loss of the organic sample containing fresh land flake particles during its compaction. The volume loss computed from the LVDT data is shown in red. The volume loss computed from the mass balance data is shown in black. The corrected value accounts for the water evaporation and the brine's salinity. The first graph is the cumulated volume change throughout the whole compaction experiment. The separate steps quantify the volume change since the beginning of each step.

To calibrate the evaporation rate the mass balance was tested with a container filled with an initial volume of water of 1L and the evaporation was recorded over a period of several hours in the same laboratory conditions used for the compaction experiments. The container used was the same as during the compaction experiments so the surface exposed to evaporation was identical. It was noticed that the temperature variations during both the experiments and the calibration were small (< 2°C) and that the main driver of the evaporation rate was the relative humidity of the air in the laboratory.

The evaporation rate in gram per second g_s can be expressed by the following equation:

$$g_s = E_c A(x_s - x) \tag{62}$$

where A is the water surface area, x_s is the maximum saturation humidity ratio in air, x is the humidity ratio in air and E_c is the evaporation coefficient. This coefficient is determined empirically and depends on the air temperature, water temperature and the velocity of air above the water surface. Given that these three parameters were near constant during the compaction experiments, we will consider this coefficient unique for all the compaction experiments. Because of the relationship between x and x_s

$$x = R_h x_s \tag{63}$$

with R_h being the relative humidity, we can rewrite equation (62) as:

$$g_s = E_c A x_s (1 - R_h) \tag{64}$$

To determine E_c a recursive algorithm was employed, that minimizes the coefficient of determination between the computed evaporation rate from equation (64) and the experimental evaporation rate by changing the value of E_c from an initial arbitrary value. The results of this process are shown in Figure 3-54. We can see that the final computed evaporation rate matches well with the experimental data.

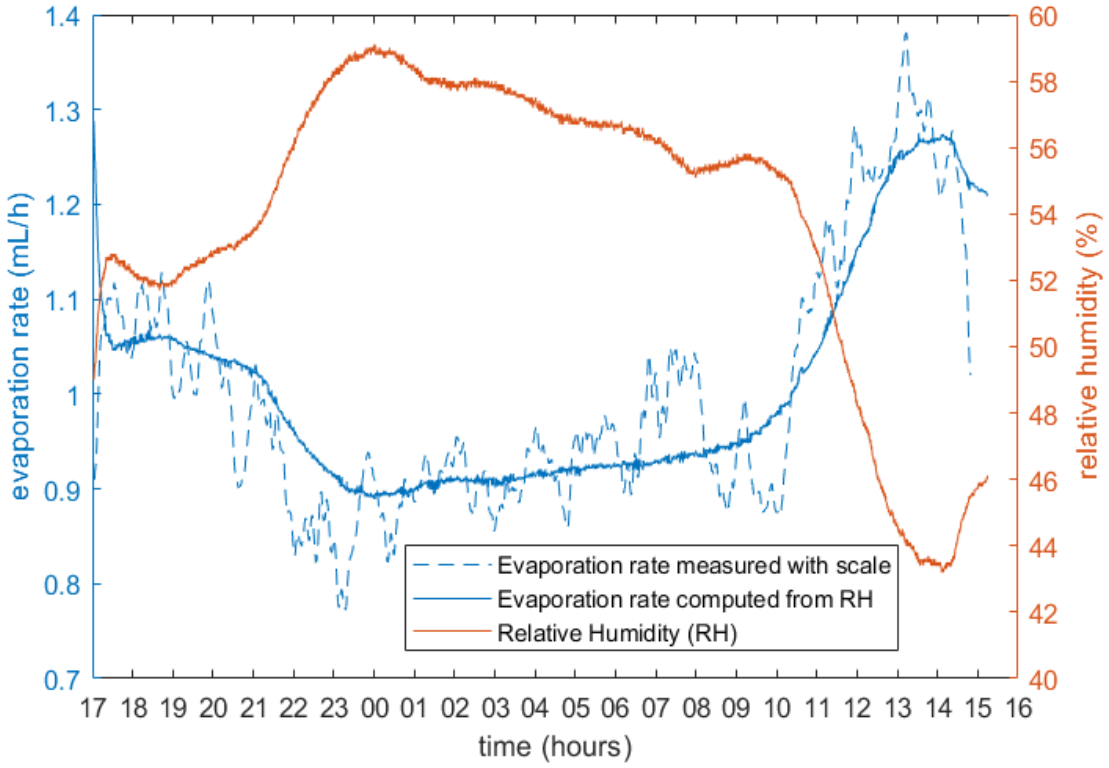

Figure 3-54: The evaporation rate computed from the relative humidity data was calibrated using the experimental data obtained during the evaporation test with a recursive algorithm minimizing the coefficient of determination R2.

The black line in Figure 3-53 represents the uncorrected volume loss in the compacting sample from the scale value. The corrected value accounting for evaporation and salinity of the pore fluid is the green line. This volume change represents only the loss of pore fluid. The volume change computed with the LVDT reading in red is higher because it is affected both by the loss of fluid and by the compressibility of the solid phase of the sample. It can also be seen that when the stress is released after the end of the compaction step 3, the LVDT volume change decreases towards a value close to the scale volume change (in *Figure 3-53*, All steps, at t=32h).

To evaluate the variations of the volume of the solid phase in more details, the mass balance volume change was subtracted to the LVDT volume change to obtain the variation in solid volume, as presented in the example in Figure 3-55. In each separate step, the change in grain volume is the highest at the beginning of the step, i.e. just after the uniaxial stress increases and then slowly decreases. This reflects the pore pressure state in the sample. When the pore pressure rises, it compresses the mineral grains and when the pore fluid progressively drains out of the sample, the load is

transferred from the fluid to the mineral matrix. Hence the grains relax elastically from the fluid pressure while grain contacts multiplies and the structure of the solid phase changes.

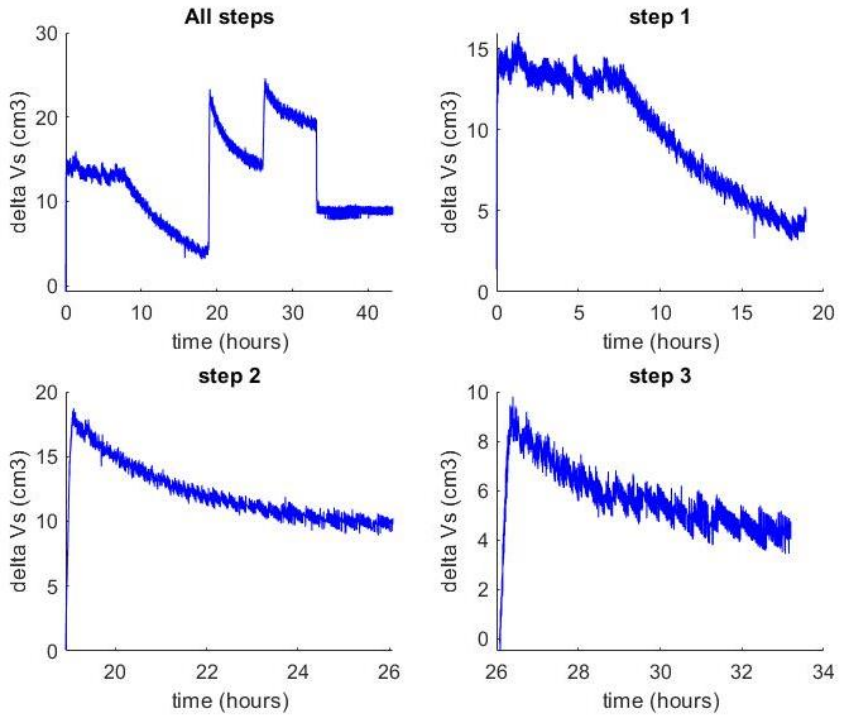

Figure 3-55: Solid matrix volume (or grain volume) change during the compaction of the organic rich sample containing fresh land flake OM particles. It is obtained by subtracting the corrected scale volume change (i.e. volume of pore fluid expelled out of the shale sample) to the LVDT volume change. The grain volume change is the highest at the beginning of the compaction steps, when pore pressure is the highest before it dissipates by drainage.

In the compaction step 1, the grain volume change remains steady for the first eight hours. This is a consequence of the very high water content of the sample at the beginning of the experiment. At this stage the sample is in a liquid state and even though pore fluid is being drained out, the contact between grains stays minimal so the load is not transferred to the mineral matrix until several hours into the experiment.

The greatest solid volume change is achieved at the beginning of compaction steps 1 and 2 (1 and 7MPa) but is much smaller in the compaction step 3, when the grains are already highly compressed. On the cumulated solid volume change graph (Figure 3-55- upper left) the maximum cumulated solid volume change at the beginning of

compaction step 3 is barely higher than at the beginning of compaction step 2. This shows that most of the grain volume change occurs at low pressure.

The trends observed for this fresh land OM particles sample (Figure 3-55) were repeatedly observed for the other samples. However some samples displayed a negative solid volume change in the compaction step 1. In two instances, this was so important that the overall solid volume change throughout the whole experiment was negative. Because step 1 is the longest, this hints at a possible limitation in the correction due to the evaporation of the expelled pore fluid. Also the maximum grain volume change in this example (approximately 25cm^3) represents 5% of the total solid volume and 4% of the final volume. At the end of compaction step 3, the total solid volume change is 20cm^3. When we use this information to correct the reading of the final porosity under stress, the porosity value changes from 30% to 33.2%. This corrected value is very close to the final unconfined porosity (computed after unmoulding of the sample) at 33.4%. **To conclude, the data obtained from the mass balance reading could be used in the future as a tool to evaluate the compression of the solid matrix to correct the porosity values, given that the container of expelled fluid is properly sealed with an accurate reading**.

3-4-3- Ultrasonic measurements

The compaction cell is equipped with P-wave and S-wave transducers that allow the quasi-continuous recording of ultrasonic wave velocities along a vertical, a horizontal and inclined direction during a compaction experiment. These data is then used to compute the evolution with compaction of the full elastic stiffness tensor of the sample. For more details about velocity computation and data processing, please refer to section 3-3-.

To give an example of the continuous recording of elastic properties, the sole results that will be presented were obtained on the sample containing marine OM of maturity level 2 prepared with the mixing method and named “Marine 2” for short. Figure 3-56 shows the computed ultrasonic velocities for that sample. The P-wave velocities are measured right from the beginning of the compaction, whereas the S-wave velocities become detectable 8 hours after the start of the compaction, when the sample transits from a liquid state to a consolidated solid material in which grain contacts in the mineral matrix contribute measurably to the overall shear stiffness of the material, and

therefore S-waves can propagate through it. Early during the compaction experiment, the velocities are also isotropic and start to diverge around the same time S-wave velocities become detectable. Horizontal and vertical velocities have the highest difference by the end of the experiment, when the sample is the most compacted. As expected, the value of the off-axes P-wave phase velocity lies in between the values of vertical and horizontal P-wave velocities. However, it is much closer to the vertical velocity value, indicating that its propagation direction is closer to the vertical direction than to the horizontal direction.

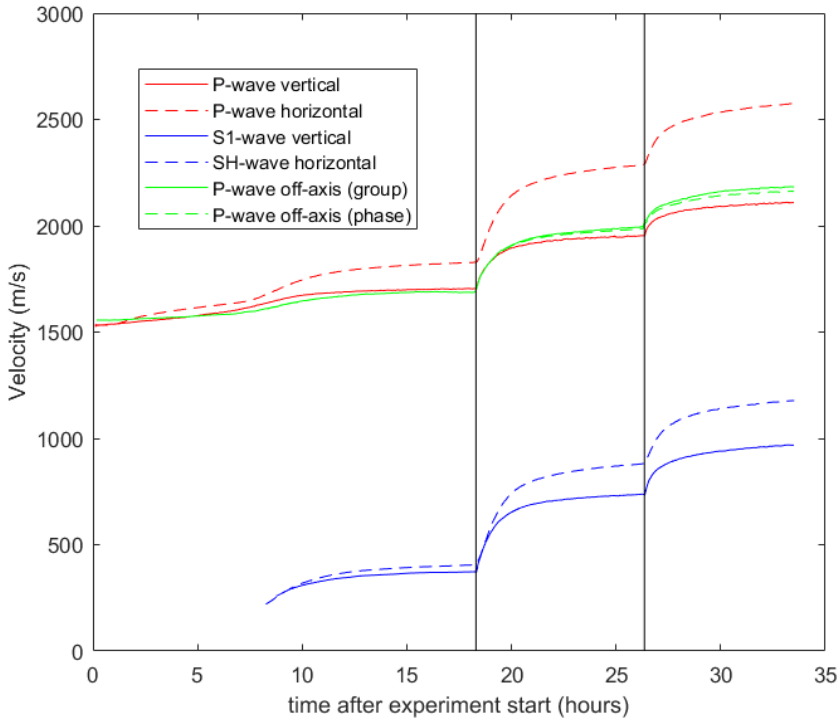

Figure 3-56: Evolution of ultrasonic velocities over time for the sample "Marine 2". The beginning of step 2 and 3 are represented by the vertical lines. P-wave velocity along the main axes are in red, P-wave velocities off-axis are in green and S-wave velocities along the main axes are in blue.

Note that the ultrasonic wave velocity data are presented in the form of continuous curves rather than distinct data points because of the quasi-continuous nature of the monitoring, i.e., each curve is composed of more than 300 distinct measurement points.

Figure 3-57 reports the computed group and phase angles for the off-axes P-wave velocity. The recording of the phase angle starts 8 hours after the compaction

experiment is initiated. This is because its estimation requires the vertical S-wave velocity, which becomes detectable only 8 hours after the initiation of the compaction experiment. The transducer pair used to measure the off-axis ultrasonic signal is composed of a fixed transducer located in the bottom plate of the compaction cell, and a moving transducer located in the piston. As the piston goes down during compaction, the group angle of the off-axes P-wave signal increases from 22^0 to 32^0, measured with respect to the vertical direction (symmetry axis). On the other hand, the phase angle remains virtually unaffected by the compaction. The phase angle data are scattered and exhibit no particular trend while compaction proceeds. This behaviour was observed in all samples. Two effects induce changes in off-axis angles during compaction. First with a constant horizontal offset, and a decreasing sample height, the relative position of the off-axis transducer pair forms an increasing large angle as the piston goes down into the cell. Secondly, as the sample stiffens, the difference in velocity between the transducer casing and the sample decreases. Hence the incident ultrasonic ray paths are less refracted and form a higher angle with regard to the vertical direction. As a consequence, the observed increase in group angle was expected, but the constant phase angle is surprising, as the combination of the two aforementioned effects were expected to have a similar effect as on the group angle.

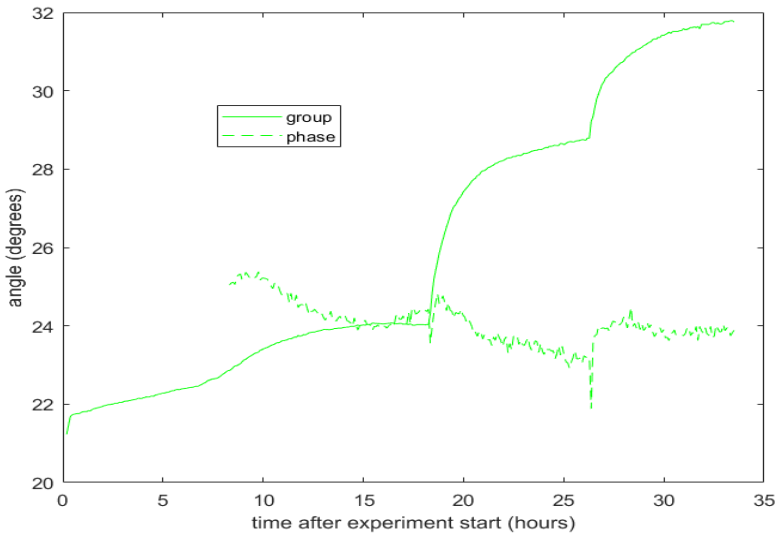

Figure 3-57: Evolution of the group and phase angle of the off-axis ultrasonic signal with respect to the vertical direction during the compaction of sample "Marine 2". The group angle varies with time because the geometric configuration of the source and receiving transducers varies during the experiment. The computed phase angle displays a very different behaviour than the group angle.

Using the five independent velocity measurements the five independent stiffness coefficients of the transversely isotropic elastic stiffness tensor of the sample were computed (see Figure 3-58). The coefficients along the symmetry axes (c_{11}, c_{33}, c_{44} and c_{66}) behave similarly to the velocities they are computed from. The highest value taken by these coefficients, c_{11}, reaches a maximum of 14.5GPa at the end of the compaction experiment. C_{13} has a lower value than c_{33}, and increases with compaction, although in a less pronounced fashion than the other coefficients.

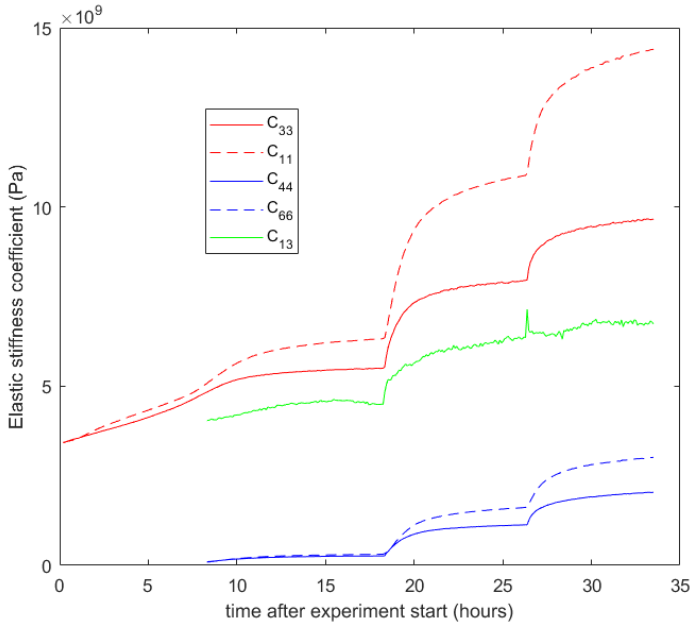

Figure 3-58: Calculated stiffness coefficient Cij for the sample "Marine 2" as a function of compaction time. The colour code of the curves is the same than in Figure 3-56, with the Cij having the same colour as the velocities that were used to compute them.

Using the five independent stiffness coefficients we compute Thomsen's anisotropy parameters: The P-wave anisotropy coefficient ε, the S-wave anisotropy coefficient γ and δ, the parameter governing the anellipticity of the P-wave front (see Figure 3-59). In this particular sample (Marine 2) ε and γ are very close to each other, which is not always the case in the other samples tested. Overall, a wide range of relative magnitudes of ε and γ was observed. What is common to all samples however is (i) an initial value of ε and γ close to zero, reflecting the isotropic nature of the mineral-water mixture at the initiation of the compaction experiment; and (ii) a negative initial value for δ. All three parameters then increase throughout the experiment, and δ always displays the lowest value.

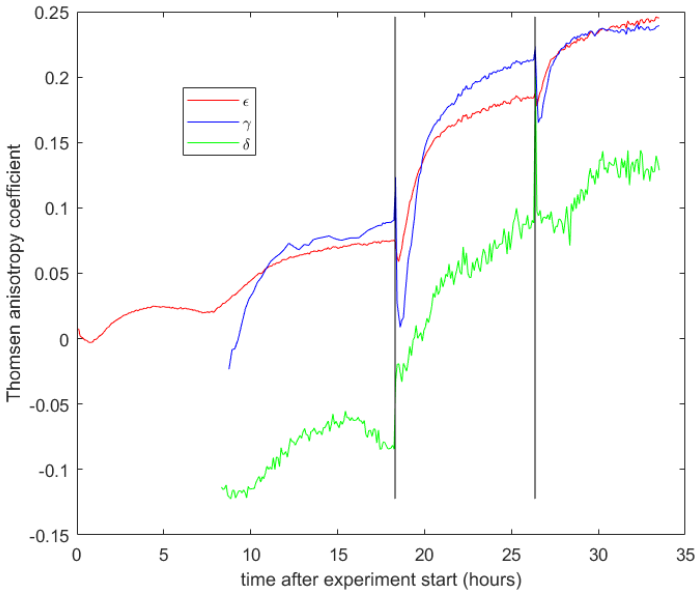

Figure 3-59: Calculated Thomsen's anisotropy coefficient during compaction for the sample "Marine 2". The variability of δ is greater than that of ε and β due to a higher sensitivity to variations in experimental data. At the beginning of steps 2 and 3, ε and β decrease temporarily due to pore pressure effects (cf. text) but this effect id not observed on δ.

Note the unexpected decrease of the anisotropy parameters ε and γ at the beginning of the compaction steps 2 and 3 (visible in Figure 3-59). They are not spurious peak values since they are composed of about 10 consecutive data points. They are rather attributed to the expected transient increase in the pore pressure within the sample at the initiation of the vertical loading. After a step increase in the applied uniaxial stress, this transient increase in pore pressure progressively dissipate at the top and bottom of the sample, near the porous plates where excess pore fluid is allowed to flow out. The main driver of the velocity increase is the consolidation of the mineral matrix, which occurs first at the top and bottom ends of the sample. Meanwhile, the horizontal P-wave and S-wave velocities are not affected by the stress increase immediately. The vertical velocities thus increase more rapidly than the horizontal ones in the early stages after the application of the vertical stress increase, and consequently the anisotropy parameters decrease. Once consolidation occurs in the centre of the sample, horizontal velocities also increase, and the anisotropy parameters increase back to a normal increase trend (cf. Section 5-5- for more information on pore pressure effects).

Figure 3-60 and Figure 3-61 show the evolution during compaction of Young's moduli and Poisson's ratios of the "Marine 2" sample computed from the stiffness coefficients c_{ij} (see chapter section 3-4-3- for details). The first value of these coefficient appears approximately 8h after the start of the compaction experiment because they both require measurement of S-wave velocity (the S-phase arrival is not detectable in the recorded waveforms before that time).

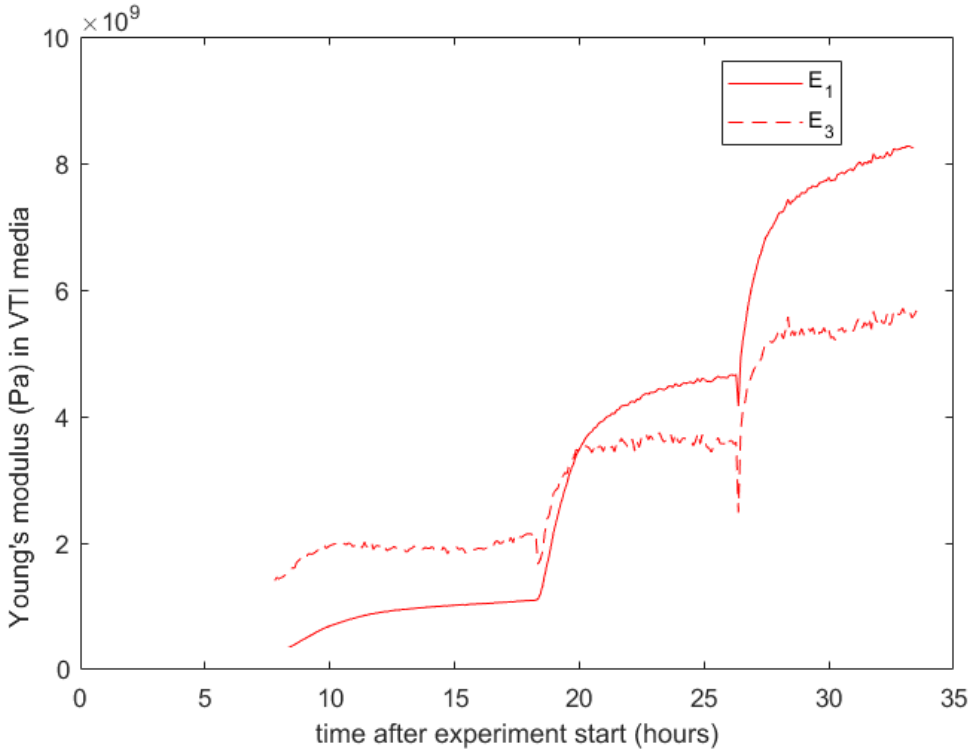

Figure 3-60: Evolution of Young's modulus during the compaction of sample "Marine 2". In VTI media, Young's modulus has two separate values: one along the main axis (E1) and one in the symmetry plane (E3).

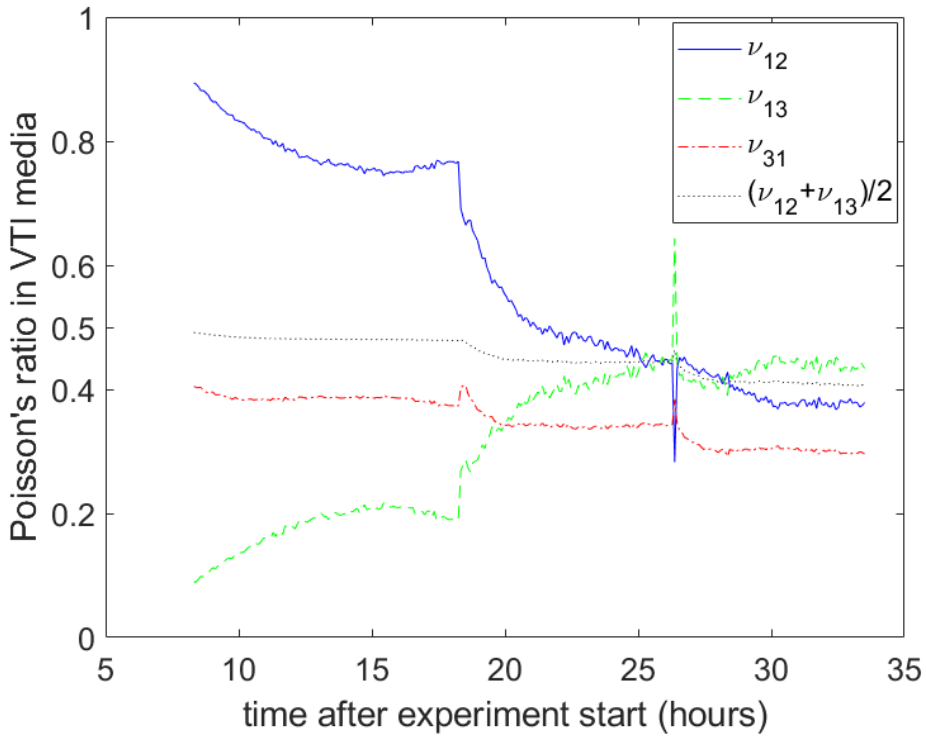

Figure 3-61; Evolution of Poisson's ratios during the compaction of sample "Marine 2". In VTI media, Poisson's ratio has three separate values: v_{31}, isotropy plane strain in reaction to a strain in the symmetry axis direction and v_{13} and v_{12}, strains in the isotropy plane and along the symmetry axis, respectively, in reaction to a strain in the isotropy plane.).

To avoid confusion here is a schematic of the cube sample in *Figure 3-62*, showing the reference frame (X1, X2, X3), where X3 is the vertical direction, the orientation of the layering along the symmetry plane, and the symmetry axis.

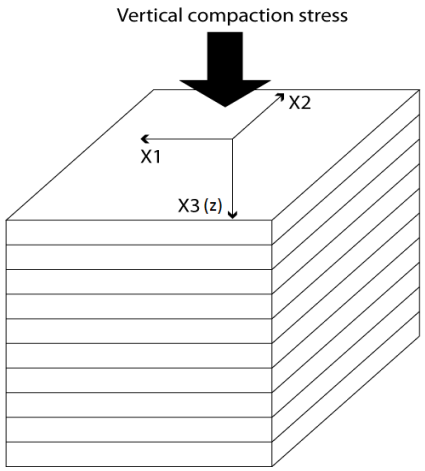

Figure 3-62: Cube representation indicating the Cartesian reference frame and its relative orientation with regard to the compaction direction.

Young's moduli (Figure 3-60) start at a low value after 8 hours of compaction. In fact, they should theoretically be equal to zero in a liquid if measurement could be performed at the very beginning at the experiment when the sample is effectively a liquid slurry (mixture of minerals and water before compaction). They then increase throughout the compaction and the consolidated parts of the curve (steps 2 and 3) feature a lower vertical Young's modulus E_3 than the horizontal Young's modulus E_1. This is expected as E_1 is a measure of the stiffness along the direction of compaction.

The Poisson's ratio values are presented in Figure 3-61. The vertical Poisson's ratio ν_{31} is a measure of the expansion within the horizontal isotropy plane in response to a vertical compression. The first value, at t = 8h, is slightly below 0.5 and decreases to reach a value of 0.32 at the end of the compaction experiment for the sample Marine 2. An initial value of 0.5 is consistent with the fact that the mineral-water mixture is in a liquid state at the initiation of the compaction. This Poisson's ratio decreases as the material develops a shear stiffness during compaction.

The results obtained on ν_{12} and ν_{13} are more complex to decipher. They are both a measure of the transverse expansion of the material for a compression along the plane of isotropy, i.e., ν_{12} measures the transverse expansion within in the plane of isotropy, whereas ν_{13} measures the expansion along the symmetry axis. At t = 8h, the expansion in the plane of isotropy is much higher than the vertical expansion (0.89 against 0.09). But the average of the two is slightly below 0.5 indicating that the strain distribution within the sample correspond to a poorly consolidated material. At the end of the compaction, these two ratios converge toward a similar value and the average decreases, indicating once again the progressive consolidation of the sample.

The relative values of the anisotropy parameters ε, γ and δ will now be discussed, for the various samples in the final set 3.

For comparison purposes, the anisotropy values of each sample was taken around the end of each phase at the time t_{90} when 90% of the pore pressure induced by the uniaxial stress increase was dissipated. This t_{90} was determined using the inflexion method for step 1 and 2 and was arbitrarily selected at t = 7 hours for step 3 as the pore pressure did not decrease enough by the end of the phase to allow a numerical determination of t_{90}.

Hence 3 data points (one per compaction step) were extracted for each sample using this method and were plotted against each other. The results were divided into the three areas of interest. i) Influence of maturity in Figure 3-63. ii) Influence of organic particles size and aspect ratio in Figure 3-64. iii) Influence of the deposition method in Figure 3-65.

All anisotropy parameters increase with compaction due to the reorganisation of the clay and OM particles. For all samples, the greatest increase in ε and γ occurs between step 1 and step 2. This suggests that most of the particle reorientation occurs at the beginning of the mechanical compaction when most of the water is expelled and slows down later on. This is not the case for δ for which a strong increase is systematically observed between phases 2 and 3. However, the error on the measurement of δ is higher than that of ε and γ. This might prevent us from seeing the same trend in δ.

Moreover, overall anisotropy values in step 1 are smaller than in step 2 and 3, and the ordering seem less organised. It is attributed to the low values of the parameters that leaves more room for random noise and measurement error.

The maturity has a very clear impact on ε. The mature samples display a higher ε than the fresh samples. The gap between fresh and mature also increases from phase 1 to step3. This effect is stronger in marine samples than in land samples. On the other hand, the variability of the two other anisotropy parameters δ and γ doesn't seem to be explained by the samples maturity.

It is rather the opposite for the OM texture. It doesn't affect ε but it has a significant influence on γ and δ. The values of ε are very similar between flake and powder samples within each OM type (land or marine). But the flake samples have a higher γ and δ than the powder samples in phases 2 and 3.

The effect of the deposition method on the anisotropy can be seen in all of the three anisotropy parameters. Samples deposited by the sedimentation method have a lower ε and a lower δ but a higher γ both for the inorganic control and the organic (land) samples.

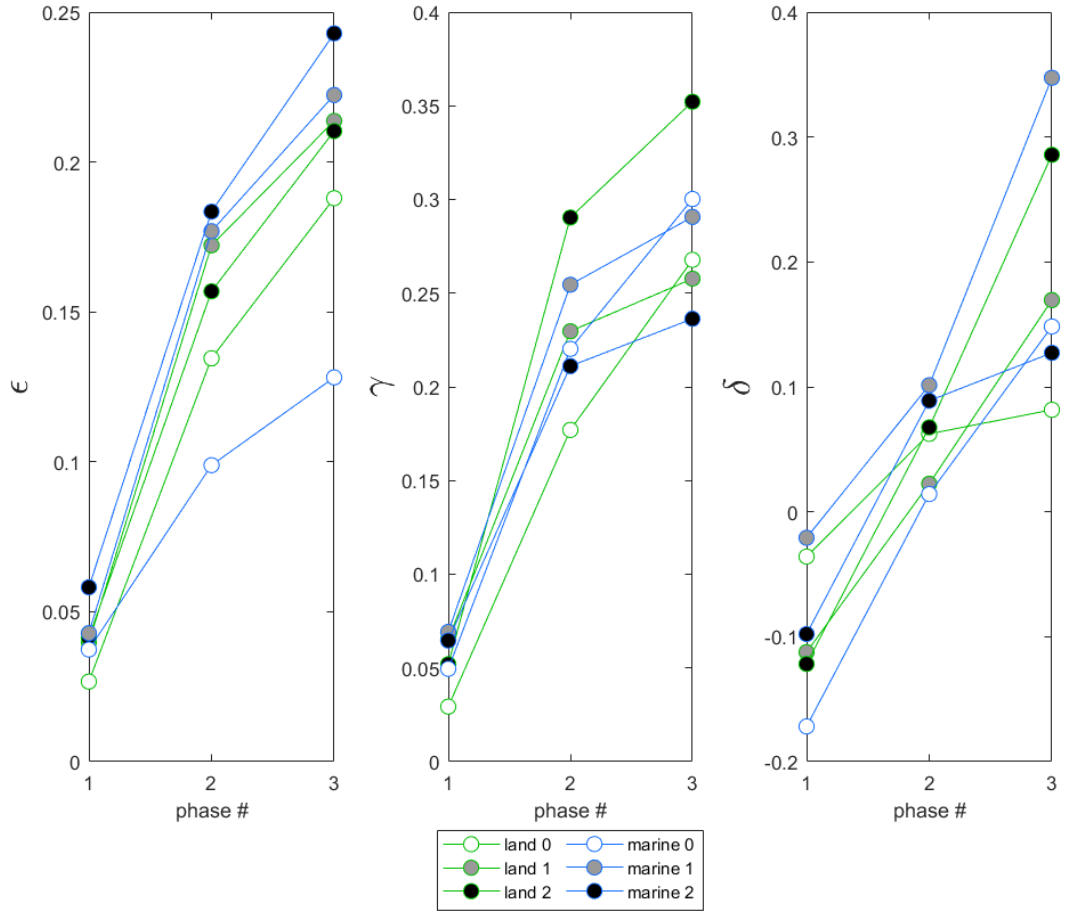

Figure 3-63: Thomsen's anisotropy parameters for synthetic samples containing either land or marine organic matter with three different maturity levels. Level 0 denotes fresh organic matter whereas levels 1 and 2 correspond to 3 weeks and 6 weeks of maturation in a hydrous pyrolysis apparatus (more details on maturation in chapter 3 section 2).

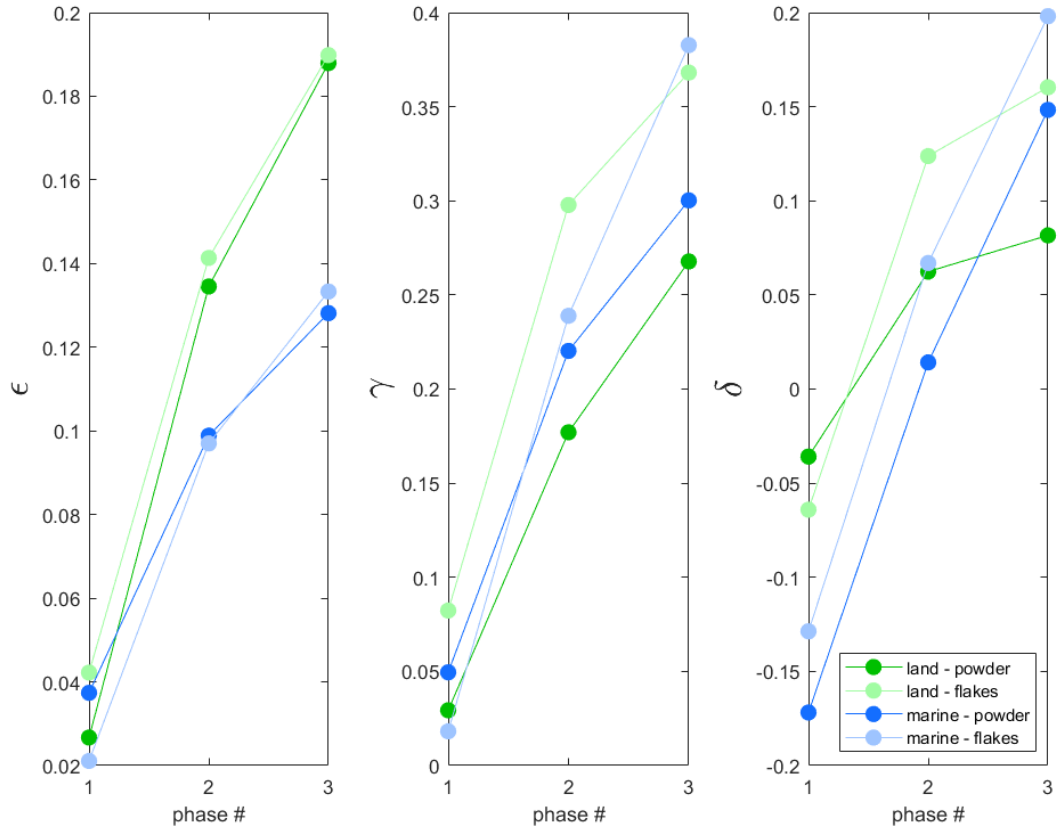

Figure 3-64: Thomsen's anisotropy parameters of sample containing either land or marine organic matter with two types of particle shape: powder with small and rounder particles and flakes with big and high aspect ratio particles.

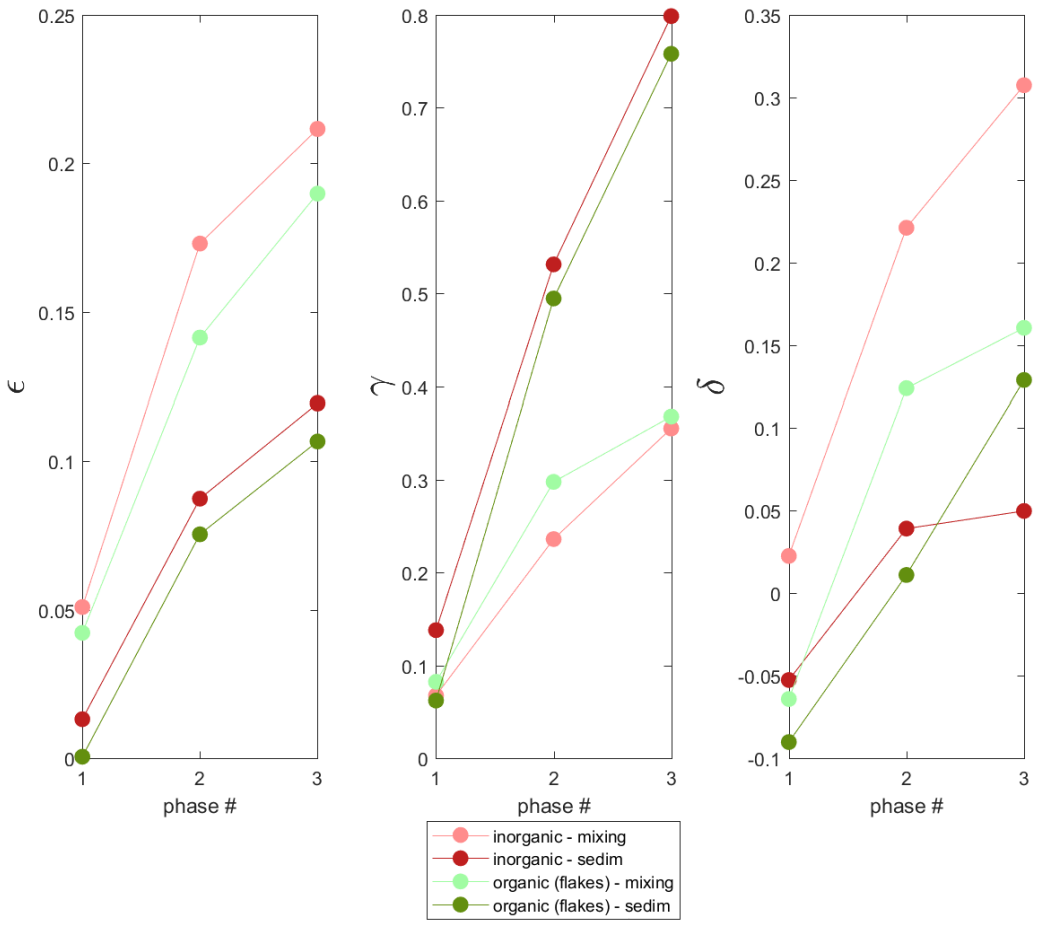

Figure 3-65: Thomsen's anisotropy parameters of samples deposited into the compaction cell with two different deposition methods: mixing and sedimentation. Both inorganic and organic (fresh land flakes) samples were tested.

3-5- Summary of chapter 3

In this chapter, all the aspects leading to the production of the artificial samples and the experimental data obtained resulting from the samples production were presented.

Firstly the sample preparation process and the choice made for the composition and compaction parameters of the different samples were detailed. The design of the samples was made so that the inorganic composition, the initial solid volume, the pore fluid salinity, the uniaxial stress and compaction time remain identical for all samples. Each compaction experiment was composed of three steps of constant uniaxial stress applied to a compacting sample. The transition between steps was a rapid increase in stress. The step 1 is a stress of 1MPa over 18h, the steps 2 and 3 are a stress of 7 and 14MPa, both over 7h. Four different target variables linked to different characteristics of OM were chosen and constitute the only source of variability in our sample set:

- OM type: OM with two different origins. Land OM represented by sphagnum peat moss that is a precursor of gas prone kerogen type III and marine OM represented by Algal phytoplankton that is a precursor of oil prone kerogen type II.
- Maturity: Three different levels of maturity for each OM type in separate samples. The maturity level 0 corresponds to fresh OM incorporated directly in the artificial shale samples. The maturity level 2 and 3 were achieved by maturing the fresh OM an in-house designed confined hydrous pyrolysis apparatus. The OM was matured on its own and incorporated in the artificial samples thereafter.
- OM texture: Two different types of texture were investigated. The powder and flake texture type. The former is composed of small sized (smaller than 100µm) and with a smaller aspect ratio. The latter is composed of bigger particles (up to 2300µm) with a bigger aspect ratio (cf. CT-scan imaging results Section 4-1-3- and Optical microscopy results section 4-3-3- for more details on aspect ratios).
- Deposition method: To investigate the effect of deposition versus compaction on the development of anisotropy identical samples were prepared, with two different deposition method. One is the standard mixing method where all the components are randomly oriented at the beginning of the compaction. The

other is a sedimentation method whose objective is to reproduce more realistically the deposition process of natural shales where the solid phase is placed in a large amount of water (95% of water in volume) and allowed to settle by gravity in the compaction cell.

The design of the hydrous pyrolysis apparatus was then presented and the different choices made to attempt to reproduce the maturation of OM in a shale sediment were detailed. The OM is put in the presence of water and swelling clay while being in a confined environment to avoid interactions with oxygen. The maturation temperature was maintained at a constant 200^0 C for 3 or 6 weeks to obtain the maturity level 1 and 2.

Thereafter a thorough description of the compaction cell designed for the purpose of this project was presented from the design stage to the experimental procedure, the data processing and the error analysis of the different sensors. This compaction apparatus allows to produce synthetic samples from a brine and mineral mix with a large final volume (~600cm^3) so that several portions of the sample can be extracted for subsequent destructive tests. The cell is equipped with different measuring tools from which we can record the porosity, bulk density, compressive uniaxial stress, expelled mass of pore fluid and elastic properties of the sample continuously during the compaction.

Finally the data delivered during the compaction of the artificial samples was presented. To compare the samples with each other, we computed from the LVDT height reading, for each compaction step the time at which 90% of the pore pressure due to the increase in stress has dissipated following the Taylor method and the inflexion point method.

The main observation were:

- The samples containing marine OM display much lower porosity after compaction than land or inorganic samples and a higher bulk density.
- The maturity of the samples did not have an effect on the porosity decrease in step 1, when the samples are poorly consolidated, but had an effect in steps 2 and 3. Namely the mature samples porosity decreased more in steps 2 and 3 than the fresh sample whereas on the contrary the porosity of mature land samples decreased less than the fresh land sample.

- The inorganic and land samples prepared with the deposition method displayed more difference in their porosity decrease throughout step 1 to 3 than their identical counterparts prepared with the mixing method.
- The samples containing OM with the flake texture type saw their porosity consistently decrease slightly less than the same samples made with powdered OM.
- The elastic rebound that induces an increase in volume of the sample at the end of the compaction when the stress is released is of the same order of magnitude than the solid volume change computed from the difference between the expelled pore fluid and the volume decrease recorded by the LVDT.
- The computation of the Young's modulus and Poisson's ratio in VTI media from the ultrasonic data display values that are physically expected in samples starting in an unconsolidated liquid state to a consolidated sediment. This shows the validity of the ultrasonic measurement, velocity computation and off-axis data processing.
- The group angle of the off-axis P-wave velocity measurement was found to increase during the compaction. This change is expected because at the beginning of the experiment the difference in ultrasonic velocity between the transducer casing and the sample is important so the incident angle of the ray path is greatly diffracted at the casing/sample interface whereas when the sample is more consolidated the difference in velocity is smaller and the diffracted ray path has a greater angle with regard to the vertical direction. On the other hand the recalculated phase angle was unexpectedly found to slightly decrease during the compaction. This is surprising as the phase angle was expected to increase similarly to the group angle.
- The anisotropy values computed at the end of step 1 seem to be ranked quite randomly with regard to the target variables but the anisotropy values in compaction steps 2 and 3 show correlations between anisotropy parameters and target variables.
- The maturity of the samples has a strong impact on the P-wave anisotropy parameter ε with mature sample displaying significantly higher values in compaction step 2 and 3.

- The samples containing OM of the flake texture type have a higher S-wave anisotropy parameter γ and a higher anisotropy parameter of anellipticity δ in steps 2 and 3.
- Samples deposited by sedimentation method have both a lower ε and δ but a higher γ than the samples deposited with the mixing method.

In the next chapter the tests performed on the artificial shale samples after compaction will be presented. The data obtained by these tests are complementary to the results acquired during the compaction experiments and will help quantify the difference in OM characteristics between samples.

Chapter 4: Further characterization of the compacted samples

4-1- CT-scan imaging

Immediately after being unmoulded from the compaction cell, the artificial shales were wrapped with cling film to limit their dehydration and imaged in a medical X-ray CT-scanner SOMATOM® Definition AS 64 slices from Siemens. The bulk density was computed from the XCT images along the "final" samples in different directions before evaporation of the water in the pores, especially closer to the sample edges more prone to atmosphere exposure and so dehydration. The purpose of the data obtained with the CT-scanner are manifold:

- Quality-check the bulk density measured from XCT and previous methods (bulk density from LVDT measurement, and from the final sample weight and volume).
- Evaluate the homogeneity of the sample from the density profile variability along the sample.
- Confirm that all major air pockets were effectively removed during the sample preparation.
- Observe the distribution and orientation of particles in the two samples containing macro-particles bigger than the CT-scanner spatial sensitivity of 400 μm (i.e. samples with OM flake particles, as explained in Section 3-1-).

In this section first the principles of X-ray computed tomography and the nature of the acquired data are presented succinctly, then the data processing is explained, to fulfil the aforementioned objectives and finally the results are presented.

4-1-1- Computed tomography (CT) basic principles

X-rays are a form of electromagnetic radiation with a wavelength much smaller than visible light (0.01 to 10nm). On the lower end of this wavelength range are hard X-rays. This type of X-ray have the property of being able to pass through relatively thick objects without much absorption or scattering by the solid material. The energy of X-ray radiation is attenuated when passing through a solid material. This attenuation is directly related to the density of the material and its thickness.

During CT imaging, an X-ray source sends a beam of X-ray into the sample to be imaged. A digital X-ray detector on the other side picks up the exiting X-rays and sends the signal to a computer. The X-ray source rotates around the sample and sends

narrow X-ray beams continuously. Once a 360^0 rotation is completed the computer can reconstruct a 2D radiodensity image that is a slice of the sample in the plane of rotation of the X-ray source. This process is repeated while the sample moves steadily in the direction perpendicular to the rotation plane to create 2D images at regular intervals throughout the sample.

The thickness of a single slice (600 µm) and the spacing between slices depends on the equipment and its settings. In this sample set, some samples had an image sequence with a slice spacing of 400µm (short sequences) and others a slice spacing of 100µm (long sequences), thanks to overlapping method to allow such resolution despite thicker single slice. The voxel resolution reached in the x-y transversal plane was ~ 200µm x 200µm. This means the images are composed of 200µm x 200 µm pixels where the radiodensity value is averaged on a 100µm or 400 µm thickness depending on the choice of sequence.

The radiodensity is expressed in Hounsfield units (HU). The CT-scanner has a resolution of 15 HU. The Hounsfield Unit is also called CT number and is directly correlated to density. The CT-number in a voxel is related to the attenuation coefficient µ of the material as follow:

$$HU = 1000\frac{\mu - \mu_{water}}{\mu_{water} - \mu_{air}} \approx 1000\frac{\mu - \mu_{water}}{\mu_{water}} \quad (65)$$

Where μ_{water} is the attenuation coefficient of water and μ_{air} is the attenuation coefficient of air and is nearly 0. Hence the CT number of water is 0 and the radiodensities of materials are scaled against that of water. Note that air will have a CT number of -1000.

The CT-number can be converted to a density (ρ in g/cm^3) via a linear relationship between the CT-number and the physical density for our range in CT number values (Massicano, et al., 2009):

$$\rho = \lambda_1 \times HU + \lambda_2 \quad (66)$$

The factors λ_1 and λ_2 are determined by calibration of the CT-scanner with standard crystals of known density with the CT-scanner in the same settings than for the imaging of the samples.

The oval-like shape samples coming from the compaction cell have dimensions of 202x49x65mm approximately (height variable between samples). They were CT-

scanned along their long axis which resulted in CT-images with dimensions of 49x55mm. The short sequences contained about 500 images and the long sequences about 2100 images.

4-1-2- Data processing

Before further processing, the images were cropped so that the limits of the images lie within the edges of the sample. The first and last images of each sequence corresponding to the two semi-circular ends of the sample were also removed to have images with a constant area. They also underwent smoothing and noise reduction processed using ImageJ image analysis software. The data processing presented in the paragraphs below were performed with Matlab R2018a.

4-1-2-1- Density

For each sample, a global average density was computed across the whole XCT image sequence to check its consistency with the bulk density calculations from other methods as well as the quality of the calibration factors λ_i in equation (66).

Thereafter, the image sequence of each sample was subdivided to measure the density in different regions. Namely the density was computed in 4 different directions to check the sample density homogeneity (Figure 4-1).

- X axis: The average density of each image was computed to monitor the density on the longitudinal direction of the sample.
- Y axis: Each image was divided into 100 vertical bands, and the average density over the whole image sequence was computed for each band.
- Z axis: Each image was divided into 100 horizontal bands, and the average density over the whole image sequence was computed for each band.
- Centre to edge: Each image was divided into 50 concentric rings of rectangular shape and the average density over the whole image sequence was computed for each ring to monitor the radial density.

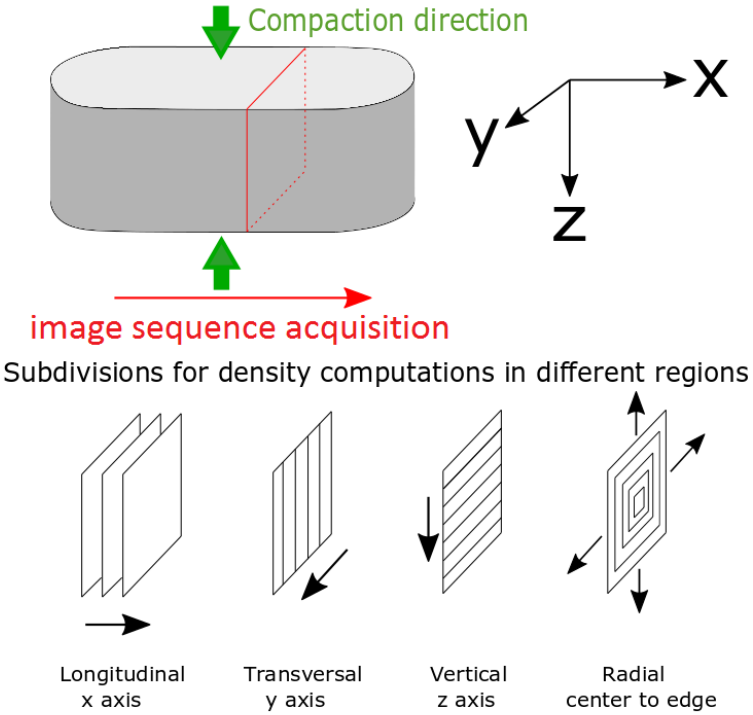

Figure 4-1: Schematic representation of the subdivisions of the image sequence of a sample to monitor the evolution of the density along 4 directions: Longitudinal, Transversal, Vertical and Radial.

4-1-2-2- Particle analysis

Three samples in set 3 contain OM particles large enough to be above the resolution of the CT-scanner (200µm). The OM particles have a lower density than the inorganic matrix and the CT images are thus a very good tool to differentiate the organic phase from the inorganic phase. For these samples a threshold was applied on each CT-scan images to isolate only the low density OM from the minerals. The equivalent density from the CT number of the thresholded OM corresponds to 1.7g/cm^3 for the land OM samples and higher for the marine OM sample with 1.9g/cm^3.

The OM particle size was then investigated by a binarization of the thresholded OM image (Figure 4-2) such that all pixels containing OM take the value 1 while the rest of the images have the value 0. The area of each OM particle was computed to obtain a particle size distribution in the samples. Similarly to the density data processing, each image was divided into 100 horizontal bands to monitor the particle distribution along the vertical direction (direction of compaction). The particles smaller than 0.2mm^2 were ignored due to the CT image resolution. The particles smaller than

0.2mm^2 are affected by the uncertainty of the measurement and the random noise acquired during the image reconstruction process. Their measured size would hence be inaccurate.

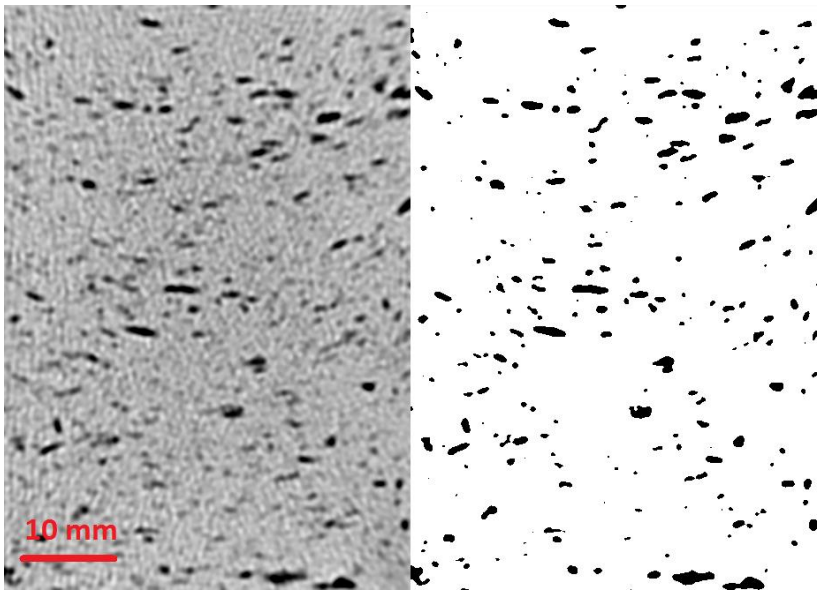

Figure 4-2: Left - CT image of the sample "land 0 sedim" containing OM macro-particles. Right - Same image binarized to isolate the OM particles.

For the rest of the processing the particles smaller than 0.4 mm^2 were removed because their shapes and edges are poorly defined. An ellipse was then fitted to each particle to quantify their aspect ratios. Finally the orientation of the ellipses was used to compute the particle orientation histogram. The particles with an aspect ratio (long axis to short axis ratio from the ellipse) smaller to 1.2 were ignored as the orientation of nearly circular objects would not bring information on the overall orientation distribution.

It is worth noting that the processing was done on each XCT 2D image. The particle analysis may then not be fully representative of the three dimensional distribution of the samples. For instance, a particle oriented perpendicular to the image plane will present a strong error on the measured aspect ratio and orientation towards the vertical. However all three samples were processed the same way so the results have a good prospect for comparison purposes and they still fulfil the main objective of the images which is to highlight the differences between the horizontal and vertical direction.

4-1-3- Results

4-1-3-1- Average density

The average radiodensity over the whole image sequence was converted to a physical density with the factors λ_1 and λ_2 for every sample and the final result is visible in Figure 4-3 with a plot of the CT densities (y axis) against the bulk density from weight and volume measurements (x axis). There is an overall good agreement between the CT densities and the bulk densities. The average difference between CT and bulk density is 0.012g/cm^3. For most samples the CT density tends to slightly overestimate the density value compared to the bulk density. Two samples have a lower CT density than bulk density. 'Land 0 flakes mixing" in particular displays the biggest difference (0.027g/cm^3). The general trends where inorganic and marine samples have similar densities and land samples have a lower density are confirmed. Those results validate the accuracy of the bulk density measurement by XCT method.

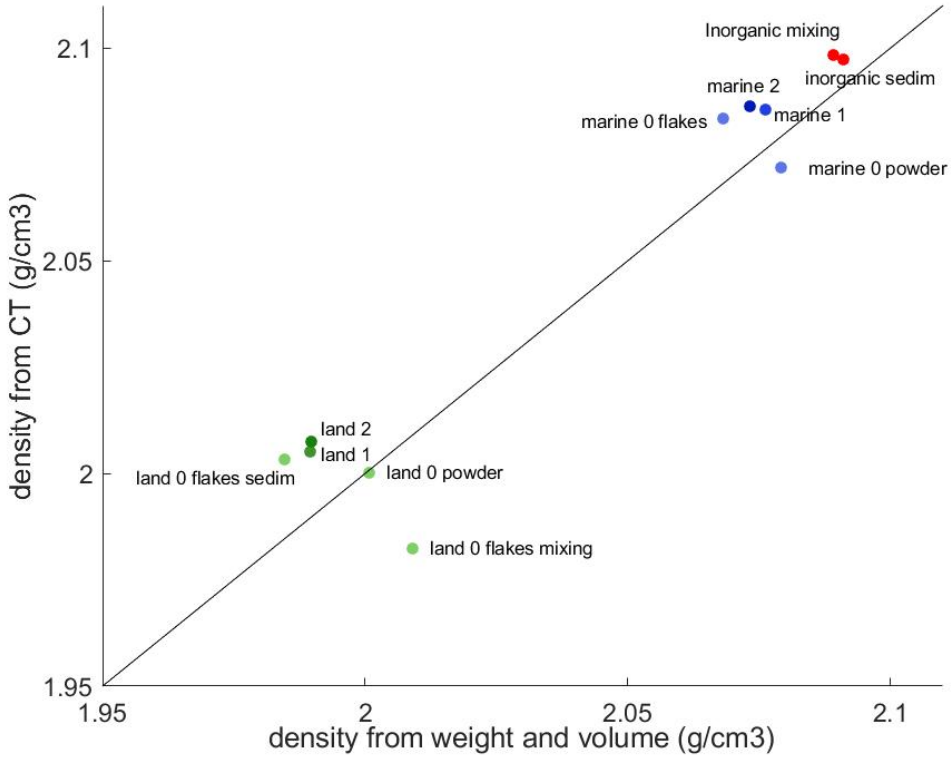

Figure 4-3: Density values computed from the average radiodensity (CT number) of the image sequence of each sample against the bulk density measured by weight and volume after the end of the compaction experiment. The black line shows where the two densities are equal (y=x).

4-1-3-2- Homogeneity of the samples

The density values along the different directions described in the data processing section 1-2-1- were analysed. Each line in Figure 4-4 shows the average density value of each CT image within each sample from the integration in the longitudinal direction (x axis in Figure 4-1). For all samples, the density remains very stable along that direction with only a slight increase around the middle of the image sequence. The samples containing land OM flakes (2 green dashed lines) display more variability though it is minimal. This is due to the variation in the amount of large OM particles from one image to the other. The images with slightly more OM bring the average density of the image down. Interestingly, this effect is less pronounced for the sample containing marine OM flakes. It would suggest a more homogeneous distribution of the particles and/or a smaller average particle size.

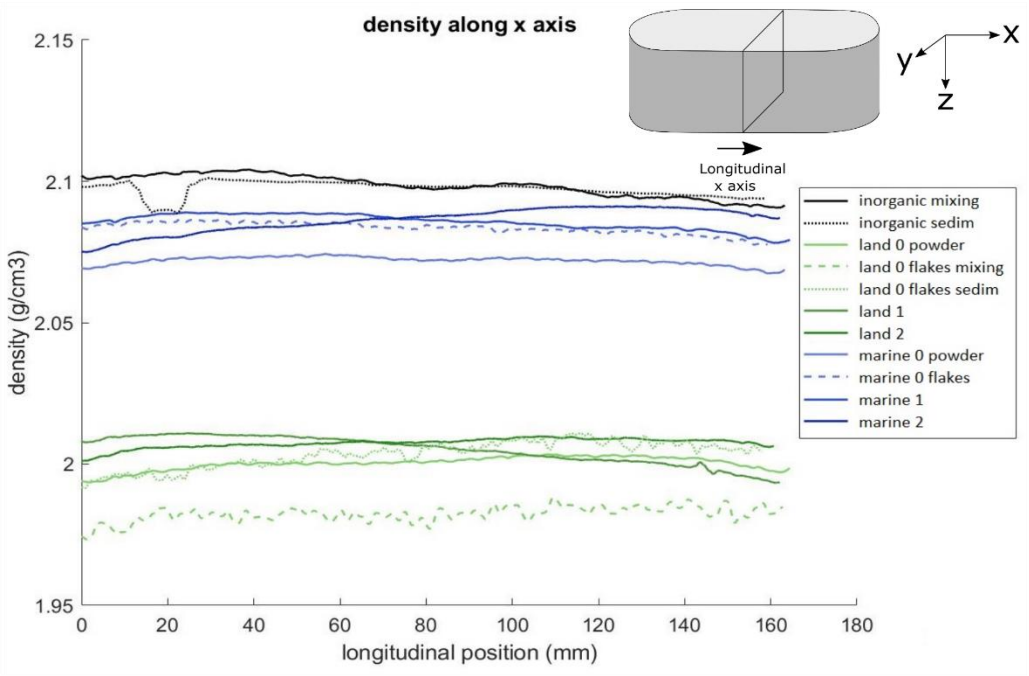

Figure 4-4: Evolution of the density along the longitudinal direction of the sample (horizontal). Each value is the average on one 2D CT image.

Figure 4-5 presents the evolution of the density in the lateral direction (y axis in Figure 4-1) of the sample, with each value being the average of a narrow vertical band within each image over the image sequence. In theory we would expect a similar density distribution in the two horizontal directions (x and y axes). Yet we see more variations along the y axis. For all samples except "inorganic sedim." where two maximums approximately 6mm from the sample edges (y = 7mm and y = 41mm) and minimums

on the edges and in the middle of the samples (y = 0mm, y = 24mm and y = 46mm) are observed. The sample "inorganic sedim." only have one minimum in the middle and maximums on the edges.

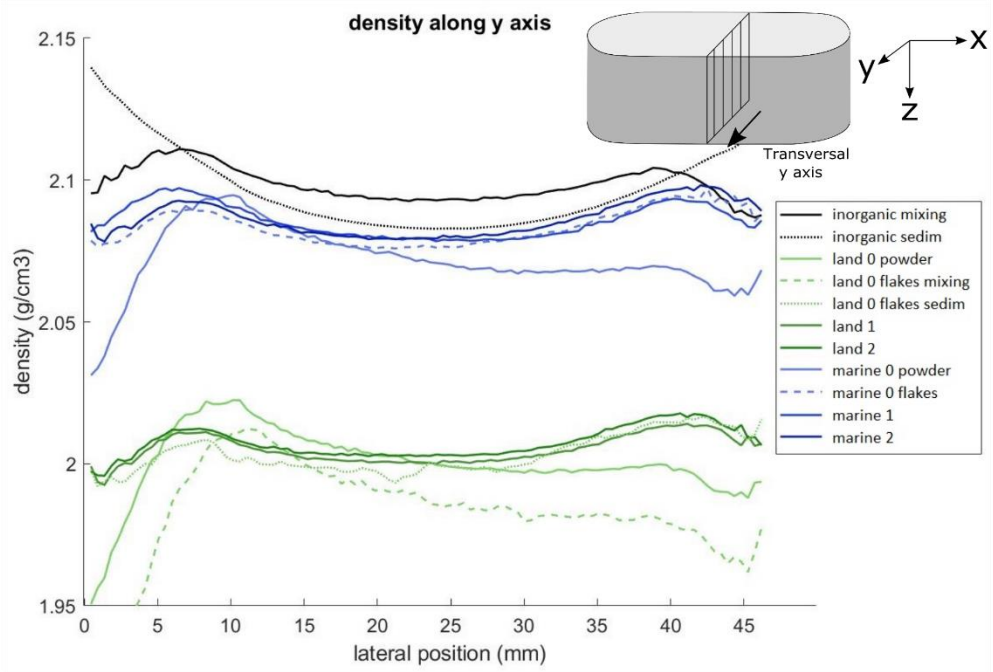

Figure 4-5: Evolution of the density along the transversal direction of the sample (horizontal). Each value is an average of a vertical band of a CT image over the whole image sequence.

Figure 4-6 presents the evolution of the density in the vertical direction of the sample (z axis), with image processing similar to the density in the transversal direction (Figure 4-5). Here all samples present a maximum on the edges (top and bottom of the sample) and a minimum in the middle of the sample.

The key difference between the x axis graph (Figure 4-4) and the y axis graph (Figure 4-5) is that each of the x axis values average an equal proportion of the edges and the centre of the sample. The values on the y axis graph average only edge density values on the extreme positions and mostly density values from the centre of the sample in the middle. The drop between the maxima and minima is more pronounced in the vertical direction than the transversal direction.

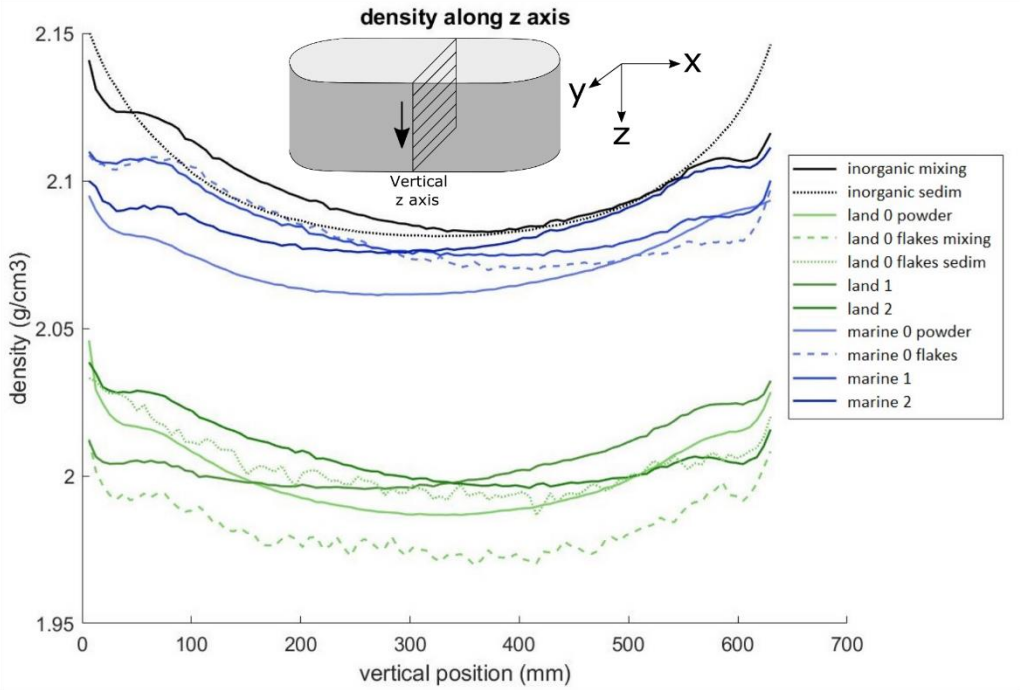

Figure 4-6 Evolution of the density along the vertical direction. Each value is the average of one horizontal band of an image over the whole image sequence. The left of the graph corresponds to the bottom of the sample and the right of the graph corresponds to the top.

Finally the Figure 4-7 shows the evolution of the density along the radial direction, with the position r = 0% corresponding to the edge and the position r=100% corresponding to the centre. Here all samples display a maximum at 20% of the edge-to-centre distance and minima on the edge and in the centre of the sample.

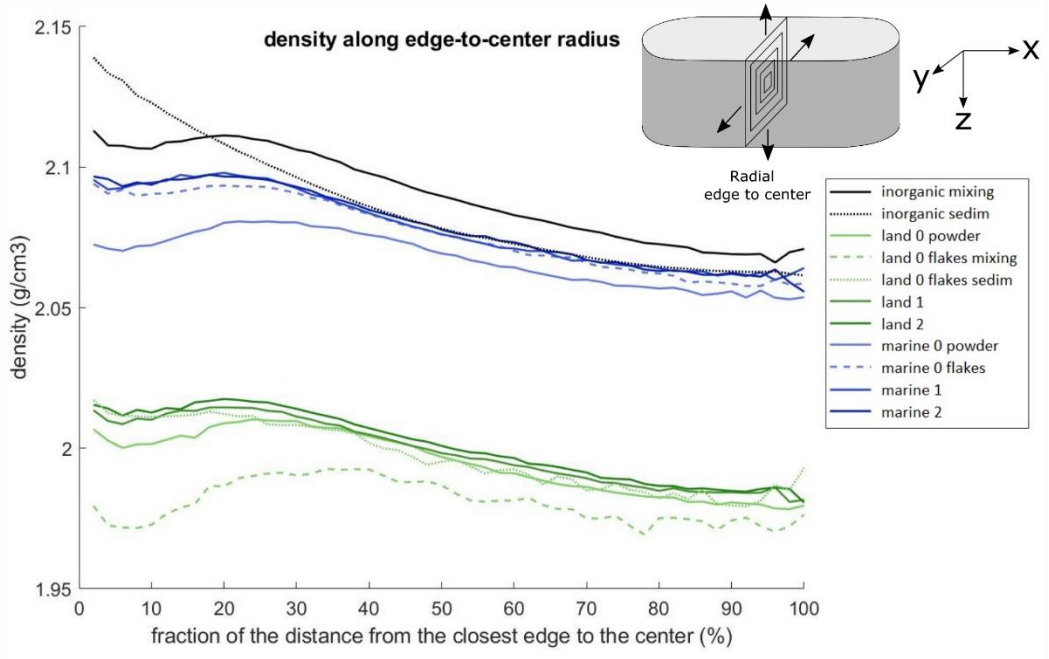

Figure 4-7: Evolution of the density over the direction from the edge to the centre of the sample. Each value is an average over a concentric ring of an image over the whole image sequence. The left of the graph corresponds to the edge and the right of the graph corresponds to the centre.

Three possible explanations were listed for the density differences observed in these graphs and under different directions inside the samples:

- (i) Desiccation of the sample between unmoulding and CT-scanning: This would decrease the density near the edges by replacement of pore water with air. This is highly unlikely because the samples were CT-scanned less than 1/2h after unmoulding and with the tight and fine-grained nature of the mineral matrix of a final sample, the water evaporation could not occur more than 1mm into the sample.
- (ii) Uneven pore pressure state in the final sample: The pore fluid in the samples is drained through the porous plates present at the top and bottom of the sample in the cell during the compaction. When the compaction stress increases, the pore pressure starts to decrease at the top and bottom of the sample and the solid matrix consolidation occurs in these regions first. A complete equilibration of the pore pressure in the sample would take a very long time due to the low hydraulic conductivity of the fine grained matrix. This is why by the end of the experiment, when most of the pore pressure has

dissipated, we can still notice that the density near the top and bottom ends of the samples is slightly higher, meaning these regions contain a little less water and have a solid matrix slightly more consolidated.

- (iii) Error in the reconstruction process of the 2D images: The reconstruction algorithm that is used to turn the X-ray attenuation data into images is optimised to reconstruct objects with rounded edges (human body, cylindrical core samples, etc.). But the images of our samples are rectangular in shape and present artefacts. We believe these artefacts materialise in bands of higher density running along the straight edges and a lower density near the corners of the rectangle.

The CT image in Figure 4-8 shows a single image taken from the image sequence of the sample "Inorganic mixing". The white part indicate a higher density than the grey parts. The image contrast was greatly enhanced to "exaggerate" small density variations and the random noise is thus more visible. The difference in density due to pore pressure effects is clearly visible at the top and bottom of the sample and the artefacts are distinguishable at the corners and on a band on the inside of the sample. This helps to interpret the behaviours observed in the density curves (Figure 4-4 to Figure 4-7). The two local maxima on the y-axis transverse direction (Figure 4-5) are due to the artefact. If we ignore these two bumps, the overall curve shape would be much more similar to the curves in the longitudinal direction (Figure 4-4). The artefacts bumps are also visible in the vertical direction (Figure 4-6) but are blended into the density increase at the top and bottom of the sample due to a better consolidation. The same effect is also seen in the radial direction where the artefact bump is located at 20% of the edge-to-centre distance.

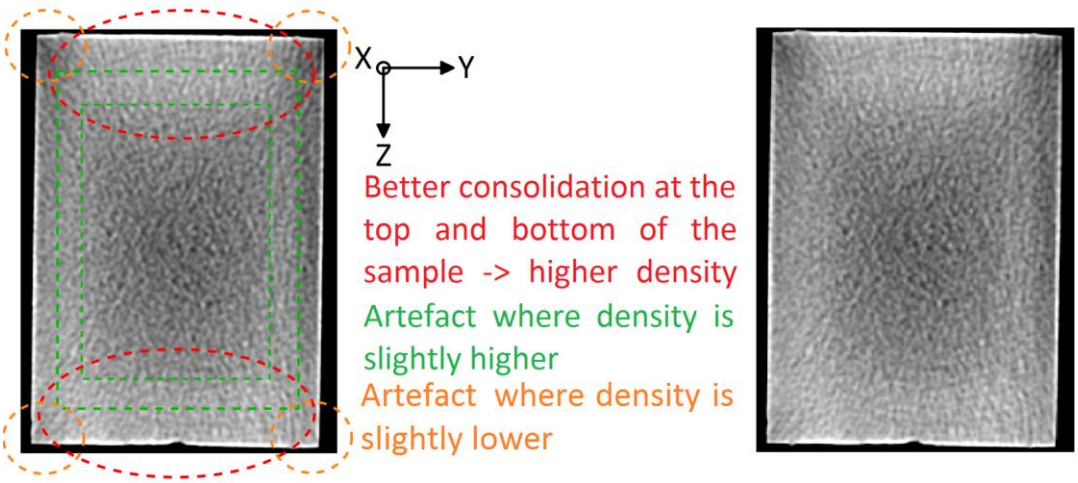

Figure 4-8: CT image from the image sequence of sample "Inorganic mixing". The contrast was enhanced to highlight the small density differences. The red ellipses indicates the zones with lower pore pressure and higher density. The green ring and the orange circles indicate the approximate location of the reconstruction artefacts. On the right-hand side is the same image without annotations.

All in all the density distribution shows a vertical inhomogeneity due to pore pressure effects. The difference between the maximum density (top and bottom of the sample) and the minimum density (centre of the sample) is on the order of 0.04g/cm^3 for all samples. The variations in other directions can be attributed to reconstruction artefacts in the CT images.

4-1-3-3- OM macro-particles analysis

The final set of data extracted from the CT images is the analysis of the OM particles big enough to be above the resolution threshold of the CT-scanner. This involves the three samples containing OM macro-particles in the form of flakes (cf. sample preparation in Section 3-1-).

The Table 4-1 summarizes the results of this particle analysis. One of the sample was made with marine OM particles following the mixing method. Two samples were made with land OM: one following the mixing method and one following the sedimentation method (cf. sample preparation in Section 3-1-).

The number of particles for the two land samples is very similar whereas the marine sample has far fewer particles. The particles coverage represents the percentage of the CT images area covered by the particles. This is directly related to the volume content

of OM macro-particles. The initial volumetric content of OM was the same for all samples (8%). The macro-particle coverage for the land samples is around 4.3%. This shows that more than half of all organic particles have a size above the CT-scanner resolution and are visible on the CT-images. The marine sample on the other hand has a macro-particle coverage of less than 1%. Hence most of the marine OM particles have a size below the detection threshold of the CT-scanner.

Sample name	Land 0 Flakes mixing	Land 0 Flakes Sedim	Marine 0 Flakes Mixing
Particles >0.2mm^2	58364	59724	11317
Particles >0.4mm^2	43852	41362	6148
Particles >0.4mm^2 and AR >1.2	40823	39347	5614
Particle coverage (%)	4.54	4.16	0.78
Particle median size (mm)	0.95	0.87	0.74
Particle average size (mm)	1.09	1.01	0.89
Particle median aspect ratio (AR)	1.83	1.98	1.74
Particle average aspect ratio	1.98	2.16	1.94
Particle median orientation (^{0})	91.6	91.7	91.8
Standard deviation from median orientation (^{0})	30.3	30.4	34.9

Table 4-1: Summary of the parameters computed during the OM macro-particles analysis.

The Figure 4-9 shows the vertical distribution (z axis) of OM particles with a size greater than 0.2mm^2. The "land mixing" sample has a homogeneous distribution with low variations of the particle count over the histogram. The "land sedim." sample sees an increase in the OM particle count from bottom of the sample (position z = 0mm) to the top of the sample. This increase is particularly marked in the first 10mm. This can be explained by the buoyancy of the organic particles. At the beginning of an experiment using the sedimentation deposition method (cf. sample preparation in chapter 3 section 1) the proportion of solid is as low as 5% in volume which results in few grain contacts. The particles thus have a certain degree of freedom to reorganise by gravity. Because OM has a lower density than the mineral matrix, they tend to rise. This led to few OM particles at the base of the sample but has a limited effect above the position z = 10mm. The marine sample seems to have a more random distribution of OM macro-particles with a particle count significantly higher between 25 and

40mm. The fact that the marine sample has a fewer particle count and a much lower particle coverage shows us that this macro-particle distribution is not representative of the full particle distribution (one that would include smaller particles).

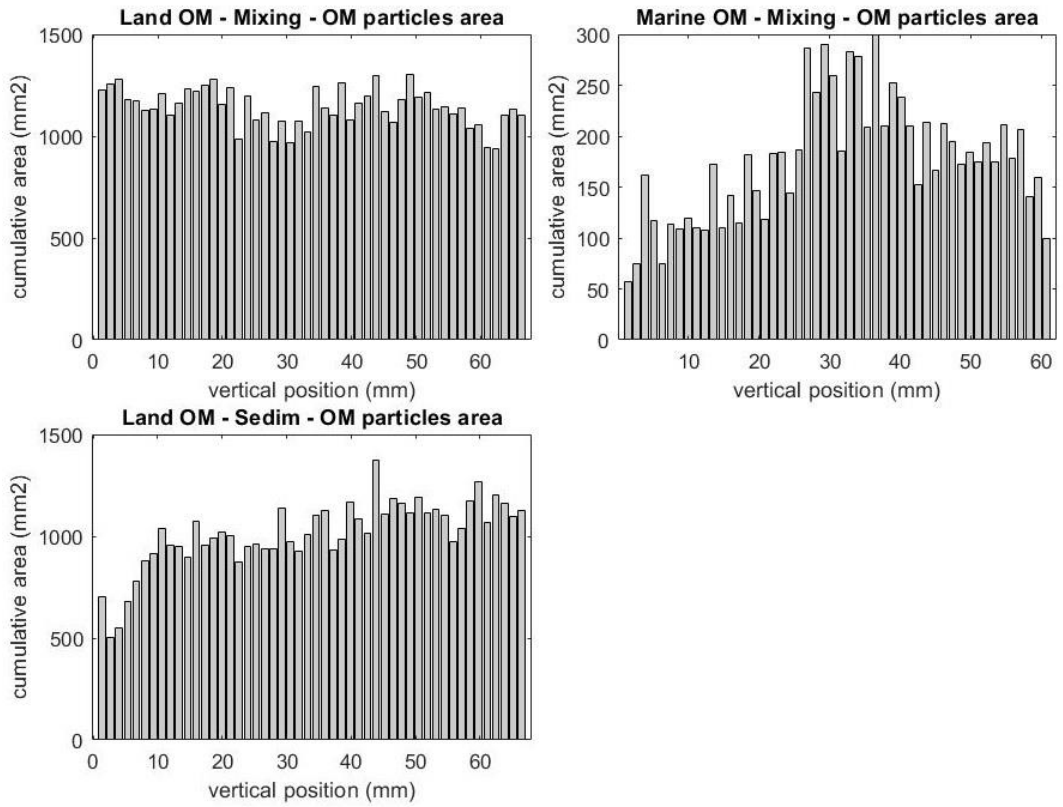

Figure 4-9: Vertical distribution of OM macro-particles with an area >0.2mm for the three "flakes" samples. The left of the histogram corresponds to the bottom of the sample and the right of the graph corresponds to the top of the sample.

The size distribution of particles with an area greater than 0.2mm^2 is visible in Figure 4-10. The median value is the highest for the "land mixing" sample (0.95mm) followed by the "land sedim" sample (0.87mm) and the "marine mixing" sample (0.74mm). The two land samples have histograms with a clear bell shape, with a maximum at approximately 1.5mm. The histograms of the marine sample has a lower maximum at 1mm and displays more particles in the lower end of the size range than the land samples.

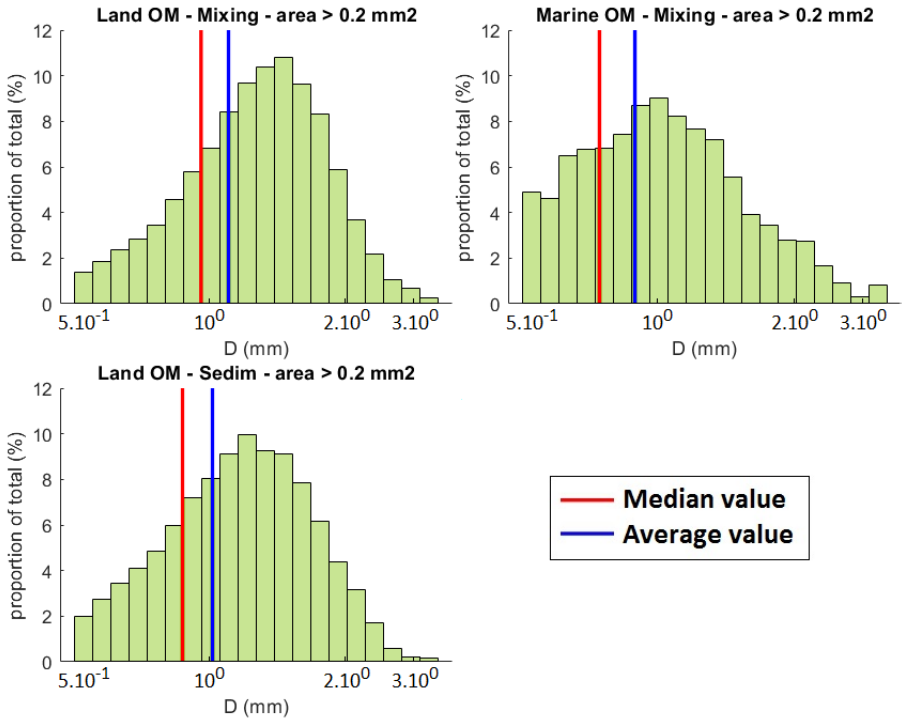

Figure 4-10: Particle size distribution of OM macro-particles with a size >0.2mm² for the three "flakes" samples.

The Figure 4-11 shows the aspect ratio of OM particles with a size greater than 0.4mm². Spherical particles (aspect ratio of 1) are a minority for all three samples and the average aspect ratio is about 2. The two "mixing" samples have similar median and average aspect ratio. In contrast the "sedim." sample presents higher aspect ratios with a median and an average both about 0.2 units higher than the "mixing" samples.

Finally the orientation of the particles bigger than 0.4mm² and with an aspect ratio above 1.2 is presented in the histograms of Figure 4-12. All three sample have an orientation distribution with a gaussian shape. The median value is around 91.7 degrees for all samples. It is believed this is slightly higher than 90^0 due to the positioning of the samples in the CT-scanner that is not perfectly aligned with the direction of compaction of the samples. The marine sample has more orientations that fall outside one standard deviation from the median because of the lower number of particles that hinder the statistical significance of the dataset. Consequently its standard deviation is the highest (34.9^0). The land samples have almost identical standard deviation values (30.2^0 against 30.3^0).

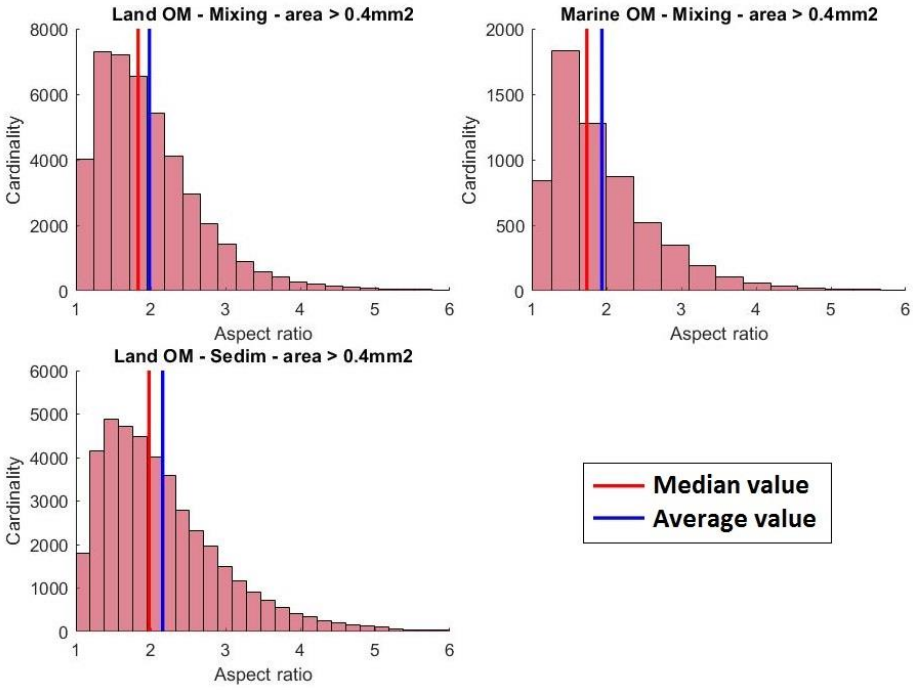

Figure 4-11: Aspect ratio distribution of the OM macro-particles with an area >0.4mm2 for the three "flakes" samples. With the CT-scanner resolution the particles smaller than this limit have poorly defined shapes.

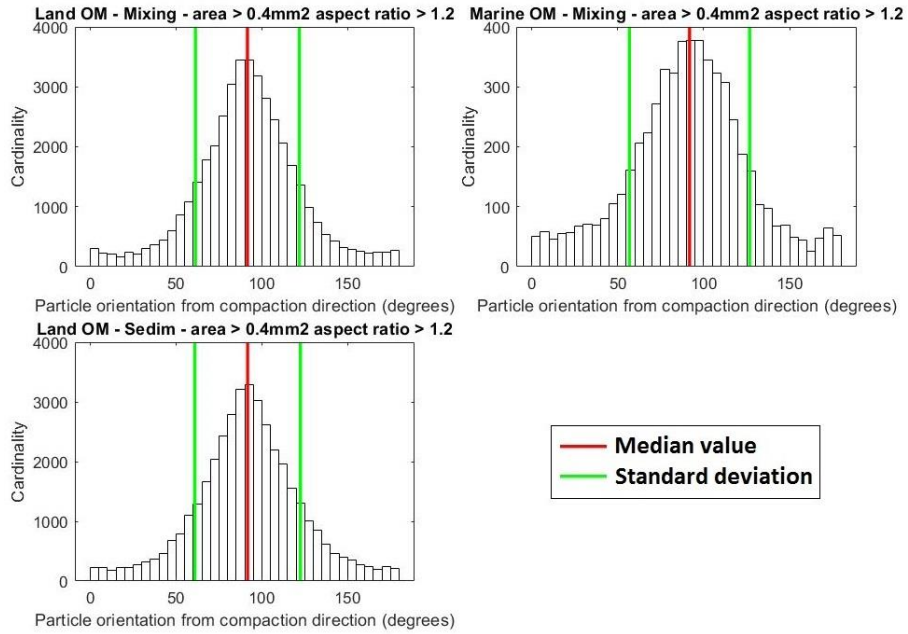

Figure 4-12: Histogram of the orientation of the OM macro-particles with an area > 0.4mm2 and an aspect ratio >1.2. The green lines are spaced with one standard deviation from either side of the median.

4-2- Dielectric measurements

The theoretical principles of dielectric phenomena are presented in the literature review section 1-4-1-. The following section details the dielectric testing device employed for this project and the preparation of the slices used for the measurements. Thereafter the dielectric results are presented.

4-2-3- Apparatus and measurement procedure

The instrument used for the dielectric measurements was developed at CSIRO (Josh, 2017). It operates by coupling the sample with two parallel plate capacitors. This type of setup is routinely used in dielectric testing (Von Hippel, 1954). It is also equipped with P-wave ultrasonic transducers to record an unconfined elastic response at the time of the dielectric measurement (Figure 4-13). The parallel plate cell is connected to an Agilent 4294A Impedance Analyser operating at frequencies from 10 kHz to 100 MHz. The P-wave transducers are connected to a Tektronix TDS 2022C oscilloscope.

Two slices about 10mm thick were extracted from each of the samples obtained after compaction and tested dielectrically. To obtain results of optimum quality, the slices preparation and measurement procedure have the following requirements:

- Preservation of the sample: The evaporation of pore water, even in small quantities, has an important impact on the dielectric response. For that reason the slices were tested immediately after being extracted from the saturated artificial shale sample.

- Slice dimensions: The two faces of a slice must be almost perfectly parallel with a constant thickness down to ±0.1mm to ensure a good coupling between the sample and the dielectric equipment without any air gap. The surface of the slices was smoothed using a finely abrasive material in order to get a surface free from irregularities. When positioned between the parallel plates the slice is pressed with a small pressure to form a uniform contact surface.

- Direction of the slices: To measure the anisotropy of the dielectric properties, a vertical and a horizontal slices were extracted from the sample. The ratio of the horizontal to vertical measured values is defined as the dielectric anisotropy. The two orientations allow us to also measure the P-wave

anisotropy parameters ε (Thomsen, 1986) in unconfined conditions from the P-wave velocity measurements. The slices were extracted so that the testing surfaces are located at least several millimetres from the original sample surface as indicated on the scheme in Figure 4-14. This avoids testing material that may have been altered by contact with air.

- Measurement with bare coupling and film coupling: Two sets of measurements were made for each slice. The bare measurement involves a direct contact between the sample and the electrodes. This method is effective to measure effective conductivity at all frequencies. However at low frequency (<1MHz), the dielectric response is dominated by the electrode polarization and the resulting dielectric permittivity does not correspond to that of the sample. This is why a second measurement is made with a thin plastic film positioned on either side of the slice at the sample/electrode interface. This prevents electrical conduction in the sample and is used to determine the dielectric permittivity for all the frequencies investigated.

Each measurement is run with the impedance analyser. The apparatus measures the real and imaginary part of the dielectric permittivity and can compute the equivalent electrical conductivity.

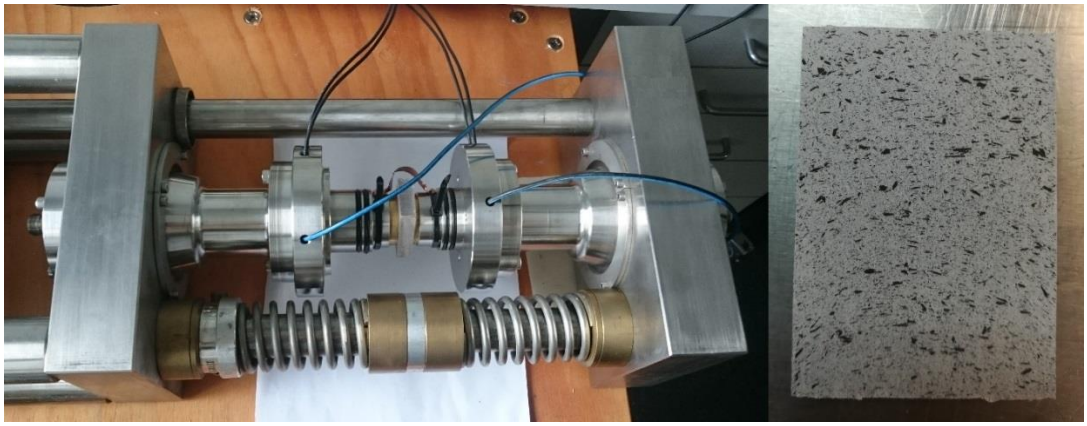

Figure 4-13: Left - Parallel plate cell with a sample slice clamped in between the electrodes with a pressure sufficient for optimal coupling. The blue cables are linked to P-wave ultrasonic transducers, the black cables are used to apply the alternating electrical field. Right - Close-up view of a 10mm thick sample slice used for the dielectric measurement.

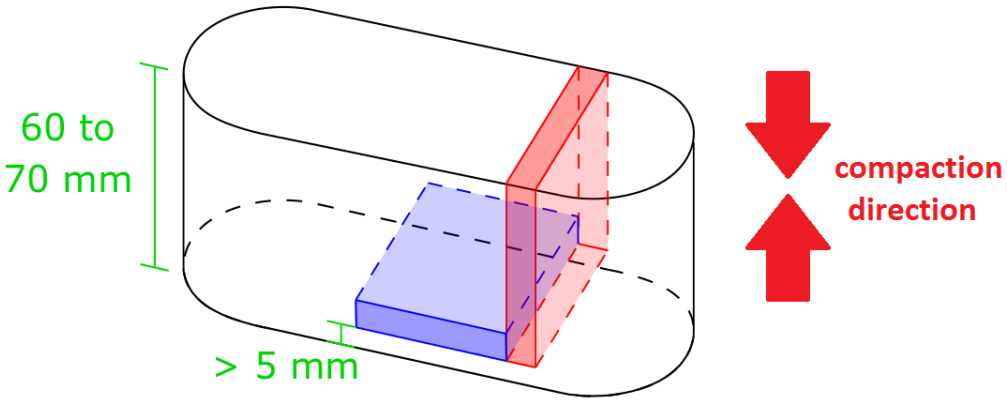

Figure 4-14: Schematic representation of an artificial sample and the location of the slices extracted to perform dielectric tests. The testing surfaces are located at least 5mm from the original sample surface. The horizontal slice (in blue) was used to perform the vertical measurements and the vertical slice (in red) was used to perform the horizontal measurements.

4-2-4- Results

The dielectric response of the samples in Set 3 are presented in four different groups according to the different target variables defined in the sample preparation Section 3-1-. For each group, we present the evolution across the frequency range of the three measured properties (real relative permittivity, imaginary relative permittivity and equivalent conductivity) along with their anisotropy.

Some general observation can be made about the data across the whole sample set. The values taken by the real permittivity are all very similar in the low frequencies and then dip at high frequencies. The dip occurs later in the horizontal direction than in the vertical direction. This yields an increase in anisotropy in high frequencies with a peak at around 2 MHz.

The imaginary permittivity presents S-shaped curves with a minimum around 0.1 MHz and a maximum around 10 MHz. Horizontal and vertical responses have the same shape but horizontal curves have a maximum shifted towards higher frequencies. Similarly to the real permittivity, this produces an increase in anisotropy at high frequencies.

The conductivity anisotropy is around 1 in the low frequencies and increases across the frequency range to reach a maximum of about 2 at 3 MHz.

These general observations across the sample set show the consistency of the sample characteristics and the quality and repeatability of the dielectric measurements.

4-2-4-1- On the influence of land OM at different maturity levels

Three organic samples containing land OM with different maturity levels and one inorganic sample are compared. All of them were prepared with the mixing method and the organic particles were all in the form of thin powder.

No obvious difference can be spotted for any of the three variables both in terms of magnitude and anisotropy (*Figure 4-15* to *Figure 4-17*). All maturity levels behave similarly except for the imaginary dielectric anisotropy of the most mature sample at frequencies below 6MHz. It has a much higher anisotropy at this frequencies but the high frequency anisotropy matches that of the other samples. It is unclear at the moment if this is due to a measurement error or to an actual physical phenomenon.

Finally a small difference can be observed at low frequencies for the inorganic sample. It has a lower imaginary permittivity and a higher conductivity below 200 kHz in the vertical and horizontal directions alike.

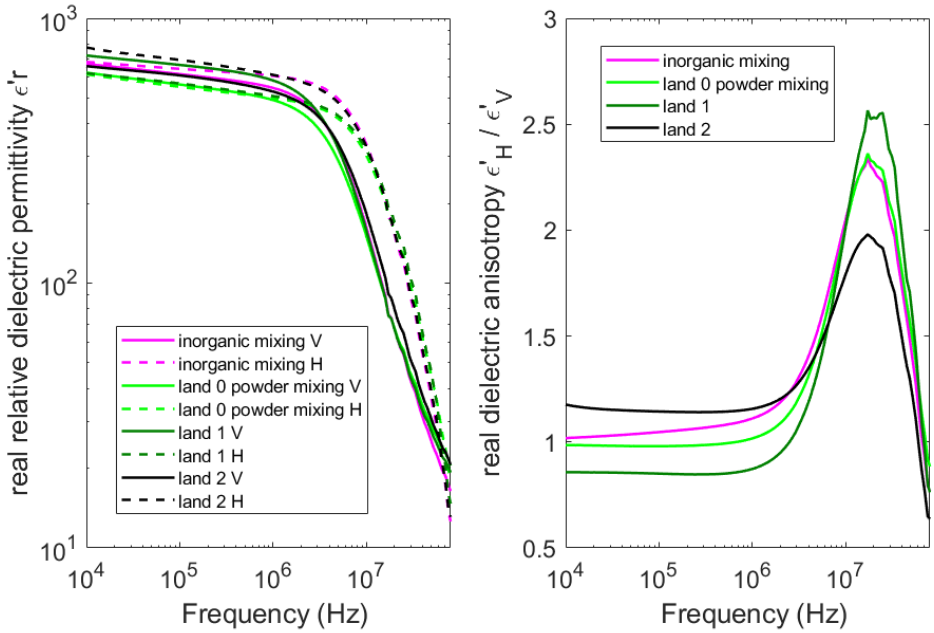

Figure 4-15: Real part of the relative dielectric permittivity for the group of samples containing land OM powder with variable maturity levels and made following the mixing method. An inorganic sample made with the mixing method is also displayed.

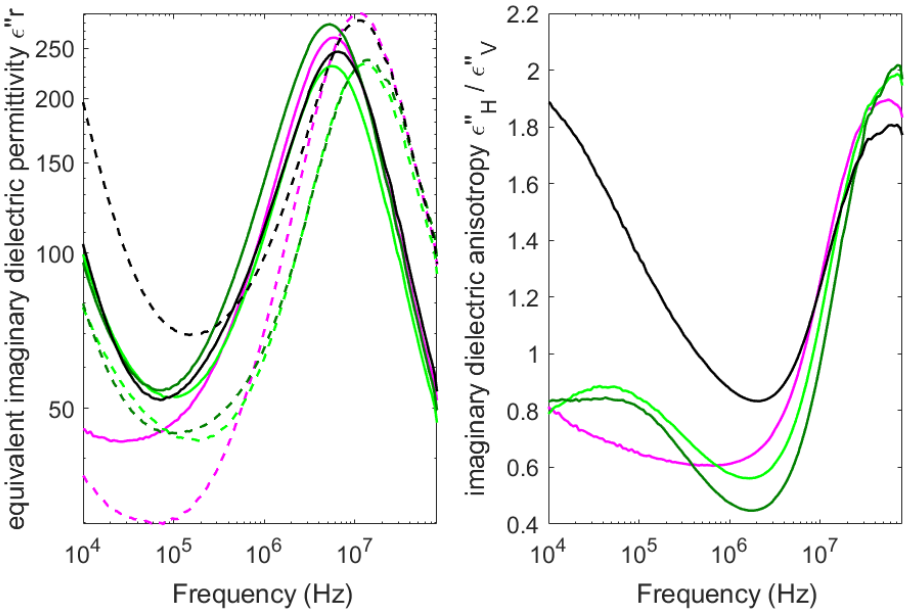

Figure 4-16: Imaginary part of the relative dielectric permittivity for the group of samples containing land OM powder with variable maturity levels and made following the mixing method. An inorganic sample made with the mixing method is also displayed.

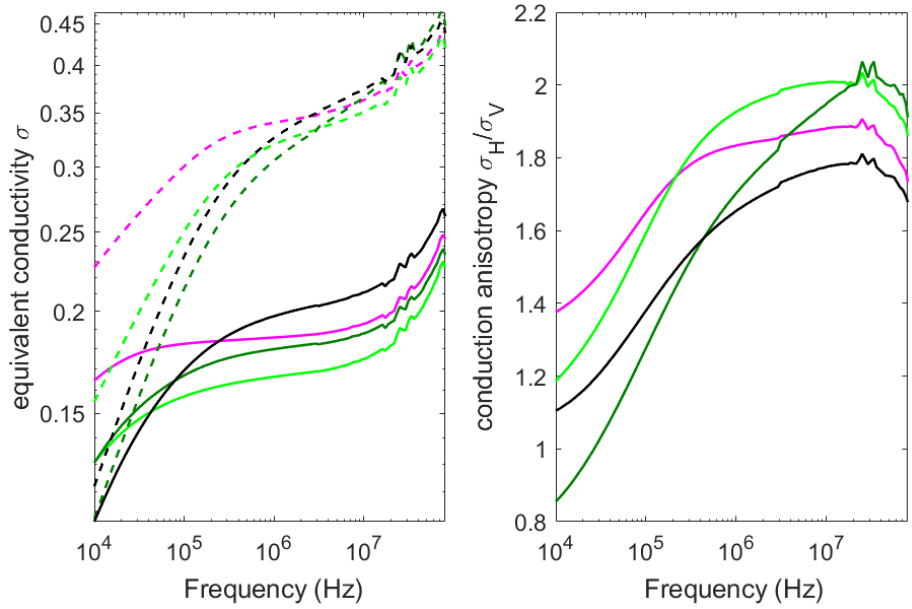

Figure 4-17: Equivalent conductivity (S/m) for the group of samples containing land OM powder with variable maturity levels and made following the mixing method. An inorganic sample made with the mixing method is also displayed.

4-2-4-2- On the influence of marine OM at different maturity levels

In the exact same way as for land OM, three maturity levels are compared with marine OM along with an inorganic sample.

Here again no clear difference between maturity levels was observed except for the imaginary permittivity anisotropy of the most mature sample that is much higher than the other sample at low frequencies (*Figure 4-18* to *Figure 4-20*). It looks like a measurement error at first but the fact that this was observed for the most mature land sample as well begs the question of whether this is an observation of an actual physical phenomenon or not.

On the other hand we can see significant differences between the marine samples and the inorganic sample. The real permittivity in both orientations dips at lower frequencies for the inorganic samples than for the other samples. Consequently the anisotropy starts rising above unity and peaks at lower frequencies for the inorganic sample than for the marine samples (20MHz against 40MHz, respectively). Also the peak of the imaginary permittivity and its anisotropy occurs at a lower frequency for the inorganic sample. Finally the marine samples have a much higher conductivity than the inorganic one. The inorganic horizontal conductivity has similar values to the marine vertical conductivity. As marine conductivity is shifted upward in equal proportions in the vertical and horizontal directions compared to the inorganic values, it does not influence the anisotropy that behaves similarly for inorganic and marine samples.

The inorganic (control) sample behaves similarly to the land samples, the inorganic/marine comparisons can thus be extended to the land/marine samples as can be seen in the next section 4-2-3-3-.

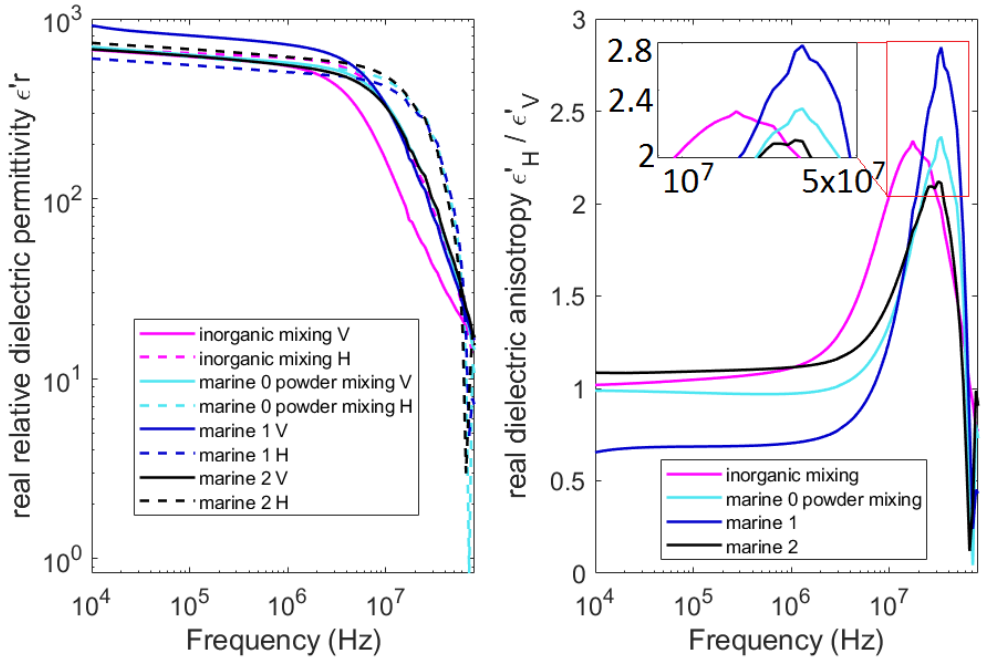

Figure 4-18: Real part of the relative dielectric permittivity for the group of samples containing marine OM powder with variable maturity levels and made following the mixing method. An inorganic sample made with the mixing method is also displayed.

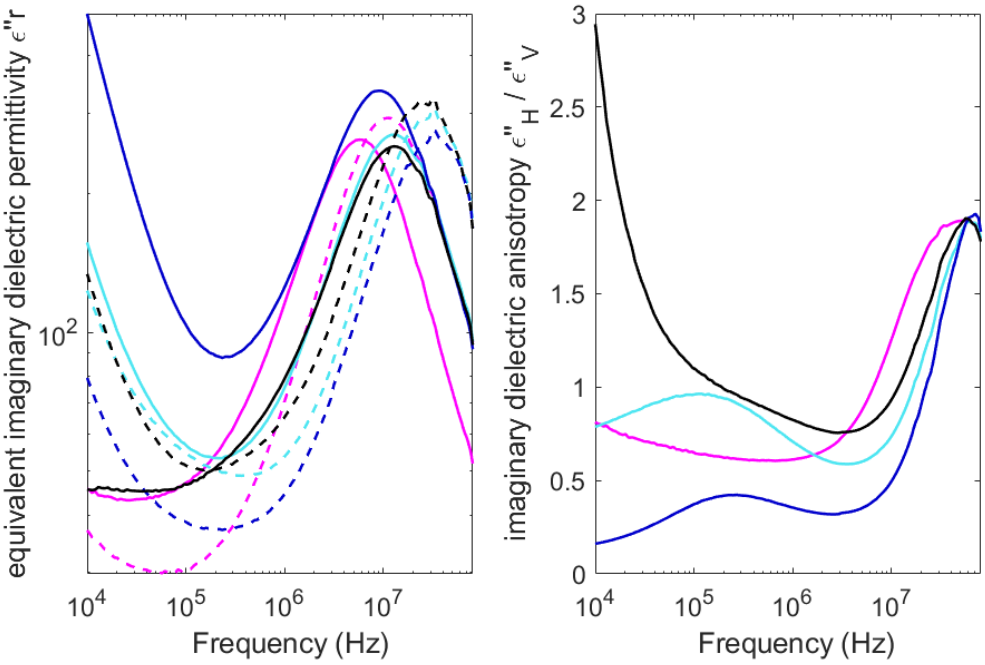

Figure 4-19: Imaginary part of the relative dielectric permittivity for the group of samples containing marine OM powder with variable maturity levels and made following the mixing method. An inorganic sample made with the mixing method is also displayed.

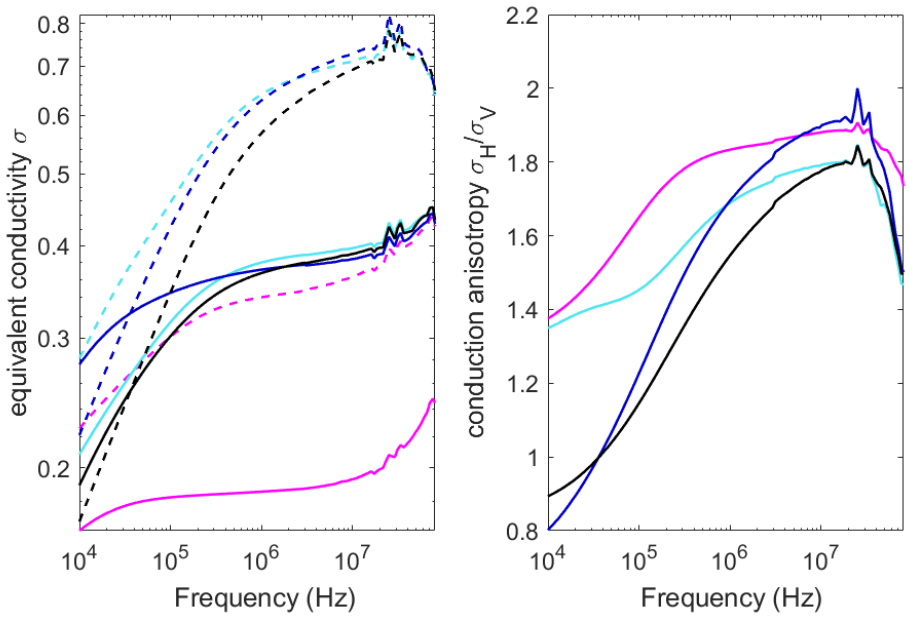

Figure 4-20: Equivalent conductivity (S/m) for the group of samples containing marine OM powder with variable maturity levels and made following the mixing method. An inorganic sample made with the mixing method is also displayed.

4-2-4-3- On the influence of OM type and texture

For each OM type (land and marine), a sample with OM made of thin powder is compared with a sample with pre-compacted OM made of high aspect ratio flakes with a long axis under 2.3mm. All OM was fresh (no artificial maturation) and all four samples were prepared with the mixing method.

When comparing the land samples with the marine samples the same observations can be drawn, as in the previous section with the inorganic and marine samples (*Figure 4-21* to *Figure 4-23*). Namely, the real dielectric permittivity anisotropy peaks at lower frequencies for the land samples (20MHz against 40MHz) and the conductivity of the marine samples is much higher.

When comparing the two particle categories (powder and flakes) within each OM type, no difference in the real and imaginary permittivity or their anisotropies can be seen. But a trend can be seen in the conductivity that is consistent for both OM types. The vertical conductivity of the powder samples is slightly greater and runs parallel to their flakes curve across the frequency range. The horizontal conductivity of the powder samples is also greater than the flakes samples at low frequencies but they gradually converge and end up having almost identical values at high frequencies.

In terms of anisotropy this translates to anisotropies slightly above unity at low frequencies for all samples. Then the flakes samples' conductivity anisotropy increases more sharply and we note substantially greater anisotropies for the flakes samples than for the powder samples above 200 kHz. It can also be noted that land samples have a greater conductivity anisotropy than marine samples at these frequencies.

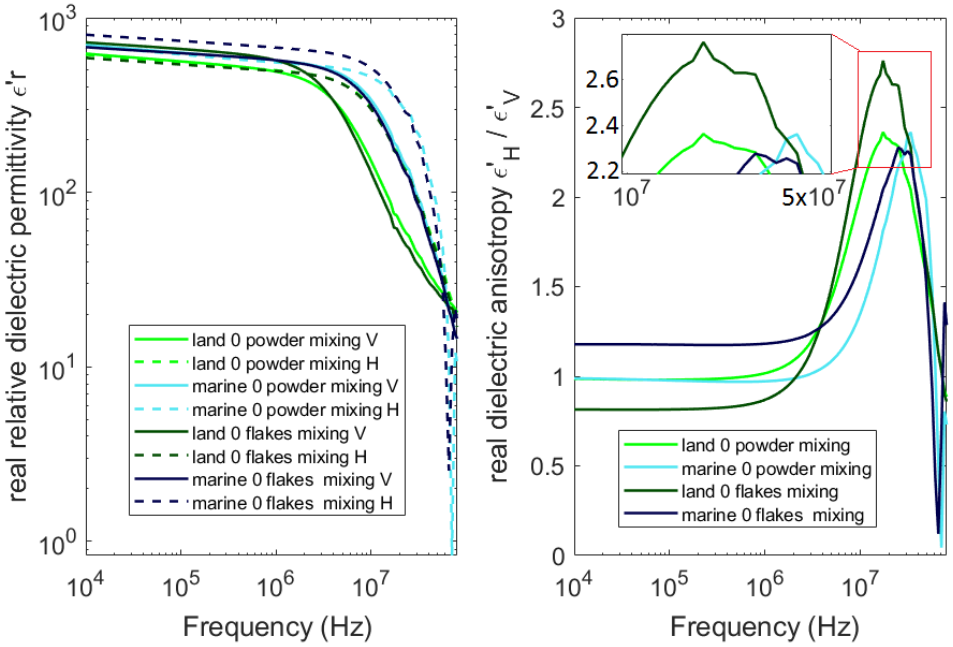

Figure 4-21: Real part of the relative dielectric permittivity for the group of samples containing land and marine OM made of two particle types: powder and flakes. They were made following the mixing method.

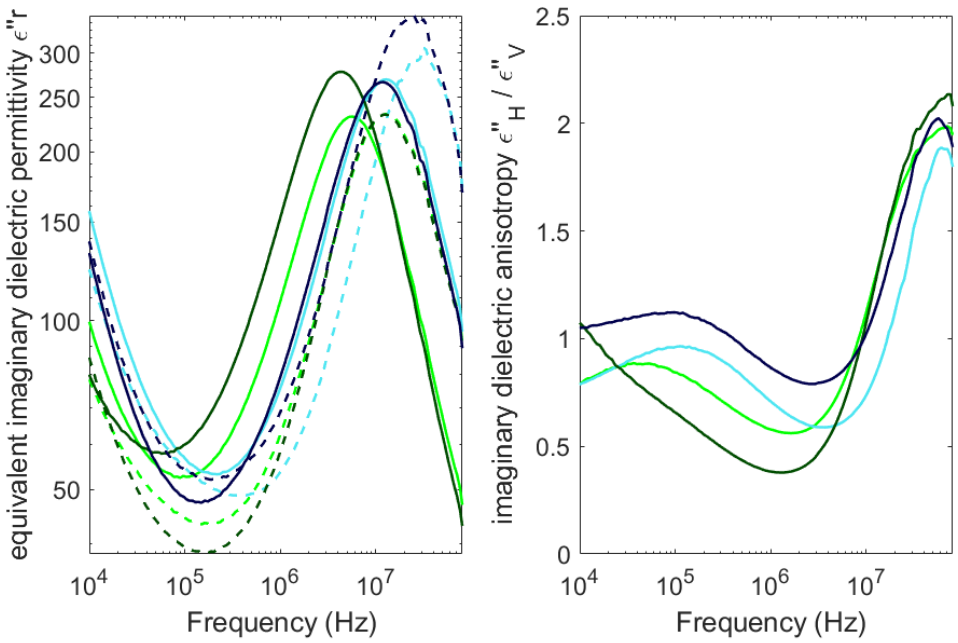

Figure 4-22: Imaginary part of the relative dielectric permittivity for the group of samples containing land and marine OM made of two particle types: powder and flakes. They were made following the mixing method.

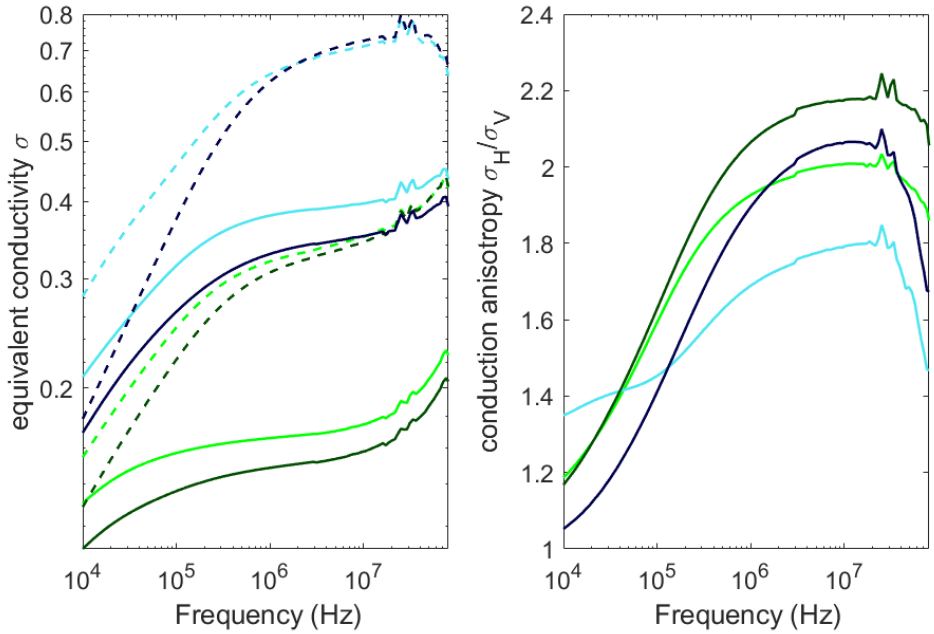

Figure 4-23: Equivalent conductivity (S/m) for the group of samples containing land and marine OM made of two particle types: powder and flakes. They were made following the mixing method.

4-2-4-4- On the influence of the deposition method

Here two inorganic and two organic samples are considered. One of each group was prepared with the mixing method and the other one was prepared with the "sedimentation" method (cf. sample preparation Section 3-1-). The OM particles are land flakes.

When looking at the amplitude of the raw values of the three properties it is hard to discern any difference between samples as all the horizontal and vertical curves are close to each other. However a pattern appears on the anisotropy graphs (*Figure 4-24* to *Figure 4-26*).

On the real and imaginary anisotropy graphs the low frequency values (<3 MHz) are around unity and then rise sharply to peak at 20 MHz for the real anisotropy and at 60 MHz for the imaginary anisotropy. What is interesting to look at is the order of the samples in the peaks:

(i) Higher anisotropy with the mixing method both for organic and inorganic samples.

(ii) Higher anisotropy with OM flakes for both deposition methods.

(iii) Higher anisotropy difference between the two organic samples and the two inorganic samples.

The exact same observations go for the imaginary and conductivity anisotropies.

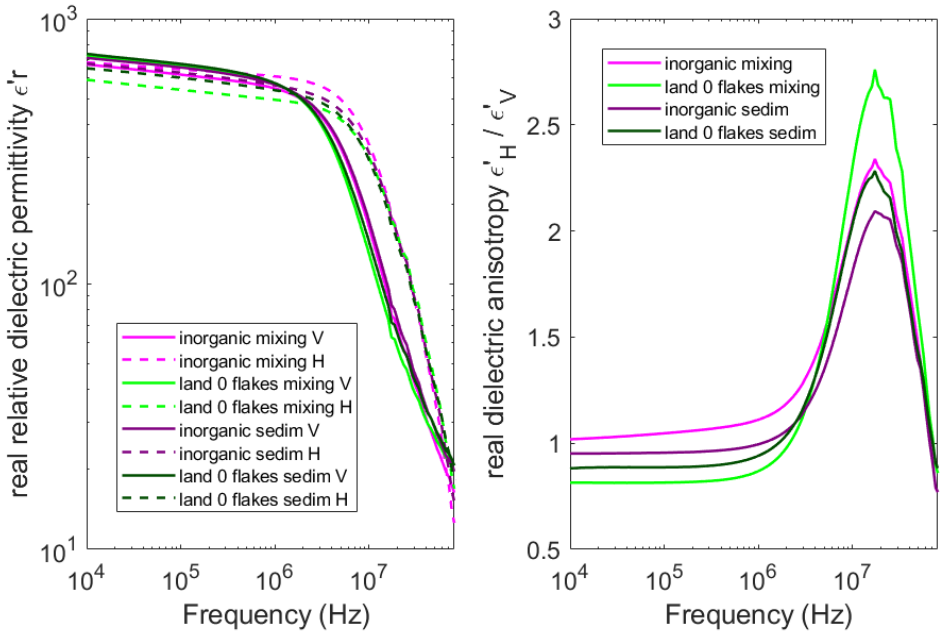

Figure 4-24: Real part of the relative dielectric permittivity for the group of samples containing made following two different deposition methods: mixing and sedimentation. Two of the samples are inorganic and the two others contain land OM of the flake particle type.

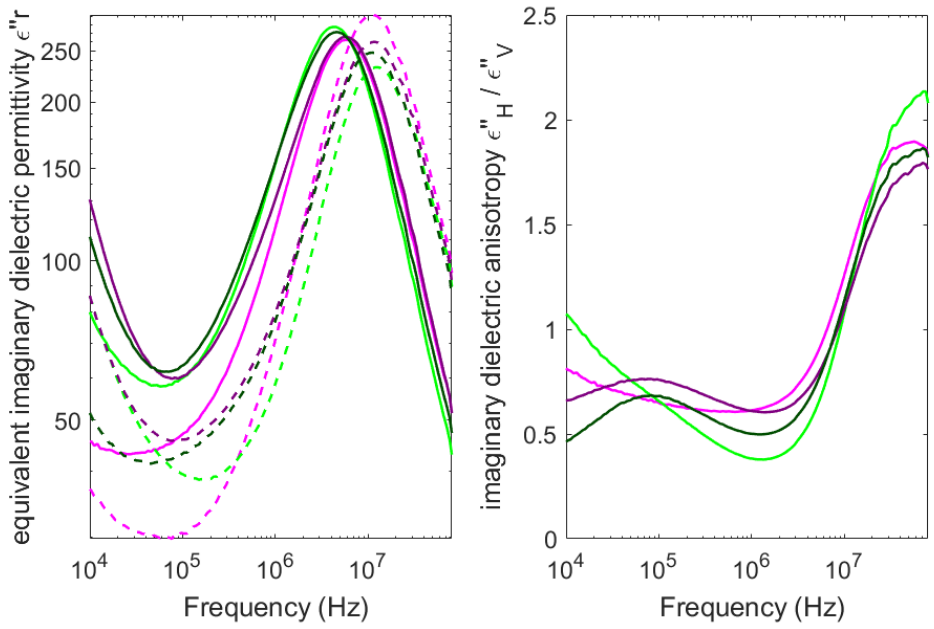

Figure 4-25: Imaginary part of the relative dielectric permittivity for the group of samples containing made following two different deposition methods: mixing and sedimentation. Two of the samples are inorganic and the two others contain land OM of the flake particle type.

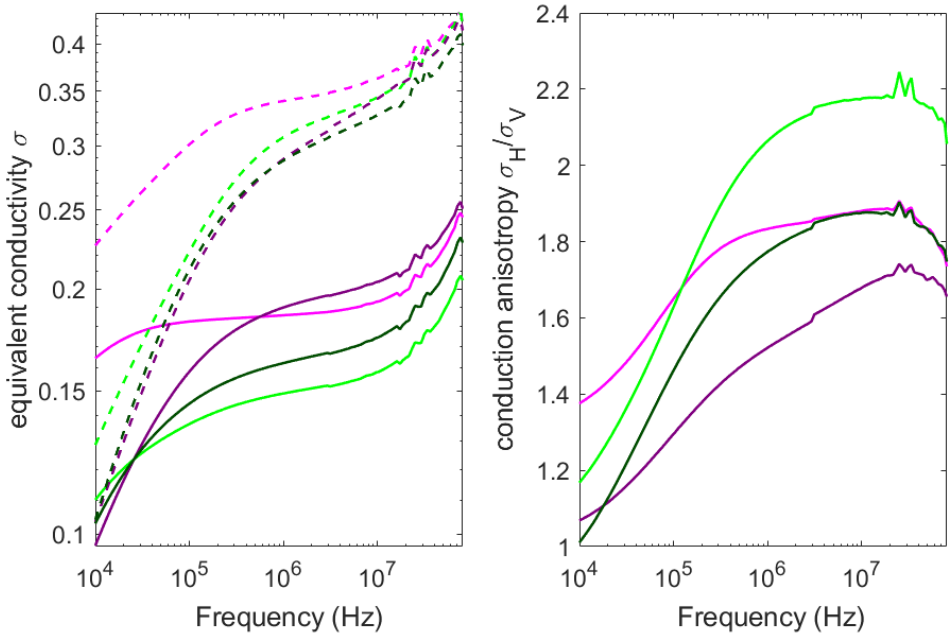

Figure 4-26: Equivalent conductivity (S/m) for the group of samples containing made following two different deposition methods: mixing and sedimentation. Two of the samples are inorganic and the two others contain land OM of the flake particle type.

As a conclusion here is a summary of the main observations:

- The maturity level of the different samples containing OM doesn't seem to affect the dielectric properties significantly in this sample set.
- The inorganic and land OM samples have very similar responses, except at low frequencies (<100 kHz) where land OM samples have a higher imaginary dielectric permittivity and a lower conductivity than the inorganic samples.
- The marine OM samples display a much higher conductivity than other samples (inorganic and land OM) over the whole frequency range. They also have a delayed increase in the anisotropy of the real part of the dielectric permittivity when the frequency increases.
- The samples containing flakes OM have a higher conductivity anisotropy at high frequencies (>0.5 MHz) than their powder counterparts (both for marine and land samples).
- The samples made using the deposition method have a lower anisotropy at high frequencies (>10 MHz) for the real and imaginary permittivity and a lower anisotropy on all the frequency range for the equivalent conductivity.

4-3- Optical microscopy

The objectives of the analysis of thin sections by optical microscopy combined with quantitative image processing are:

- To assess the morphological characteristics of inorganic phases present in the different samples and compare results obtained to demonstrate whether or not these phases have similar characteristics across the sample set.
- To characterize the texture of the OM particles present in the various samples.

4-3-1- Material and method

A thin section (25 x 50mm) was cut through each of the 11 samples in Set 3. The long axis of the thin section is parallel to the direction of compaction (vertical). The thin section target thickness was 30µm. However, due to poor polishing behaviour of the samples, the actual thickness of the sections is variable. The artificial samples are only mechanically compacted, and as such, they do not contain any kind of cement in contrast to that observed in natural shales. For that reason the cohesion of the fine grained matrix is lower in the artificial samples making the thin section preparation process more difficult. When the surface of the thin section is polished some particles or aggregates of particles can be entirely chipped off the section. Therefore the thin sections present a number of "holes" covering 1 to 3% of the surface. These portions of the thin sections were ignored during the processing of the microscopy images. In addition, the average thickness throughout each thin sections was found to be variable by observing the amount of light transmitted through the sample in different areas of the thin section. However areas of even thickness were selected for the image analysis as described below.

Each thin section was placed under a transmitted light microscope equipped with a polarizer to observe the samples under plain polarized light (PPL).The microscope is fitted with a Zeiss N-ACHROPLAN 2.5x/0.07na objective. Images of the entire thin section were recorded with a ZEISS AxioCam MRc camera at a pixel size of 2.6µm.The numerical aperture of the objective allowed to record images about 2.9 x 2.6mm wide. To cover completely a thin section, a series of image slightly overlapping each other were recorded and were then stitched with the Zeiss ZEN software to generate a single mosaic image.

4-2-2- Data processing

A region of interest (ROI) of 5000 pixel square was cropped from the image of each sample. This represents an area of 169mm^2. The ROI in each image was selected in an area of constant thickness (i.e. of constant average image brightness).

For each ROI, the red (R), green (G) and blue (B) components of each pixel were used to segment the holes, the OM and the non-clay minerals from the surrounding matrix. The non-clay minerals are composed of quartz, K-feldspar (orthoclase) and calcite. In PPL they appear as white particles. The fine-grained matrix composed mainly of clay has a beige hue. The fresh land OM takes on a brown colour, the fresh marine OM has an orange colour and the mature OM of both types has a colour ranging from dark brown to black.

To isolate the non-clay particles, the colour image was converted to a greyscale image by averaging the three RGB components. The greyscale image was thresholded using equation (1) to determine whether or not a pixel belongs to a mineral particle:

$$\frac{R+G+B}{3} > \lambda_{threshold} \tag{67}$$

Where R, G and B are the RGB components on a scale from 0 to 255 and $\lambda_{threshold}$ is the threshold value for mineral particles. $\lambda_{threshold}$ varies between 110 and 150 depending on the average brightness of the ROI for a given sample.

To segment the fresh OM particle from the matrix, we used the fact that the brown and orange OM particles have a higher red component compared to the surrounding matrix. Sometimes single pixels in the matrix have an unusually high red component but do not belong to an OM particle. To avoid counting these isolated pixels, for a pixel of coordinates (i, j) a threshold was applied on the RGB values of 9 pixels from coordinates (i-1, j-1) to coordinates (i+1, j+1) according to the following criterion:

$$\frac{\bar{R}}{\bar{G}+\bar{B}} > \lambda_{threshold} \tag{68}$$

where $\bar{R}$, $\bar{G}$ and $\bar{B}$ are the averages of the corresponding colour components over the 9 pixel selection and $\lambda_{threshold}$ is the threshold value for OM particles and is equal to 0.62 for the fresh land OM and 0.64 for the fresh marine OM.

To segment the mature OM from the matrix a threshold was applied to the average RGB greyscale image already used for the non-clay mineral particles with the following criterion:

$$\frac{R+G+B}{3} < \lambda_{threshold} \tag{69}$$

Where the threshold value varies between 40 and 55 depending on the average brightness of the ROI for a given sample. But this method has a major flaw because the holes on the thin section appear dark under PPL, with very similar RGB values than mature OM particles. To filter the holes out of the OM particle selection we relied on the appearance of such holes. They are on average bigger than the OM particles, they sometimes have mineral particles within them, and they have irregular and intricate outlines. Therefore filters were applied that remove a dark particle from the OM selection if it presents one or more of the following characteristics:

- Area > 1500 pixel^2.
- Holes in the particle (which indicates the presence of mineral grains).
- [Perimeter of fitted ellipse/actual particle perimeter] < 0.4.

This method for separating holes from OM particles has its drawbacks. For instance the threshold on several adjacent OM particles will produce a single particle with an intricate outline and will be counted as a hole and some small holes will have less irregular shapes and will be considered as OM particle. Also some mature samples display crack features that were formed during the thin section preparation process which should be considered as holes. Most of these cracks are thin and have an average RGB value higher than the threshold in equation (69). The wider cracks however are counted as OM particles. The images in Figure 4-27 illustrates the different thresholds and filters employed on a small subsection of the sample containing mature OM particles named "marine 2".

For each sample, binary images of each phases (inorganic minerals and OM) were used to measure the particle size distribution, particle aspect ratio and their orientation. The particles smaller than 10 pixel^2 (i.e. below image resolution) were ignored. These small particles usually have RGB values very close to the set thresholds and small variations of the threshold values change drastically their population. Hence the

minimum size of the particle size distribution is 68µm². This corresponds to an equivalent circle diameter of 9.3µm. For the determination of the particle orientation we ignored the particles with an aspect ratio smaller than 1.2 as the orientation of near equant particles is not indicative of the overall orientation of the particle population.

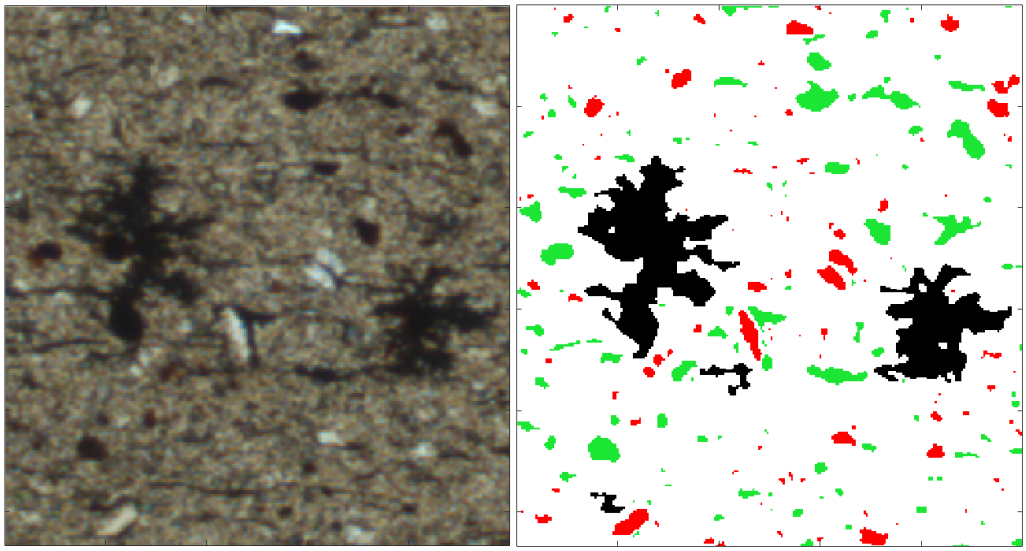

Figure 4-27: Left - Portion of the microscopy image of sample "marine 2" (650 x 700µm). Right – Same portion with applied thresholds: The fine grained matrix is white, the non-clay minerals are red, the OM particles are green and the holes are black.

4-3-3- Results

Firstly the results on the non-clay particles will be presented and then the results on the OM particles will be shown. In each section, the statistic on the overall populations will be examined (*Table 4-2* and *Table 4-3*). Then the characteristics of the distribution of the particles characteristics will be detailed (size, aspect ratio and orientation) on the histograms in Figure 4-29 to Figure 4-35. For all figures, the following colour code was applied:

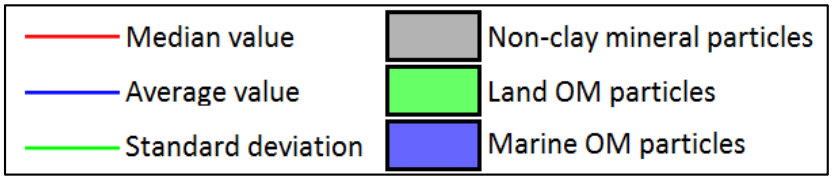

Figure 4-28: Colour code for the histogram figures.

4-3-3-1- Non-clay mineral particles

The different parameters describing the non-clay mineral particles are very similar across the sample set (*Table 4-2*). All the indicators hover around the average value over the sample set with a standard deviation value always lower than 10% of the value of the average. The differences between average and median values are also almost constant between samples, with average values always greater than median values. The variability in the orientation angles can be attributed to the misalignment of the thin section long axis with the direction of compaction.

Non-clay mineral particles										
Sample name	Particle count >68µm²	Coverage (%)	Average size (µm)	Median size (µm)	Average aspect ratio	Median aspect ratio	Particle count AR>1.2	Average orientation degrees	Median orientation degrees	Standard deviation angle degrees
inorganic mixing	12800	3.12	22.9	15.5	1.9	1.71	11900	92.21	91.02	33.51
inorganic sedim	11900	2.74	22.3	15.2	1.99	1.78	11100	90.72	90	33.19
land 0 powder mixing	16200	3.05	20.1	13.8	1.92	1.72	15000	93.04	2.66	36.3
land 0 flakes mixing	14500	3.04	21.2	14.1	1.94	1.73	13400	89.76	90	38.36
land 0 flakes sedim	15500	2.8078	22	16.1	1.97	1.785	14458	89.65	89.69	39.55
land 1	14000	2.7	20.4	14.1	1.91	1.7	13000	92.01	91.91	34.81
land 2	13000	2.89	21.9	14.7	1.9	1.7	12000	91.15	0.23	33.58
marine 0 powder mixing	13400	2.55	20.2	13.8	1.99	1.78	12600	86.79	86.41	32.66
marine 0 flakes mixing	13600	2.85	21.3	14.4	2.03	1.83	12700	87.22	86.48	34.43
marine 1	16200	3.22	20.7	14.1	1.88	1.7	15000	90.72	90	32.08
marine 2	14900	2.8	20.1	13.8	1.9	1.7	13900	90.31	90	39.1
average	14200	2.89	21.2	14.5	1.94	1.74	13200	90.33	89.85	35.23
Standard deviation	1400	0.2	0.96	0.79	0.048	0.04	1300	1.94	1.92	2.68

Table 4-2: Statistics on the size, aspect ratio (AR) and orientation of non-clay mineral particles >68µm. On the two last rows, the average and standard deviation are computed over the 11 samples. The "orientation" columns are a measure of the orientation of the long axis of the particles in regard to the direction of compaction (vertical).

The particle coverage is the ratio of the area covered by the particles to the total area of the microscopy image ROI. Its value is around 3% for all samples. However we know that the samples are composed of 60% in volume of non-clay minerals which are quartz, K-feldspar and orthoclase (cf. sample preparation section 3-1-). Therefore most of the mineral particles are embedded in the fine-grained matrix and are too small

to be detected on the microscopy images with this magnification. This indicate us that 95% of the volume of non-clay minerals have a particle size below 68µm² (9.3µm equivalent diameter).

On the particle size distribution histograms of Figure 4-29 we can see that the maxima lie around 40µm, given that 95% of the volume of minerals is not visible on this histogram, this means either the total particle size distribution is bimodal with another peak at a value below 10µm or that the particles at the lower end of the size range are under-represented due to the limits of the method.

The shape of the distributions, as well as the position of the average and median values of the particle size (Figure 4-29), aspect ratio (Figure 4-30) and orientation (Figure 4-31) are very similar for samples prepared either with the mixing or the deposition methods. This illustrates that the deposition method has little to no influence on the final texture of the non-clay minerals.

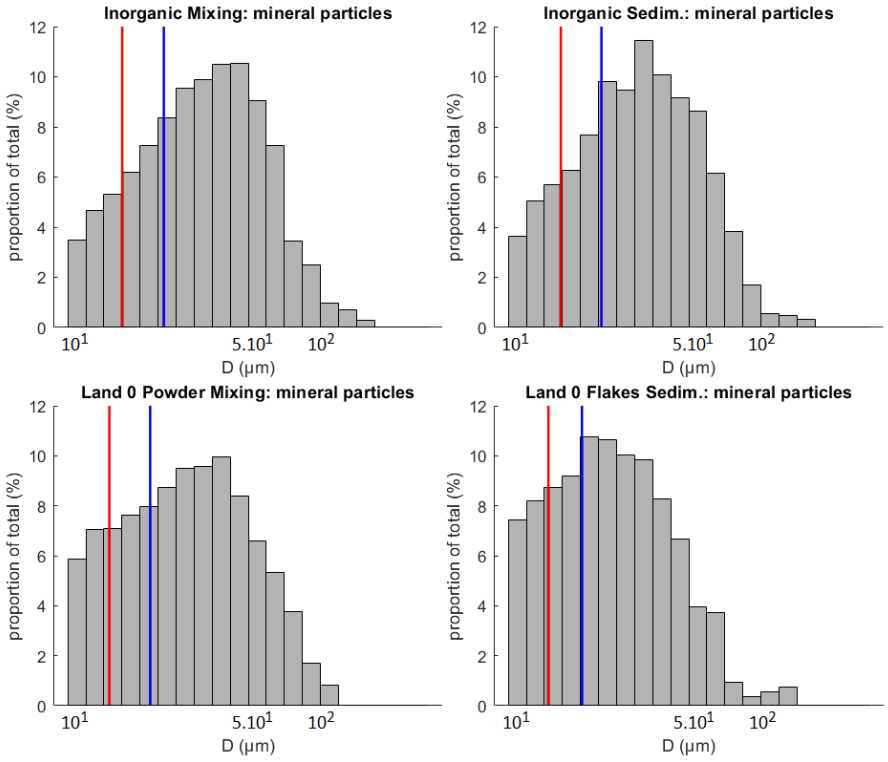

Figure 4-29: Particle size distribution of non-clay mineral particles >68µm for 4 of the samples. Left column: mixing method. Right column: Sedimentation method. First row: inorganic samples. Second row: Fresh land OM samples.

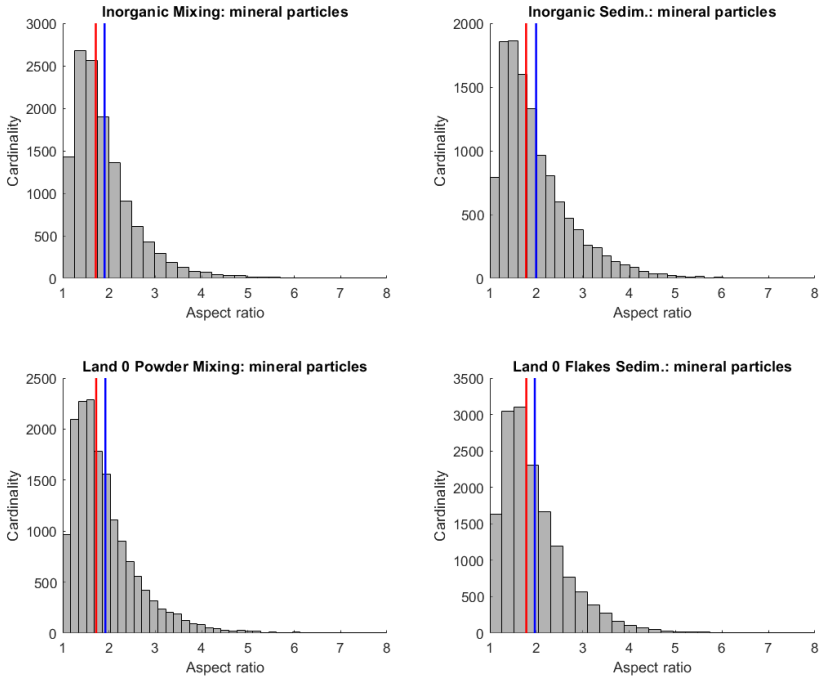

Figure 4-30: Aspect ratio distribution of non-clay mineral particles >68µm for 4 of the samples. Left column: mixing method. Right column: Sedimentation method. First row: inorganic samples. Second row: Fresh land OM samples.

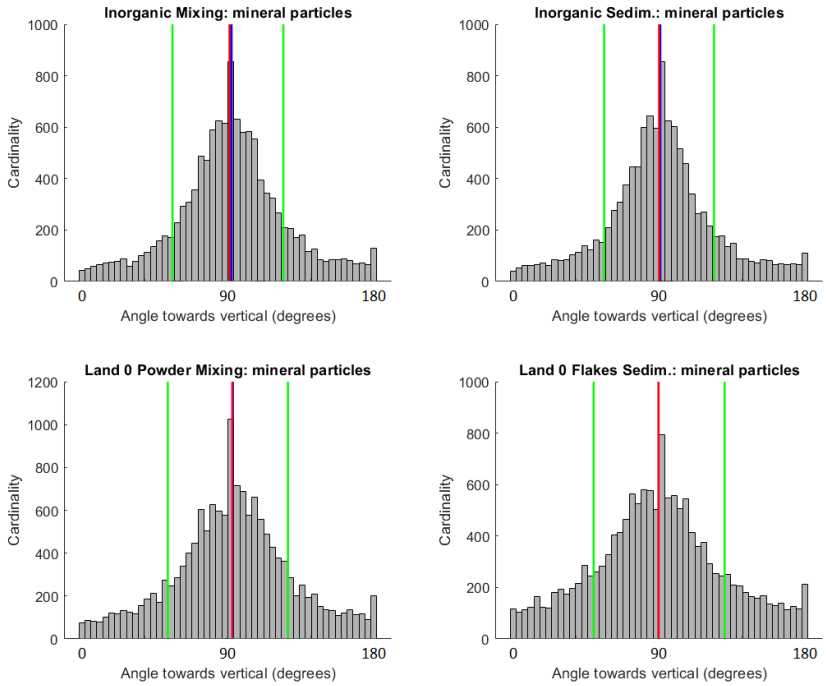

Figure 4-31: orientation distribution of non-clay mineral particles >68µm and with an aspect ratio >1.2 for 4 of the samples. Left column: mixing method. Right column: Sedimentation method. First row: inorganic samples. Second row: Fresh land OM samples.

4-3-3-2- OM particles

Contrary to the mineral particles, the OM particles show much more variability (Table 10). The particle coverage is quiet variable and is the highest for the two samples containing fresh land OM flake particles. This is directly related to the amount of particles that are higher than the detection threshold (68µm^2) where samples that have an OM particle size distribution located mostly above the detection threshold will have a coverage that is close to the OM volume content. As presented in the sample preparation in Section 3-1- the OM volume content is 8% for all organic samples. The minimum representative volume (or representative area for 2D images) increases when the size of the particles increases. The samples containing the largest OM particles thus have a minimum representative area that is bigger than the investigated square section of 169mm^2. For instance the OM particles are over-represented in the sample "land 0 flakes sedim" as they cover 12.75% of the investigated area. The samples with the bigger particles also have the lowest particle count and inversely the samples with the smallest particles have the highest particle count.

A stark difference can be noticed, in particle size between powder and flake particles for the land samples, whereas the same difference for marine samples is less pronounced. Furthermore the mature samples which were prepared to match a "powder" particle type, have bigger particles than the fresh powder particles, both for land and marine samples. It can inferred that the mature OM particles tend to clump into aggregates bigger than the powder typical size. The particle size is very similar across all four mature samples.

The land flake samples have a substantially higher average aspect ratio than other samples (about 2.5 against a global average of 2.25). But the aspect ratio of the marine flake sample does not seem to follow that trend.

The standard deviation of the average orientation in regard to the compaction direction is weakly correlated to the average aspect ratio, with samples containing more elongated particles having a narrower orientation distribution. However, the accuracy of the aspect ratio and orientation measurements are affected by the particle size as the shape of the small particles is less accurately defined with the threshold method.

Therefore all particles above a size of 20µm were analysed and the standard deviation of the orientation distribution was computed as long as the median aspect ratio (Figure

4-32). It shows that the median aspect ratio of the particles is the strongest predictor of their final orientation for identical compaction conditions. Figure 4-34 and Figure 4-35 show the actual aspect ratio and orientation distributions of the organic samples. The aspect ratio distributions present always the same shape with the interval with the most particles slightly below the median and few particles above the value 5. The orientation distributions are also similar with a gaussian shape of variable narrowness. The two land flake samples and the marine 2 samples have the narrowest orientation distributions and also present a greater population of aspect ratios above 5, strengthening the link between particle aspect ratio and orientation after compaction.

OM particles										
Sample name	Particle count >68µm²	Coverage (%)	Average size (µm)	Median size (µm)	Average aspect ratio	Median aspect ratio	Particle count AR>1.2	Average orientation degrees	Median orientation degrees	Standard deviation angle degrees
inorganic mixing	0	0	0	0	0	0	0	0	0	0
inorganic sedim	0	0	0	0	0	0	0	0	0	0
land 0 powder mixing	30200	6.08	20.8	13.8	2.22	1.96	28700	90.56	90	37.4
land 0 flakes mixing	6400	7.99	51.8	18.8	2.55	2.23	6200	90.33	90.19	24.89
land 0 flakes sedim	10000	12.75	52.4	17.1	2.45	2.16	9600	88.93	88.95	33.14
land 1	25000	7.29	25.1	16.9	2.12	1.89	23700	93.32	93.19	33.89
land 2	26000	7.52	24.9	16.6	2.11	1.88	24600	89.41	89.87	33.73
marine 0 powder mixing	53000	4.74	13.9	11.4	2.28	2.09	51300	90.46	90	38
marine 0 flakes mixing	41300	5.18	16.4	11.4	2.16	1.99	39700	90.44	90	44.15
marine 1	17100	4.39	23.5	14.7	2.02	1.78	16000	90.41	90	35.69
marine 2	25700	6.17	22.7	16.1	2.44	2.02	24300	88.49	88.5	32
average	26400	6.92	27.9	15.2	2.25	1.99	25300	90.31	90.14	35.04
Standard deviation	14100	2.57	14.2	2.6	0.17	0.14	13700	1.34	1.25	5.16

Table 4-3: Statistics on the size, aspect ratio and orientation of OM particles >68µm. On the two last rows, the average and standard deviation are computed from the 9 organic samples. The "orientation" columns are a measure of the orientation of the long axis of the particles in regard to the direction of compaction (vertical).

On the particle size distributions (Figure 4-33), the land 0 powder, land 1 and land 2 samples present very similar distributions with a most populated interval around 40µm and with almost all particles with a size smaller than 100µm. The two land flake samples have less organised size distributions that extend to sizes up to 1000µm. The marine flake sample has more particles in the upper end of the size range than the

marine 0 powder sample. However they both have the most populated interval adjacent to the detection threshold (9µm). This suggests they have an important population of particles smaller than that. On the other hand the mature marine samples, marine 1 and marine 2 have a distribution more similar to the mature land samples.

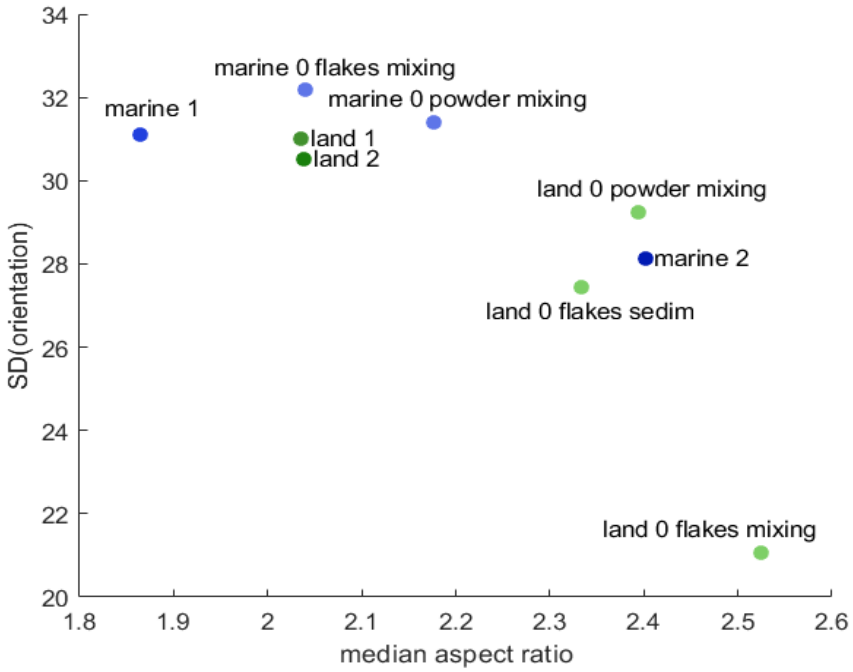

Figure 4-32: Standard deviation of the orientation distribution of OM particles as a function of the median aspect ratio for the subpopulation of big particles (D>20µm).

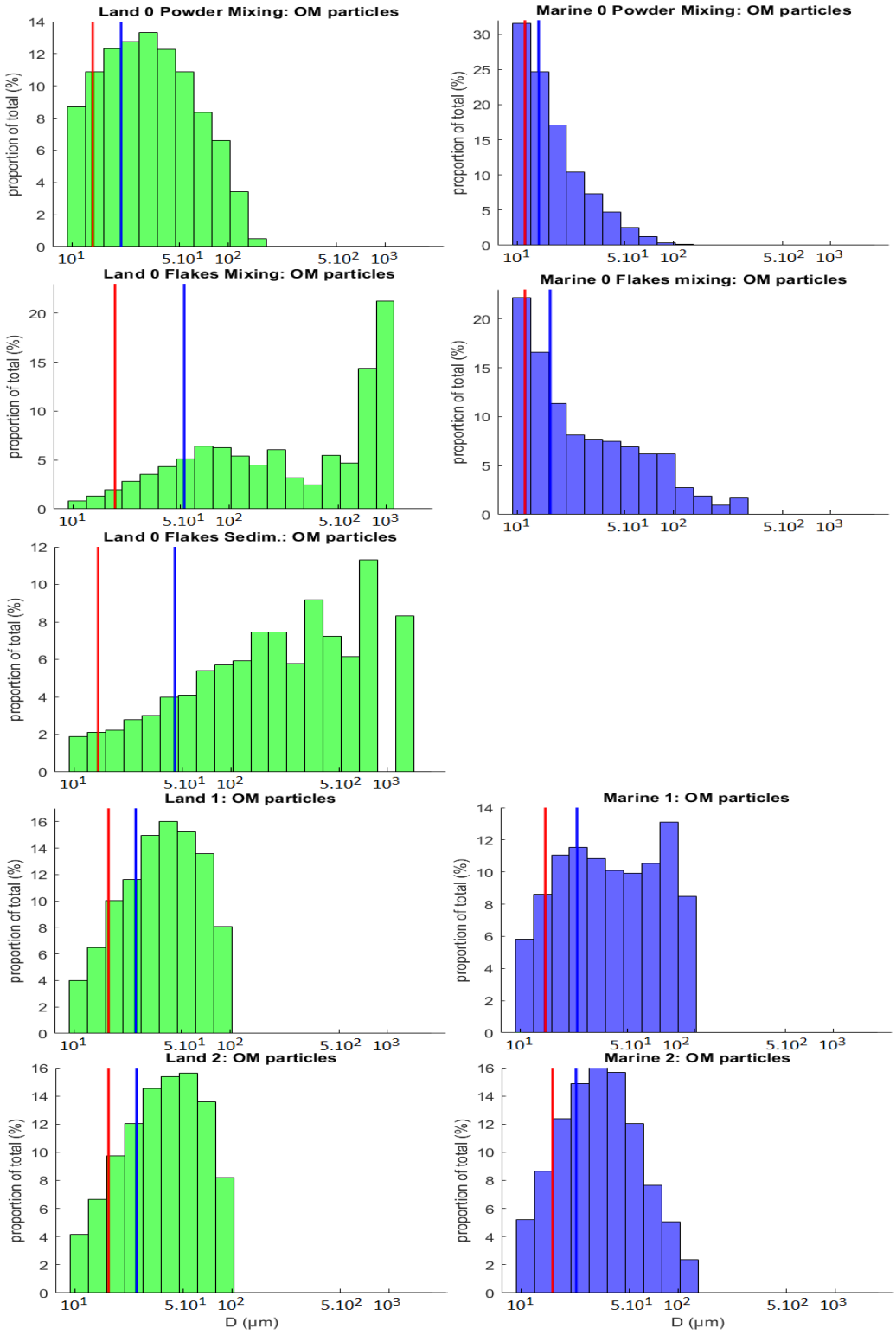

Figure 4-33: Particle size distribution of OM particles >68µm of the organic samples. Left column: Land OM. Right column: Marine OM. First row: Fresh OM powder, mixing method. Second row: Fresh OM flakes, mixing method. Third row: Fresh OM fakes, sedimentation method, Fourth row: OM maturity level1. Sixth row: OM maturity level 2.

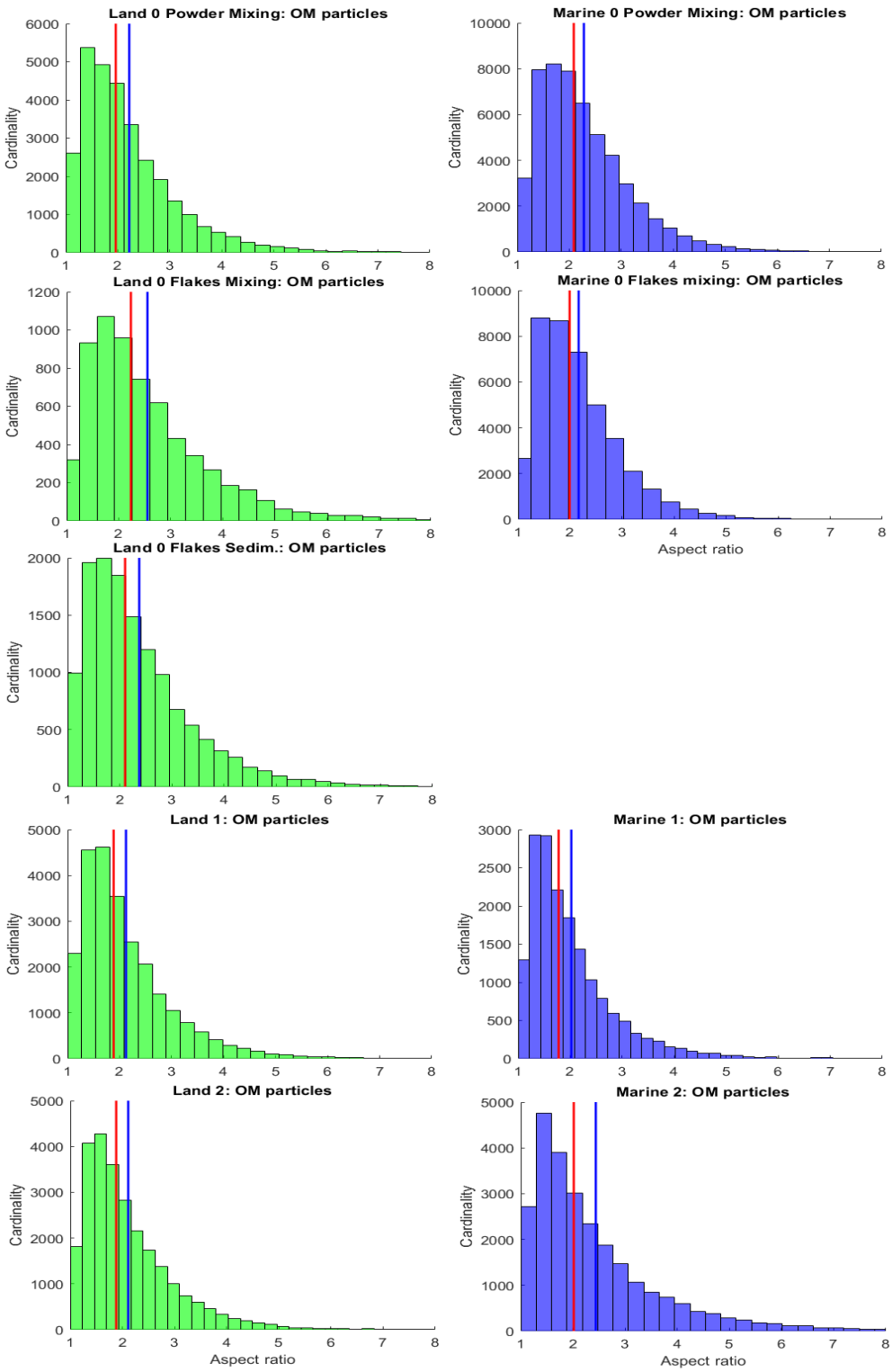

Figure 4-34: Aspect ratio distribution of OM particles >68µm of the organic samples. Left column: Land OM. Right column: Marine OM. First row: Fresh OM powder, mixing method. Second row: Fresh OM flakes, mixing method. Third row: Fresh OM flakes, sedimentation method. Fourth row: OM maturity level1. Sixth row: OM maturity level 2.

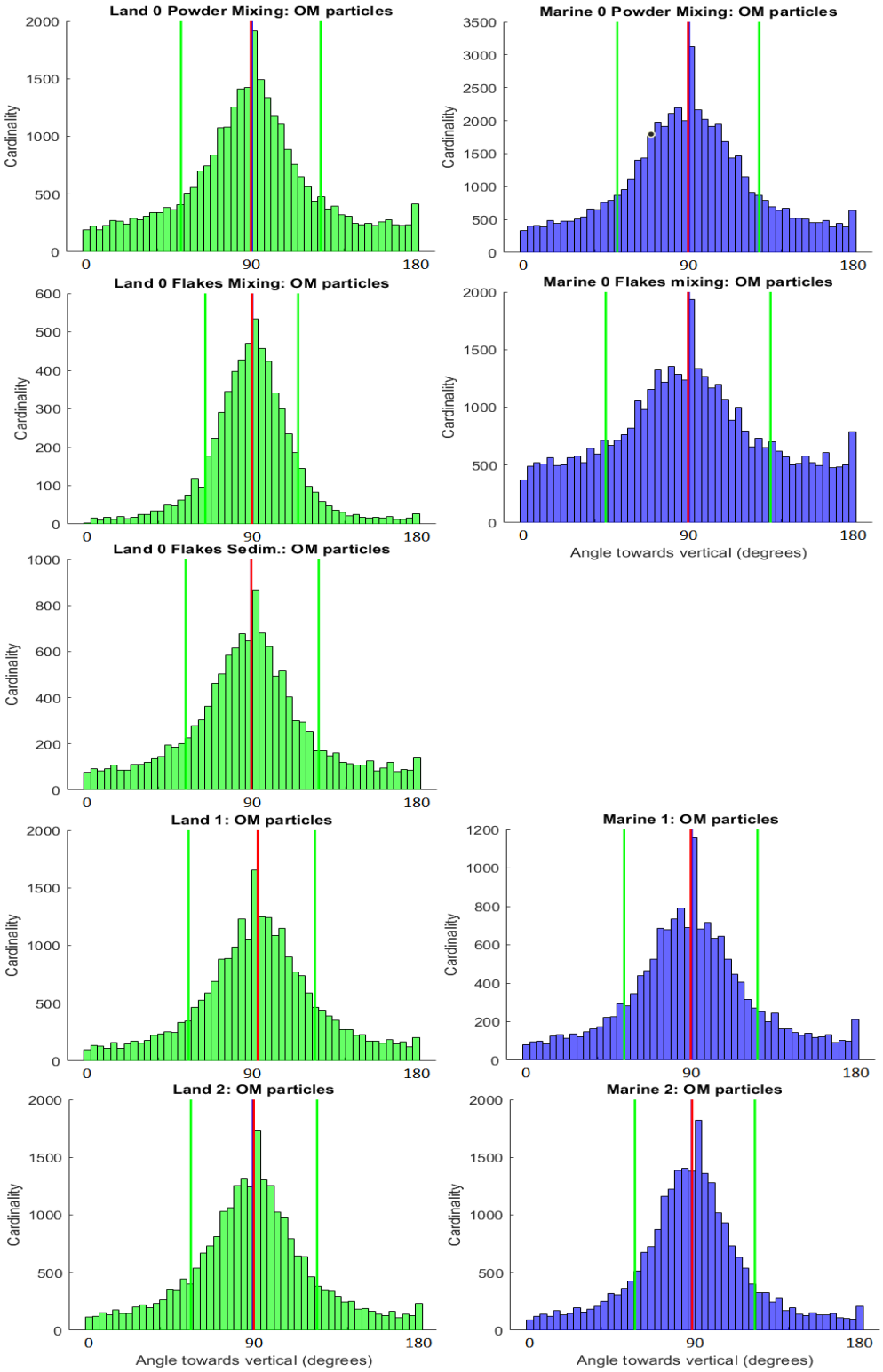

Figure 4-35: Orientation distribution of OM particles >68µm and with an aspect ratio > 1.2 of the organic samples. Left column: Land OM. Right column: Marine OM. First row: Fresh OM powder, mixing method. Second row: Fresh OM flakes, mixing method. Third row: Fresh OM flakes, sedimentation method. Fourth row: OM maturity level1. Sixth row: OM maturity level 2.

4-4- Rock-Eval tests

To evaluate the maturity level of the artificial samples produced during the project, 6 samples were sent to the ISTeP (Institut des Sciences de la Terre de Paris) to undergo a Rock-Eval pyrolysis test in a "Rock-Eval Turbo 6" apparatus. The principles of this technique and the results obtained on our samples will be presented in this section.

4-4-1- Rock-Eval pyrolysis principles

During a Rock-Eval test a small amount of dry, powdered sample – approximately 100mg – is heated in a chamber filled with an inert gas (N_2) at different temperatures; the amount of gas emitted by the sample is then measured and expressed in milligrams of gas per gram of rock (mg/g). The pyrolysis starts with a constant temperature of 300^0C and then increases to 650^0C at a rate of 25^0C/min. At 300^0C the free hydrocarbons (HC) in the sample are volatilised and a first peak of emission called S1 is recorded. In the interval from 300 to 650^0C the heavy HC compounds are volatilised and recorded in the peak S2. The volatilised HC of the peaks S1 and S2 are measured with a flame ionisation detector whereas the carbon monoxide and carbon dioxide (CO and CO_2) are measured with an infrared detector which forms the peak S3.

Thereafter the sample is transferred to an oven ventilated with a constant air flow to allow oxidation processes to occur. In this phase the sample is heated from 300^0C to 850^0C and the emitted CO and CO_2 are measured with a second infrared detector to record the peak S4 and S5. Altogether, a single analysis cycle lasts 45min.

The following parameters can be computed from the measurements:

- Amount of free oil and gas in the sample with the peak S1.
- HC production potential by kerogen cracking with the peak S2.
- T_{max} which is an indicator of the degree of maturity of the OM and corresponds to the oven temperature at the moment of the peak S2.
- Residual HC with the peak S4.
- Mineral carbon.
- Total organic carbon (TOC) which is the sum of the pyrolysed carbon (S1and S2) and residual carbon (S4).

- Hydrogen index (HI)

$$HI = \frac{S2}{100\ TOC} \tag{70}$$

- Oxygen index (OI)

$$OI = \frac{S3}{100\ TOC} \tag{71}$$

Altogether a total of 6 artificial samples were tested. Three of them contained land OM and three of them contained marine OM. For each OM type one sample contained fresh OM (maturity level 0), and the two other samples contained matured OM of maturity level 1 and 2 (for more information about OM maturation and sample preparation, please refer to Section 3-1- and 3-2-). All samples contained powdered OM. After their compaction a small chunk of each sample was extracted and ground to be sent for Rock-Eval tests. Each sample underwent two consecutive tests to test repeatability.

4-4-2- Results

The measurement summary in Table 4-4 shows the average value of the two Rock-Eval tests carried out on each sample. The repeatability of the measurements for each sample was in the order of magnitude of the precision described by Espitalié et al. (1985-86), except for the sample marine 2 where the variability is more important between the two analysis cycles. The mean absolute deviations from the mean, which is just the distance from the average for a set of two measurements, is displayed in Table 4-5. The weight content percentages computed here are measured on dry samples. We will thus compare these values with the dry weight content measured during the preparation of the artificial samples (cf. Section 3-1-).

Sample name	S1 (mg/g)	S2 (mg/g)	S3 (mg/g)	Tmax (^{0}C)	Pyrolysed carbon (%)	Residual Carbon (%)	TOC (%)	HI (mg HC/g TOC)	OI (mg CO_2/g TOC)	Mineral Carbon (%)
Land 0	0.675	4.55	4.2	433	0.63	1.375	2.01	227	209	1.175
Land 1	0.155	5.34	0.89	429	0.54	2.28	2.82	189.5	31.5	1.46
Land 2	0.18	5.37	0.68	432	0.53	2.145	2.68	200.5	25.5	1.285
Marine 0	0.15	1.56	0.8	434	0.175	0.17	0.35	453.5	232	1.265
Marine 1	0.055	1.555	0.505	440	0.155	0.38	0.54	290.5	94.5	1.395
Marine 2	0.085	1.685	0.485	444	0.17	0.25	0.42	404.5	116.5	1.165

Table 4-4: Summary of the Rock-Eval pyrolysis results on 6 artificial organic shales.

Sample name	S1 (mg/g)	S2 (mg/g)	S3 (mg/g)	Tmax (^{0}C)	Pyrolysed carbon (%)	Residual Carbon (%)	TOC (%)	HI (mg HC/g TOC)	OI (mg CO_2/g TOC)	Mineral Carbon (%)
Land 0	0.035	0.16	0.24	0	0.03	0.075	0.105	4	1	0.025
Land 1	0.005	0.1	0.01	0	0.01	0.01	0.02	2.5	0.5	0.02
Land 2	0.01	0.06	0	1	0.01	0.025	0.015	3.5	0.5	0.015
Marine 0	0	0.02	0.01	0	0.005	0.02	0.015	25.5	7	0.125
Marine 1	0.005	0.065	0.005	0	0.005	0.02	0.025	1.5	5.5	0.005
Marine 2	0.005	0.015	0.005	1	0	0.04	0.04	34.5	12.5	0.025

Table 4-5: Mean absolute deviation from the mean of the different Rock-Eval parameters. This corresponds to the distance from the average. High dispersion of the data is marked in red.

The mineral carbon computed from the S5 peak has an average of 1.3% in weight. This corresponds approximately to a 10% weight content of $CaCO_3$. This is in agreement with the initial weight content of calcite embedded in the samples of 10% in weight.

Overall the land samples emitted more HC (S1 and S2) during the oxygen free phase of the test. This translates to a lesser hydrocarbon potential for the marine samples as well as a lower TOC. The TOC of the land samples is around 2% in weight. As the OM is composed mainly of a mix of carbon, hydrogen and oxygen elements this TOC values agree well with the initial OM content in weight close to 5% for all land samples (cf. cell compaction dataset Section 3-4-). The TOC values for the marine samples on the other hand are very low despite an initial OM weight content around 6% for all marine samples. The TOC values computed from Rock-Eval tests are an indirect

measurement. This means the OM in the marine samples has a low HC productivity and the mix of elements of the fresh marine OM is probably relatively poor in carbon compared to the land OM. This is confirmed by the HI and OI that are higher for the marine samples, indicating a lower organic carbon content.

It can also be noted that strong differences between the samples containing fresh OM (maturity level 0) and the mature ones. Within each OM type, the fresh samples have an S1 value approximately three times higher than the mature samples. This is due to the natural oils and other volatile compounds found in fresh OM that were eliminated during the maturation process that leads to maturity levels 1 and 2. The fresh samples also have slightly lower S2 values which indicate that the fresh OM was partially transformed into kerogen from level 0 to levels 1 and 2 and thus the maturation process increased the HC production potential of the samples. The S3 value is higher for the fresh samples which is directly correlated to a higher OI and indicates a lower thermal transformation, especially for the land sample (Hetényi, 1998).

The Tmax value is a proxy for the maturity of the samples. It is measured with a precision of ±1°C. The marine samples show an increase of Tmax from 434^0C at maturity level 0 to 444^0C at maturity level 2. This corresponds to a shift of the OM from immaturity to the middle of the oil window (Espitalié, et al., 1985-86). In contrast the Tmax values of the land samples are almost constant with an average of 431^0C. This would mean that the land OM has a constant maturity across all three levels. However a closer look at the emitted HC curves during the Rock-Eval tests, called pyrograms (Figure 4-36) allows us to nuance this conclusion.

The part of the curve under t = 3 minutes where the temperature is at a constant 300^0C corresponds to the peak S1. The HC emission of the peak S2 is located on the part of the curves where the temperature is increasing between t = 3 minutes and t = 19 minutes. We can see that the fresh samples have an S2 peak with a bimodal shape which is more pronounced for the fresh land sample. The first peak of S2 is located at a lower temperature than the main peak (around 350^0C). This highlights the presence of functional groups (acids, ketones, alcohols, etc.) and shows the very low thermal maturity of the fresh OM. The mature samples however display a single S2 peak above 400^0C and are thus thermally more mature.

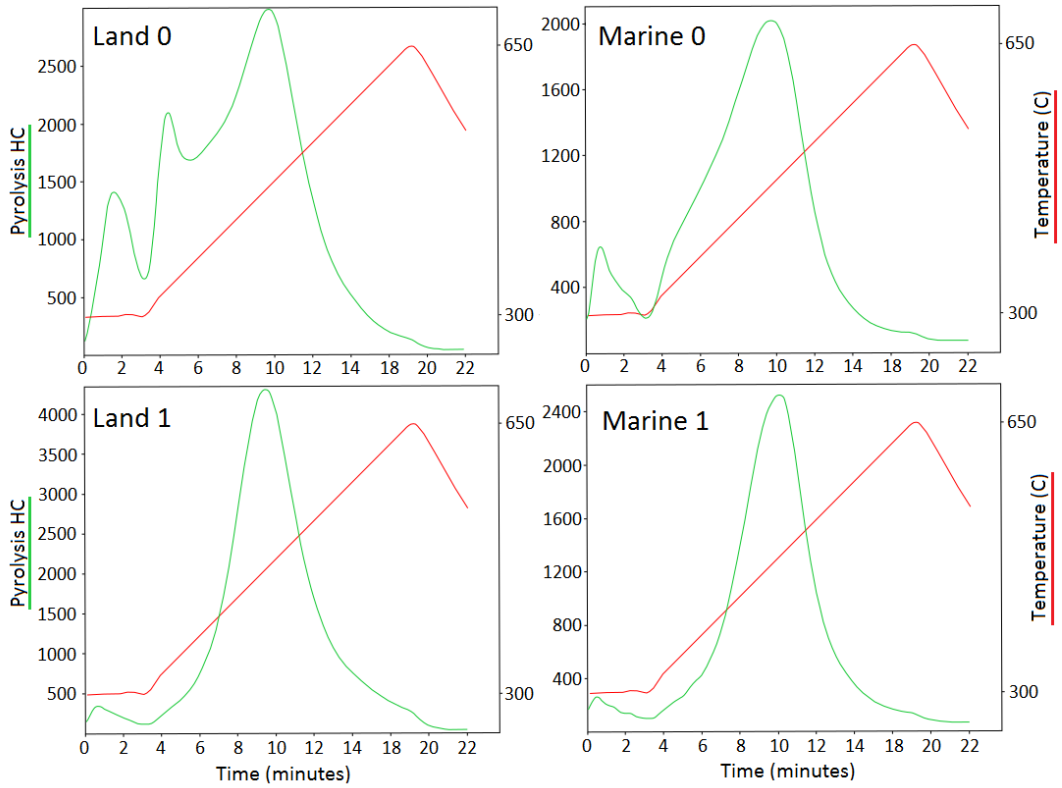

Figure 4-36: Pyrogram of the volatilised hydrocarbons measured with a flame ionisation detector during the heating of the samples in an inert atmosphere (N_2).

The HI and OI can be used to determine the maturity and kerogen type embedded in OM. To check that our samples are a good proxy for kerogen type II and III (phytoplanktonic and land plants origin, respectively) and to have another indication of their maturity we plotted the HI an OI values on a Krevelen-type diagram (Figure 4-37). The OM in the land samples can be considered as type III kerogen as it ranks low on the diagram. The OM in the marine samples has higher HI values but appears as intermediate between type II and III. Nevertheless it has been found by many authors that Rock-Eval HI can underestimate the HC potential of oil prone kerogen (Peters, et al., 2016); (Baudin, et al., 2015) such as phytoplanktonic type II and the actual H/C ratio as could be measured with an elemental analysis may place the marine samples closer to the type II line on the Van Krevelen diagram.

On the Van Krevelen diagram the most mature sample tend to cluster on the lower left corner of the diagram. As expected the fresh samples have the lowest maturity but surprisingly the mature land samples appear more mature than the mature marine samples. This is in opposition with the results found by observing the Tmax values.

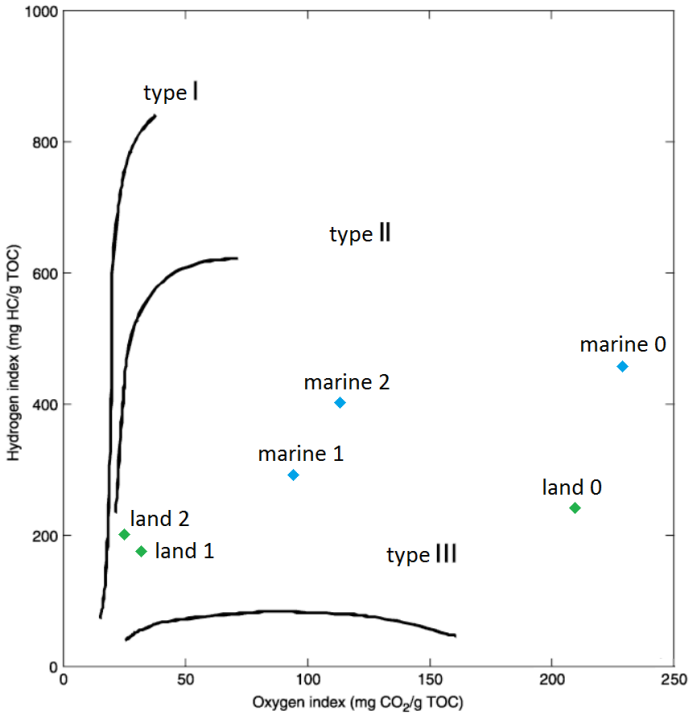

Figure 4-37: Modified Van Krevelen diagram that uses Rock-Eval computed HI and OI for the six samples tested by Rock-Eval pyrolysis.

Summary

The maturity level of 6 artificial samples covering the full range of OM type investigated in this thesis (both land and marine, with fresh and 2 different levels of maturity each) was quantified by performing Rock-Eval pyrolysis tests. The set of parameters deduced from these tests, leads to the conclusion that **the OM in the land samples can be considered as type III kerogen and the OM in the marine samples as type II kerogen. This quantitative analysis will be used in the next chapters to link thermal maturity with the evolution of porosity during compaction and elastic parameters such as P-wave anisotropy and Vp/Vs ratio.**

4-5- Summary of chapter 4

In the fourth chapter of this thesis the focus was placed on imaging and characterization testings on the artificial samples after their compaction. Hence the results reflect the final state of the samples after unmoulding from the compaction cell. This series of separate experiments were used to (i) assess the similarity of the inorganic matrix between samples and quantify the differences in OM characteristics and (ii) supplement the dataset of physical properties obtained during compaction with dielectric measurements.

Imaging of the samples was carried out at two different scales: the macroscopic scale wherein the totality of each sample was imaged with a medical CT-scanner and the microscopic scale with an optical microscopy image of a thin section extracted from each sample.

The CT images were used to assess the bulk density and the values found match very closely the bulk density measured by volume and weight measurements with an average difference between the CT-scan bulk density and the physical bulk density of 0.012g/cm^3 and a maximum difference of 0.027g/cm^3. This confirms the good accuracy of our measurement. Thereafter the density was computed in different areas of the samples along four different directions (vertical, horizontal, lateral and radial) to monitor the homogeneity of the sample. It was found that some of the differences in CT number inside the samples were due to reconstruction artefacts. However once they were taken into account, the only significant density variation with a physical origin was found in the vertical direction. The density close to the top and bottom of the samples, near the location of the porous plates during compaction are denser than the centre of the samples. The difference between the highest and the lowest density within a single sample is of the order of 0.04g/cm^3. The three samples containing OM macro-particles ("land 0 flakes mixing", "marine 0 flakes mixing" and "land 0 flakes sedim.") were analysed to evaluate the size, aspect ratio and orientation distribution of the particles with a size above the detection threshold of the CT-scanner (0.2mm^2 or an equivalent diameter of 0.5mm for a spherical particle). The vertical distribution of the sample made with the sedimentation method was not as homogeneous as the sample made with the mixing method and its average aspect ratio was found to be the highest. The marine sample contains much less visible macro-particles (diameter

between 100µm and 2300µm) than the land samples. This lesser number of particles induced a more dispersed orientation distribution for the marine samples whereas the two land samples have a nearly identical orientation distribution.

In the microscopy images the OM particles and non-clay mineral particles were isolated from the matrix to compute the distribution of their size, aspect ratio and orientation in a similar way than for the OM macro-particles in the CT images. The non-clay mineral particles covered on average 3% of the studied area. Considering they make up about 60% of the initial mineral volume this means that 95% of them were smaller than the detection threshold of the microscopy images (68µm^2 or an equivalent diameter of 9.3µm for a spherical particle). However all the computed parameters on the non-clay mineral population indicate a very stable inorganic phase among the sample set. The OM particles on the other hand display much more variability. The fresh marine OM particles are on average smaller than their land counterparts, both for the powder and flake texture (average of 15µm against 40µm, respectively). Consequently, the area covered by fresh marine OM particles is smaller than that of land samples. This indicates that fresh marine samples have a higher proportion of OM particles below the detection threshold. All mature samples have a similar particle size distribution with particle sizes similar to that of the fresh land powder sample. The land flake samples have the biggest particle size (average of 50µm) but their particle size distribution displays a more disorganised shape above 100µm. This is due to the size of the studied area that is too small to be representative of the distribution of the bigger particles. The standard deviation of the orientation distribution relates to how strongly the particles are oriented with regard to the main orientation (perpendicular to the compaction direction). A strong correlation was found between aspect ratio and the orientation standard deviation. The samples with the most elongated OM particles, including the land flake samples, thus have the strongest horizontal orientation of OM particles.

To test the dielectric properties of the samples two 10mm thick slices were extracted from each sample. The orientation of the two slices was perpendicular to each other so that the dielectric response could be measured in the compaction direction and in the horizontal direction in order to compute the dielectric anisotropy. It was found that the maturity range in our sample set had little to no influence on the dielectric properties. However other OM characteristics influenced the results significantly. The

OM type has an influence on the equivalent conductivity and on the increase of the anisotropy of the real dielectric permittivity with frequency. Namely the presence of marine OM increases the conductivity twofold for most of the frequency range in both the horizontal and vertical direction and it delays the occurrence of the maximum of the real dielectric anisotropy from 20MHz to 40MHz compared with the land and inorganic samples. The samples containing flake OM particles show slightly higher anisotropy of the real and imaginary permittivity at high frequency than their powder equivalents but most significantly the flake samples have a greater conductivity anisotropy above 200MHz. Finally the samples produced with the sedimentation method present lower anisotropies for all three measured parameters than the samples produced with the mixing method and the presence of OM increases the anisotropy differences between sedimentation and mixing method.

Six of the samples were tested using the Rock-Eval pyrolysis technique to evaluate their maturity and the composition of the OM they contain. For each OM type one fresh sample containing the powder texture type OM and two mature samples of maturity level 1 and 2 were tested. Overall the land samples emitted more hydrocarbons and thus have a greater production potential and a higher computed TOC than the marine samples that are relatively poorer in organic carbon as indicated by higher Oxygen and Hydrogen indexes. On the other hand the land samples did not show any evolution of thermal maturity as measured by the parameter Tmax and are all ranked just below the immature/oil window limit. The marine samples display an increase of Tmax from the fresh sample to the maturity level 2 sample ranging from immature to the middle of the oil window. The two fresh samples had a high oxygen content and a bimodal hydrocarbon pyrogram which indicates the presence of functional groups in the OM. This shows a very low degree of thermal transformation and was not observed for any of the mature samples.

In conclusion the tests described in this chapter provided a confirmation of a very low variability of the inorganic phase across the sample set, strong differences in the OM type, texture and maturity which in turn lead to different dielectric behaviours between samples with different OM characteristics. In the next chapter the results obtained with the different tools are combined to carry out interpretations.

Chapter 5: Interpretations - Combined analysis of the different data sets

5-1- Impact of Maturity

One of the main objectives of this project was to investigate how the maturity of OM in shales affects their physical properties and their anisotropy. This stems from the fact that the elastic and electrical properties of OM change during thermal maturation. For instance it was found that as maturity increases, OM becomes less electrically resistive (Yang, et al., 2016), elastic velocity Vp/Vs ratio decreases (Zhao, et al., 2016) and the elastic young's modulus measured with nanoindentation techniques also decreases (Zargari, et al., 2013). In this section the results of 6 samples containing OM with two different origins (land and marine) will be analyzed, at different maturity levels, and one inorganic sample as a comparison. It is important to mention that besides OM maturity all the characteristics of the samples were aimed to be constant (mineralogy type and content; rate of compaction, etc.). However a few differences remain: (i) the OM particle size is smaller in the marine sample with the lowest maturity and (ii) all marine samples have lower porosities (and so higher bulk densities) than the land samples.

First of all the metrics to quantify the maturity level were identified. The maturation process by hydrous pyrolysis and the Rock-Eval pyrolysis tests provided us with three measures of maturity:

- Length of time in hydrous pyrolysis cell: the maturity level 0 corresponds to fresh OM incorporated directly in the samples. The maturity level 1 and 2 corresponds to 3 and 6 weeks respectively of artificial maturation at 200^0C, in a confined environment and in the presence of water and swelling clays (cf. section 3-2-).

- Tmax parameter: this is the main indicator of maturity during Rock-Eval pyrolysis. During the step where temperature increases from 300^0C to 650^0C at 25^0C/min, this is the temperature value for which the maximum rate of HC emission is attained. The Tmax data is presented in Table 5-1. The marine samples show an increase in Tmax with the maturity level that corresponds to an increase in maturity from immaturity to the middle of the oil window. The land samples have a stable Tmax value around 431^0C, below the immature/oil window limit of 435^0C.

- Oxygen index (OI) and Hydrogen index (HI): HI decreases with increasing maturity but OI is also a good indicator of maturity for low maturities as it decreases drastically early in the maturation process. The combination of OI and HI shows that the two samples of maturity level 0 are highly immature with a high OI and that the mature land samples appear more mature with OI and HI both lower than the marine samples. This can be explained by an overall lower carbon content in the initial microalgae material constituting the marine OM and a probable error in the estimation of HI for oil prone OM such as marine OM that is typical in Rock-Eval tests (Peters, et al., 2016).

Maturity level	Tmax Land samples			Tmax Marine samples		
	Tmax °C	ρ_{OM} g/cm3	max(ε'r) anisotropy	Tmax °C	ρ_{OM} g/cm3	max(ε'r) anisotropy
0	433	1.45	2.362	434	1.84	2.361
1	429	1.63	2.565	440	1.88	2.845
2	432	1.43	1.98	444	1.82	2.119

Table 5-1: Tmax, dry OM density (ρ_{om}) and maximum anisotropy of the real dielectric permittivity (ε'_r) values for the six samples tested by Rock-Eval pyrolysis.

As a result, Tmax is a better parameter to evaluate the maturity of marine OM but is not suitable for the land samples as they have a very narrow range of Tmax values. On the contrary OI and HI are a good indicator for the land maturity but are not suitable to evaluate the maturity of marine samples due to the inherent error of Rock-Eval tests with samples containing oil-prone OM. On a Van Krevelen diagram (as pictured in section 4-4- Figure 4-37), the more mature sample tends to be located on the bottom left corner, where HI and OI are closer to 0. We will therefore take the value $\sqrt{HI^2 + OI^2}$ as an indicator of the maturity of the land samples which is the distance from the point of coordinates (0, 0) on the Van Krevelen diagram.

Besides, the density of the dry OM and the maximum value of the anisotropy of the real part of the dielectric permittivity are presented in Table 5-1. The density does not evolve like the maturity. For both OM types, the OM density is the highest for maturity level 1 and the lowest for maturity level 2, with maturity level 0 falling in between. Interestingly, the real dielectric anisotropy variations follow the same order as the OM density (Figure 5-1). Though the thermal maturity does not affect the dielectric

properties, it influences the evolution of the dry OM density. Two mechanisms during the maturation of OM impact its density:

- The density of kerogen increases with maturity (Okiongbo, et al., 2005).

- As HC are generated, part of the kerogen is converted to bitumen, which has a significantly lower density close to the density of water (Pepper, 2017). This explains the evolution of density seen in our samples, which increases between maturity levels 0 and 1, and then decreases at level 2 when more bitumen is generated. This is a strong indication that cracking reactions did happen in significant proportions during the artificial maturation of our samples.

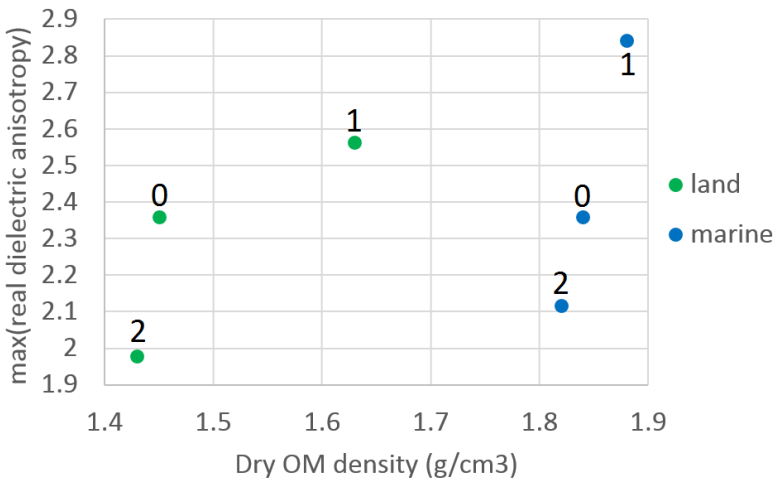

Figure 5-1: Maximum of the real dielectric permittivity anisotropy as a function of the dry OM density contained in the samples. The labels next to the data point indicate the maturity level.

The decrease in porosity ($\Delta\Phi$) in the three different steps of compaction is clearly influenced by the sample maturity (Figure 5-2). The difference is not visible in step 1 where for each OM type the mature samples have values similar to that of the fresh samples. But in steps 2 and 3 the mature marine samples display more porosity loss than the fresh marine sample and on the contrary the mature land samples display less porosity loss than the fresh land sample. From an elastic point of view, we can see in Figure 5-3 that the mature samples have a higher P-wave anisotropy (ε) and a lower Vp/Vs ratio than the fresh samples.

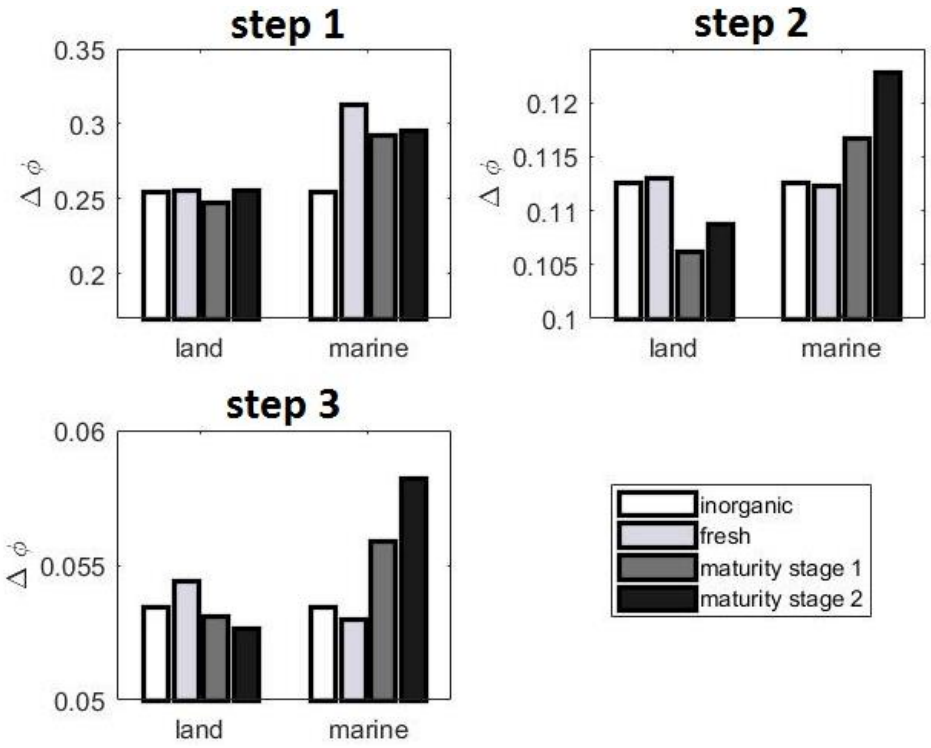

Figure 5-2: Porosity drop at each compaction step for samples of different OM maturities and for an inorganic shale sample. These organic shale samples were produced using the mixing method with OM particles of the powder type.

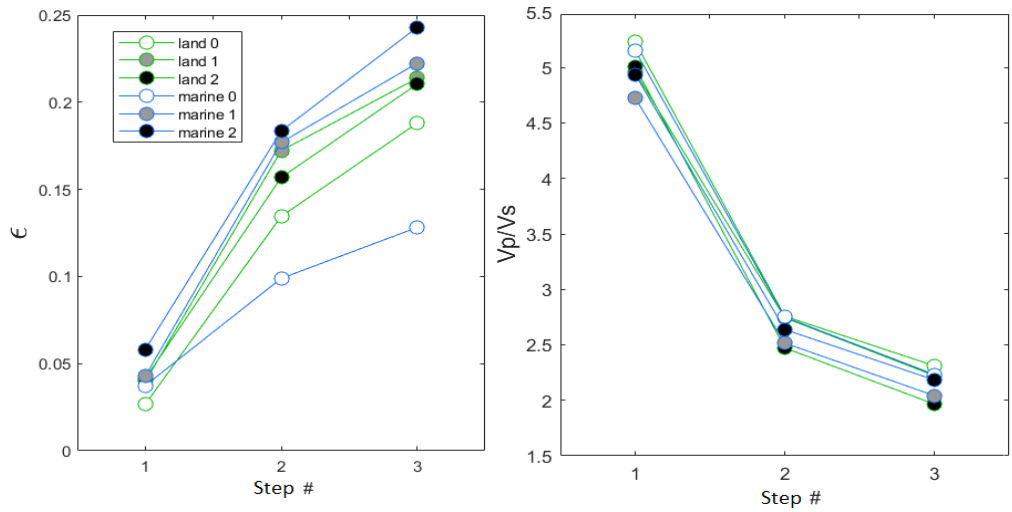

Figure 5-3: Thomsen's anisotropy parameter ε (left) and Vp/Vs ratio (right) for synthetic samples containing either land or marine organic matter with three different maturity levels for the three compaction steps. Level 0 denotes fresh organic matter whereas levels 1 and 2 correspond to 3 weeks and 6 weeks of maturation in a hydrous pyrolysis apparatus (more details on maturation in chapter 3 section 2).

Investigating further the OM maturity, porosity and elastic parameters are well related. In Figure 5-4 are presented the change in porosity values (ΔΦ) for each compaction step as a function of HI and Tmax for step 1; and as a function of Tmax only for steps 2 and 3. In step 1, ΔΦ does not seem to be affected by Tmax in a significant way and the most obvious difference in Tmax is due to the OM type. However ΔΦ in step 1 is positively correlated with HI. Marine OM with algal origin typically has a higher atomic H/C ratio than land OM composed of terrestrial plants (Durand, 1980). Furthermore the cellular structure of land OM is stiffer than that of marine algae due to the presence of some phenolic compounds, such as lignin, that provides terrestrial chlorophylian organisms a protection against desiccation, UVs and a higher structural rigidity (Waters, 2003). By extension it can be surmised that a higher HI implies a lower stiffness, for immature OM at least. Hence the OM with a higher HI will be more prone to deformations and reorganization in the quickly changing porous space of the rock in its early consolidation process.

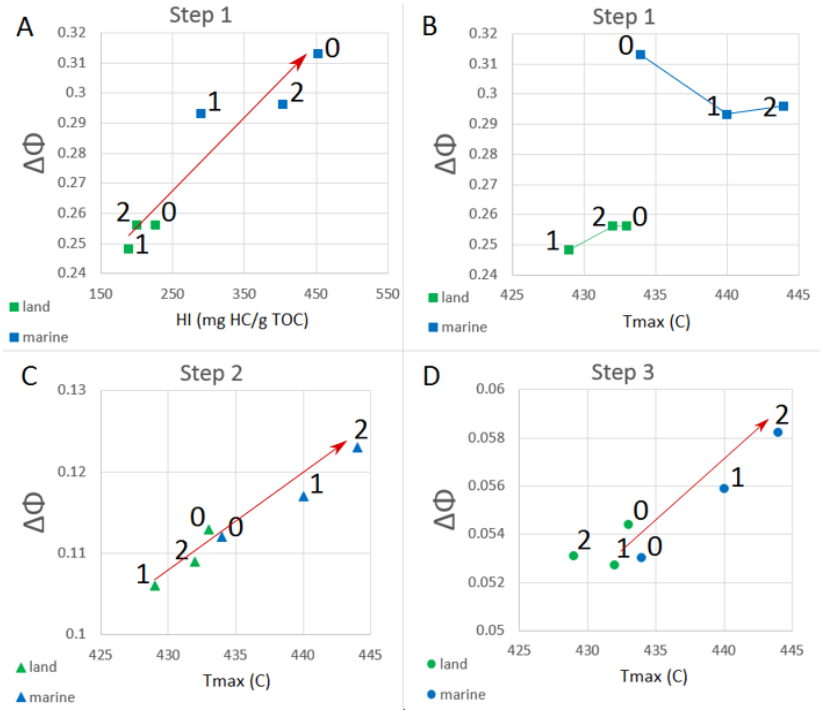

Figure 5-4: Drop in porosity (ΔΦ) from the beginning of a compaction step to the time when 90% of the pore pressure dissipated. A- ΔΦ as a function of HI in compaction step1. B- ΔΦ as a function of Tmax in compaction step 1. C- ΔΦ as a function of Tmax in compaction step 2. D- ΔΦ as a function of Tmax in compaction step 3. The labels next to the data point indicate the maturity level.

$\Delta\Phi$ in steps 2 and 3 on the other hand is positively correlated to Tmax. The link is less clear in step 3 for the land samples that form a cluster of points where small differences in $\Delta\Phi$ are close to the uncertainty on the porosity measurement. Mature OM tends to be more porous than fresh OM by transformation of part of the kerogen into HC (Curtis, et al., 2012). Thus in the later stages of a rock compaction when most of the solid phase reorganization occurred and grains are tightly packed (steps 2 and 3), the prime mechanism of porosity loss in OM will be pore collapse. Therefore the samples with the higher Tmax, which have a more porous OM, will have an increased $\Delta\Phi$ compared to more immature samples.

Moreover the anisotropy parameter ε is heavily impacted by the maturity indicator Tmax for the marine samples and the maturity indicator $\sqrt{HI^2 + OI^2}$ for the land samples (Figure 5-5). Indeed increasing maturities increases Thomsen's anisotorpy ε in all compaction steps. Note that the land samples of maturity level 1 are rated as more mature than the maturity level 2 with this indicator. We also see that in both OM types the most important differences both in terms of maturity and increase in anisotropy is seen between maturity levels 0 and 1. The maturity and anisotropy difference between the two mature samples is less pronounced.

In Figure 5-6 is a graph of Vp/Vs ratio as a function of OI. Because P- and S-wave velocities vary with the direction of measurement we took the average of the vertical and horizontal velocity to compute the Vp/Vs. The maturity has an influence on the Vp/Vs ratio whereby decreasing OI reduces Vp/Vs. Indeed it was found that OI is a good indicator of maturity for immature OM (Hetényi, 1998). It can also be noticed the impact of OM type with marine samples having a higher OI and the compaction that decreases Vp/Vs because S-wave velocity is the most affected by the consolidation of the solid phase.

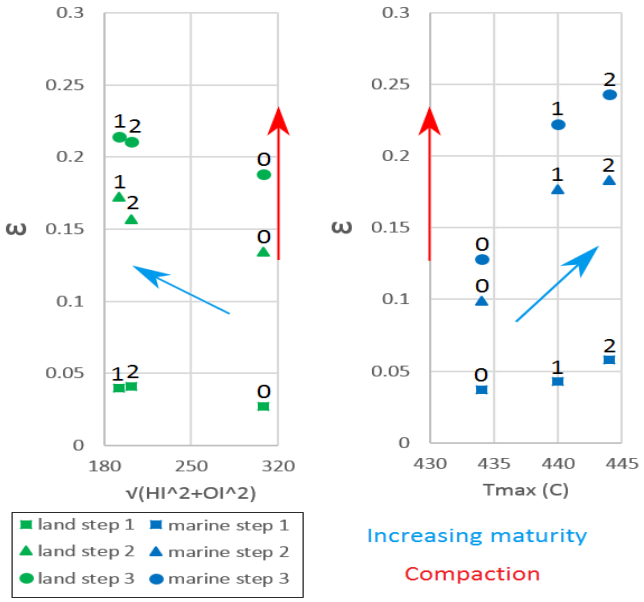

Figure 5-5: Thomsen's anisotropy parameter ε as a function of the maturity indicator $\sqrt{HI^2 + OI^2}$ *(left) and as a function of Tmax for different OM types (green for land OM and blue for marine OM). The labels next to the data point indicate the maturity level. The blue arrow shows the increasing maturity while the red arrow marks the increasing compaction.*

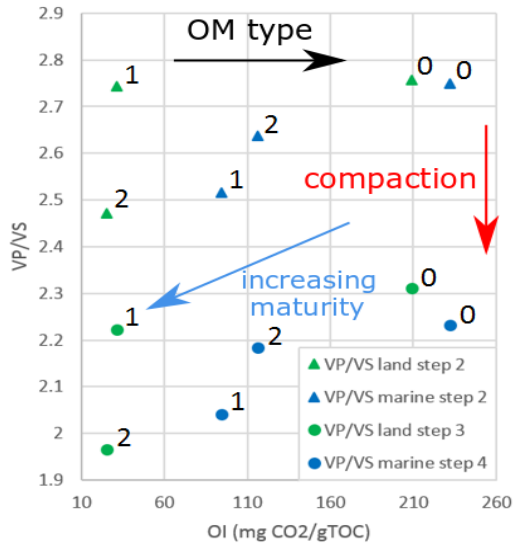

Figure 5-6: OM maturity effect between elastic Vp/Vs ratio as a function of Oxygen Indicator (OI) for different OM types (green for land OM and blue for marine OM). The labels next to the data point indicate the maturity level. The blue arrow shows the increasing maturity while the red arrow marks the increasing compaction intensity. Note the shift in OI from low to high values in OI between Land and Marine OM (black arrow).

Summary

The maturity, in terms of HC content and HC potential affects the porosity loss during compaction only when the solid phase is tight with many grain contacts. In these conditions further deformations induce pore collapse within the OM particles. But the porosity loss during early consolidation is rather influenced by the OM type. The maturity as measured with indicators such as Tmax, HI and OI also increases the P-wave anisotropy parameter ε. When looking at the OI, a maturity indicator for low maturities, a reduction of the Vp/Vs ratio with maturity can be observed. Finally, the density of OM is correlated to the real dielectric anisotropy but the evolution of density with thermal maturity is not linear. Furthermore the impact of maturity is concomitant with other characteristics of the sample such as OM type and stress history.

5-2- Impact of OM texture

To relate the effect of texture on the physical properties of different samples, the differences in texture between these samples needs to be quantified. To do so the particle size distributions obtained with the CT-scan images were combined (see Section 4-1-) with the ones obtained with the microscopy images (see Section 4-3-). For the powder texture type, the OM particles were too small to be visible on the CT-scan and it did not require combination though it was necessary for the flake texture type that includes a wider range of OM particle sizes.

The size range of the particles detected with the optical microscopy data is [9µm - 1000µm] and the size range of the CT-scan data is [500µm - 2300µm] allowing some overlap between both particle size datasets. On the interval from 500µm to 1000µm it was decided to only take into account the CT-scan data as it covers the entire sample volume and is thus more representative than the subsection of the sample represented in the microscopy 2D image. The microscopy size range was thus limited to [9µm - 500µm].

To calibrate the relative amplitudes of the two size distributions, the coverage of OM out of the total area of the images for each dataset was used. The samples were designed so that the OM volume represents close to 8% of the sample. If a 2D image perfectly representative of the whole sample could detect all particle sizes, the coverage of the image should be 8%. The particle coverage in CT and optical microscopy images varies from this value because of the presence of particles smaller than the detection threshold and because of the representativity of the image compared to the whole sample:

(i) For the two land flake samples, the sum of the microscopy and the CT coverage of the OM volume exceeds 8%. This is most likely due to an over-representation of particles bigger than 100µm in the investigated area of the microscopy images. This line of reasoning is strengthened by the low representativity of particles above that size which manifests by a high variability of the size distribution of the optical microscopy data and deviates significantly from the bell shape otherwise observed for the rest of the size distributions (red interval in Figure 5-7).

(ii) For the marine flake sample, the sum of coverages OM volume is lower than 8%. This is due to an important quantity of particles below the detection threshold of the optical microscopy data (9µm). We also suspect an under-representation of particles above 100µm, where the size distribution presents a gap (Figure 5-7).

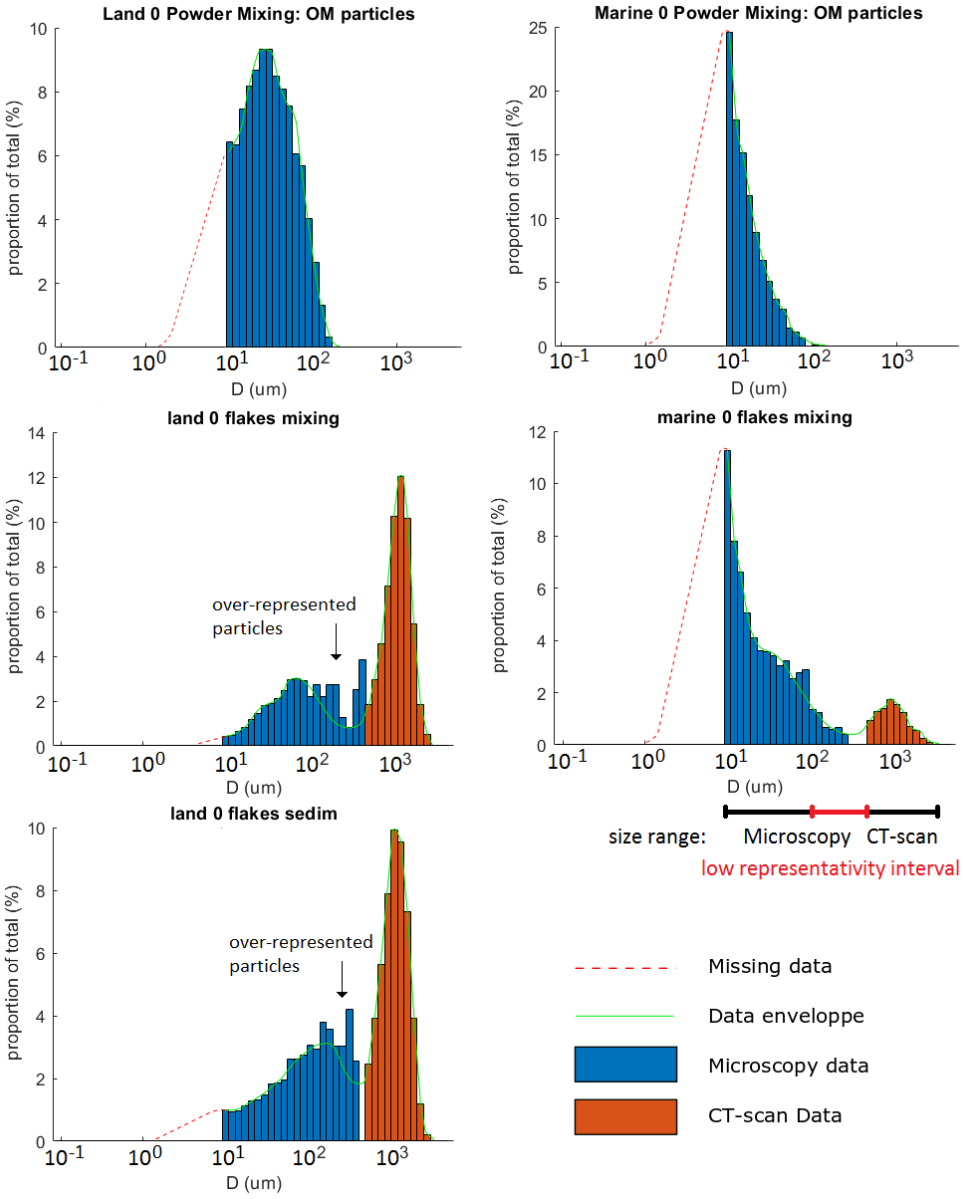

Figure 5-7: Combined OM particle size distribution from the CT-scan and microscopy data for the samples with different texture types. Left column: land samples. Right column: Marine samples. First row: powder texture type. Second and third row: flakes texture type.

With this information, for the two land flake samples where the sum of OM volume coverages exceeds 8%, the proportion of the total size distribution covered by the CT

data was thus defined as the ratio of CT coverage to the total volume content of OM and the remaining proportion of the OM was attributed to the size distribution in the microscopy data. The different OM coverage values and the relative proportions of each dataset are presented in Table 5-2.

Sample name	CT-scan coverage (%)	Microscopy coverage (%)	CT Proportion of total OM (%)	Microscopy Proportion of total OM (%)	Proportion of total OM included in the size distribution (%)	Median size vol. (µm)
Land 0 flakes mixing	4.5	5	56.3	43.7	100	871.4
Land 0 flakes sedim	4.2	8.6	52.5	47.5	100	648.1
Land 0 powder mixing	0	6.1	0	76	76	32.94
Marine 0 flakes mixing	0.8	5.2	9.8	65	74.8	58.1
Marine 0 powder mixing	0	4.7	0	59	59	16.25

Table 5-2: OM particle volumetric coverage and relative proportions out of the total amount of OM for each dataset. The median size in volume computed from the particle size distribution in Figure 5-7 represents the particle size for which 50% of the OM volume is made of smaller particles and the other 50% of bigger particles.

This joint 3D-XCT & 2D-optical images method is certainly not accurate enough due to image resolution limitations and the true relative coverage of each dataset may vary from what was defined. However it provides a first order range of particle sizes and the general shape of the whole particle size distribution of the flake texture type. The results of the two datasets combination are presented in Figure 5-7. Note that in the particle size distribution, the width of the bins were modified from the particle size distribution presented in Sections 4-1- and 4-3- such that all bins have an equal width. The data envelopes in green are an estimation of the shape of the particle size distributions taking into account the over- or under-representation of particles in the upper end of the optical microscopy size range. The missing data curves are only a rough extrapolation considering a gaussian distribution that is also proportional to the amount of OM not present in the data.

If the flake texture OM type presents a bimodal particle size distribution, the powder OM type shows a unimodal distribution in the investigated size range (Figure 5-7). The land OM particles have bigger particles than their marine equivalent; and are even bigger on average than the marine flake particles size. The land flake samples are the only ones that do not have a significant amount of OM particles with a size below the microscopy detection threshold (9 µm). The land flake sample prepared with the deposition method displays fewer particles in the CT size range and more in the microscopy size range than its equivalent made with the mixing method.

As a reminder from Sections 4-1- and 4-3-, we present the median and average values of the distributions of the aspect ratio and standard deviation of the orientation with regards to the direction of compaction computed from the CT-scan and optical microscopy images in Table 5-3:

Sample name		Aspect ratio		Standard deviation of orientation (degrees)
		Median	Average	
Land 0 flakes mixing	CT	1.83	1.98	30.3
	MI	2.23	2.55	24.89
Land 0 flakes sedim	CT	1.98	2.16	30.4
	MI	2.16	2.45	33.14
Land 0 powder mixing	MI	1.96	2.22	37.4
Marine 0 flakes mixing	CT	1.74	1.94	34.9
	MI	1.99	2.16	44.15
Marine 0 powder mixing	MI	2.09	2.28	38

Table 5-3: Aspect ratio and orientation parameters for the samples of interest for the analysis of the impact of OM texture. CT is for CT-scan data and MI is for optical microscopy data.

The aspect ratio of the particle size derived from the CT-scan images is lower than the corresponding microscopy images. Such discrepancy is attributed to the accuracy of the CT-scanner that reconstructs images with slightly more rounded particles than reality. The marine flake sample has the lowest aspect ratios of the three flake samples in both datasets but the ranking of the two land flake samples is reversed. From a particle orientation point of view, the standard deviation of the particle orientation no matter the OM type and texture is smaller for the CT data but the flake samples appear

in the same order of increasing standard deviation as land flakes mixing followed by land flakes sedimentation and marine flakes mixing. The overall aspect ratio and standard deviation of particles orientation are inversely proportional within each OM type, with higher aspect ratios being linked to lower standard deviations.

For comparison purposes the two dielectric parameters (presented in Section 4-2-) that were found to be the most affected by the OM texture type were compiled in Table 5-4. They both correspond to a maximum in anisotropy. The maximum anisotropy of the imaginary permittivity was located between 55 and 70 MHz depending on the sample. The conductivity anisotropy was found to be ordered by texture type above 200 kHz and it was decided to take the values near the maximum anisotropy at 7MHz. The land flake sample prepared with the sedimentation method has anisotropy values that do not match the trends of the other samples. However the deposition method was found to have a strong influence on the dielectric properties (cf. Section 5-4-). Therefore we will ignore this sample for the cross-property analysis related to the texture type.

Sample name	Maximum anisotropy of imaginary permittivity	Anisotropy of equivalent conductivity at 7MHz
Land 0 flakes sedim	2.13	2.18
Land 0 flakes sedim	1.86	1.88
Land 0 powder mixing	1.99	2.01
Marine 0 flakes mixing	2.02	2.07
Marine 0 powder mixing	1.89	1.8

Table 5-4: summary of the dielectric parameters the most affected by the texture type.

The anisotropy of the imaginary permittivity and of the conductivity have similar values and are ranked in the same order among the different samples. It is noticeable that the flake samples have the highest anisotropies in dielectric properties and the marine samples have lower anisotropies than their land equivalent. It is thus abundantly clear these values are linked to the particle size as shown in Figure 5-8. **The particles with a bigger size thus have a more important effect on the dielectric anisotropy**. The imaginary dielectric permittivity is linked to the work exerted (i.e. energy loss) by the polarization mechanisms. A higher anisotropy means the horizontal value (along the particle preferred orientation) becomes relatively more

important than the vertical value. Hence big particles, at high frequencies, induce more energy loss through polarization processes in the preferred orientation direction but promote the conduction processes in that same direction.

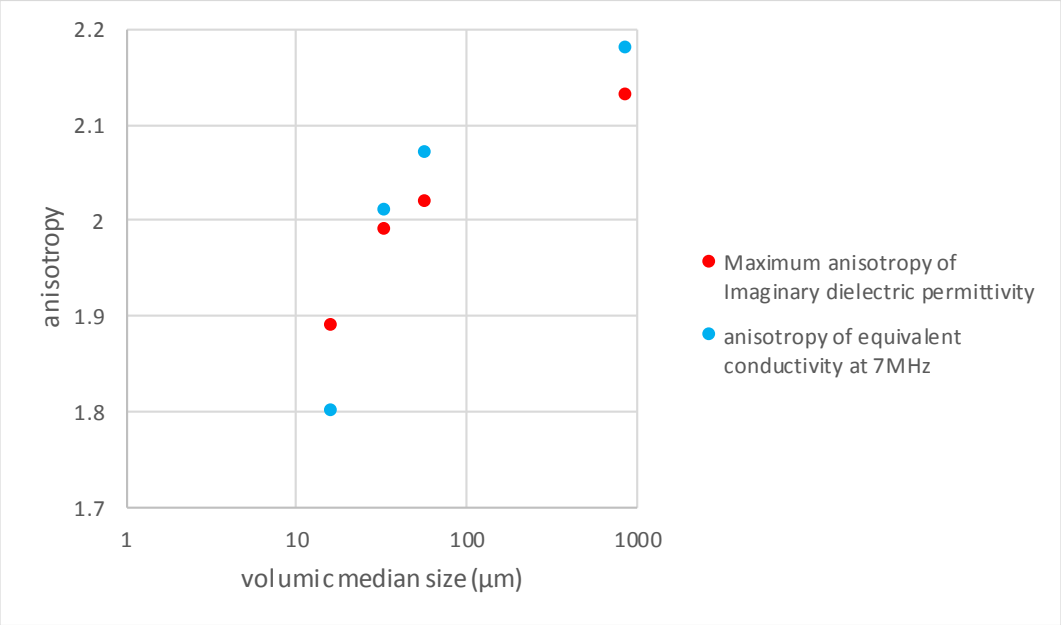

Figure 5-8: Anisotropy of two dielectric parameters (imaginary dielectric permittivity and electrical conductivity) as a function of volumetric median OM particle size.

Furthermore the texture has an effect on the elastic anisotropy. In particular, within each OM type, γ and δ parameters are consistently higher for the flake samples in compaction step 2 and 3 (Figure 5-9). The difference in the γ parameter shows the OM texture affects the propagation of S-wave. δ is computed with the stiffness coefficient c_{33} c_{44} and c_{13}. C_{13} was found to be the most impacted by the texture type (Figure 5-10) whereas c_{33} and c_{44} were roughly similar between textures in the same OM type. Hence the differences in the δ parameter with regard to the texture stem almost exclusively from c_{13}. Contrary to the dielectric anisotropies shown above, the OM type seems to have an effect on the elastic anisotropy that gets in the way of analysing the effect of texture. For both flakes and powder samples, the anisotropy of marine OM increases at a faster rate from compaction steps 1 to 3 and ends up systematically at higher values than the land OM in step 3. However the differences between the two textures are smaller for the marine samples than the land sample, just as there is less difference in particle size between the two marine samples than there is between the land samples. **It can thus be inferred that particle size has an influence on the γ and δ anisotropy parameter only second to the OM type**.

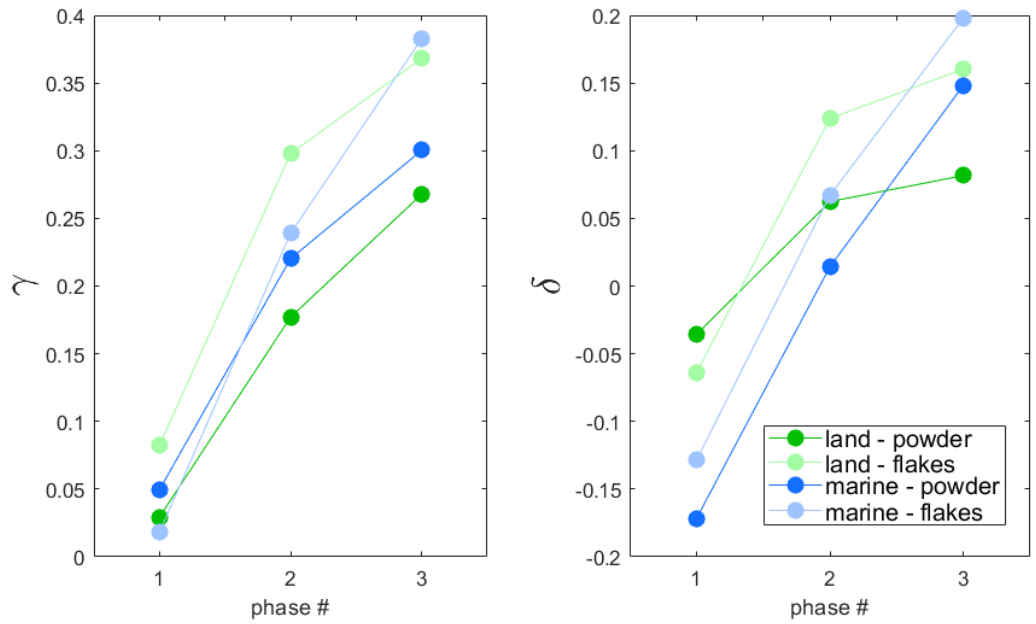

Figure 5-9: Evolution of elastic γ and δ parameters over the course of the three steps of samples compaction experiment with different OM texture types (flakes and powder) between land and marine OM.

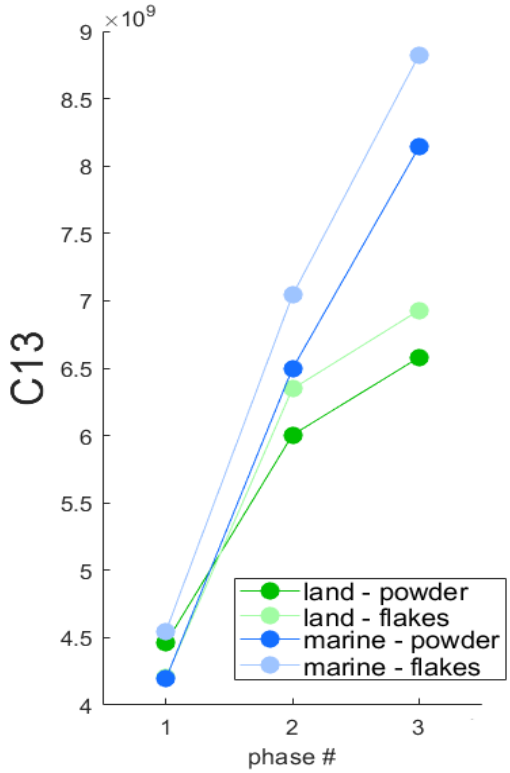

Figure 5-10: C_{13} stiffness coefficient computed from P-wave off-axis phase velocity, phase angle, vertical P- and S-wave velocities.

Summary

It has been demonstrated that the maximum anisotropy of the imaginary dielectric permittivity as well as the anisotropy of electrical conductivity are strongly correlated with the OM particle size. Namely particles with a bigger particle size will exhibit an increase in anisotropy at high frequencies. This can be used as a tool to assess the nature of the OM particles that can occur in shales as particulate of various size or nanocomposite embedded in the clay matrix. The type of particle is an important parameter as the contact surface between clay and OM will dictate the catalytic and retention effect of clays on cracking reactions and HC expulsion. The elastic anisotropy parameters γ and δ were also found to be influenced by the texture with flake particles increasing the anisotropy values but the additional influence of the OM type (land vs. marine) prevents the definition of cross-property correlations between elastic and dielectric parameters.

5-3- Impact of the OM type (land vs. marine)

In the two previous sections, where the focus was on the influence of maturity and texture of OM on the physical properties, mentions were made of the differences seen between samples of different OM type. Indeed it was found that the origin of the OM (land vs. marine) has the strongest impact on all properties studied in this work (density, porosity, dielectric and elastic) and is therefore visible in the majority of the measured properties. In this section the differences observed between land and marine samples will be summarized, while also displaying the behaviour of the inorganic control sample. All samples discussed here were prepared with the mixing method to highlight the effect of OM for analogous samples and this section will only focus on the results at the end of compaction step 3.

All differences linked to the OM type that were observed result from two factors: the lower elastic stiffness and the kinetics of thermal maturation of marine OM. The values taken by the physical properties presented here are consequences in a chain effect from these two initial governing factors.

As described in Section 5-1-, marine OM particles have a lower elastic stiffness than land OM particles and are thus more compliant (Waters, 2003). During the early consolidation, when a sediment evolves from a liquid slurry to a solid state with increasing grain contacts, the marine OM becomes less mechanically resistant to deformation leading to some structural reorganisation to fill in part of the decreasing porosity. Additionally the marine OM yields oil-prone kerogen whereas land OM yields gas-prone kerogen. Typically the production of light hydrocarbons such as natural gas occurs later in the burial of naturally occurring organic-rich sediments and therefore at a higher temperature (Philp, 2003). In a laboratory simulated maturation such as hydrous pyrolysis this means that when exposed to the same constant temperature for the same amount of time, marine OM will mature to produce a greater proportion of its total HC potential. A greater thermal maturity implies a greater OM internal porosity (Curtis, et al., 2012). In turn during later mechanical consolidation when the solid phase of the sediment gets progressively tighter and bears a higher portion of the compressive load, the more porous OM will be subject to a greater extent

to pore collapse, further reducing the porosity. In summary the higher compliance and higher thermal maturity of marine OM in the samples will induce more porosity loss, and consequently increase the bulk density of the final artificial samples (Figure 5-11). The bulk density of the marine samples is close to the bulk density of the inorganic control sample. However the porosity of the land samples, whose OM is more resistant to mechanical consolidation, is closer to that of the inorganic sample. The difference in bulk density and porosity between land and marine samples averages 0.07g/cm^3 and 5%, respectively. **From these observations it can be inferred that a shale sediment containing mostly OM with a terrestrial origin will appear less consolidated and less mature than a shale sediment containing mostly OM with a marine origin despite having the same stress and thermal history.**

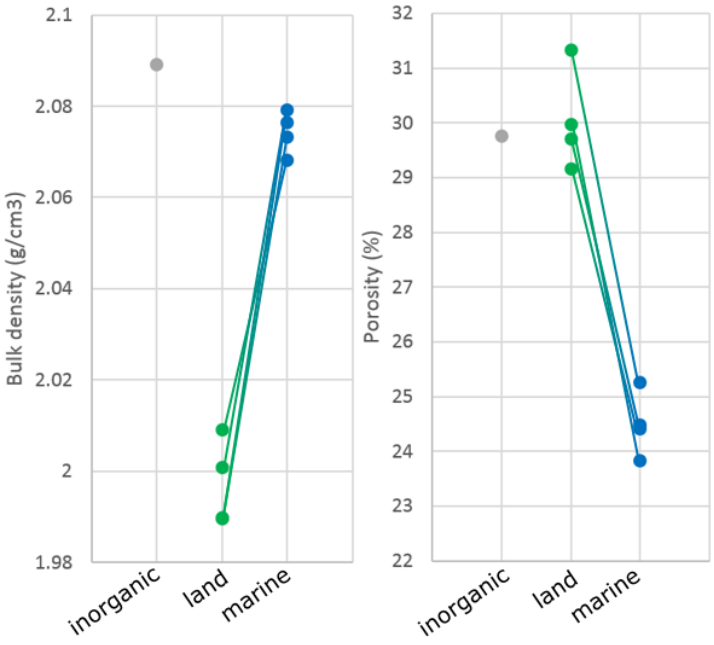

Figure 5-11: Bulk density and porosity of the 8 artificial samples at the end of the compaction. The land and marine samples are linked to their equivalent in each OM type (same texture type and maturity level).

The higher degree of consolidation of the marine samples results in higher ultrasonic velocities. This is true for P-waves but not for S-waves because S-waves are also strongly affected by the OM maturity level and its texture type. Among the three different directions of P-wave measurements, the vertical direction is the most consistent in terms of increase between land and marine samples (Figure 5-12 and Figure 5-13). The lower porosity of the marine samples also has a significant effect on

the dielectric parameters in the high frequency range (Figure 5-14). Indeed the inorganic samples and the land samples, which have similar porosities, also have similar dielectric properties. **The marine samples on the other hand have electrical conductivity values on average twice as large as other samples, and a maximum real permittivity anisotropy occurring at frequencies on average 50% higher than other samples**.

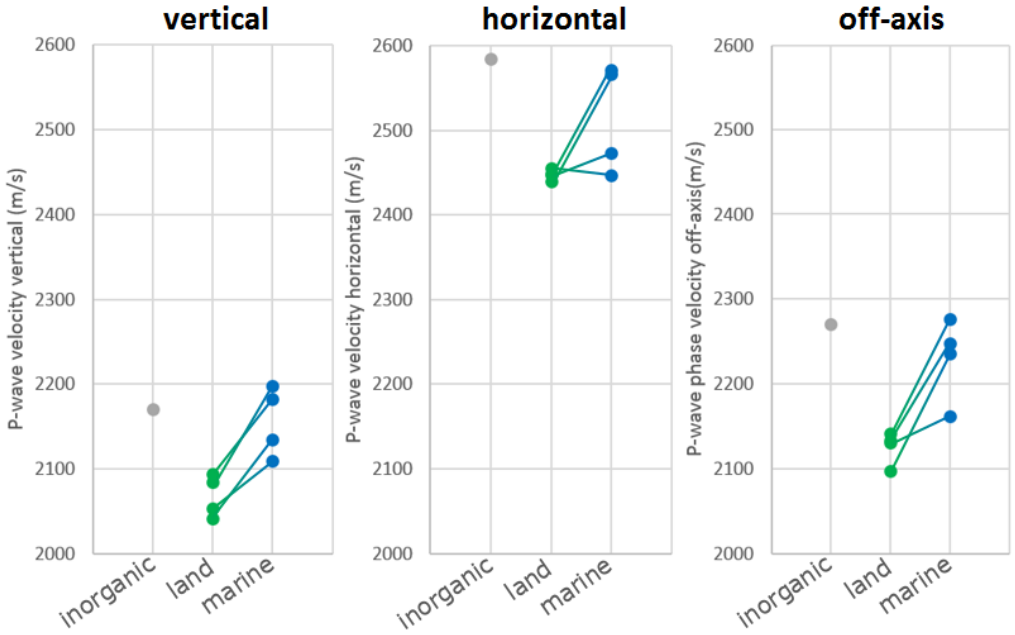

Figure 5-12: P-wave velocities of the artificial samples in three different directions (vertical, horizontal and at an intermediate off-axis angle) at the end of the compaction. The land (green symbols) and marine (blue symbols) samples are linked to their equivalent in each OM type (same texture type and maturity level). Inorganic samples in grey dot.

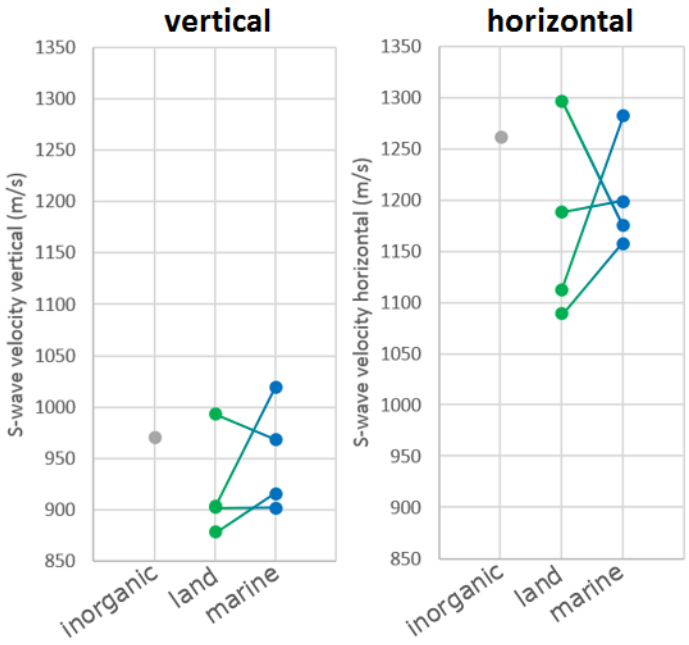

Figure 5-13: S-wave velocities of the artificial samples in two different directions (vertical with horizontal polarization and horizontal with horizontal polarization) at the end of the compaction. The land (green symbols) and marine (blue symbols) are linked to their equivalent in each OM type (same texture type and maturity level). Inorganic samples in grey symbols.

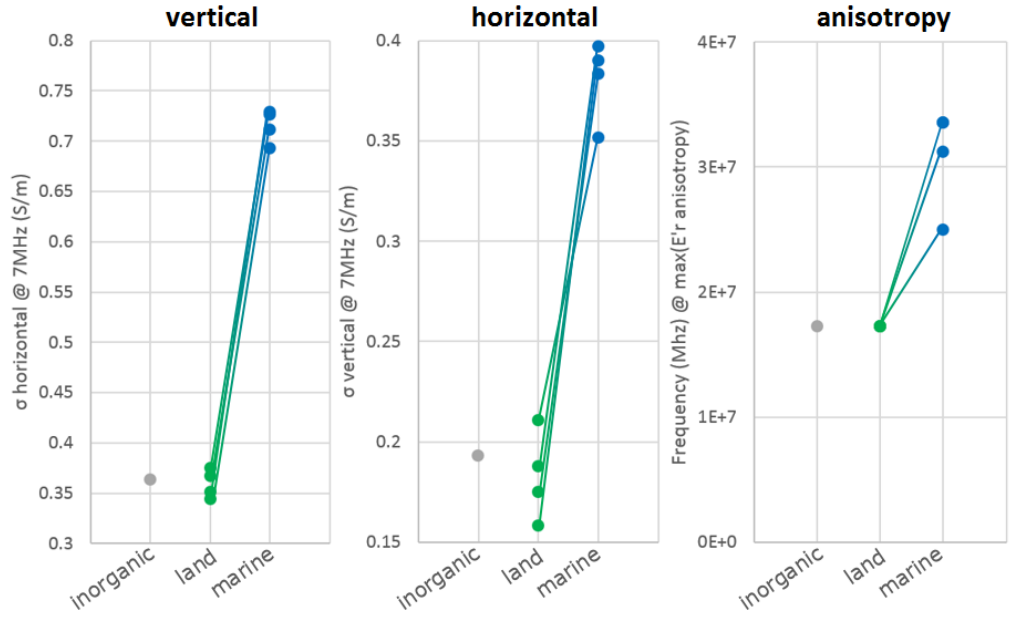

Figure 5-14: equivalent conductivity (σ) at 7MHz of the samples in the horizontal and vertical directions and maximum anisotropy of the real part of the dielectric permittivity (ε'_r) at the end of the compaction. The land (green symbols) and marine (blue symbols) are linked to their equivalent in each OM type (same texture type and maturity level). Inorganic samples in grey symbols.

To compare dielectric and elastic properties, we plotted both of them as a function of the strongest predictive parameter: porosity. Because vertical P-wave velocity is the most affected by the OM type, we decided to focus on the vertical P-wave velocity and vertical electrical conductivity only. On Graph A of Figure 5-15 the samples containing fresh OM display a quasi-perfect linear correlations between porosity and P-wave velocity (coefficient of determination R^2=0.99). The mature samples also display the same trend but with a smaller slope and with a smaller R^2 of 0.89. This shows that maturity also has an impact on P-wave velocity and the different mature samples do not have the same thermal maturity as measured by Tmax (cf. section 4-4- and 5-1-). Note that the sample 'land 1' is roughly at the intersections of the two linear trends. This can be explained by the fact that the sample 'land 1' displayed the lowest Tmax of all organic samples. The inorganic sample lies well outside the linear trends due to a significantly higher grain density.

On the graph showing the vertical electrical conductivity as a function of porosity (Figure 5-15-B), there are two clusters of points: (i) inorganic and land samples and (ii) marine samples. However the mature samples have on average higher conductivity values and are aligned well with a linear trend that has an R^2 of 0.98. The linear trend of the fresh samples has a lower R^2 of 0.95 because the conductivity is also affected by the texture type (cf. section 4-2-). The two linear trends are roughly parallel.

A relationship between P-wave velocity and conductivity can be established (Figure 5-15-C). It is clear that the separation of mature and fresh OM still occurs, with two linear trends roughly parallel to each other and a shift to lower velocities and higher conductivities from the fresh group to the mature group. However, their R^2 of 0.94 is slightly lower than the optimum linear relationships observed in Graphs A and B. Indeed if the porosity is the strongest predictor for both the P-wave velocity and the conductivity, the secondary influence of maturity and OM particle texture makes the establishment of cross-property relationships more complex.

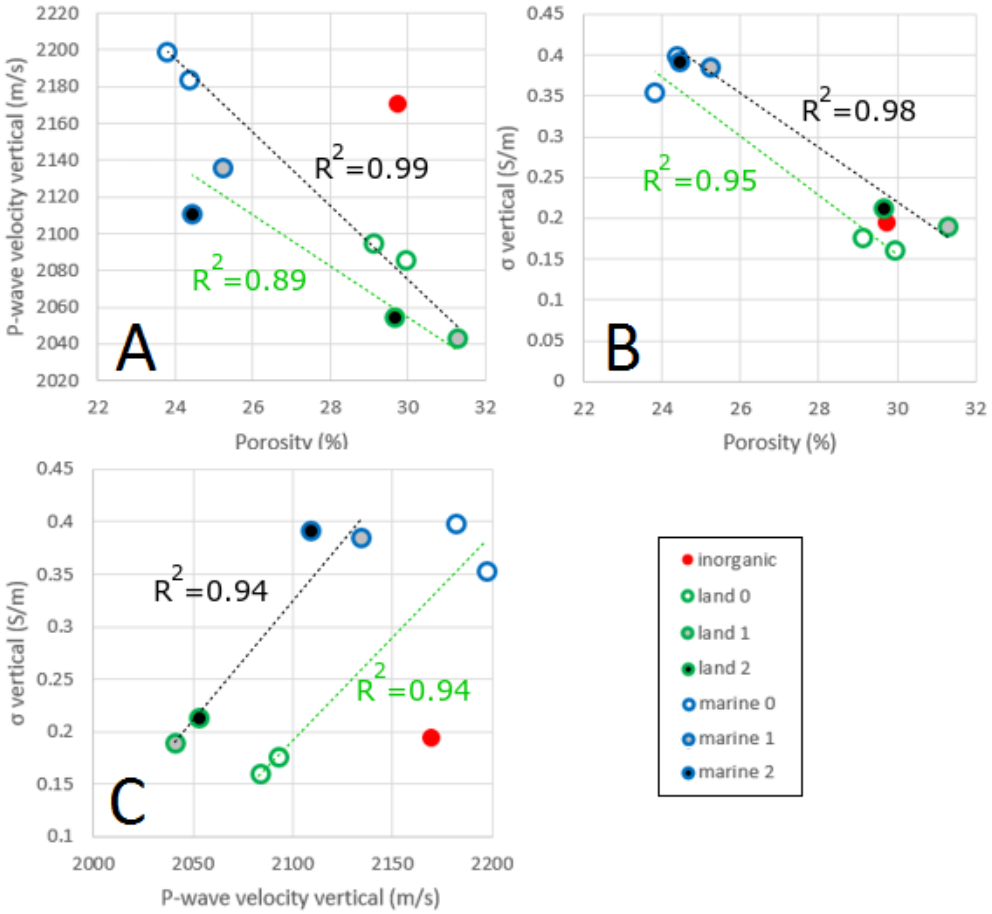

Figure 5-15: vertical P-wave velocity relationship with the vertical equivalent electrical conductivity of the samples at the end of the compaction. The relationship of each of these physical properties with porosity is the bridge that allows us to link them with each other. Linear relationships were established separately for the samples containing fresh OM (green dashed lines) and samples containing matured OM (black dashed lines).

Comparison with data from the literature

Han et. al. (2011) developed "*a three-phase effective medium model based on the combined self-consistent approximation and a differential effective medium model for quartz, brine and pore-filling clay minerals*". This model uses different parameters to model electrical resistivity (the inverse of conductivity) and P-wave velocity. The parameters are: Brine salinity, volume content and aspect ratio of the different phases (quartz, clay and brine), critical porosity and the water saturation (defined as =1 for the purpose of their study). The critical porosity is a porosity used to compute the properties of a two-phase effective medium which are then integrated in the

differential effective model as the matrix. There are two rounds of two-phase effective medium property computation to account for the three phases of the samples. This model is applied separately to compute P-wave velocities and electrical resistivity. The elastic and electrical models can then be joined by cross-plotting the modelled properties with the same model parameters (critical porosity and aspect ratio). Their results are compared with an experimental set of 67 natural sandstone samples with different clay contents. They show that the model gives reasonable agreement with their observations for both clean and clay-rich sandstones when a critical porosity of 0.5 and inclusions with an aspect ratio of 1, although the authors mention that a lower aspect ratio could be used to model more accurately samples with a higher clay content, which typically have a lower aspect ratio than other minerals..

This model assumes an isotropic material, which is not the case for the samples presented in this thesis. The P-wave velocity and electrical conductivity of the synthetic samples are tentatively compared in each direction: vertical (in the direction of compaction, i.e. along the symmetry axis of the transversely isotropic samples) and horizontal (in the plane of isotropy) with the model having the same parameters as in the study (critical porosity of 0.5 and aspect ratio of 1) in Figure 5-16.

It is interesting to see how the synthetic samples compare to natural samples of reservoir rock with a significant clay content. The synthetic samples are not as consolidated as the natural sandstones. For instance their porosity ranges from 0.24 to 0.31 whereas the natural samples range from 0.02 to 0.29. This results in an overall lower P-wave velocity and lower resistivity for the synthetic samples. The properties measured in the plane of isotropy (horizontally), are more in line with the isotropic model predictions than the vertical values. The inorganic sample horizontal data point is the closest to its actual clay content value (0.39). The horizontal land data points are above their corresponding model value while the horizontal marine data points are below it, which shows the OM has a significant impact on the cross-property relationship.

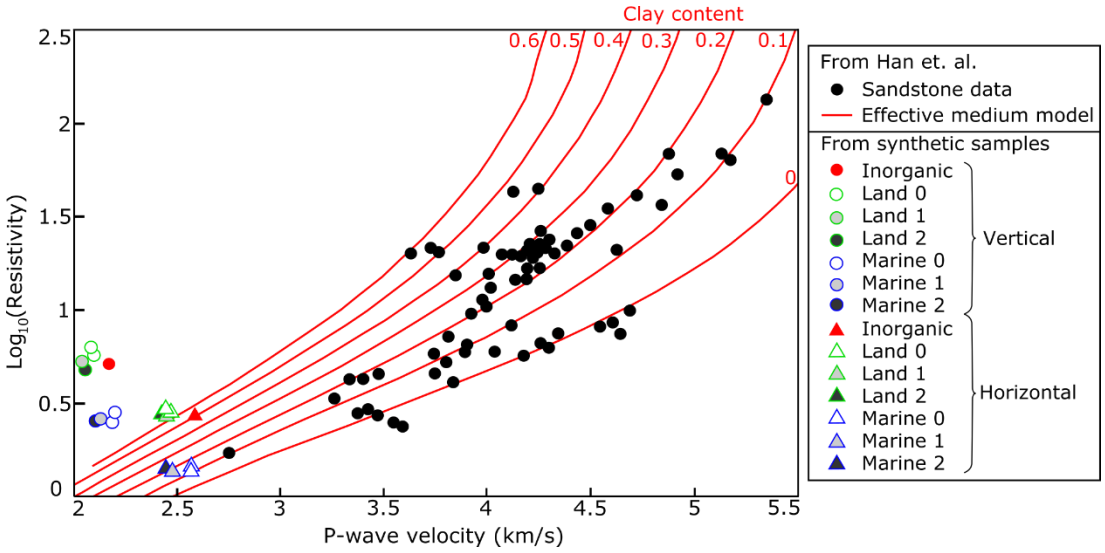

Figure 5-16: joint elastic-electrical effective medium model from Han et. al. (2011). The black dots and red lines are the experimental data of sandstones containing clay (2 to 29% in volume) and model from the original study. The other dots on the left are from the synthetic shale samples.

However it must be noted that the two sample sets present many differences that makes further comparison purely speculative. Firstly the sandstones were saturated with a brine at 35g/L and the resistivity was measured at 2Hz, whereas the synthetic sample brine was at 15g/L and the resistivity measured at 7MHz, making the different resistivity values non comparable. Moreover, the sandstones have clay volume contents ranging from 0 to 0.3. The synthetic samples have clay volume contents ranging from 0.38 to 0.42. The model from *Han et. al.* (2011) assumes a matrix of non-clay minerals containing pore-filling clays. The synthetic samples on the other hand have a clay content that represents more than 50% of their dry mass, and therefore present a structure of non-clay mineral particles embedded in a clay matrix. Also the author mentioned that the changing the aspect ratio of the inclusions shifts the model curves upward, without changing their shape. Clay minerals, with their platelet grain structure, have a low aspect ratio. Thus the model would be more representative with a lower aspect ratio parameter, and the model curves would shift away from the horizontal values toward the vertical values. Finally a modified version of the model would require to take into account the preferential alignment of the particle to account for the anisotropy of the synthetic samples.

Summary

The relationship between conductivity and P-wave velocity was theorized by Carcione *et al.* (2007), by linking the two with different equations establishing relationships between physical properties and porosity. The experimental data presented here confirms the validity of this method. However for accurate predictions of one property with the other, some additional parameters must be taken into account. Here we demonstrate that the OM type and maturity indirectly affect this cross-property relationship by affecting the final porosity of the artificial samples. Also maturity and OM particles texture have a direct effect on P-wave velocity and conductivity that further increase the part of the variability unexplained by the porosity alone. Besides, the anisotropy of the said properties indicates that the relationships may differ in function of the direction of measurement. It is worth noting that cross-property relationship between dielectric and elastic data could be further explored with other correlated parameters such as S-wave velocities, stiffness coefficients and the anisotropy of the real part of the dielectric permittivity. Finally, the comparison between the synthetic samples and data from the literature (Han, et al., 2011) shows the potential of the present data to be used in conjunction with an effective medium approach to try and model the effect of OM on the elastic-electrical response of the samples.

5-4- Origin of the anisotropy of the physical properties

One advantage of artificial samples is the control over the different stages of the consolidation experiment. In this section the focus is set on two aspects of the physical process of consolidation of a shale sediment: the deposition and the mechanical compaction. The main objective is to understand how the structure of the solid phase evolves and how the anisotropy of the physical properties develops. Also the interaction between particulate OM and inorganic minerals during each stage is investigated.

Therefore the results of 4 samples will be analysed, two of which were made using the mixing method and the two others with the sedimentation method. In short the mixing method consists in combining the solid constituents with pore fluid with an initial fluid volume content of approximately 76% and starting the compaction immediately after, without possibility for the particles to reorganise by gravity (i.e. decantation). On the contrary the deposition method involves combining the solid constituents with pore fluids to reach a fluid volume content of 95% and allowing the particles to settle by gravity for about 3 days (see sample preparation Section 3-1-). For each deposition method, one inorganic and one organic sample containing fresh land OM with the flake texture type were made. The two land samples and the two inorganic samples, beside the deposition method, are identical.

The CT-scan images (cf. Section 4-1-) showed that the distribution of OM particles in the mixing organic sample is constant in the vertical direction. On the other hand the sedimentation organic sample has a lower particle concentration in the first 10mm from the bottom but becomes very stable above that limit (the final sample height is approximately 65mm). This shows the OM particles that are less dense than the mineral matrix travelled upward, relative to the mineral particles, by buoyancy during the initial settlement. This effect is however very limited and the sedimentation is still very homogeneous as shown by the average density profile from CT images that remains stable in the vertical direction.

One hypothesis we formulated before the experiments is that non-spherical particles depositing on the sediment interface at the bottom of the water column would be

preferentially oriented with their long-axis in the horizontal direction, which in turn would make the particles in samples made with the sedimentation method (both OM and minerals) more strongly oriented in the direction perpendicular to compaction than the particles in the mixing samples. The analyses of the microscopy images (cf. Section 4-3-) allowed the measurement of the strength of the alignment of the particles via the standard deviation of the orientation distribution. It showed that the non-clay mineral particles (with an aspect ratio closer to 1), made of quartz, calcite and K-Feldspar have a very similar orientation distribution for identical samples with different deposition methods. The OM particles, on the other hand, actually have a higher orientation standard deviation in the sedimentation sample than in the mixing sample (Table 5-5), invalidating the initial hypothesis. It may be due to the methodology employed for the sedimentation method. The initial water content of 95% could be too low so that the proximity of the particles impedes their freedom of movement to such an extent that the deposition occurs differently than in a natural setting and the buoyancy of OM particles make their orientation insensitive to the gravity effect. However, we can also surmise that the orientation of a particle at the time of deposition depends more on the layout of the underlying particles than the direction of gravity. As a conclusion, **the arrangement of the particles along the horizontal direction in our samples was developed mainly during the mechanical compaction.**

Sample name	Standard deviation of orientation distribution (degrees)	
	Non-clay mineral particles	OM particles
Land 0 flakes mixing	38.36	24.89
Inorganic mixing	33.51	-
Land 0 flakes sedim	39.55	33.14
Inorganic sedim	33.19	-

Table 5-5: Standard deviation of the orientation distribution as a measure of the strength of the particle alignment with the horizontal plane for the four samples of interest.

Nevertheless the physical properties displayed important variations, despite a lack of significant textural differences between samples made by the sedimentation and the mixing methods. Firstly, the porosity and bulk density of the organic and inorganic samples were affected differently by the deposition method (Figure 5-17). The two samples made with the mixing method have almost the same porosity in all

compaction steps and have a difference in bulk density between 0.04 and 0.06 g/cm^3, essentially due to the difference in grain density. The inorganic sedimentation sample has a lower porosity and a higher bulk density than its mixing equivalent. On the contrary the land sedimentation sample has a higher porosity and a lower bulk density than its mixing equivalent. As a reminder, the OM particles are of the flake texture type and have high aspect ratio, irregular shapes. This type of shape can create more pore space because of gaps on the particle surface that is not in contact with other particles. Furthermore the clays and OM particles can form aggregates that further enhance this effect (Nimmo, 2013). Hence the mixing method produces a similar particle layout and a similar porosity independently of the texture of the particles. **However, in a natural depositional setting, the organisation of mineral particles will decrease the pore space compared with the mixing method and the presence of OM particles with irregular shapes will increase it.**

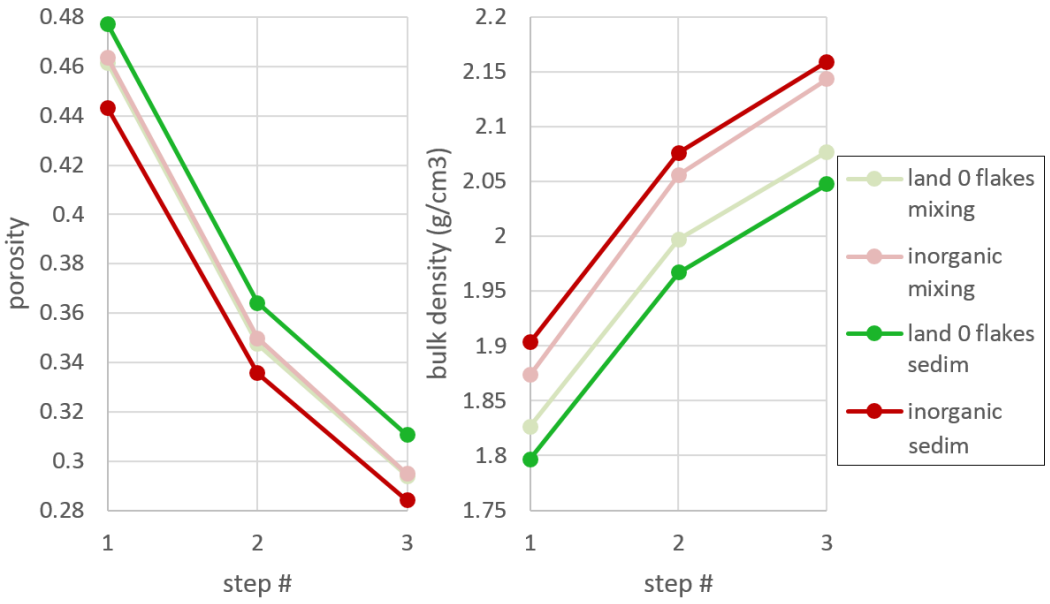

Figure 5-17: Porosity and bulk density at the end of each compaction step. (1 to 3) for two organic and two inorganic samples with identical composition but prepared using two deposition methods: mixing and sedimentation.

Next the bulk density data shown above was used with the ultrasonic velocity measurements to compute the 5 independent stiffness coefficients (c_{ij}) of a VTI medium for all four samples at the end of each compaction step (Figure 5-18). The coefficients computed from S-wave velocities (c_{44}, c_{66} and c_{13}) are only shown at steps 2 and 3 because the error on S-wave velocity measurement early in the compaction is

high. Overall the inorganic samples have higher c_{ij} than the organic samples because of their lower porosity and higher density. When comparing the sedimentation samples with their mixing equivalent, the values of c_{11} and c_{44} are close to each other. But the values of c_{33} and c_{66} are consistently higher for the sedimentation samples. C_{13} is clearly less affected, with similar values in step 2 and higher sedimentation values in step 3.

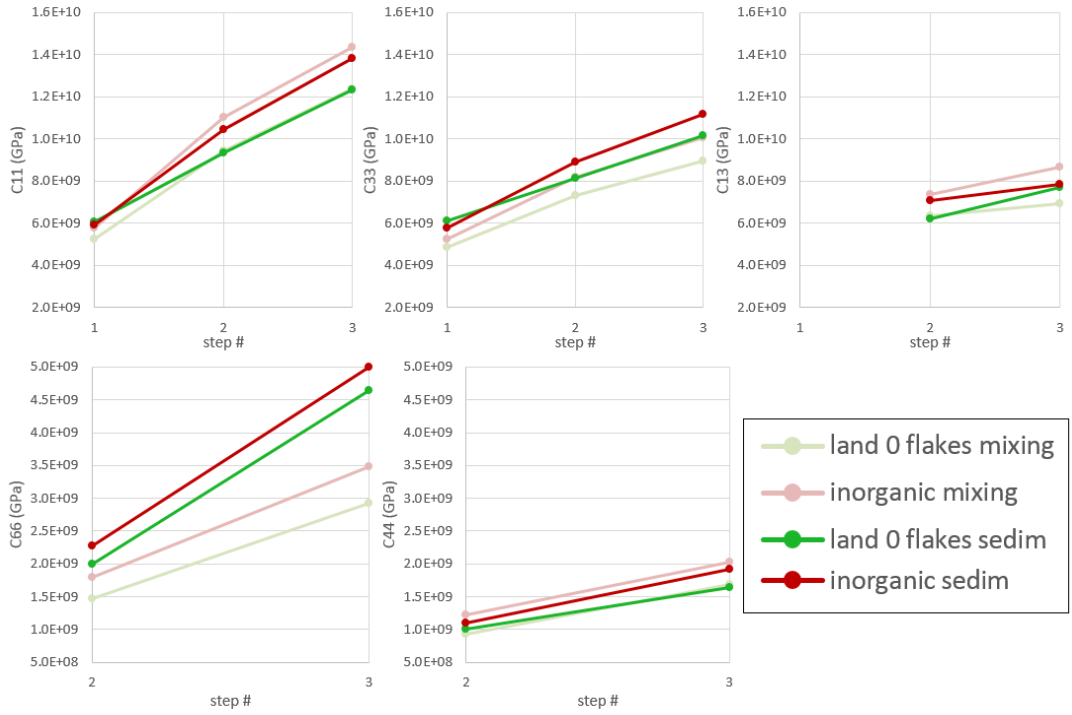

Figure 5-18: Five independent stiffness coefficients c_{ij} for a VTI medium computed from velocity and bulk density measurements at the end of each compaction step: (1 to 3) for two organic and two inorganic samples with identical composition but prepared using two deposition methods: mixing and sedimentation. C_{33} and c_{44} display stronger differences between the sedimentation and mixing method.

As a consequence the anisotropy of the samples, as measured with Thomsen's anisotropy coefficients, is affected by the deposition method (Figure 5-19). The differences between sedimentation and mixing values for each Thomsen's parameters are presented on the right hand-side as:

$$\Delta(anisotropy) = anisotropy(mixing) - anisotropy(sedimentation) \qquad (72)$$

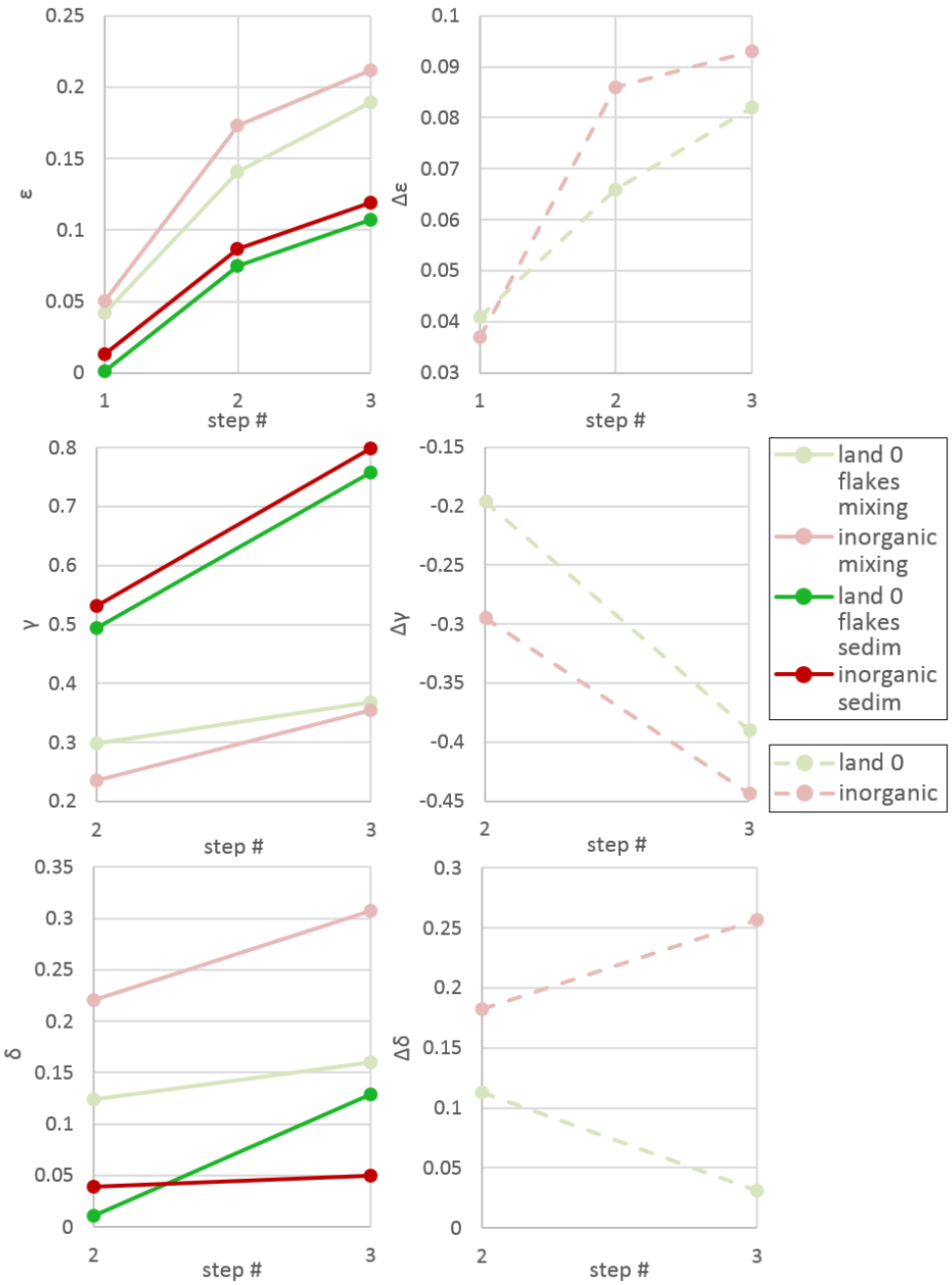

Figure 5-19: Elastic anisotropy evolution with compaction steps in different OM types, shapes and depositions: Left - Thomsen's elastic anisotropy parameters at the end of each compaction step. (1 to 3). Right – Difference of anisotropy between the mixing and sedimentation method within each sample type (organic and inorganic).

Because c_{33} is increased in the sedimentation samples, the difference between c_{11} and c_{33} is reduced and therefore the P-wave anisotropy parameter ε is smaller than for the mixing samples. In contrast the increased c_{66} in the sedimentation samples increase the disparity between c_{44} and c_{66}, thus increasing the S-wave anisotropy parameter γ greatly in the sedimentation samples. The wavefront anellipticity parameter δ is

computed from c_{13}, c_{33} and c_{44}. The sedimentation samples have greater δ values but this effect is more prominent in the inorganic samples.

It can be surmised that during the long settlement time of the sedimentation samples, the particles have time to organise themselves in an optimal way so that the load induced from the weight of the water column is spread out as evenly as possible between all particles. This favours numerous grain contacts in any direction and a limited decrease of the pore space whereas the mixing samples will have some grain contacts that bear more load than others. When submitted to a much higher uniaxial stress during compaction, the better organised structure of the sedimentation samples will have an increased vertical compressional stiffness (c_{33}), thus homogenising the P-wave velocities in different directions and reducing the P-wave anisotropy (ε) as well as the anellipticity of the P-wave wavefront (δ). The increase in S-wave anisotropy (γ) is more challenging to explain. The probable cause is that the faster horizontal S-waves, despite having a horizontal polarization, are affected by the better distribution of grain contacts and thus have a higher velocity in the sedimentation samples, in turn increasing c_{66} and γ.

Finally, the anisotropy of the dielectric parameters (Figure 5-20) is affected by the deposition method in the same way as ε and δ. The mixing samples that have a less organised initial structure are more strongly anisotropic for all three parameters. The sedimentation samples are likely to have an increased ability to convey dielectric polarisation and conduction of electrical charges at the frequency of the maximum anisotropy.

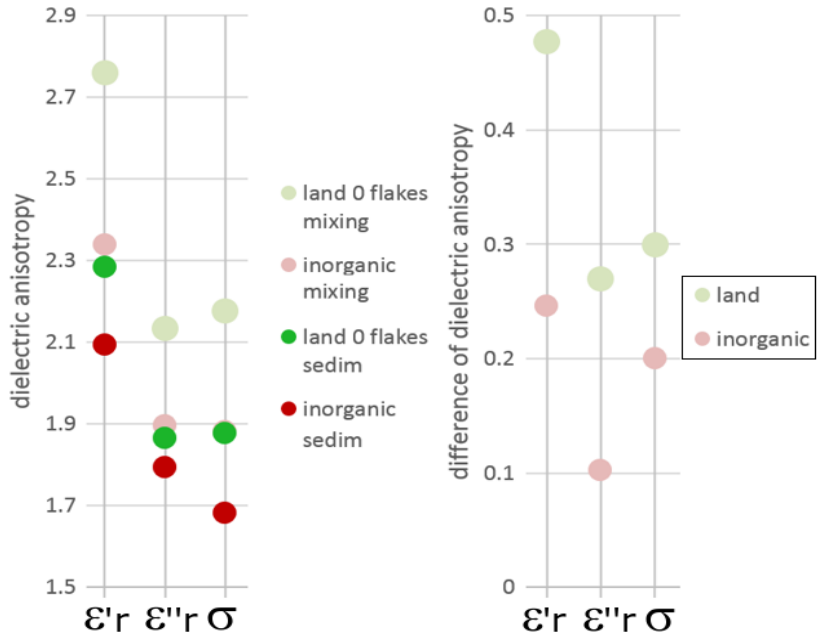

Figure 5-20: Anisotropy of dielectric properties between land and marine OM with different shapes and depositions: Maximum value of for the real part of the dielectric permittivity (ε'r) and the imaginary part of the dielectric permittivity (ε''r). Value at 7MHz for the equivalent conductivity (σ).

Initial grain texture and its impact on the properties after compaction

The sedimentation samples fabric can be considered to be controlled by bottom up formation of grain contact during the initial settlement phase. In the mixing method on the other hand, the initial mixing procedure randomizes the grain orientation and contacts with an overall viscosity that doesn't allow reorganisation by gravity in the time frame between the end of the mixing and the start of the compaction. Therefore there is no buoyancy effect of particles with a lower density than others as can be seen in the sedimentation method. The initial particles are trapped in between other grains at the beginning and can only travel short distances, their displacement is mainly the result of the compaction-related reorientation of their long-axis by contact with adjacent grains.

In the sedimentation method, the grains are allowed to fall and reorganise under the weight of the water column for a long period of time. Hence, at the moment of the compaction initialization, the amount of grain contacts is greater and the load is better distributed across the horizontal cross-sectional area of the sample than with the mixing method. It can be argued that the sedimentation samples start undergoing

primary consolidation before the start of the compaction experiment and have a consolidation head start compared to the mixing samples. This explains the lower porosity of the inorganic sedimentation sample.

However, the particle concentration in the sedimentation column is not low enough for the particles to be in free fall. They are still interacting even at a water content of 95%. Therefore the horizontal alignment is not greater for sedimentation samples than it is for mixing samples.

One interesting aspect in the development of anisotropy is the opposite effect of particle realignment and grain inter-fusion by creeping and compression (illustrated in Figure 5-21). North & Best (2014) describe this in a study of electrical anisotropy of natural sandstones and with finite element modelling of compacted spherical grains. They show that the compression and interfusion of grains from a vertical compaction strain leads to an increase in the cementation coefficient in the horizontal direction. This effect has for consequence to decrease the conductivity in the horizontal direction and thus decreases the conductivity anisotropy ($\sigma_{horizontal} / \sigma_{vertical}$). On the contrary the alignment of particles along the horizontal direction induces a higher tortuosity in the vertical direction, which decreases the conductivity in the vertical direction and increases the anisotropy. The present results show the elastic anisotropy of P-waves is affected in a similar fashion by these two opposing effects. This is not surprising since compressional elastic properties and conductivity were previously shown to be correlated. For instance, with cross-property correlations using Archie's law for the modelling of electrical properties and Gassmann's equations for elastic velocities (Carcione, et al., 2007),

When applied to the present dataset, it can be concluded that the different methods of deposition did not affect the final orientation distribution leading to similar tortuosity anisotropy of the pore network. On the other hand the deposition method allowed a better distribution and number of initial grain contacts and subsequently a higher degree of grain interface compression and inter-fusion during the compaction experiments, which increased the mechanical cementation of the samples in the horizontal direction. In turn the latter mechanism increased the capacity of samples produced with the sedimentation method to transmit electrical charges and

compressional elastic waves in the vertical direction, therefore decreasing their electrical, dielectric and P-wave (ε) anisotropies.

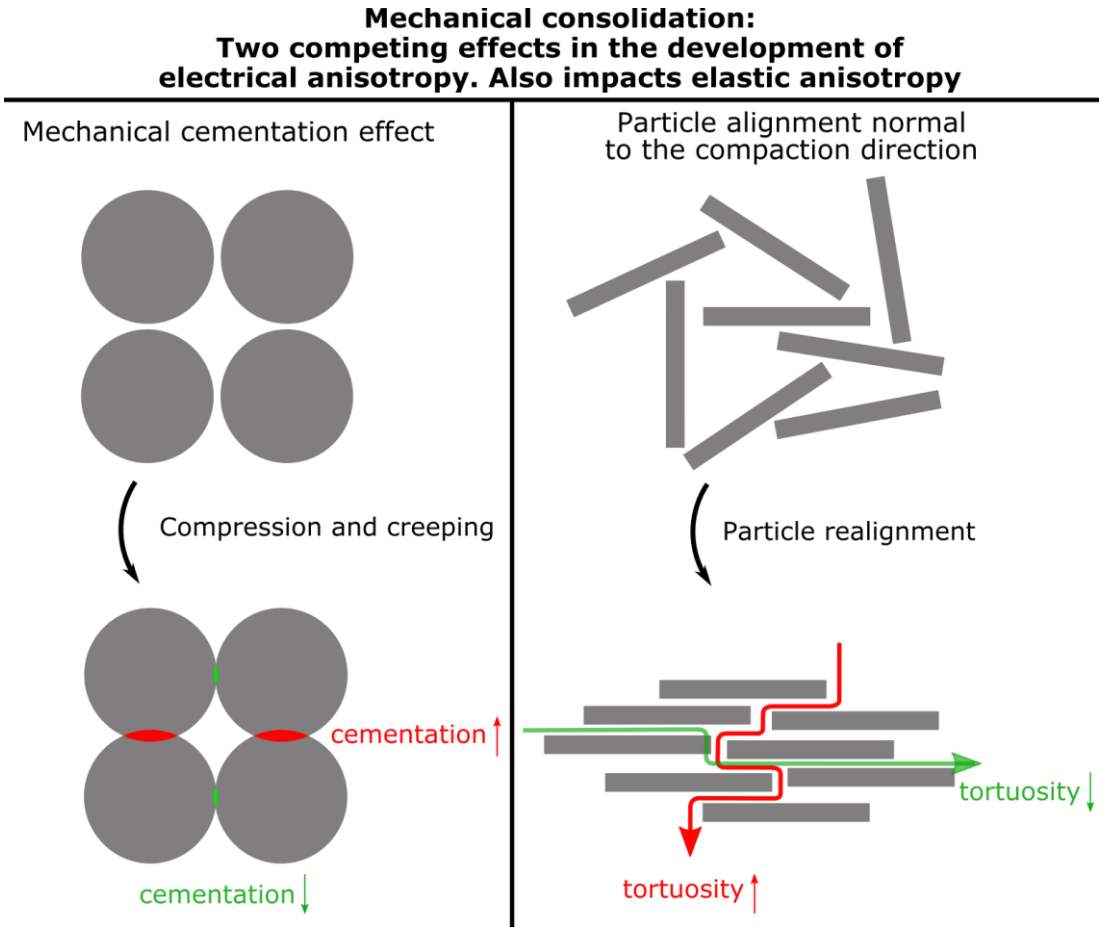

Figure 5-21: conceptual diagram illustrating the impact of two opposing consolidation mechanisms on the physical properties of consolidating samples. (Left) Mechanical cementation of spherical grains (no particle realignment) by compression and creeping increases the degree of cementation in the horizontal direction, reducing electrical and compressional elastic anisotropies. This effect is more important in the sedimentation samples than in the mixing samples. (Right) High aspect ratio particle realignment (no cementation effect) increases tortuosity in the vertical direction, thus increasing electrical and compressional elastic anisotropies. This effect occurs to a similar degree in the mixing and sedimentation samples.

Summary

The preferred orientation of particles and the development of anisotropy in our samples were found to be mostly related to the mechanical compaction rather than by the deposition method. However, the samples prepared with the sedimentation method

were found to have an increased vertical compressional stiffness, thus reducing the anisotropy parameters ε and δ, as well as lowering the maximum anisotropy of the dielectric parameters but increasing the elastic anisotropy γ. These observations are attributed to an overall better initial distribution and greater number of grain contacts after the settlement phase in sedimentation samples. This resulted in a better mechanical cementation of the samples in the horizontal direction that increase both the compressional elastic stiffness and ability to carry electrical charges in the vertical direction. On the contrary the samples prepared with the mixing method were only restructured by the particle reorientation during compaction that increases the ability of the samples to carry ultrasonic waves and electrical charges mainly in the horizontal direction. These two opposing effect on anisotropy result in a lowering of anisotropy of electrical properties and compressional elastic waves in the sedimentation samples. If doubts remain as to whether the sedimentation method employed for our samples is a true analogue to the natural deposition of shales, it is however certain that the initial deposition has an important influence on the microstructure of the consolidated samples.

5-5- Effect of pore pressure on the elastic properties of compacting shale samples

During the analysis of the ultrasonic results, unusual features right after the transitions between compaction steps were noticed. As a reminder, each artificial sample was compacted in three steps of vertical uniaxial stress of 1MPa, 7MPa and 14MPa with a rapid step increase between steps at a rate of 0.6MPa/min. (cf. sample preparation Section 3-1-). The origin of this behaviour was identified as the consequence of an uneven distribution of the pore pressure in different regions of the sample after the stress increase (before pore pressure dissipation could occur). An attempt was then made to measure the corresponding error in the computed ultrasonic properties that are calculated with the assumption that the samples have a homogenous porosity distribution. This is important as errors greater than the error corresponding to the uncertainty of the ultrasonic arrival time picking could invalidate all the elastic behaviour presented in earlier sections. The example of the sample "marine 0 powder mixing" will be shown here for succinctness as the other samples displayed very similar behaviours.

The first indication of the pore pressure effect were the velocities at the transition from compaction step 1 to step 2. At this stage the samples are weakly anisotropic and consequently the vertical and horizontal velocities have relatively close values. In Figure 5-22 we can see that right after the beginning of step 2 the vertical velocity, typically the slower one, starts to increase at a faster rate than the horizontal velocity, even momentarily exceeding the horizontal velocity for S-waves.

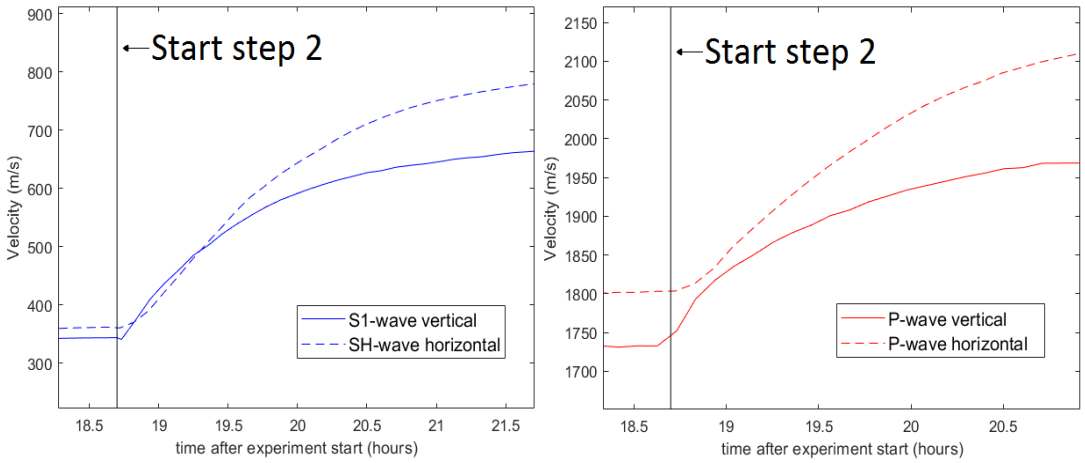

Figure 5-22: Ultrasonic velocities in the vertical and horizontal direction at the beginning of compaction step 2 (7MPa) in sample "marine 0 powder mixing". Left – S-wave velocities. Right – P-wave velocities.

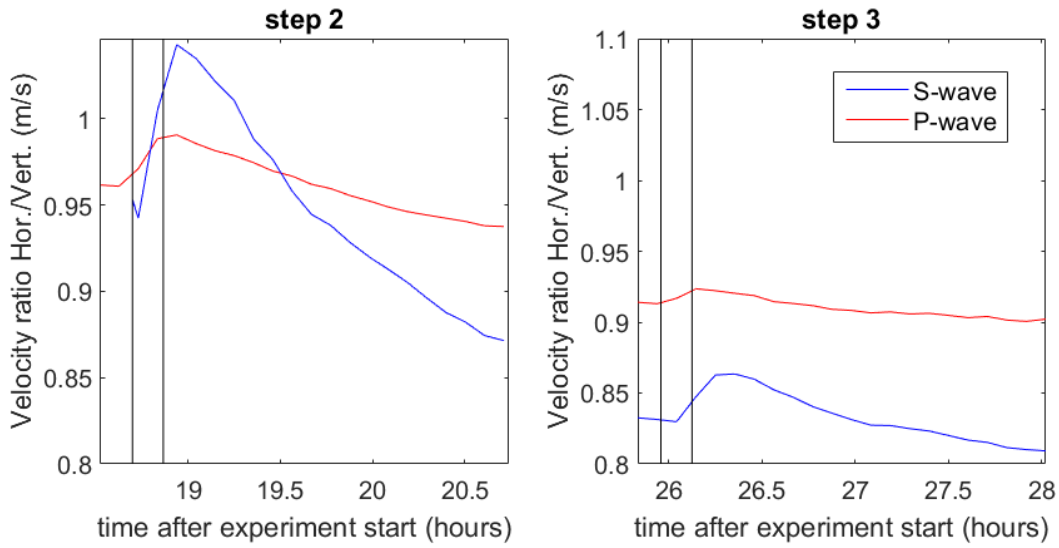

Figure 5-23: Horizontal to Vertical ultrasonic velocity ratio for P- and S-waves. At the start of compaction step 2 (left) and at the start of compaction step 3 (right). On each graph, the first vertical line indicates the start of stress increase and the second line the end of the stress increase. (Approximately 10min).

To better represent this difference in the initial velocity increase rate, the horizontal to vertical velocity ratio was plotted in Figure 5-23. The ratio increases during the transition period when the stress passes from 1 MPa to 7 MPa in step 2 and 7 Mpa to 14 MPa for step 3. The ratio reaches a maximum a few minutes after the end of the stress increase (up to two data points increasing after target stress is reached). It takes approximately 1 hour for the ratio to return to the value it had before the start of the

stress increase. The ratio increase is more marked for S-waves because they have lower velocities but the absolute difference between horizontal and vertical velocities is relatively similar for P-waves and S-waves.

This evolution of velocities results in strong variations of the P-wave and S-wave anisotropy parameter ε and γ, respectively around the compaction step transitions (Figure 5-24). The faster initial increase of the vertical velocities induces a lowering of the computed ε and γ of 180% and 75% in early step 2 and 25% and 15% in early step 3, respectively, in the span of 15 minutes.

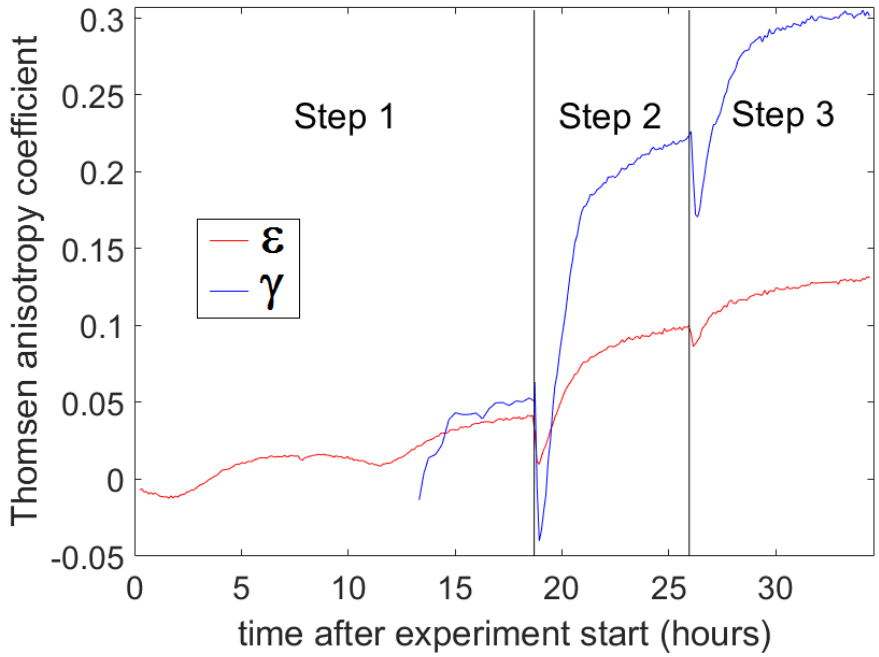

Figure 5-24: Thomsen's anisotropy parameters ε and γ throughout the compaction experiment of sample "marine 0 powder mixing".

The relationship between pore pressure variations and ultrasonic velocities is straightforward. The samples during compaction are drained from the bottom and top ends via the porous plates. When an increase in uniaxial stress is applied to the sample the load is beared entirely by the pore fluid (Figure 5-25). The fluid then starts to drain, diminishing the pore pressure near the top and bottom ends of the sample. Consequently the load is going to be transferred to the solid grains earlier in these regions and the solid matrix will consolidate more in these regions. This implies a lower porosity and a higher bulk density in the extremities, and an overall better consolidation. In turn the more consolidated areas will have higher elastic moduli and higher measured velocities.

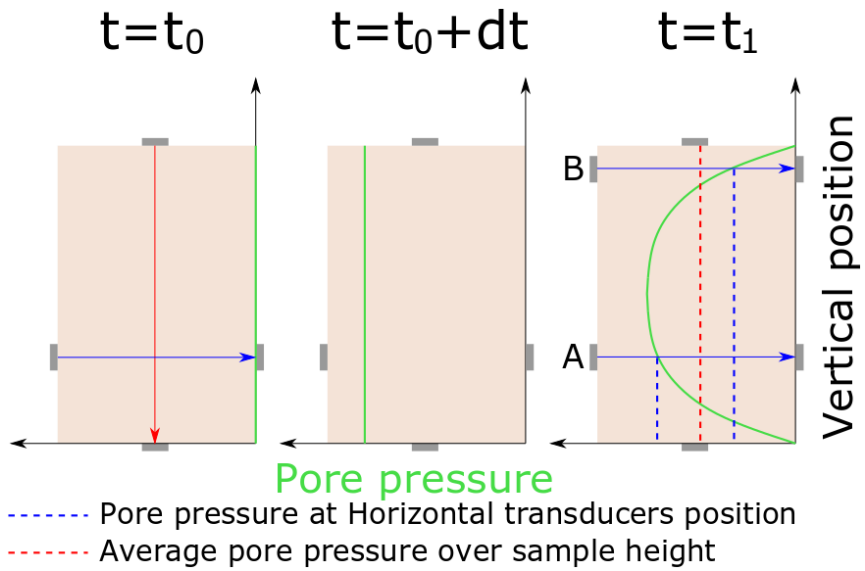

Figure 5-25: Schematic representation of the evolution of pore pressure when an increase in compaction stress is applied to the sample. At $t=t_0$ (left) the sample is totally drained and the load is beared by the solid matrix. At $t=t_0+dt$ (middle) the compaction stress has increased to the target stress in the time dt that is small at the scale of the compaction experiment. In an ideal case with an instantaneous stress increase the additional load is beared entirely by the pore fluid and the matrix remains unchanged. At $t=t_1$ (right), the pore fluid is drained from the bottom and top of the samples and therefore the pore pressure is maximum in the middle of the sample height. The vertical ultrasonic waves will pass through regions of different pore pressures. The horizontal ultrasonic waves will pass through a single pore pressure level.

The ultrasonic transducers recording the vertical ultrasonic response will pass through all the pore pressure levels and therefore the vertical velocities will correspond to the velocity of a medium of constant pore pressure equal to the average of the vertical pore pressure gradient. The horizontal transducers on the other hand will only propagates ultrasonic waves in a constant pore pressure level. The vertical position of the transducer pair and the pore pressure gradient profile will thus determine the difference in pore pressure between horizontal and vertical measurement.

In our compaction experiments, the sample height varies greatly, but the horizontal transducers are fixed. The proportion of the vertical distance between horizontal transducers and the centre of the sample to the half-height of the sample will vary too as a result. In the situation A in Figure 5-25 the horizontal transducers are closer to the

centre, which is the case in early step2. Hence they will remain at a pore pressure level greater than the average pore pressure long after the stress increase. The horizontal velocity they record will thus be under-estimated and so will be the anisotropy compared to an equivalent medium with a pore pressure equal to the average. On the contrary in situation B the transducers are very close to the top porous plate like it is the case in late step 3. This implies a pore pressure lower than average and higher velocities, thus increasing the measured anisotropy.

To evaluate the magnitude of the pore pressure effect, without any direct measure of it, we used the difference in bulk density at the edges and the centre of the sample from the CT-scan images (cf. Section 4-1-). We found that for this sample, the difference in bulk density between the highest and lowest values to be 0.03 g/cm^2. The section where the horizontal transducers were positioned at the end of the compaction experiment, near the top end, has a density 0.011 g/cm^3 higher than the average bulk density. Because we know the difference in bulk density between the horizontal and vertical transducer path ($\Delta\rho$) as well as the grain density (ρ_g) and the pore fluid density (ρ_w) we could then compute the difference in porosity ($\Delta\Phi$) as follow:

$$\Delta\Phi = \frac{\Delta\rho}{\rho_g - \rho_w} \tag{73}$$

This gave a difference in porosity of 0.72%. We then used the linear relationship between vertical P-wave velocity and porosity defined for organic samples containing fresh OM in Section 5-3-. This gave a velocity difference of 14m/s, or 0.7% of the vertical P-wave velocity. Such values do not seem much, but when we use it to correct the vertical velocity to recompute the final ε value as if the vertical P-wave was propagating in a medium of same porosity as the horizontal P-wave, we found a difference close to 0.01 or 6.8% of the uncorrected value.

The ε curve, within each compaction step, can easily be fitted with a power equation of the type

$$\varepsilon(time) = a * time^b + c \tag{74}$$

With the knowledge that ultrasonic measurements in a medium with a constant pore pressure would have ε values increasing during consolidation from the value before the stress increase to the final value re-computed with the CT-scan information, we can modify the power fit to match the corrected value. We can see in Figure 5-26 that

initially, the corrected ε values are higher than the measured values because the horizontal transducer are at a pore pressure level higher than average. Two hours after the stress increase, the corrected ε values become lower because the pore pressure at the horizontal transducer level, near the top porous plate, is lower than the average. The same method was applied to correct the S-wave anisotropy parameter γ.

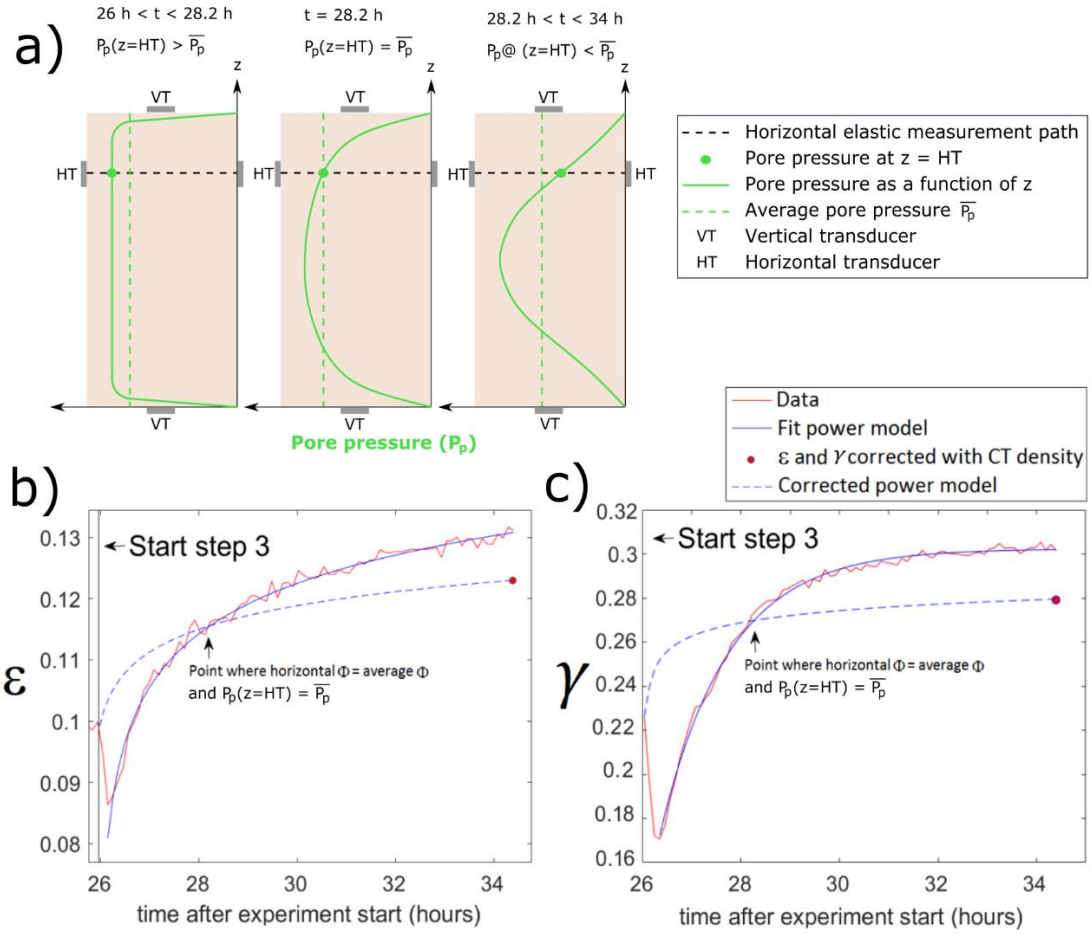

Figure 5-26: a) Evolution of pore pressure along the vertical axis (z) during compaction step 3. The pore pressure at the height of the horizontal transducers is initially higher than the average pore pressure, then it decreases and becomes equal to average pore pressure at t=28.2h, where the corrected power model crosses the data. Finally, it becomes lower than the average pore pressure. b) Evolution of Thomsen's anisotropy parameter ε in the final compaction step 3. The actual data is affected by pore pressure effects. The corrected ε value at the end of the experiment with the use of the CT-scan density data allows us to modify ε values for a medium where the pore pressure is constant and equal to the pore pressure at the level of the horizontal transducers. c) Same corrections applied to the anisotropy parameter γ.

The same observations made for ε also apply to γ. The difference between the experimental γ value and the corrected one amounted to 7.4% of the original value, slightly higher than for ε.

The ε and γ differences observed here are smaller than the difference observed between samples. Therefore the observations and interpretations made across the sample set in previous sections are still valid. Moreover all samples have identical clay content and compaction paths so that the pore pressure gradient is relatively similar for all samples. This is confirmed by the vertical variations in bulk density measured with the CT-scan images (Section 4-1-). Therefore the error on anisotropy values is systematic and evolves in a similar way for different samples.

It can be noted that the vertical position of the horizontal transducers is at a height of 55mm. The final height of the samples at the end of the compaction experiments range from 60.7mm to 67.1mm. Therefore in compaction step 3, the horizontal measurements are made relatively close to the top of the sample. This means the pore pressure at the level of the horizontal transducers will become lower than the average pore pressure relatively rapidly in the compaction step. In the sample above, this occurred in a little over 2 hours in the 8 hour long compaction step 3.

Summary

Pore pressure effects were detected in the elastic properties measured in the artificial shale samples that induce an error that either decreases or increase the values of the anisotropy parameters ε and γ. The error depends on the position of the horizontal transducer pair in relation to the centre of the compacting sample as well as the vertical pore pressure gradient profile. A method was proposed, using the density measured with the CT-scan images and the linear relationship between P-wave velocity and porosity to correct this error. This correction method could be applied for the laboratory testing of natural shale samples if their grain density is relatively constant. Indeed the very low hydraulic conductivity of shales makes it difficult to fully equilibrate the pore pressure even in a small plug sample. Therefore this method offers potential application to correct ultrasonic data accounting for pore pressure effects without a complete equilibration of pore pressure, thus reducing the testing times significantly.

Chapter 6: Conclusion

The primary objective of this work was to explore the influence of a wide array of OM characteristics on the physical properties (dielectric and elastic) of organic-rich shales. This objective was chosen because despite evidence that many different OM characteristics influence the physical properties, the study of OM in rock physics experiments and models is often limited to the TOC or volume content. Therefore models describing organic shale properties are restricted by the poor characterisation of OM. The evaluation of the effect of other characteristics, such as maturity level, origin (marine or land), or texture, is rising but a lot remains to be done.

Several indications of what sort of OM characteristics are likely to influence the physical properties were identified during the literature review and also by an understanding of the basic electrical and mechanical properties of OM. Moreover relationships between electrical and elastic properties were found in shales but are still in their infancy. Cross-property relationships between properties are useful when one of the properties is unavailable or more expansive to perform. Also the combination of these two sets of results can lead to an improvement of the characterization of the OM content. The models used to describe the physical properties of unconventional shale reservoirs can also greatly benefit from this study. The findings could also be of help to explain the part of the variability of laboratory data obtained on natural samples that is unexplainable with inorganic parameters only.

The achievements of this study are twofold: one is of technical nature and the other one of scientific nature. Indeed before being able to obtain data to answer the scientific question raised in this thesis, new apparatuses first needed to be developed.

To obtain sufficient quantities of OM with different levels of maturity but a common origin (land or marine) for all maturity levels, an artificial maturation system was created that allows to perform a confined hydrous pyrolysis on a volume of 200mL constituted of a mix of OM, water and swelling clay (smectite). The conditions during the maturation are (i) oxygen-free, (ii) a temperature of 200°C, (iii) a water vapour and HC gas generated pressure of up to 10MPa, (iv) a maturation time of three or six weeks to achieve two levels of maturity, (v) a clay to OM ratio of 0.1, (vi) a water to solid ratio of 1. These conditions permitted the maturation of fresh OM that is similar to the natural thermal maturation of OM in shale sediments.

A compaction cell was engineered with an innovative design to fabricate artificial samples that are homogeneous and free of air inclusions in a repeatable manner while recording accurately the porosity, bulk density, mass of expelled pore fluid and the full elastic stiffness tensor of a transversely isotropic medium. The design and implementation of the new cell was challenging but allowed us to better understand the behaviour of artificial samples undergoing compaction.

A suite of artificial samples was produced thanks to this two apparatuses and resulted in high quality data. The experiments results and the subsequent interpretations helped answer the following subject matters:

- **Relevance of the artificial approach**

The use of mechanically compacted artificial samples was justified by the need to deconstruct the inherent complexity of naturally occurring shales to create homogeneous, well-characterized samples with a simple structure so that our results are unambiguously linked to a few sets of variables. Several methods were used to confirm the validity of these assumptions. Firstly CT-scan images confirmed the homogeneity of our samples with bulk densities showing very few variations between different regions of a single sample along with the absence of detectable air inclusions. The only source of variability we detected was due to an uneven distribution of pore pressure resulting in a higher density in the areas near the pore fluid draining surfaces, which lead to a difference in bulk density of about $0.04 g/cm^3$ between the least and most dense regions. Moreover the analysis of the OM macro-particles showed they have an overall even distribution, except for the sample prepared with the sedimentation method that displayed a lower OM macro-particle count in the first 10mm from the bottom of the sample. Then the optical microscopy images showed the similarity of the inorganic characteristics across the sample set. The amount of inorganic particles detected along with their size distribution, aspect ratio and orientation proved to be very homogenous across the sample set. Finally the overall bulk density measured with the CT number was found to be very close to the density determined from weight and volume measurements which is a good indicator of the accuracy of the different methods employed.

Besides, the precise determination of the amount and density of the initial constituents of the artificial samples combined with well-calibrated instruments allowed the

determination of the porosity and bulk density throughout the compaction experiments with relative uncertainties as low as 0.65% and 0.18%, respectively. The error on the sample height measurement and on the ultrasonic arrival times gave maximum relative uncertainties of about 2% for P-wave velocities and 4% for S-wave velocities at the end of the compaction experiments. We also evaluated sources of systematic errors in the compaction cell dataset. Namely the porosity and bulk densities are computed with the assumption that the solid phase is quasi-incompressible. However the comparison of the mass of expelled of pore fluid with the volume reduction measured with the LVDT showed us that the solid phase volume decreases with increasing compaction stress in a significant way. When the final porosity value was corrected to account for solid volume change, a value very close to the porosity measured after the sample unmoulding was found. This error is observed in all samples and the average difference between final confined and unconfined porosity averages 3.5%. An example of correction of the error on the elastic measurement was also shown, that is due to the uneven vertical distribution of the pore pressure gradient. The error on the anisotropy parameter ε was found to be about 6.8% of the uncorrected value while it was 7.4% for γ. These two systematic sources of error evolve similarly for all samples and the amplitude of the errors is smaller than the variation observed between samples. Therefore this validates the physical origin of the variations observed in our sample set.

- **Porosity evolution with organic content**

Porosity loss during compaction is driven by OM stiffness (related to HI index) in early consolidation. Indeed the more compliant OM particles, such as marine OM, are subject to more deformations to fill up the decreasing pore space early in the compaction. Later the porosity loss due to OM particles is driven by the collapse of the internal pores within the OM, hence more mature samples (higher Tmax), that are more porous, will induce more porosity loss. Marine OM produces HC earlier in the maturation process, which results in a higher Tmax and a lower internal porosity. Therefore the marine OM, that has both a lower stiffness and a higher maturity loses significantly more porosity and has a higher bulk density. For that reason a shale containing marine OM will appear thermally more mature and mechanically more consolidated than a sample with land OM, despite the same thermal and stress history.

- **Elastic properties variations with different OM characteristics**

The Thomsen's anisotropy parameter ε (P-wave anisotropy) increases with increasing maturity. However we used different maturity indicators for each OM type. Land OM, which has Tmax values in a too narrow range was evaluated for maturity with OI and HI. Marine OM, which has problematic HI due to the limitations of the Rock-Eval method, was evaluated for maturity with Tmax. Previous research found that maturity increases P-wave anisotropy partly because of the development of microcracks produced during kerogen cracking. However in our study the OM was added after maturation and the samples were crack-free, which shows that the intrinsic properties of OM also play a role in the development of anisotropy.

The samples presented in this study are quite immature, from just below the immature/oil window to the middle of the oil window. Therefore OI is a good indicator of maturity. Vp/Vs was found to decrease with decreasing OI. But different OM types have different OI levels and for the same Vp/Vs ratio, marine OM will typically have a higher OI. Besides, the degree of compaction also decreases Vp/Vs.

The S-wave anisotropy parameter γ and the parameter of anellipticity of the wavefront δ increase for flakes particles. The difference for land samples is greater as there is a greater difference in particle size between powder and flakes in this OM type. This shows that bigger OM particles, which have less resistance to shear deformations than inorganic minerals, induce a more important lowering of S-wave velocity in the vertical direction. At the same time the size of the OM particles seems to affect P-wave propagation by modifying the ultrasonic wavefront shape rather than having a direct impact on vertical and horizontal P-wave velocities.

- **Dielectric properties variations with different OM characteristics**

The maximum real dielectric anisotropy which occurs at high frequency increases with increasing OM dry density. These densities are linked to the OM maturity. However it does not evolve linearly. At the beginning of the maturation, the highly functionalised fresh OM thermally decompose to become kerogen rich, which translates to an increase of the OM density between maturity level 0 and 1. With further maturation, the kerogen cracking produces bitumen that has a lower density

than kerogen. The OM density thus decreases between maturity level 1 and 2. This is why maturity can't be predicted from dielectric data but these data can still provide an indication of the ratio of kerogen to bitumen.

The anisotropy of the imaginary dielectric permittivity and of the equivalent conductivity at high frequency increases when particle size increases. The imaginary part of the dielectric permittivity quantifies the work exerted by polarization processes. It is therefore linked to the energy lost during displacement of electrical charges. Thus, in the same way as for S-wave propagation, bigger particles decrease the ability of a sample to conduct electrical current in the vertical direction but cause less energy loss related to polarization processes.

The samples with marine OM, because of their higher degree of consolidation have higher dielectric anisotropies in the high frequency range for all three parameters. This shows that the consolidation state and hence the age of the samples, has a strong impact on the development of the dielectric anisotropy.

All these observations were made in the high frequency range, and especially for the dielectric permittivity where we focused on the maximum anisotropy values that occur between 10 and 40MHz. At these frequencies, the polarization processes occur only at a relatively small scale (<1µm). For example these frequencies are typical of polarization of the ions in the clay inter-layers and the dipolar polarization of water. Therefore, rather than being a direct effect of the dielectric processes occurring within the OM, we believe that the differences observed are a consequence of the interference of the OM in the network of the clay matrix. Hence if the dielectric properties are highly dependent on the clay content, the different characteristics of OM will alter the dielectric responses of clays in different ways.

Furthermore the only dielectric parameter that wasn't related to the amplitude of the anisotropy at high frequencies is the equivalent conductivity of marine OM. It turned out samples containing marine OM are much more conductive at all frequencies than the land samples and also the inorganic samples. This demonstrates that OM type is an important factor for the overall organic shales conductivity and should be taken into account in resistivity models.

- **Deposition**

Compared to the samples prepared with the mixing methods, the samples prepared with the sedimentation method exhibit an increased compressional stiffness and ability to transmit charge carriers in the vertical direction, whereas the the shear stiffness is increased horizontally. Consequently, the anisotropy parameters ε and δ as well as the anisotropy of the three dielectric parameters (real and imaginary part of the relative dielectric permittivity and equivalent conductivity) are smaller in sedimentation samples but the S-wave anisotropy parameter γ is higher. We attribute this effect to a more optimal arrangement of particles in the sedimentation samples. The initial settlement time before compaction is much longer for the sedimentation method and the solid particles during this stage have time to arrange themselves in an optimal way to spread the load of the water column evenly on the sample area. This provides a better network of grain contacts in the vertical direction, and this initial distribution effect induces an increase of cementation in the horizontal direction by creeping and compression during compaction.. We notice that this better distribution of the load in the inorganic samples, that have a more homogenous particle size distribution, reduces the final porosity. However, the longer settlement time for the samples containing OM particles of the flake texture type leads to samples with a higher porosity. Hence the optimal configuration for the distribution of the load in a sample with a heterogeneous size distribution induces more pore space.

- **Cross-property relationships**

An array of elastic and dielectric properties were found to evolve in similar ways in different sample groups each covering a different target variable. However several factors influence each measurement therefore it is difficult to establish direct correlations between properties. For instance we established linear relationships between P-wave vertical velocities and vertical equivalent conductivity as they both evolve linearly with porosity. But the P-wave velocity/conductivity relationships are different for different maturity levels and to a smaller extent are also affected by the OM particle texture. The determination of general empirical relationships is thus arduous and will depend on many unrelated parameters that will vary for every shale formation they are applied to. Hence it is necessary to define models with a physical basis that can take into account all the different variables of the sample set to

successfully establish cross-property relationships. For instance we can use different established models that link dielectric and elastic properties through an intermediate parameter. An example of this type of work was done by Carcione et al. (2007) where electrical and elastic properties were linked together through their relationship with porosity. However they highlighted the lack of experimental data that should validate these results.

- **Statistical significance**

It is worth discussing the statistical validity of the results given the low number of samples investigated. The small number of data points is counteracted by the quality of the constraints on the samples fabrication parameters. Contrary to natural samples that have a high degree of variability, the synthetic samples are all extremely similar in mineralogy, compaction stress history, porosity, fluid content, etc. The variable characteristics that differentiate the different samples are very well defined. Therefore the variations in the measured properties can be attributed with confidence to the variables of interest (OM characteristics). However the interpretation of such results can only be qualitative as the data required to define empirical relationships requires a lot more data points.

Another way to verify the validity of the results is by comparison with the literature. It was found that compared with other datasets from the literature, the synthetic samples are less consolidated than natural sediment samples, which is expected given that the synthetic samples aren't chemically cemented. Nevertheless previous studies on the electrical and elastic properties of shales focus on parameters such as porosity, clay content, brine salinity, etc. but the OM parameters studied in this project are very rarely investigated. Comparison with data from previous studies is therefore inherently limited. Another way of testing our results is through modelisation methods such as effective medium property models or finite element simulation of compaction. The existing body of work on these subjects can be applied to the present sample set but it needs to be customized to account for the unique variations OM characteristics that were presented here.

Perspective

With the experience accumulated with the various experiments we were able to point out the limitations of our methods and come up with possible improvements for further work.

First of all the texture of OM in natural shales can take multiple forms that are divided into two categories, that affect the physical properties and the HC production differently: the particulate texture where the OM is deposited into aggregates and the nano-composite texture where extremely small OM particles, that can correspond to individual microorganisms are adsorbed onto the clay particles before the initial deposition. This is important because as we have seen in this project the texture has a strong influence on the elastic and dielectric properties but also because the clay/OM interactions will be very different between these two different types. In the nano-composite texture the OM and the clays will have a very high surface of contact. This has two consequences: (i) the catalysis effect of clays on cracking reactions will increase the HC yield early in the diagenesis and (ii) the mobility of HC will be reduced because of the adsorption of HC into the clay structure. The OM particle texture is thus a crucial information as it will in turn influence the production potential of an unconventional reservoir. In the present samples, even the smallest OM particles are analogous to the particulate texture type. To better highlight the dielectric and elastic behaviour resulting from the smallest OM texture present in natural shales, it would be necessary to develop a new sample preparation technique whereby extremely small OM particles are combined to clay particles to form an indistinguishable mineral/organic matrix.

In addition, the method of incorporation of OM into the samples after maturation is a great way to test for the influence of the intrinsic properties of OM on the physical properties such as the chemical composition, thermal maturity, OM stiffness and internal porosity. However the methodology would have to be modified to account for all the effects that the maturation of OM in-situ has on the surrounding inorganic matrix, such as the microcracks generated by the overpressure due to generated HC, or the stored HC that can result in a contrasting pore fluid content with OM particles porous space being filled with HC while the mineral matrix is water saturated. To do so organic samples need to be produced pre-maturation, then plugs need to be

extracted to undergo maturation in a hydrous pyrolysis apparatus with control of the confining pressure and finally run tests on the final matured plugs.

Besides, the range of maturity level of our samples turned out to be quite narrow, especially for the land OM. To achieve higher maturities, the hydrous pyrolysis apparatus has to be upgraded to be able to sustain higher gas pressure. Indeed the temperature of maturation was limited by the combined pressure of water vapour and HC gas. With a pyrolysis vessel rated for higher pressures we could increase the temperature and reach higher maturities in the same time frame or in even shorter times. Also the high content in functional groups detected in our samples containing fresh OM is not representative of natural consolidated shales. A pre-treatment should be carried out with substances such as hydrochloric acid or hydrofluoric acid that reproduce in a short time frame the hydrolysis undergone by OM at low temperature in the presence of water during early diagenesis (Alpern, 1980). This would in effect break down the functional organic macromolecules to produce OM resembling immature kerogen.

Finally the shortcoming of the sedimentation technique can be addressed in different ways. Its initial objective was to reproduce the natural deposition of shaly sediments. If it allowed the particles to slowly settle and give the solid phase a homogeneous distribution, we noted that the orientation of the particles analysed in the microscopy images was similar to the mixing method. The initial water volume content (95%) may not have been high enough to allow the particles a total degree of freedom at the time of deposition. To increase the initial water content, we would have to increase the height of the extension placed atop the compaction cell. In this case, to avoid a separation of the denser mineral particles and the OM by buoyancy, the OM and the minerals would have to be added in small quantities and alternatively, or find a way to form OM/clay aggregates by adsorption in the case of nano-composite OM texture.

On top of the possibilities of further experimental work, there are also many potential theoretical modelling work to be done with the current data. The synthetic samples are well suited for modelling because they have well known and precisely defined physical parameters. For instance effective medium models of anisotropic elastic and electrical properties could be carried out with four different phase (brine, minerals, clay and OM). The lower stiffness, variable internal porosity and resistivity of the

different types of organic matter could be inputs to the model, and could be the subject of a journal paper. Also, finite element simulation of grain deposition and compaction could help validate the observations made on the samples created with the two different deposition methods. Finally, a technical paper regarding the design of the compaction cell is planned, explaining how the stiffness coefficients, especially c_{13} can be computed continuously during compaction, and how the elastic measurements can be used to study pore pressure effects in shale samples, that have otherwise a very low permeability that makes analysis of fluid flow phenomena challenging.

All in all the data acquired during this project is a needed addition to the field of organic shales rock physics. It is an opportunity to improve the characterization of the elastic and dielectric anisotropy of shales in relation to their organic characteristics. With the four variables investigated and the great stability of other parameters in the data presented here there is a great potential for the modelling of the elastic and dielectric properties as well as establishing innovative cross-property correlations in organic shales. As a result the conclusions of this project could help redefine the assumptions made during the processing of seismic, sonic log and dielectric log data in unconventional reservoirs to reduce errors due to a poor evaluation of OM. Also the relationships between OM and physical properties could help identify the variability of OM within a shale sediment column and select the areas of interest for coring and laboratory analysis. Moreover an important amount of work is necessary to transpose the conclusions obtained on artificial samples to natural samples. This would involve removing the influence of mineral parameters used in well-established models such as the clay type and content from the measured physical properties of well-characterized natural organic shale samples, and analyse the remaining variability in the data in terms of OM characteristics.

List of Figures

List of Tables

References

Ahmadov, R., Vanorio, T. & Mavko, G., 2009. Confocal laser scanning and atomic-force microscopy in estimation of elastic properties of the organic-rich Bazhenov Formation. *The Leading Edge,* 28(1), pp. 18-23.

Allan, A. M., Kanitpanyacharoen, W. & Vanorio, T., 2015. A multiscale methodology for the analysis of velocity anisotropy in organic-rich shale. *Geophysics,* 80(4), pp. C73-C88.

Allan, A. M., Vanorio, T. & Dahl, J. E., 2014. Pyrolysis-induced P-wave velocity anisotropy in organic-rich shales. *Geophysics,* 79(2), pp. D41-D53.

Alpern, B., 1980. *Kerogen: Insoluble organic matter from sedimentary rocks*. Durand B. ed. Paris: TECHNIP.

Altowairqi, Y., Rezaee, R., Evans, B. & Urosevic, M., 2015. Shale elastic property relationships as a function of total organic carbon content using synthetic samples. *Journal of Petroleum Science and Engineering,* Volume 133, pp. 392-400.

Baudin, F., Disnar, J. R., Aboussou, A. & Savignac, F., 2015. Guidelines for Rock–Eval analysis of recent marine sediments. *Organic Geochemistry,* Volume 86, pp. 71-80.

Beloborodov, R. et al., 2016. Compaction of quartz-kaolinite mixtures: The influence of the pore fluid composition on the development of their microstructure and elastic anisotropy. *Marine and Petroleum Geology,* Volume 78, pp. 426-438.

Berryman, J. G., 1979. Long-wave elastic anisotropy in transversely isotropic media. *Geophysics,* 44(5), pp. 896-917.

Biot, M. A., 1941. General theory of three-dimensional consolidation. *Journal of applied physics,* 12(2), pp. 155-164.

Boles, J. R. & Franks, S. G., 1979. Clay diagenesis in Wilcox sandstones of Southwest Texas; implications of smectite diagenesis on sandstone cementation. *Journal of Sedimentary Research,* 49(1), pp. 55-70.

Carcione, J. M., Ursin, B. & Nordskag, J. I., 2007. Cross-property relations between electrical conductivity and the seismic velocity of rocks. *Geophysics*, 72(5), pp. E193-E204.

Cole, K. S. & Cole, R. H., 1941. Cole, K. S., & Cole, R. H. (1941). Dispersion and absorption in dielectrics I. Alternating current characteristics. *The Journal of chemical physics*, 9(4), pp. 341-351.

Comparon, L., 2005. *Étude expérimentale des propriétés électriques et diélectriques des matériaux argileux consolidés*, Paris: Doctoral dissertation. Institut de physique du globe.

Curtis, M. E., Cardott, B. J. & Sondergeld, C. H., 2012. Development of organic porosity in the Woodford Shale with increasing thermal maturity. *International Journal of Coal Geology*, Volume 103, pp. 26-31.

Delle Piane, C. et al., 2015. Texture and diagenesis of Ordovician shale from the Canning Basin, Western Australia: Implications for elastic anisotropy and geomechanical properties. *Marine and Petroleum Geology, 59, 56-71.*, Volume 59, pp. 56-71.

Delle Piane, C. et al., 2018. *Contrasting anisotropy of velocity and electric/dielectric response in the Marcellus and Utica Shales*. SEG Technical Program Expanded Abstracts 2018, Society of Exploration Geophysicists, pp. 3608-3612.

Dewhurst, D. N. et al., 2008. *Elastic, geomechanical and petrophysical properties of shales*. The 42nd US Rock Mechanics Symposium (USRMS), American Rock Mechanics Association.

Dewhurst, D. & Siggins, A., 2006. Impact of fabric, microcracks and stress field on shale anisotropy. *Geophysical Journal International*, 165(1), pp. 135-148.

Dietrich, A. B., 2015. *The impact of organic matter on geomechanical properties and elastic anisotropy in the Vaca Muerta shale*. Doctoral dissertation, Colorado School of Mines. Arthur Lakes Library.

Edwards, A. et al., 2015. *Cemented Shales and their Impact on Exploration, Offshore Newfoundland and Labrador-Identification and Implications*. 77th EAGE Conference and Exhibition 2015.

Emmanuel, S. et al., 2016. Impact of thermal maturation on nano-scale elastic properties of organic matter in shales. *Marine and Petroleum Geology*, Volume 70, pp. 175-184.

Espitalié, J., Deroo, G. & Marquis, F., 1985-86. La pyrolyse Rock-Eval et ses applications. *Revue Institut français du Pétrole*, 40-40-41(5-6-1), pp. 563-579;755-784;73-89.

Ewy, R. T., 2015. Shale/claystone response to air and liquid exposure, and implications for handling, sampling and testing. *International Journal of Rock Mechanics and Mining Sciences,* Volume 80, pp. 388-401.

Gong, F. et al., 2018. Experimental investigation of the effects of clay content and compaction stress on the elastic properties and anisotropy of dry and saturated synthetic shales. *Geophysics,* 83(5), pp. C195-C208.

Guéguen, Y. & Palciauskas, V., 1994. Introduction to the Physics of Rocks. Princeton University Press, p. 392 pp..

Guo, S. J., Zhang, F. H., Song, X. G. & Wang, B., 2015. Deposited sediment settlement and consolidation mechanisms. *Water Science and Engineering,* 8(4), pp. 335-344.

Hetényi, M., 1998. Oxygen index as an indicator of early organic maturity. 29(1-3), 63-77. *Organic geochemistry,* 29(1-3), pp. 63-77.

Hillier, S., 2006. Appendix A. Mineralogical and chemical data, in GM Reeves, I Sims, and JC Cripps eds., Clay materials used in construction: London, Geological Society. *Engineering Geology Special Publications,* Volume 21, pp. 449-459.

Holt, R. M. & Fjær, E., 2003. *Wave velocities in shales–a rock physics model.* 65th EAGE Conference & Exhibition.

Jianzhong, Q. I. N., Baojian, S. H. E. N. & Guoliang, T. A. O., 2014. Hydrocarbon-forming organisms and dynamic evaluation of hydrocarbon generation capacity in excellent source rocks. *Petroleum Geology & Experiment,* 36(4), pp. 465-472.

Johns, W. D., 1979. Clay mineral catalysis and petroleum generation. *Annual Review of Earth and Planetary Sciences,* 7(1), pp. 183-198.

Johns, W. D., 1979. Clay mineral catalysis and petroleum generation. *Annual Review of Earth and Planetary Sciences,* 7(1), pp. 183-198.

Josh, M., 2014. Dielectric permittivity: A petrophysical parameter for shales. *Petrophysics,* 55(04), pp. 319-332.

Josh, M., 2017. *Dielectric and Acoustic Properties with a Single Laboratory Instrument.* Vienna, International Symposium of the Society of Core Analysts.

Josh, M., Clennell, B. & Cauchefert, M., 2016. *Dielectric permittivity and anisotropy of intact multi-saturated organic shales.* SPWLA 57th Annual Logging Symposium, Society of Petrophysicists and Well-Log Analysts.

Josh, M. et al., 2012. Laboratory characterisation of shale properties. *Journal of Petroleum Science and Engineering,* Volume 88, pp. 107-124.

Kaarsberg, E. A., 1959. Introductory studies of natural and artificial argillaceous aggregates by sound-propagation and X-ray diffraction methods. *The Journal of Geology,* 67(4), pp. 447-472.

Labani, M. M. & Rezaee, R., 2015. The importance of geochemical parameters and shale composition on rock mechanical properties of gas shale reservoirs: A case study from the Kockatea Shale and Carynginia Formation from the Perth Basin, Western Australia. *Rock Mechanics and Rock Engineering,* 48(3), pp. 1249-1257.

Law, C. A., 1999. Chapter 6: Evaluating Source Rocks. In: E. Foster, A. Beaumont & H. Norman, eds. *Treatise of Petroleum Geology/Handbook of Petroleum Geology: Exploring for Oil and Gas Traps.* The American Association of Petroleum Geologists, pp. 6-1 - 6-41.

Lee, M., 2003. *Velocity ratio and its application to predicting velocities.* US Department of the interior, US Geological Survey.

Lewan, M. D., 1992. Water as a source of hydrogen and oxygen in petroleum formation by hydrous pyrolysis. *Am. Chem. Soc. Div. Fuel Chem,,* Volume 37, pp. 1643-1649.

Luan, X. et al., 2016. Creation of synthetic samples for physical modelling of natural shale. *Geophysical Prospecting,* 64(4), pp. 898-914.

Lyons, W.C., Plisga, G.J., 1984. Standard Handbook of Petroleum and Natural Gas Engineering. Gulf Professional Publishing, MA, USA.

Massicano, F. et al., 2009. *Analysis of CT and PET/SPECT images for dosimetry calculation*. Rio de Janeiro, Associacao Brasileira de energia nuclear.

McTavish, R., 1978. Pressure retardation of vitrinite diagenesis, offshore north-west Europe. *Nature, 271, 1978, pp 648-650.*, 271(5646), p. 648.

Mesri, G. & Rokhsar, A., 1974. Theory of consolidation for clays. *Journal of Geotechnical and Geoenvironmental Engineering*, Volume 100, p. (10740 Proc Paper).

Mondol, N. H., 2012. *Velocity anisotropy in experimentally compacted clay-silt and clay-clay mixtures*. SEG Technical Program Expanded Abstracts 2012, Society of Exploration Geophysicists, pp. 1-5.

Mondol, N. H., Bjørlykke, K., Jahren, J. & Høeg, K., 2007. Experimental mechanical compaction of clay mineral aggregates—Changes in physical properties of mudstones during burial. *Marine and Petroleum Geology*, 24(5), pp. 289-311.

Musharfi, N. et al., 2012. *Combining wireline geochemical, NMR, and dielectric data for formation evaluation and characterization of shale reservoirs*. Society of Petrophysicists and Well-Log Analysts.

Nimmo, J. R., 2013. *Porosity and Pore Size Distribution. Reference Module in Earth Systems and Environmental Sciences.*, Elsevier.

Ogebule, O. Y., Mondol, N. H. & Jahren, J., 2015. *Seal Integrity of Late Jurassic to Early Cretaceous Mudrocks of the South-Western Barents Sea Area*. 77th EAGE Conference and Exhibition 2015.

Orem, W. H. & Finkelman, R. B., 2003. (2003). Coal formation and geochemistry. *Treatise on geochemistry*. p. 407.

Patchett, J. G., 1975. *An investigation of shale conductivity*. SPWLA 16th Annual Logging Symposium, Society of Petrophysicists and Well-Log Analysts.

Pepper, A. S. & Dodd, T. A., 1995. Simple kinetic models of petroleum formation. Part I: oil and gas generation from kerogen. *Marine and Petroleum Geology,* 12(3), pp. 291-319.

Pervukhina, M. & Rasolofosaon, P. N., 2015. *Burial/compaction and seismic anisotropy in shaly formations.* 77th EAGE Conference and Exhibition 2015.

Petersen, H. I., Lindström, S., Nytoft, H. P. & Rosenberg, P., 2009. Composition, peat-forming vegetation and kerogen paraffinicity of Cenozoic coals: Relationship to variations in the petroleum generation potential (Hydrogen Index). *International Journal of Coal Geology,* 78(2), pp. 119-134.

Peters, K., Xia, X., Pomerantz, A. & Mullins, O., 2016. Geochemistry Applied to Evaluation of Unconventional Resources. *Unconventional Oil and Gas Resources Handbook: Evaluation and Development.*

Philp, R. P., 2003. Formation and geochemistry of oil and gas. Volume 7, p. 407.

Pytte, A. M. & Reynolds, R. C., 1989. *The thermal transformation of smectite to illite. In Thermal history of sedimentary basins (pp. 133-140).* New York, NY, Springer, pp. 133-140.

Rahman, H. M., Kennedy, M., Löhr, S. & Dewhurst, D. N., 2017. Clay-organic association as a control on hydrocarbon generation in shale. *Organic geochemistry,* Volume 105, pp. 42-55.

Rahman, H. M., Kennedy, M., Löhr, S. & Dewhurst, D., 2018. The influence of shale depositional fabric on the kinetics of hydrocarbon generation through control of mineral surface contact area on clay catalysis. *Geochimica et Cosmochimica Acta,* Volume 220, pp. 429-448.

Rich, J. L., 1951. Three critical environments of deposition, and criteria for recognition of rocks deposited in each of them. *Geological Society of America Bulletin,* 62(1), pp. 1-20.

Sayers, C. M., 2013. The effect of kerogen on the elastic anisotropy of organic-rich shales. *Geophysics,* 78(2), pp. D65-D74.

Sayers, C. M., Guo, S. & Silva, J., 2015. Sensitivity of the elastic anisotropy and seismic reflection amplitude of the Eagle Ford Shale to the presence of kerogen. *Geophysical Prospecting,* 63(1), pp. 151-165.

Seleznev, N. V., 2005. *Theoretical and laboratory investigation of dielectric properties of partially saturated carbonate rocks.* DUP Science.

Stern, O., 1924. The theory of the electrolytic double-layer. *Z. Elektrochem,* 30(508), pp. 1014-1020.

Tannenbaum, E., Huizinga, B. J. & Kaplan, I. R., 1986. Role of minerals in thermal alteration of organic matter--II: a material balance. *AAPG bulletin,* 70(9), pp. 1156-1165.

Taylor, D. W., 1942. *Research on consolidation of clays.* Cambridge(Massachussets): Massachusetts Institute of Technology.

Taylor, J. R., 1982. *An Introduction to Error Analysis: The Study of Uncertainties in Physical Measurements.* Sausalito(CA): University Science Books.

Thomsen, L., 1986. Weak elastic anisotropy. *Geophysics,* 51(10), pp. 1954-1966.

Tsvankin, I., 2001. Seismic Signatures and analysis of Reflection Data in Anisotropic Media. *Elsevier Handbook of Geophysical Exploration.*

Vernik, L. & Landis, C., 1996. Elastic anisotropy of source rocks: Implications for hydrocarbon generation and primary migration. *AAPG bulletin,* 80(4), pp. 531-544.

Vernik, L. & Liu, X., 1997. Velocity anisotropy in shales: A petrophysical study. *Geophysics,* 62(2), pp. 521-532.

Vernik, L. & Milovac, J., 2011. Rock physics of organic shales. *The Leading Edge,* 30(3), pp. 318-323.

Vernik, L. & Nur, A., 1992. Ultrasonic velocity and anisotropy of hydrocarbon source rocks. *Geophysics,* 57(5), pp. 727-735.

Voltolini, M. et al., 2008. Anisotropy of experimentally compressed kaolinite-illite-quartz mixtures. *Geophysics,* 74(1), pp. D13-D23.

Von Hippel, A., 1954. *Dielectric Materials and their Applications.* The Technology Press of M.I.T..

Waters, E. R., 2003. Molecular adaptation and the origin of land plants. *Molecular phylogenetics and evolution,* 29(3), pp. 456-463.

Yan, F. & Han, D. H., 2013. *Measurement of elastic properties of kerogen.* Society of Exploration Geophysicists, pp. 2778-2782.

Appendices

A- Conference papers

Josh, M., Clennell, B., Cauchefert, M., & Han, T. (2016, June). Dielectric permittivity and anisotropy of intact multi-saturated organic shales. In *SPWLA 57th Annual Logging Symposium (Reykjavik 25-29 June 2016)* (pp. 1-14).

Cauchefert, M., Josh, M., Esteban, L., Vialle, S., Lebedev, M., Dautriat, J. & Maney, B. (2018). Impact of artificially matured organic matter on the dielectric and elastic properties of compacted shales. *ASEG Extended Abstracts*, *2018*(1), 1-8.

B- Main results obtained with earlier sample sets

B-1- Synthetic shale samples containing Paraffin as organic material

The results obtained with these samples was published in *SPWLA 57th Annual Logging Symposium*. The organic material used (Paraffin) is an excellent electrical insulant. It is not representative of the electrical properties of OM occurring naturally in shales, and therefore, these results weren't used in the main body of the thesis.

"*The relationship between TOC and anisotropy was investigated using a batch of synthetic shales to achieve a more consistent and quantifiable level of TOC, with better control over the form factor and orientation of the organic content.*

The samples were manufactured using an equal mixture of kaolinite and 70 µm quartz flour mixed with paraffin wax, which was shaved to produce flattened slivers of inert organic material with a highly oblate form factor. A small amount of Portland cement was added to the mixture which was then evacuated then mixed with water, evacuated to remove air bubbles and then pressed at 20 MPa uniaxial stress and allowed to set. Dielectric analysis was performed on both orientations using sliced discs Figure 0-1.

It is clear from that the organic matter does have an effect of enhancing the dielectric anisotropy of shales. Anisotropy in shales is frequently attributed to the clay particle alignment, but non-clay silt alignment is also important and in organic rich shales, a far larger contribution can come from aligned organic matter that blocks conduction pathways and leads to extremely high tortuosity in the (vertical) direction transverse to bedding. The degree of anisotropy, for a given amount of organic matter depends on frequency."

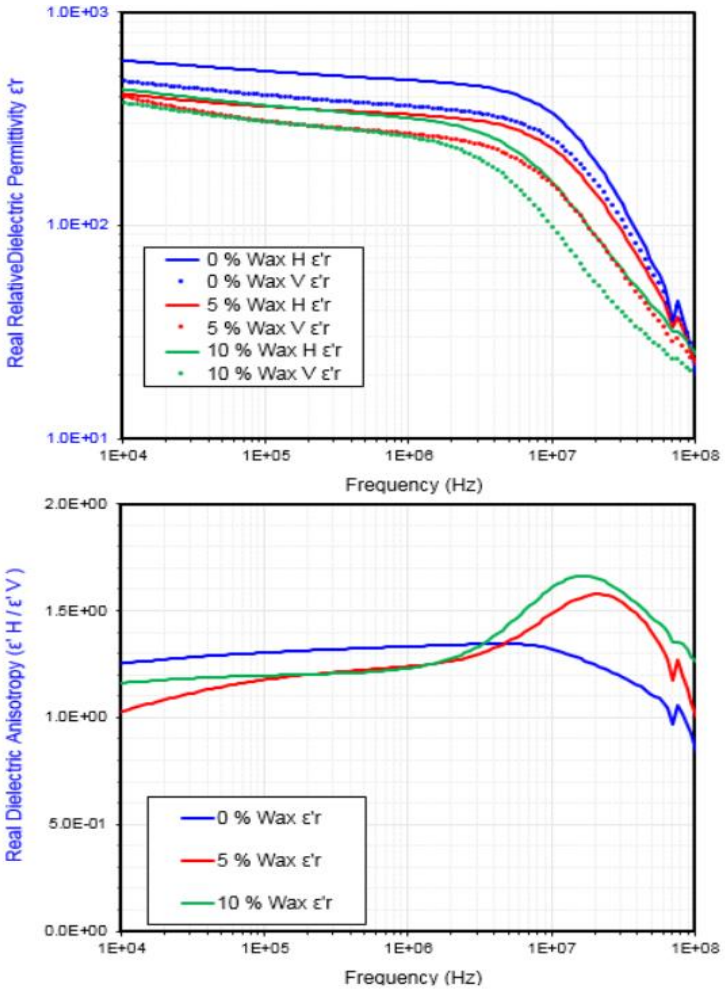

Figure 0-1: (a) real permittivity dispersion curves and (b) anisotropy values for artificial shale samples loaded with wax. Anisotropy is greater than 1 across all frequencies and for the wax loaded samples, demonstrates a peak at approximately 20 MHz. At all frequencies above approximately 5 MHz the anisotropy is increasing with the amount of wax added which as suggestedin figure 4. Furthermore the anisotropy remains consistent with paraffin up to beyond 100 MHz, which in the frequency range of the currentgeneration of dielectric logging tools on the market

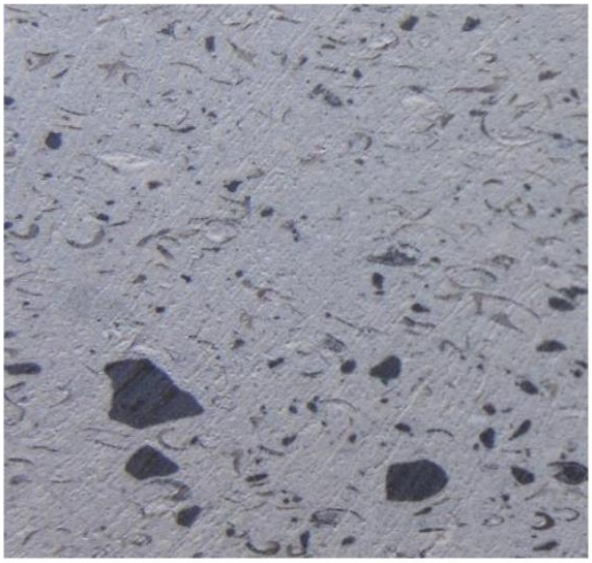

Figure 0-2: Photograph of the "horizontal" synthetic shale with 5 % wax. The flattened and sometimes curly objects in the photo are the wax material that were used to achieve a macroscopic version of organic matter in a resource shale. Field of view 20 mm.

B-2- Synthetic shale samples containing land OM

The results obtained with these samples were published in *ASEG Extended Abstracts, 2018. These 3 synthetic samples were fabricated in a similar manner as described in the main body of the thesis. One sample was lean, and two samples contained organic matter. Moreover, one of the two organic samples contained matured OM by hydrous pyrolysis, as described in Section3-2-. The OM was the same land OM described earlier (Canadian sphagnum peat moss from Nova Scotia) and the compaction was carried out with the same compaction cell described in Chapter 3. The mineral composition and compaction parameters are shown in* Table 0-1 and Table 0-2, *respectively. The porosity curves of the samples are visible in* Figure 0-3.

Sample name	Dry mineral composition (wt%)				
	Quartz	K-Feldspar	Calcite	Clay (Kaolinite)	Organic (immature /mature peat)
lean	20	10	10	60	0
M0	18.2	9.1	9.1	54.7	8.9
M1	18.3	9.1	9.1	54.7	8.8

Table 0-1: Mineral composition of each sample. M0 stands for maturity 0, the sample containing immature peat whereas M1 is the sample containing artificially matured peat. The lean sample is the inorganic witness sample.

Sample name	porosity (%)				maximum vertical stress (Mpa)	pore fluid salinity (g/L)	First phase @1MPa (hours)
	initial	At the end of the first phase	final under stress	final unconfined			
lean (no OM)	79.42	46.7	34.9	37.4	10.2	14.5	11.7
M0	78.99	50.6	36.5	38.8	10.2	15.1	6.5
M1	78.84	50.9	37.2	39.5	10.2	15.3	6.2

Table 0-2: information summary from the compaction experiments.

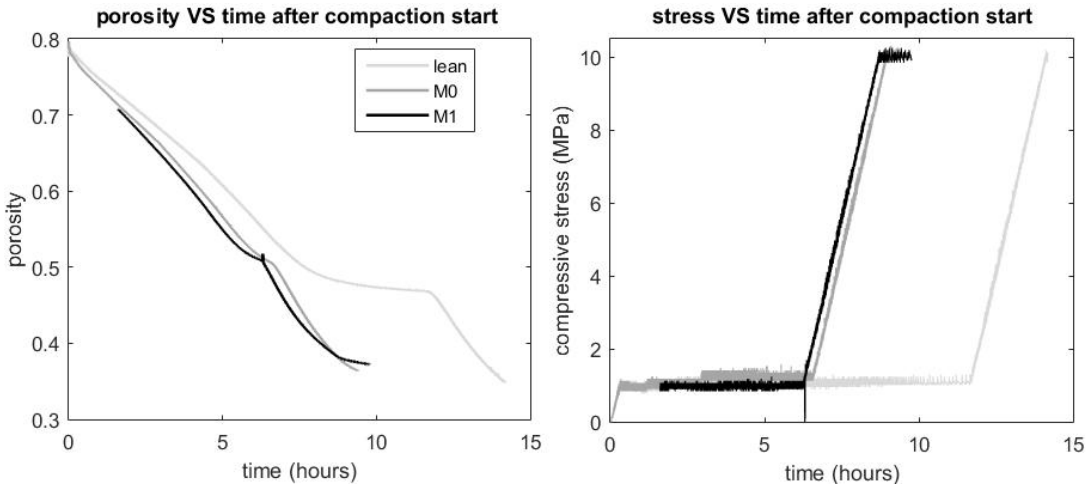

Figure 0-3: Porosity (left) and compressive stress (right) evolution during the compaction experiments. The arrows show the inflexion of the porosity curve at the end of the liquid phase.

The main results of this sample set was that *"highly immature peat when compacted in a shale mineral matrix seems to lessen the development of elastic anisotropy, whereas matured peat doesn't (*Figure 0-4*). Also organic-rich samples decrease the electrical conductivity anisotropy (*Figure 0-5*), and the more mature sample is more conductive than its immature counterpart. Finally, OM appears to strongly influence the imaginary dielectric permittivity at low frequencies, effectively reversing it with increasing maturity."*

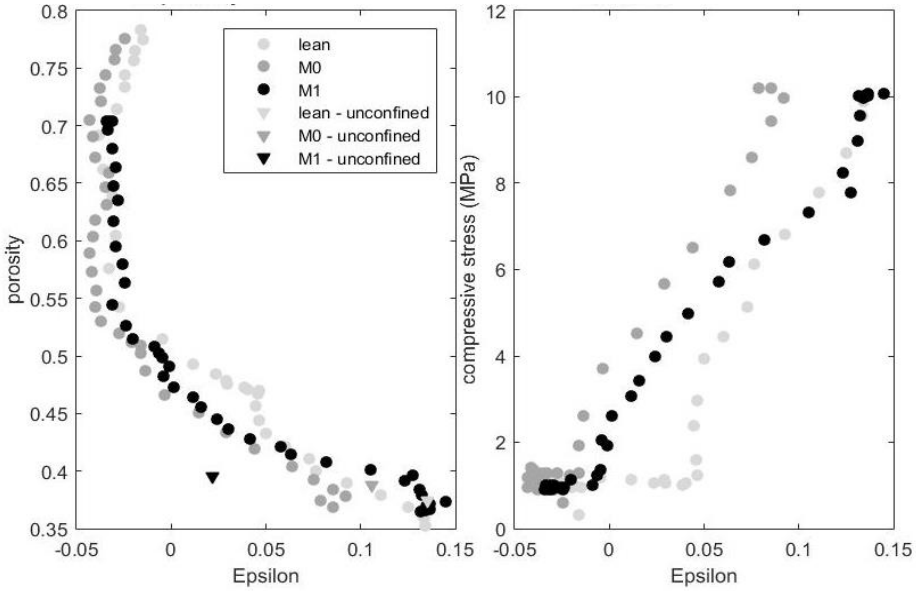

Figure 0-4: Porosity (left) and compressive stress (right) as a function of Thomsen's anisotropy parameter ε.

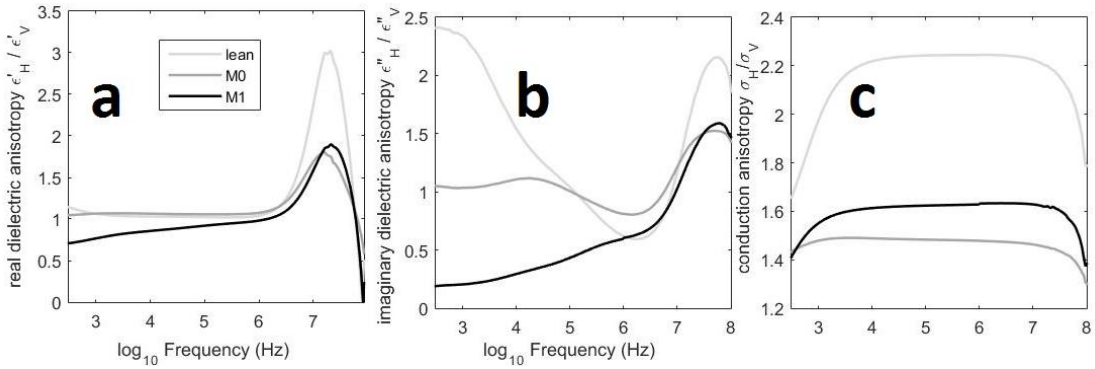

Figure 0-5: Anisotropy of the real permittivity, imaginary permittivity and the equivalent conductivity for each sample.

However there were several issues with this sample set that prevented the inclusion of this results in the main body of the thesis. i) The volume content of clay was constant when considering the inorganic phase only, but after inclusion of OM in the samples, the volume ratio of clay in the whole sample was smaller for the organic samples than for the control lean sample. Therefore the properties measured are not only the result of different organic contents but also of a varying clay content. Furthermore, the duration of the compaction experiments (shown in Figure 0-3) was too short for the sample to reach a near equilibration of pore pressure and thus the samples presented a pressure gradient that induced an inhomogeneity of the porosity and consolidation state throughout the samples that is difficult to quantify.